Use of a Helicon Source for Development of a Re-Entry Blackout Amelioration System

by

Kristina Marian Lemmer

A dissertation submitted in partial fulfillment
of the requirements for the degree of
Doctor of Philosophy
(Aerospace Engineering)
in The University of Michigan
2009

Doctoral Committee:

Professor Alec D. Gallimore, Chair
Professor Iain D. Boyd
Associate Professor John E. Foster
Peter Peterson, ElectroDynamic Applications, Inc.

To my mom. She has been there every step of the way. She has been by my side through the good times and offered a shoulder through the difficult.

ACKNOWLEDGEMENTS

As I write this massive document that is the culmination of almost six years of my life, I am deeply humbled by all the love and support that I have received throughout this process. From family to friends, advisors to fellow lab mates, I cannot thank you all enough for all you have done.

Of course I must begin with thanking my advisor, Professor Alec Gallimore, from the bottom of my heart. I think he realized what I wanted before even I knew. I met Alec when I first came to the University of Michigan as a senior in high school visiting campus. From that day forward, he has been a fantastic mentor throughout my years at UM. Beginning as my professor for various undergraduate classes, I moved up through the ranks from undergraduate researcher all the way to senior lab member at PEPL. The entire way, he supported me, not only financially, but emotionally and as a mentor as well. Alec gave me the freedom to make the necessary mistakes so that I could learn, but he never let me fall too far (I'll let that little mishap with prelims slide). I cannot say it enough, but Thanks!

I would also like to give thanks to the other members of my thesis committee: Professor Iain Boyd, Professor John Foster and Dr. Peter Peterson. You have been there to answer questions and guide me in the right direction. Your advice has been invaluable and this thesis would never have been finished without your knowledge and contributions.

Within the Aerospace Engineering Department, there are countless people to thank. Suzanne and Denise were always there to help me out with ordering stuff or fixing my account. To Michelle, Lisa, Cindy, Cindy and Margaret, thanks for everything. Many thanks go to Dave McLean and Tom Griffin who got the very fun job of dealing with my meltdowns when the "big blue scary box" would freak out. Terry built me some fantastic flanges and probes. I could not have finished this thesis without his amazing skills. Support for this research came from many different people and foundations. I would like to begin by thanking the NASA CUIP program, and Bonnie Bryant and the Michigan Space Grant Consortium. Bonnie provided much more than just funding. She has been a friend and mentor to me as well. That amazing grant allowed me to go to Australia to learn about helicon sources and to do a "bit of traveling." Additional funding came from Zonta International and the Amelia Earhart Fellowship, the Rackham Graduate School and the Susan Lipshultz Award and various GSI positions within the Aerospace Engineering Department.

I need to thank the folks over at ElectroDynamic Applications Inc. Along with funding much of the equipment used for this research, Pete, Dean, Jonathan and especially Chris have been very helpful in finishing this up. Thanks Chris for being patient with me and explaining the ins and outs of the network analyzer.

PEPL has been a truly awesome place to work. I have made some great friends while working there. I learned from the best and hope to pass my current knowledge down to the best. I would like to start by thanking past PEPL students: Brian Beal, Mitchell Walker, Dan (Hermo) Herman, Jesse Linnell, Allen (Abs) Victor, Dave (Floppy) Kirtley (yeah Smallville and Jimmy Johns!), Prashant Patel and Bryan Reid ("Quiet"). I also give thanks to Tim Smith (your expertise has been invaluable on many occasions) and the current PEPL students: Robbie (LT) Lobbia, Dan Brown, Tom Liu, Adam Shab...um... (who not only baby-sat me for countless hours in the lab, but was integral in getting this thesis completed), Dave (Shuffles) Huang, Laura Spencer, Mike McDonald, Ricky Tang, Rohit (Giggles, Damien, Doomed) Shastry, Bailo Ngom, Ray Liang and Roland (I still can't believe you sorted through the wire box of terror!) Florenz. Thanks to those of you who babysat all those hours so that if I fried myself, or god forbid three hundred pounds of magnets fell on me, somebody would be around to take me to the hospital, and than you Sonca Nguyen for being that person to take me to the hospital and for staying with me. To the new PEPL students: make sure you learn all you can from those who've come before you. It will serve you well in the future. When I joined PEPL, the only machining skills I had were "righty tighty, lefty loosey," and look at me now (we're going to just go ahead and ignore that magnet incident).

Without the friends I've made and kept in contact with, these last years would have been pretty unbearable. I'll start with my best friend from the day I was born (she's a month older than me), Laurie. No matter what happens, I know she's there for me. Guess what babe, we're both out of school and on to the real world. Floppy, we've had some awesome times together, and I can't wait for more. You could not have found yourself a better woman than Ellie, I love you both (even though you leave the cupboard doors open Ellie). Tristan, you have been a wonderful friend to me for the past nine years. We've been through a lot together and we'll continue to make memories in the future. You found yourself a fantastic person in Meghan, and I look forward to many skiing trips with you both in the future. Jonny Blow...what can I say. You got me through undergrad, both academically and socially. You're always good for some random comment. I can't wait for my next conference in an exotic location so we can continue our travels and ski trips. Prashant, those years living with you made me a little bit fatter and a lot bit happier. You are a great and generous friend. Alex, Adam and Danny you have been great fun to hang out with and the Ice Devoring Sex Tornados will live forever! Adam, thanks in advance for letting me crash at your place in Germany (anybody know where the bald Canadian lives in this town?). Elena, Hyce and Erin have been great girlfriends in a world where I'm surrounded by males. Dean, although we haven't been friends all that long, you have made this last year great fun as my friends continued to leave me behind. I have to acknowledge the Babes n' Bums Ski Team regulars (Steve, Tim, Brian K. and Brian S.) for keeping me grounded in the real world. I have looked forward to Thursday nights at Timber Ridge for the past six years. Thank you Colin, you are an amazing person. Jan...what can I say. You have been a good friend to both my mom and I. You not only let me live with you that summer out in LA, but you have let me stay in your Ann Arbor place for the past nine months. I cannot thank you enough.

Finally, I thank my family. My mom has been my best friend and my support throughout this whole process. She encouraged me when I wanted to quit and stood by me when I wasn't sure if I would continue. In the end, I knew she would be there for me no matter what I chose to do. Thanks for helping me to make the correct decision. I hope that one day, I have half the relationship with my children that I have with you. I don't think I can ever express the gratitude and love I have for you. I thank my dad for his continual encouragement. From the time you took me to Kennedy and I decided I wanted to be an astronaut, you have stood behind me. I thank you for driving me down to space camp and for your continual support. I love you. Thanks brother for getting married in the Dominican Republic, for marrying such an awesome sister-in-law and for your many hours fixing the escort.

Lastly, I need to thank Wikipedia and everyone who contributed to the endless

articles that I have “researched” on there. From finding the size of a low-frequency antenna, to finding out that Pukaki is not only a real place, but the portal to New Zealand’s Mt. Cook National Park, that website has saved me, and cost me, countless hours.

TABLE OF CONTENTS

DEDICATION . . . . **ii**

ACKNOWLEDGEMENTS . . . . **iii**

LIST OF FIGURES . . . . **xi**

LIST OF TABLES . . . . **xv**

LIST OF APPENDICES . . . . **xvi**

NOMENCLATURE . . . . **xvii**

CHAPTER

1. Introduction **1**

1.1 Motivation 1
1.2 Goals and Contribution of Research 4
1.3 Organization 5

2. Background **7**

2.1 Communications Blackout 7
2.1.1 Physical Understanding 8
2.1.2 Plasma Frequency Derivation 9
2.1.3 Electromagnetic Wave Interaction 11
2.2 Previous Hypersonic Experiments and Models 12
2.3 Previous Blackout Amelioration Research 14
2.4 Atmospheric Re-entry Parameters 16
2.5 Summary of Background 20

3. Simulating an Atmospheric Re-Entry Plasma **21**

3.1 Plasma Source Selection 21
3.2 Helicon Source Theory 25
3.3 PEPL Helicon Source Design 27
3.4 PEPL Helicon Source Final Setup 33

3.5 Summary of Simulating an Atmospheric Re-Entry Plasma 36

4. Plasma Mitigation System 38

4.1 ReComm System Theory of Operation 38
4.1.1 Electrostatic Sheath 39
4.1.2 E × B Drift 40
4.2 Concurrent Computer Simulation Work 42
4.3 ReComm System Setup 44
4.4 Summary of Plasma Mitigation System 50

5. Facilities, Diagnostics and Analysis Techniques 52

5.1 Cathode Test Facility (CTF) 52
5.2 Experimental Layout 54
5.3 Diagnostic Tools 55
5.3.1 Single Cylindrical Langmuir Probe 57
5.3.1.1 Radio Frequency Compensation and Probe Tips . 58
5.3.1.2 Langmuir Probe Theory of Operation 61
5.3.1.3 Langmuir Probe Data Acquisition 62
5.3.1.4 Langmuir Probe Data Analysis 63
5.3.1.5 Environmental Effects 67
5.3.1.6 Error Analysis 69
5.3.2 Hairpin Resonance Probe 70
5.3.3 Signal Attenuation Probe 75
5.3.4 Retarding Potential Analyzer 77
5.3.4.1 RPA Data Analysis 79
5.3.4.2 RPA Verification with a Gridded Ion Source . . . 81
5.3.4.3 RPA Error Analysis 82
5.3.4.4 PEPL RPA 83
5.3.4.5 Micro RPA Version 1 85
5.3.4.6 Micro RPA Version 2 87
5.4 Summary of Facilities, Diagnostics and Analysis Techniques 89

6. Helicon Source Characterization 90

6.1 Helicon Mode Confirmation 90
6.2 Downstream Plasma Characterization 93
6.2.1 Plasma Characterization with an Empty Vacuum Chamber 93
6.2.2 Plasma Characterization with ReComm System Downstream 98
6.3 Ion Energy Distribution Function 104
6.4 Summary of Helicon Source Characterization 107

7. ReComm System Effect 109

7.1 Density Reduction . . . 110
7.2 Plasma Frequency . . . 116
7.3 Signal Attenuation . . . 118
7.4 Comparison with Simulation Data . . . 125
7.5 Electric Field Effects . . . 130
7.6 Summary of ReComm System Effect . . . 131

8. ReComm System Magnetic Field Effects . . . 133

8.1 Plasmadynamics in a Non-Uniform Magnetic Field . . . 134
8.2 COMSOL Modeling of ReComm System . . . 137
8.3 Summary of ReComm System Magnetic Field Effects . . . 145

9. Conclusions . . . 147

9.1 Helicon Source Development . . . 148
9.2 ReComm System Development . . . 148
9.3 Helicon Source Plasma Properties . . . 149
9.4 ReComm System Effect . . . 150
9.5 System Impact . . . 152
9.6 Suggestions for Future Work . . . 154

APPENDICES . . . 158

BIBLIOGRAPHY . . . 204

ABSTRACT . . . 214

LIST OF FIGURES

Figure

1.1	Sketch of Tracking and Data Relay Satellite	2
1.2	Genesis Capsule After Re-entry	3
2.1	RAM-C Re-Entry Capsule Layout	16
2.2	Electron Number Density the in RAM-C Plasma Sheath	17
2.3	Electron Temperature in the RAM-C Plasma Sheath	18
2.4	Re-Entry Capsule Bow Shock and Boundary Layer Locations During Hypersonic Flight	19
3.1	Photography of the Helicon Source First Attempt	28
3.2	Photograph of the Pi-Style Matching Network	31
3.3	Photography of the Boswell-Type Antenna	31
3.4	Axial (y-direction) Magnetic Field Strength Along Helicon Centerline	32
3.5	Photograph of the Double-Helix Half-Wavelength Antenna	33
3.6	Electrical Layout of PEPL Helicon Source	34
3.7	Photographs and Schematic of Final Version of PEPL Helicon Source	35
4.1	Plasma Mitigation Concept	40
4.2	Particle Motion in an $E \times B$ Field	42
4.3	Schematic Drawing of the ReComm System	44
4.4	ReComm System Magnetic Field Vector Plot	46
4.5	ReComm System Peak B_z	47
4.6	Modeled ReComm and Helicon Source Magnetic Fields	47
4.7	Contour Plots of the Total Magnetic Field Strength for No ReComm System Magnetic Field and Peak ReComm System Magnetic Field	48
4.8	Photograph of the ReComm System	50
5.1	Photograph of the Cathode Test Facility	53
5.2	Experimental Layout	54
5.3	Langmuir Probe I-V Characteristic Example	58
5.4	RF Compensation of the Langmuir Probes	59
5.5	Hiden Langmuir Probe Tip	60
5.6	PEPL Langmuir Probe Tip	61
5.7	Smoothed Langmuir Probe I-V Curve	63
5.8	Example of a Saturated and an Unsaturated I-V Curve	66
5.9	Hairpin Resonance Probe Photograph and Schematic	70
5.10	Hairpin Probe Layout	71

5.11 Sample Reflected Power Trace from the Hairpin Probe 71
5.12 Dielectric Constant ϵ, Response to the Ordinary and Extraordinary waves 73
5.13 Photograph of the S2-1 Probe 75
5.14 S2-1 Probe Layout 76
5.15 Example S2-1 trace 77
5.16 RPA Schematic Drawing 78
5.17 Potential and Circuit Diagram for a Four Grid RPA 80
5.18 Sample of a current vs. voltage sweep from an RPA 81
5.19 Normalized RPA Curve Measured Downstream of the Ion Gun . . . 82
5.20 Example of Errors Associated with RPAs 83
5.21 PEPL RPA Photograph and Schematic 85
5.22 Micro RPA Version 1 Photograph and Schematic 86
5.23 Micro RPA Version 2 Photograph and Schematic 88
6.1 Verification of Helicon Mode Operation 92
6.2 Photographs of Helicon Mode Confirmation 93
6.3 Helicon Source Characterization Testing Location 94
6.4 Ion Number Density Downstream - Empty Chamber 95
6.5 Electron Temperature Downstream - Empty Chamber 96
6.6 Plasma Potential Downstream - Empty Chamber 97
6.7 Ion Number Density Downstream - ReComm System Present 99
6.8 Ion Number Density Downstream - Comparison With and Without ReComm System 100
6.9 Electron Temperature Downstream - ReComm System Present . . . 101
6.10 Electron Temperature Downstream - Comparison With and Without ReComm System 102
6.11 Plasma Potential Downstream - ReComm System Present 103
6.12 Plasma Potential Downstream - Comparison With and Without ReComm System 104
6.13 Plasma Potential and Most Probable Ion Voltage 105
7.1 B_z Along the Two Planes where Plasma Mitigation Data were Found 110
7.2 Percent Density Reduction for 925 G Peak Magnetic Field at z = -70 mm 111
7.3 Percent Density Reduction for 925 G Peak Magnetic Field at z = -75 mm 112
7.4 Percent Density Reduction for 1385 G Peak Magnetic Field at z = -70 mm 113
7.5 Percent Density Reduction for 1385 G Peak Magnetic Field at z = -75 mm 113
7.6 Percent Density Reduction for 1850 G Peak Magnetic Field at z = -70 mm 115
7.7 Percent Density Reduction for 1850 G Peak Magnetic Field at z = -75 mm 116

7.8 Plasma Frequency for 2000 G Peak Magnetic Field at z = -75 mm and x = 0 mm . . . 117
7.9 Comparison of Plasma Frequency Measurements from Hairpin Probe and the Minimum of S2-1 Response Curve . . . 120
7.10 Relative S2-1 Response as a Function of Signal Input Frequency at y = 360 mm (trial 2) . . . 121
7.11 Relative S2-1 Response as a Function of Signal Input Frequency at y = 370 mm (trial 2) . . . 121
7.12 Relative S2-1 Response as a Function of Signal Input Frequency at y = 380 mm (trial 2) . . . 122
7.13 Relative S2-1 Response as a Function of Signal Input Frequency at y = 390 mm (trial 2) . . . 122
7.14 Relative S2-1 Response as a Function of Signal Input Frequency at y = 350 mm (trial 1) . . . 123
7.15 Relative S2-1 Response as a Function of Signal Input Frequency at y = 360 mm (trial 1) . . . 123
7.16 Relative S2-1 Response as a Function of Signal Input Frequency at y = 370 mm (trial 1) . . . 124
7.17 Relative S2-1 Response as a Function of Signal Input Frequency at y = 380 mm (trial 1) . . . 124
7.18 Relative S2-1 Response as a Function of Signal Input Frequency at y = 390 mm (trial 1) . . . 125
7.19 Relative S2-1 Response as a Function of Signal Input Frequency at y = 400 mm (trial 1) . . . 125
7.20 Simulation Results: Density Reduction as a Function of y and z-Positions . . . 127
7.21 Simulation Results: Density Reduction as a Function of y-Position and Magnetic Field Strength . . . 128
7.22 Simulation Results: Density Reduction as a function of Cathode Potential . . . 129
7.23 Expected vs. Actual Potential Drop Between Electrodes . . . 130
8.1 Solid Frame Model and Generated Mesh for ReComm COMSOL Modeling . . . 137
8.2 Electric Field and Potential Map Modeled by COMSOL when V_c = -250 V . . . 138
8.3 Magnetic Field Modeled by COMSOL . . . 139
8.4 Electron Particle Tracing Using COMSOL . . . 141
8.5 Electron Particle Tracing Using COMSOL . . . 142
8.6 Electron Particle Tracing Using COMSOL . . . 143
8.7 Electron Particle Tracing Using COMSOL . . . 143
8.8 Electron Particle Tracing Using COMSOL . . . 144
8.9 Electron Particle Tracing Using COMSOL . . . 144
8.10 Electron Particle Tracing Using COMSOL . . . 145
8.11 Electron Particle Tracing Using COMSOL . . . 145

9.1 Diagram Showing Region of Greatest ReComm System Effect . . . 152
A.1 Langmuir Probe Analysis Flow Chart 160
B.1 Residual Gas Analyzer Setup 162
B.2 Species Molar Concentration as a Function of Helicon Source Input Power 163
D.1 Ion Number Density Downstream - Empty Chamber for z = -10 mm, -20 mm, -40 mm, -50 mm and -70 mm 193
D.2 Electron Temperature Downstream - Empty Chamber for z = -10 mm, -20 mm, -40 mm, -50 mm and -70 mm 194
D.3 Plasma Potential Downstream - Empty Chamber for z = -10 mm, -20 mm, -40 mm, -50 mm and -70 mm 195
D.4 Ion Number Density Downstream - ReComm System Present for z = -10 mm, -20 mm, -40 mm, and -50 mm 196
D.5 Electron Temperature Downstream - ReComm System Present for z = -10 mm, -20 mm, -40 mm, and -50 mm 197
D.6 Plasma Potential Downstream - ReComm System Present for z = -10 mm, -20 mm, -40 mm, and -50 mm 198
E.1 Density Reduction as a function of y-position and cathode voltage along x = -20 mm for B_z = 925 G. 200
E.2 Density Reduction as a function of x and y-position, and cathode voltage along the line $x = y - 390$ for B_z = 925 G. 200
E.3 Density Reduction as a function of y-position and cathode voltage along x = -20 mm for B_z = 1385 G. 201
E.4 Density Reduction as a function of x and y-position, and cathode voltage along the line $x = y - 390$ for B_z = 1385 G. 201
E.5 Density Reduction as a function of y-position and cathode voltage along x = -20 mm for B_z = 1800 G. 202
E.6 Density Reduction as a function of x and y-position, and cathode voltage along the line $x = y - 390$ for B_z = 1800 G. 203

LIST OF TABLES

Table

3.1	Plasma Parameters of PEPL Sources	22
3.2	Plasma Parameters of Various Plasma Generators	23
4.1	Maximum ReComm System Vertical Magnetic Field Strength for Various Input Currents	45
4.2	Maximum Possible Potential Difference Between the Electrodes	50
5.1	Diagnostic Probe Testing Locations	56
5.2	Important Probe Dimensions	57
7.1	Differences Between Simulation and Experimental Operating Conditions	126
8.1	Summary of Electron Initial Conditions for Particle Tracing Using COMSOL	140
9.1	Helicon Source Characterization Summary	150
9.2	ReComm System Results Summary	151
C.1	Testing Matrix for Verifying Helicon Mode	166
C.2	Testing Matrix for Plasma Characterization: No ReComm System Present Downstream	167
C.3	Testing Matrix for Plasma Characterization: ReComm System Present Downstream	175
C.4	Testing Matrix for Plasma Characterization: Ion Energy Distribution Functions	181
C.5	Testing Matrix for Plasma Density Reduction Measurements with the Langmuir Probe	182
C.6	Testing Matrix for Plasma Frequency and Signal Attenuation Measurements: Trial 1	189
C.7	Testing Matrix for Plasma Frequency and Signal Attenuation Measurements: Trial 2	191

LIST OF APPENDICES

Appendix

A. Langmuir Probe Analysis Flow Chart 159

B. Residual Gas Analyzer (RGA) 161

B.1 RGA Setup 161
B.2 RGA Results 162

C. Testing Matrices for All Data Points 165

D. Additional Downstream Results from Langmuir Probe Testing 192

D.1 Empty Chamber Downstream 193
D.2 ReComm System Present Downstream 196

E. Axial Plots of Density Reduction Along Two Axes 199

E.1 Peak B_z = 925 G 200
E.2 Peak B_z = 1385 G 201
E.3 Peak B_z = 1800 G 202

NOMENCLATURE

Symbol	Description
a	Hairpin probe wire radius (m)
A_c	Area of RPA collector (m^2)
A_p	Langmuir probe tip surface area (m^2)
b	Hairpin probe space-charge sheath radius (m)
B	Scalar magnetic field (G)
$\mathbf{B}$	Magnetic field vector (G)
B_0	Absolute value of initial magnetic field (G)
c	wave phase velocity/speed of light (m/s)
C	Pipe conductance (cm/s)
C_f	Pressure correction factor
E	Scalar electric field (V/m)
$\mathbf{E}$	Electric field vector
f_c	Electron cyclotron frequency (Hz)
$\mathbf{F}_{ext}$	External force vectors (N)
f_o	Vacuum resonant frequency (Hz)
f_p	Plasma frequency (Hz)
f'_p	Corrected plasma frequency (Hz)
f_r	Measured resonance frequency from hairpin probe (Hz)

$\mathbf{F}_r$	Centrifugal force vector (N)
I	Current (A)
I_i	Ion current (A)
I_{sat}	Ion saturation current (A)
j	Scalar Current density (A/m^2)
$\mathbf{j}$	Current density vector (A/m^2)
J_1	First zero of the Bessel function
k	Wave number (m^{-1})
$\mathrm{K_n}$	Knudsen number
ℓ	Hairpin probe length (m)
m	Mass (kg)
m_i, M_i	Ion mass (kg)
n	Number density (m^{-3})
n_c	Critical plasma density (m^{-3})
n_e	Electron number density (m^{-3})
n_i	Ion number density (m^{-3})
$n_{i,o}$	Ion number density without ReComm system operating (m^{-3})
$n_{i,OML}$	Orbital motion limited ion number density (m^{-3})
$n_{i,R/C}$	Ion number density with ReComm system operating (m^{-3})
$n_{i,thin}$	Thin sheath ion number density (m^{-3})
n_o	Reference number density (m^{-3})
P_1	Measured pressure from the gauge (T)
P_b	Chamber base pressure (T)
P_c	Corrected pressure (T)
p_o	Vessel pressure (T)

P_s	Gas sample pressure (T)
$\mathbf{r}$	Particle position vector (m)
R	Radius of curvature of magnetic field lines (m)
r_c	Scalar cyclotron radius (m)
$\mathbf{r}_c$	Particle gyroradius position vector (m)
r_e	Electron gyroradius (m)
$\mathbf{r}_g$	Particle guiding center position vector (m)
r_h	Helicon source radius (m)
r_p	Langmuir probe radius (m)
S_{2-1}	Antenna response (W)
$S_{2-1,0}$	Vacuum antenna response (W)
S_p	Pumping speed (m/s)
t	time (s)
T	Temperature (K or eV)
T_e	Electron temperature (K or eV)
$\mathbf{v}$	Velcoity vector (m/s)
V	Probe voltage (V)
$\mathbf{v}_c$	Gyro-velocity vector (m/s)
V_c	Cathode voltage (V)
V_d	Voltage difference between retarding and repelling grids (V)
v_e, V_e	Scalar electron velocity (m/s)
$\mathbf{V}_e$	Electron velocity vector (m/s)
V_f	Floating potential (V)
v_g, v_{gc}	Guiding center drift velocity (m/s)
V_i	Scalar ion velocity (m/s)

$\mathbf{V}_i$	Ion velocity vector (m/s)
$v_{i,y}$	Initial velocity of electrons in y-direction (m/s)
V_{mp}	Most probable ion voltage (V)
V_p	Plasma potential (V)
V_{TH}	Thermal velocity (m/s)
$v_{\perp,gc}$	Guiding center velocity perpendicular to magnetic field lines (m/s)
$v_{\perp,o}$	Initial velocity perpendicular to magnetic field lines (m/s)
$\ddot{v}_x$	Acceleration in the x-direction (m/s^2)
$\ddot{v}_y$	Acceleration in the y-direction (m/s^2)
w	Hairpin probe width (m)
W_z	Kinetic energy (J)
x	Grid spacing(m)
x_{gc}	x-location of the guiding center (m)
y_{gc}	y-location of the guiding center (m)
z_{gc}	z-location of the guiding center (m)
Z_i	Charge state of an ion (C)
β_e	Hall parameter
δ	Sheath thickness (m)
ϵ	Dielectric constant
ζ_c	Sheath correction factor
θ	Angle of the wave number relative to the magnetic field
λ_D	Debye length (m)
λ_{MFP}	Mean free path (m)

ν	Electron-heavy particle collision frequency
ν_c	Ion collision frequency
ν_e	Electron collision frequency
σ	Electron conductivity (s^{-1})
ϕ	Potential distribution (V/m)
φ_0	Arbitrary phase
ω	Frequency (rad/s)
ω_c	Electron frequency (rad/s)
ω_p	Plasma frequency (rad/s)

Constants

e, q	Charge on an electron 1.6022×10^{-19} C
i	Imaginary number $\sqrt{-1}$
k_B	Boltzmann's constant 1.38×10^{-23} J/K
m_e	Electron mass 9.1094×10^{-31} kg
ϵ_o	Permittivity of free space 8.854×10^{-12} F/m
μ_o	Permeability of vacuum $4\pi \times 10^{-7}$ H/m

Subscripts

0	Equilibrium quantity
1	Perturbation quantity
e	Electron
i	Ion
$\|\|$	Parallel
$\perp$	Perpendicular

Acronyms

AFRL	Air Force Research Laboratory
ANU	Australia National University
CEM	Channel Electron Multiplier
CEV	Crew Exploration Vehicle
CFD	Computational Fluid Dynamics
CTF	Cathode Test Facility
DC	Direct Current
DSMC	Direct Simulation Monte Carlo
E×B	Crossed electric and magnetic fields
ECR	Electron Cyclotron Resonance
EEDF	Electron Energy Distribution Function
GPS	Global Positioning System
IEDF	Ion Energy Distribution Function
I-V	Current vs. Voltage
MRPA	Micro Retarding Potential Analyzer
MRPAv1	Micro Retarding Potential Analyzer version 1
MRPAv2	Micro Retarding Potential Analyzer version 2
NASA	National Air and Space Administration
NEXT	NASA Evolutionary Xenon Thruster
NSTAR	NASA Solar Electric Propulsion Technology Applications Readiness
OML	Orbital Motion Limited
PEPL	Plasmadynamics and Electric Propulsion Laboratory

RAM	Radio Attenuation Measurements
ReComm	Re-entry and hypersonic vehicle plasma Communication
RF	Radio Frequency
RGA	Residual Gas Analyzer
RPA	Retarding Potential Analyzer
TDRS	Tracking and Data Relay Satellite
UM	University of Michigan
USAF	United States Air Force
WOMBAT	Waves on Magnetized Beams and Turbulence

CHAPTER 1

Introduction

The purpose of this chapter is to discuss the motivation behind the research presented in this dissertation. In addition, the contributions of this work are introduced as well as the organization of the document.

1.1 Motivation

When a vehicle travels at hypersonic velocities within an atmosphere, a shock wave forms in front of the vehicle due to the large amount of kinetic and potential energy it possesses. This shock wave compresses and heats the air, dissociating and ionizing the air molecules. This layer of ionized gas enveloping the hypersonic vehicle is referred to as the reentry plasma sheath (1). This sheath causes either the attenuation or complete reflection of radio frequency (RF) communication signals below the plasma frequency. Such communication "blackouts" can last for ten minutes and have been, and continue to be, a problem for human space exploration, sample return missions, ballistic trajectories and scramjet research (2).

The blackout phenomenon first came to the public's attention during the 1960's when humans began traveling in space, and jumped to the forefront of the public eye during Apollo 13's failed attempt at a moon landing. During the return, the National Air and Space Association (NASA) engineers were not sure whether the capsule was re-entering the atmosphere at the correct angle. The blackout lasted longer than was expected. During the six-minute blackout, there was no way for mission control to know what was happening onboard the capsule or the status of the crew.

When the US began using the space shuttle to ferry humans to and from space, and with the launch of the Tracking and Data Relay Satellite (TDRS) system, the blackout phenomenon was no longer an issue because the orbiter is not fully encapsulated in plasma during atmospheric re-entry. Due to the shape of the orbiter, areas on the top of the vehicle are not engulfed in the plasma sheath, allowing radio signals to be sent from the orbiter to TDRS in orbit, and then be relayed back down to earth (Figure 1.1).

However, re-entry blackout is still a problem for the human space flight programs of other countries and sample return missions that utilize capsules. One example of

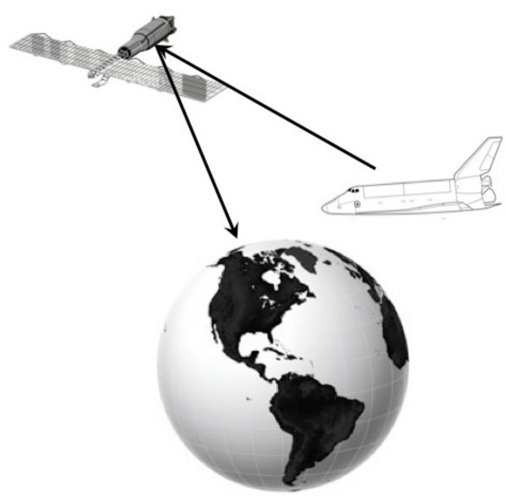

Figure 1.1: Sketch of how Tracking and Data Relay Satellite. TDRS works by relaying communication signals from the Space Shuttle orbiter to Earth during atmospheric re-entry.

a sample return mission that crashed due to an error during the re-entry phase is the Genesis mission that returned to Earth with solar wind samples. Upon re-entry, a sensor failure prevented the drogue parachute from opening and decelerating the capsule, letting it crash into the Utah desert. This failure may have been prevented had mission control been in constant contact with the re-entry vehicle. As a backup, the parachute could have been manually deployed.

Figure 1.2: Genesis capsule after re-entry (3).

In addition, after the tragic accident in 2003 of Columbia, NASA decided to retire the Space Shuttle early and discontinue research on a replacement. In addition, the desire to return to the moon and the lunar-type architecture means a return to a capsule style re-entry vehicle. Thus NASA is developing the crew exploration vehicle (CEV) with the Orion capsule-type re-entry vehicle, and communications blackout will again be an issue for U.S. human spaceflight.

Furthermore, the U.S. military is interested in ameliorating the communications blackout in order to maintain constant contact with hypersonic vehicles traveling within the atmosphere. Continuing interest in scramjet research results in a desire to have constant sensor and telemetry communication with the vehicle. Finally, maintaining constant Global Positioning Satellite (GPS) contact with objects on ballistic trajectories allows for greater accuracy in achieving the destination target.

1.2 Goals and Contribution of Research

The overall goal of this research is to first simulate an atmospheric re-entry plasma in a laboratory setting, and then use crossed electric and magnetic fields ($E \times B$) to create a region of lower density plasma surrounding an antenna. This dissertation presents contributions to the following areas of research:

1. **Helicon source development:** A helicon source was developed, built, refined and tested at the Plasmadynamics and Electric Propulsion Laboratory (PEPL). This is the first such source developed at the laboratory. Continuing research in a variety of interest areas utilize the same source.

2. **Re-entry plasma simulation:** The plasma downstream of the helicon source, inside the Cathode Test Facility was characterized. It was determined that the plasma was sufficient for simulating the density of the plasma sheath that develops during atmospheric re-entry.

3. **Development of diagnostic probes for helicon source:** Due to the nature of the helicon source, various diagnostic probes needed to be modified or built in order to be used inside and downstream of the source. The radio frequency power that was used to operate the helicon source required special compensation and filtering.

4. **Development of a model for simulating electron particle traces in crossed electric and magnetic fields:** The electric and magnetic fields were modeled using the COMSOL Multiphysics modeling package. The effects of the magnetic field alone and the magnetic field combined with the electric field were both studied.

5. **Development of a plasma mitigation system:** The ***re***-entry and hypersonic vehicle plasma ***comm***unication (ReComm) system was designed and built. Then, tests were performed in the region downstream of the helicon source to determine its effectiveness in mitigating the plasma number density.

1.3 Organization

This dissertation is divided into a variety of chapters. In general, the first chapters provide background and experimental setup information. Then, the diagnostic probes and analysis techniques are described, followed by the results. Finally, there is a discussion of the results and a conclusion. In detail, the chapters are as follows:

Chapter 1: The introduction includes the motivation behind the research and the goals and contributions of the dissertation.

Chapter 2: This chapter contains necessary background information. There is a literature review of previous atmospheric re-entry work, a discussion of the communications blackout phenomenon and a description of the parameters that need to be recreated in order to simulate a re-entry plasma in the laboratory.

Chapter 3: This chapter goes into the process of selecting a plasma source for simulating the re-entry plasma sheath. The reasons behind choosing a helicon source are discussed, and a short section about helicon source theory is presented. Then, the (PEPL) helicon source is described.

Chapter 4: The ReComm system is discussed in this chapter. It begins with an analytic development of the $E \times B$ drift and then moves into a discussion of the computer simulation work that was being done concurrently with this dissertation. Finally, a description of the PEPL ReComm setup is presented.

Chapter 5: The overall experimental layout and setup are discussed here. In addition, descriptions of the diagnostic probes and the analysis methods for each probe are described.

Chapter 6: Verification that the plasma source was operating in helicon mode is presented. Then, the downstream plasma characterization results are discussed for two cases: (1) an empty chamber downstream, and (2) the ReComm system present but turned off. Finally, the ion energy distribution function produced by the helicon source is given.

Chapter 7: The effect of the ReComm system on the plasma downstream of the helicon source is discussed. Density reduction data, plasma frequency data and signal response data are presented.

Chapter 8: Results from operation of the ReComm system are discussed. Possible explanations for the results are given and COMSOL modeling of the ReComm system is presented.

Chapter 9: Major conclusions from the research are summarized. Suggestions for future work and a system impact study are presented.

CHAPTER 2

Background

This chapter describes how plasma blocks electromagnetic waves and at what frequency a communications signal becomes attenuated. The description of the blackout phenomenon is described both physically and analytically. Then, a discussion of previous work in the areas of simulating and measuring the characteristics of a hypersonic plasma are presented. In addition, previous blackout amelioration work is discussed. The results of experiments performed in the 1960's to measure plasma number density and electron temperature in a re-entry plasma sheath are shown. Finally, the characteristics of the re-entry plasma that require simulation in a laboratory for the scope of this dissertation are determined.

2.1 Communications Blackout

In order to overcome the communications blackout phenomena, one must have a thorough understanding of why blackout occurs in the first place. It is good to first have a physical understanding of how the communications signal is blocked before looking at the relevant Maxwell equations (4; 5).

2.1.1 Physical Understanding

Assuming that a re-entry plasma sheath is quasineutral, and thus has an equal number of electrons and ions, the charged particles maintain an average equilibrium separation distance between them. If an electron is displaced, the other particles will remain in equilibrium while electrostatic forces will work to return the electron to its original position. Because of inertia, the displaced electron will overshoot the equilibrium position and oscillate about it until collisions with neutral particles damp out the oscillations. This is similar to a mass on a spring where the charged particle represents a mass, the electrostatic forces represent a spring and collisions with neutrals represent damping.

When the displacing force is an electromagnetic wave, it acts as a periodic driving force. When a plasma has low neutral pressure, it can be assumed that the electron neutral collision frequency is low with respect to the driving frequency. If the frequency of the electromagnetic wave (the driving frequency) is significantly less than the frequency of the oscillating electron, then the electron will oscillate at the driving frequency. In this case, the electron acts as a dipole radiator, producing both a forward and a backward traveling electromagnetic wave. The forward moving wave is out of phase and tends to cancel out the driving signal. The backward moving wave appears as a reflection of the driving signal. The thicker the plasma layer, the more attenuation and reflection of the original driving signal.

For the opposite case, when the driving frequency is significantly larger than the frequency at which the electron oscillates, then the electron exhibits large inertial effects and can only weakly oscillate at the driving frequency. Thus, the electromagnetic wave propagates through the plasma sheath unattenuated. When the driving frequency is equal to the electron oscillation frequency, then the incident electromagnetic wave is completely reflected, and there is no penetration into the plasma.

We now consider the case when not just one, but all of the electrons are displaced from their equilibrium position within the quasineutral plasma. The electric forces now work to restore all electrons to their equilibrium positions, resulting in an overall plasma oscillation at a frequency referred to as the plasma frequency (ω_p in radians/second). Since the electrons are so much less massive than the ions, the speed with which the oscillations occur is too short for the ions to respond. Thus, they can be considered fixed with respect to the electrons (6).

2.1.2 Plasma Frequency Derivation

The above physical explanation of the plasma frequency and its electromagnetic wave response can be proven by first deriving an expression for the plasma frequency and then looking at the plasma response to an applied electromagnetic field (6). We assume the following:

- The plasma is quasineutral and uniform at rest
- The magnetic field is negligible
- Thermal motions are negligible (i.e. $k_B T = 0$)
- The ions are fixed in a uniform distribution
- The plasma is infinite in space
- Electron motion is only in one direction (x-direction for this analysis)

Based on the above assumptions, the electrons will only experience an electrostatic oscillation when they are displaced. The equation of motion for the electrons is

$$mn_e\left[\frac{\partial \mathbf{v}_e}{\partial t}+\left(\mathbf{v}_e\cdot\nabla\right)\mathbf{v}_e\right]=-en_e\mathbf{E} \tag{2.1}$$

where m is the particle mass, n_e is the electron number density, $\mathbf{v}_e$ is the velocity of the electrons, e is the charge of an electron and $\mathbf{E}$ is the electric field. The continuity equation is

$$\frac{\partial n_e}{\partial t}+\nabla\cdot\left(n_e\mathbf{v}_e\right)=0 \tag{2.2}$$

Since the magnetic field was assumed to be negligible and the ions fixed, the only Maxwell equation that will be used is Poisson's equation.

$$\epsilon_0\nabla\cdot\mathbf{E}=\epsilon_0\frac{\partial \mathbf{E}}{\partial \mathbf{x}}=e\left(n_i-n_e\right) \tag{2.3}$$

where ϵ_0 is the permittivity of free space and n_i is the ion number denisty

By assuming the amplitude of the oscillation is small, Equations 2.1 - 2.3 can be linearized, transforming each dependent variable (n_e, $\mathbf{v}_e$ and $\mathbf{E}$) into the sum of an equilibrium part (0) and a perturbation part (1). This results in the following:

$$\nabla n_0=\mathbf{v}_0=\mathbf{E}_0=0 \tag{2.4}$$

$$\frac{\partial n_0}{\partial t}=\frac{\partial \mathbf{v}_0}{\partial t}=\frac{\partial \mathbf{E}_0}{\partial t}=0 \tag{2.5}$$

Applying the above to Equations 2.1 - 2.3 and maintaining the small amplitude assumption gives

$$m\left[\frac{\partial \mathbf{v}_1}{\partial t}+\left(\mathbf{v}_1\cdot\nabla\right)\mathbf{v}_1\right]=-e\mathbf{E}_1 \tag{2.6}$$

$$\frac{\partial n_1}{\partial t}+n_0\nabla\cdot\mathbf{v}_1=0 \tag{2.7}$$

$$\epsilon_0\nabla\cdot\mathbf{E}_1=-en_1 \tag{2.8}$$

Since the oscillations are sinusoidal, the time derivatives can be replaced with $-i\omega$ and the gradient can be replaced with $ik\hat{\mathbf{x}}$, where ω is the angular frequency and $2\pi/k$ is the wavelength. This gives the following system of equations.

$$-i\omega m v_1 = -eE_1 \tag{2.9}$$

$$-i\omega n_1 + n_0 ikv_1 = 0 \tag{2.10}$$

$$ik\epsilon_0 E_1 = -en_1 \tag{2.11}$$

This system can be solved for ω (in radians/second), which is referred to as the plasma frequency.

$$\omega_p = \left(\frac{n_0 e^2}{\epsilon_0 m}\right)^{1/2} \tag{2.12}$$

2.1.3 Electromagnetic Wave Interaction

In order to study how electromagnetic waves (light and radio waves) travel in a quasineutral plasma, first the relevant Maxwell equations must be examined (6).

$$\nabla \times \mathbf{E}_1 = -\dot{\mathbf{B}}_1 \tag{2.13}$$

$$c^2\nabla \times \mathbf{B}_1 = \frac{\mathbf{j}_1}{\epsilon_0} + \dot{\mathbf{E}}_1 \tag{2.14}$$

where $\mathbf{B}$ is the applied magnetic field, c is the phase velocity (usually the speed of light) and $\mathbf{j}$ is the current density.

Taking the time derivative of 2.14, inserting it into the curl of 2.13 and assuming a sinusoidal oscillation of transverse waves $(\mathbf{k} \cdot \mathbf{E}_1)$ gives the following.

$$\left(\omega^2 - c^2k^2\right)\mathbf{E}_1 = \frac{-i\omega\mathbf{j}_1}{\epsilon_0} \tag{2.15}$$

Assuming the electromagnetic waves are of sufficiently high frequency, the frequency is high enough such that the ions can be considered fixed, and thus, the current comes from the motion of the electrons only.

$$\mathbf{j}_1 = -n_0 e\mathbf{v}_{e1} \tag{2.16}$$

Combining Equation 2.16 with the linearized electron equation of motion given earlier (Equation 2.9) results in

$$\left(\omega^2 - c^2k^2\right) = \frac{n_0e^2}{\epsilon_0 m} \tag{2.17}$$

in which the expression for the plasma frequency is on the right hand side.

$$\omega^2 = w_p^2 + c^2k^2 \tag{2.18}$$

Equation 2.18 is the dispersion relation for an electromagnetic wave propagating in plasma with no dc magnetic field (6). This dispersion relation behaves in such a way that if a microwave beam with a given frequency, ω is passed through a plasma, the wavelength in that plasma will follow Equation 2.18. Thus, as the plasma density increases (and therefore ω_p^2 increases), the value of k^2 will decrease, resulting in a longer wavelength. At some point, the density will increase to where k^2 will become zero and any further increase in density results in a situation where the dispersion relation cannot be solved for any real value of k. Therefore, the electromagnetic wave can no longer propagate through the plasma. The frequency at which this occurs ($\omega = \omega_p$) is referred to as the cutoff frequency and happens at a critical plasma density, n_c. If the plasma density is too high or the wave frequency too low, then k becomes imaginary. Since the electromagnetic wave has an exponential dependence on k, the signal is exponentially attenuated and reflected when k is imaginary.

2.2 Previous Hypersonic Experiments and Models

In the early days of the U.S. space program, a great deal of work was done to understand phenomena that occur during atmospheric re-entry. Both simulation work and laboratory experiments were done as well as actual flight tests. Most of the laboratory work concentrated on simulating the thermal and chemical phenomena that occur near the surface of a hypersonic vehicle. The purpose of these experiments was to test heat shields and qualify thermal protection systems (4; 5; 7; 8). While this line of research allowed for knowledge advancement with regards to the extreme environment the vehicle encounters during hypersonic flight, not much laboratory work was done to extensively look at the communications blackout that occurs in this environment.

Previous research efforts into the communications blackout phenomenon include simulating a re-entry plasma with large plasma tunnels (9; 10) and hypersonic shock tunnel experiments done by Chadwick, *et.al.* to measure the electron number density at hypersonic velocities (11). Plasma tunnels and hypersonic shock tunnels are great tools for simulating the conditions that occur during atmospheric re-entry, but they are costly to build and maintain, and require a large amount of space. In addition, plasma tunnels require massive amounts of input power (up to and over 100-kW-RF power) (10).

Several flight experiments have been launched in order to further understanding of the re-entry environment. Project Fire consisted of a large blunt-nosed vehicle that NASA used to determine the thermal loads experienced during atmospheric re-entry (12; 13). NASA also performed an extensive study looking at the effects of the atmospheric re-entry plasma sheath on vehicle communications. This series of flights was called Project RAM (radio attenuation measurements) (14; 15). Flight experiments allow testing to be done during an actual atmospheric re-entry, thus negating the necessity for simulating the plasma sheath in a laboratory. However, they are expensive and short in duration. In addition, if there is a failure during the flight, re-performing the experiment is usually not an option. If that option does exist, the turnaround time is generally longer than is acceptable.

More recently, an extensive effort has been made to create complex computer simulations of the gas flow field that occurs during atmospheric re-entry and hypersonic flight in general. Schwartzentruber, *et al.* developed a hybrid Direct Simulation Monte Carlo (DSMC)-Computational Fluid Dynamics (CFD) code at the University of Michigan to simulate rarified gas flows, including simulations of non-equilibrium hypersonic blunt body flow fields (16; 17). In addition, Keidar, *et al.* simulated the hypersonic plasma sheath so that the effects of crossed electric and magnetic fields on the sheath can be studied (18).

2.3 Previous Blackout Amelioration Research

In addition to the experiments and flight tests done to characterize the plasma sheath surrounding a hypersonic vehicle, a number of techniques have been researched for ameliorating the communications blackout condition. Some methods have shown promise, while many have serious disadvantages that make their use unfeasible. Increasing the power to the antennas seems logical; however the increased power creates an electrical breakdown of the atmosphere, further ionizing the air and contributing to the original problem (19). Increasing the frequency of the communications to one that is greater than the plasma frequency would solve the blackout problem, but installing new equipment at all NASA and military tracking facilities would be prohibitively expensive (20), and frequencies greater than about 10 GHz are attenuated by atmospheric interference. In addition, the USAF extensively uses the GPS communication system (with a frequency of 1176 MHz) with most of its equipment. For low frequency communications (substantially below the plasma frequency) the signal attenuation is decreased because the long wavelength allows propagation further into a plasma layer without attenaution, but low-frequency transmitters are too large to be mounted on a hypersonic vehicle.

Aerodynamic shaping is an option that has shown promise. The U.S. military uses the concept to reduce the thickness of the plasma sheath surrounding ballistic missile re-entry vehicles (21). This method lowers the amount of signal attenuation but must be combined with another method in order to completely alleviate the blackout. Also, in order to reduce the sheath thickness, the re-entry vehicle must be as sharply pointed as possible, which reduces the payload capacity and increases the aerodynamic heating of the vehicle (20).

Magnetic fields can create a region of lower density plasma surrounding an antenna if properly placed. For this method to work, the magnetic field lines must be oriented such that the electrons are tightly bound to them via gyration and cannot respond to the electric field component of the electromagnetic driving wave (22). The main issue with this approach is the size and weight of the equipment required to create a magnetic field of sufficient strength. Another blackout amelioration strategy is injecting electrophilic liquid into the plasma in a region upstream of an antenna. Electrophilic materials have the ability to consume free electrons, thus lowering the electron density (23). While this method has been proven to decrease the electron density around an antenna, that reduction is not sufficient to completely alleviate blackout (14; 15).

2.4 Atmospheric Re-entry Parameters

During the RAM-C experiments in the 1960's, a number of hemispherical cone-shaped capsules were launched on ballistic trajectories (14; 15). These capsules re-entered the atmosphere at a velocity of 7.5 km/s. The capsules had an aerodynamic fin to which electrostatic rake probes and microwave antennas were attached (Figure 2.1). The probes and antennas were used to determine the ion number density,

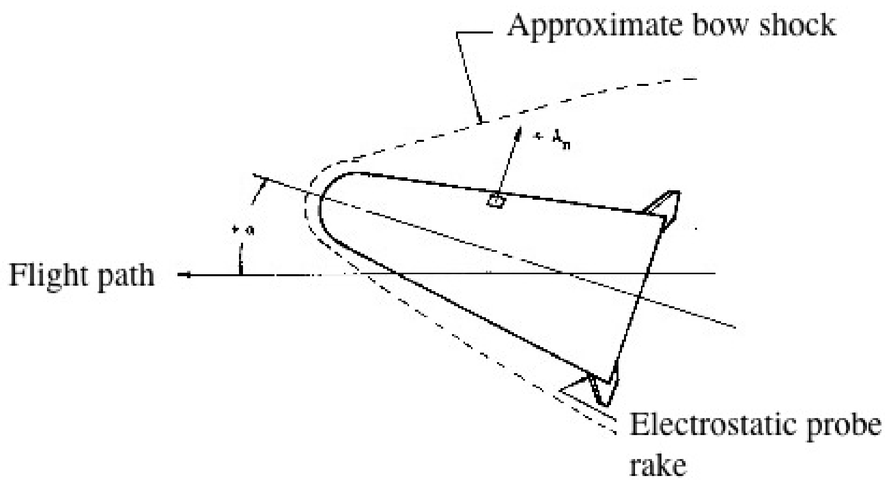

Figure 2.1: RAM-C re-entry capsule layout. Sketch of the capsule with the bow shock and electrostatic probe rake indicated (15).

electron number density and electron temperature of the plasma sheath at various standoff distances from the vehicle surface (up to 7.0 cm). At an altitude of 55 km, the probes were retracted due to the severe heating of the environment at lower altitudes, so re-entry data are only available above 55 km. The probe data measured the region of maximum plasma density to be at the furthest location from the vehicle surface. Thus, the data from 7.0 cm were used as the starting point for the density that would be simulated in the laboratory for this dissertation.

Figure 2.2 shows the electron number density measured during the RAM-C experiments as a function of altitude (14; 15; 24). As expected, the plasma density increased as the re-entry vehicle descended further into the atmosphere where there is a greater neutral pressure. Also indicated on Figure 2.2 are the densities of the

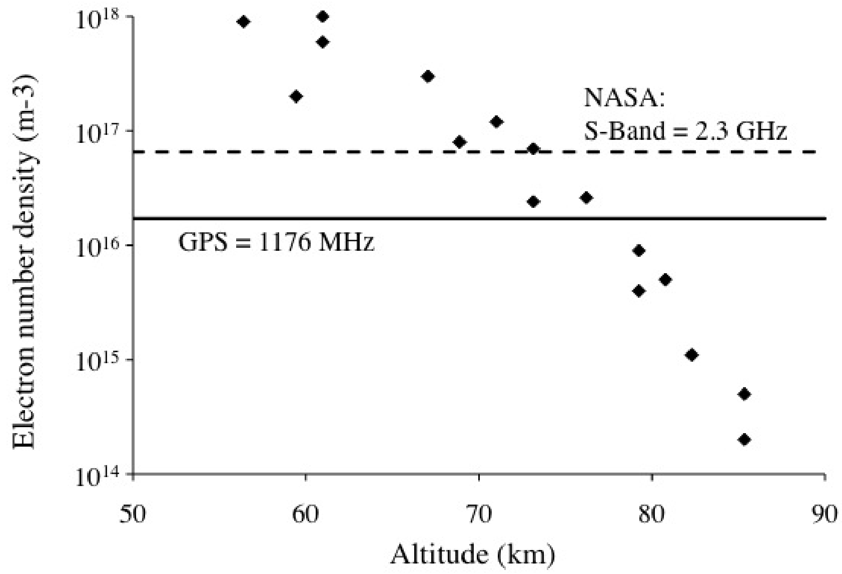

Figure 2.2: Electron number density the in RAM-C plasma sheath. Also indicated are the plasma densities at which the NASA S-band (dashed) and GPS (solid) frequencies are cutoff.

plasma sheath at which communications with two commonly used frequencies are attenuated. The dashed line indicates the frequency used by NASA for voice communications with the Space Shuttle, and the solid line indicates the GPS frequency.

In addition to the plasma density, electron temperature was measured throughout the re-entry process. Figure 2.3 shows that the electron temperature decreased as the capsule descended through the atmosphere (5; 15; 24).

The properties of the plasma sheath are characterized by both the electron concentration and the collision frequency of the electrons with neutral atoms (25). Therefore, the goal of this research is to simulate only the number density in a laboratory while maintaining an electron temperature of similar magnitude to that found during atmospheric re-entry. This last caveat is because the mechanism behind

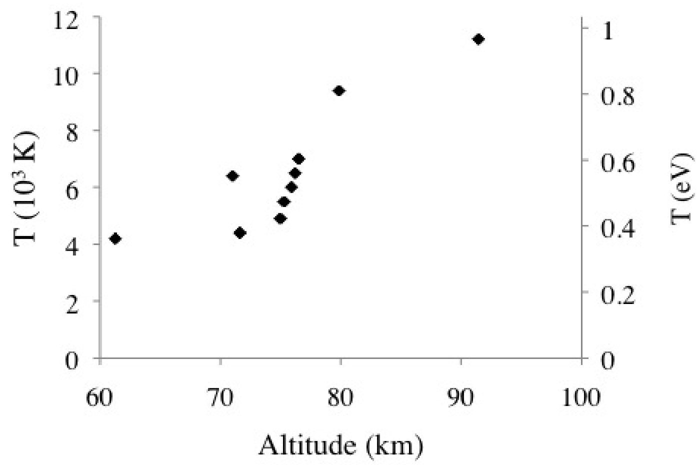

Figure 2.3: Electron temperature in the RAM-C plasma sheath.

the communications blackout, namely the plasma cutoff frequency, is only a function of number density, as was seen in Equation 2.12. The desire for generating a plasma with an electron temperature on the same order of magnitude as that found during atmospheric re-entry stems from the $E \times B$ method used for density attenuation discussed in Chapter 4. Basically, the magnetic field lines trap electrons. The warmer the electrons, the larger the electron gyroradius, r_e, resulting in less possibility of electrons being caught in the magnetic field.

$$r_e = \frac{\sqrt{kT_e m_e c^2}}{eB} \tag{2.19}$$

In Equation 2.19, T_e is the electron temperature and m_e is the mass of an electron. The relation shows that the electron gyroradius has only a square root dependence on the electron temperature, so as long as the electron temperature is of the same order of magnitude as that found in the re-entry sheath, the electron gyroradius will also be of the same order magnitude.

During atmospheric re-entry, the vehicle is traveling at hypersonic speeds, but simulating those hypersonic velocities is not necessary. This is because the plasma sheath forms behind a bow shock, decreasing the flow to subsonic speeds with respect to the vehicle surface. In addition, the sheath occurs within the boundary layer (5), further reducing the flow velocity (Figure 2.4).

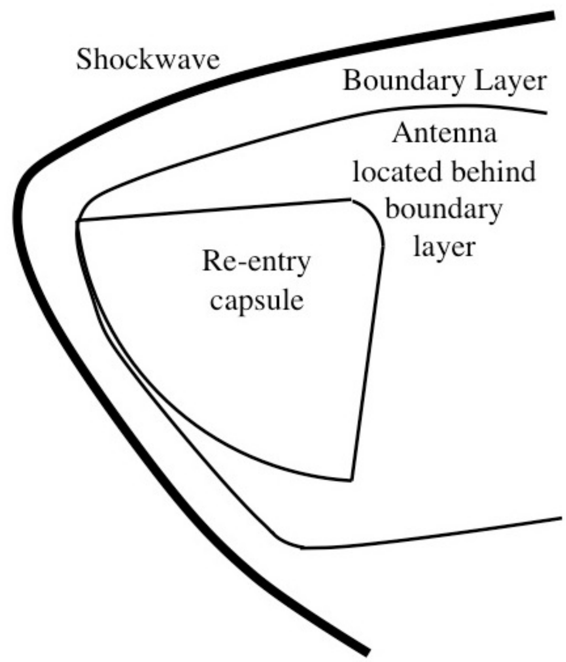

Figure 2.4: Re-entry capsule bow shock and boundary layer locations during hypersonic flight (5).

Another aspect of re-entry is that the vehicle is traveling through air. However, since the main goal of this research is to ameliorate the re-entry blackout, air does not need to be used to simulate the re-entry plasma sheath. This conclusion also comes from Equation 2.12 for the plasma frequency, which is not a function of the gas type or mass, only the number density. Therefore, argon gas was used in this dissertation to operate the plasma source. Using argon gas ignored the effects of a reacting species within the plasma layer. In addition, the neutral density of the gas in the boundary layer is ignored for now, as this is a first attempt at simulating the re-entry conditions. The first step is to create the correct plasma densities and temperatures.

2.5 Summary

This chapter discussed the dynamics that occur when a communications signal interacts with a plasma. Both a physical description as well as an analytical description were presented. A derivation of the plasma frequency was shown prior to the development of the equations for the interaction of an electromagnetic wave with plasma.

A discussion of previous experimental and computer simulation work on hypersonic flows was included, and plasma parameters measured during an atmospheric re-entry flight were presented. Finally, the reasons behind the decision to concentrate on simulating the plasma number density were discussed.

The goal of this chapter was to give the reader an understanding of the physics involved in the interaction of an electromagnetic wave with plasma. In addition, the reader should have gained an understanding of previous research done in the area of atmospheric re-entry and the scope of the plasma simulation done for this dissertation.

CHAPTER 3

Simulating an Atmospheric Re-Entry Plasma

The first step in creating a system for ameliorating atmospheric re-entry blackout was to create plasma with conditions similar to those found during hypersonic travel within the atmosphere in a laboratory setting. This chapter discusses a comparison of different plasma sources, how the determination was made to use a helicon source, the theory behind helicon source operation and the setup of the PEPL helicon source.

3.1 Plasma Source Selection

A variety of plasma sources were looked at and researched for this work. Initially, plasma sources already present in the lab were compared for their plasma density and electron temperature (the two parameters mentioned earlier in Section 2.4). Table 3.1 shows the relevant parameters for various plasma sources at PEPL.

The sources in Table 3.1 have the benefit that they were already present at PEPL and required no development; however, there were also issues with all of the sources that prevented their use. The Hall thrusters would not have been appropriate because either the electron temperature was too high or the density was too low. Near the discharge channel of the thruster, the number density reached 10^{18} m^{-3},

Plasma Source	Number Density (m^{-3})	Electron Temperature (eV)	Downstream Distance (cm)
NASA 173M Hall Thruster	5×10^{17} - 1×10^{18}	10 - 20	10
UM-USAF P5 Hall Thruster	5×10^{15} - 1×10^{17}	2 - 5	33
NSTAR-Class Ion Thruster beam	1×10^{15} - 1×10^{16}	1 - 1.6	20
NEXT-Class Ion Thruster beam	1×10^{15} - 1×10^{16}	0.5 - 1.3	45
Hollow Cathode Assembly	8×10^{15} - 6×10^{16}	0.2 - 2.5	10
Target values	10^{17} - 10^{18}	0.1 - 10	20

Table 3.1: Plasma parameters PEPL sources. Data come from the following references: NASA 173M = (26), UM-USAF P5 = (27; 28), NSTAR = (29; 30), NEXT = (31), Cathode = (32).

but the electron temperature was also very high (26). Further downstream of a Hall thruster, where the plume is less energetic, tests performed on the University of Michigan\Air Force Research Laboratory (UM-AFRL) P5 Hall thruster show that the electron temperatures were low enough to be of the same order of magnitude as those found during re-entry, but the number density of the plasma was only representative of those found at altitudes above 80 km (27; 28). The two ion engines and the hollow cathode produced low enough electron temperatures as well, but similarly the number densities they produced represent plasma that is only found in the very upper atmosphere during re-entry (29–32). A cathode assembly could have possibly been modified to work for this work, but since one was not readily available in the laboratory, a hollow cathode was not used.

Since none of the plasma sources previously used at PEPL would give the desired plasma properties for simulating atmospheric re-entry, other types of plasma sources

Plasma Source	Number Density (m^{-3})	Electron Temperature (eV)	Downstream Distance
Capacitively Coupled	10^{15} - 10^{17}	3 - 5	Inside
Inductively Coupled	10^{17} - 10^{18}	2 - 10	inside
ECR	10^{16} - 10^{18}	5 - 10	30 cm downstream
Helicon Source	10^{18} - 10^{20}	2 - 6	Inside
	10^{16} - 10^{18}	2 - 10	20 cm downstream
Theta Pinch	10^{20} - 10^{21}	30 - 50	Inside
Target values	10^{17} - 10^{18}	0.1 - 10	20

Table 3.2: Plasma parameters of various plasma generators. Data come from the following references: capacitively coupled and inductively coupled plasma = (33), ECR = (34; 35), helicon source = (36–38), theta pinch = (39; 40).

were researched. Table 3.2 contains a comparison of the number density and electron temperature found in a variety of different types of plasma sources.

Capacitively coupled plasmas, those sources where the RF or microwave power is coupled to the plasma via direct connection with an electrode, have sufficiently low electron temperature, but the number density is too low for the purposes of this research (33). In addition, the plasma remains in the vicinity of the electrodes. Inductively coupled plasma sources couple the power to the plasma through a dielectric of some sort. One advantage of inductively coupled plasma sources is that they are very simple to build, requiring no external magnetic field. Inductively coupled plasmas have sufficient density and low enough electron temperature; however, the plasma cannot be sustained away from the antenna (33). Electron cyclotron resonance (ECR) discharges are capable of sustaining plasma in the region downstream of the source, but a downstream magnetic field is required to sustain the discharge.

The presence of this required downstream magnetic field could cause interactions between the magnetic field required to sustain the plasma and that being used for the plasma mitigation system (34; 35). Helicon plasma sources provide sufficient density in the downstream region, but they can be complicated to operate as both an RF electric field and a DC magnetic field must be maintained. The electron temperature in a helicon source is a bit higher than those found during re-entry, but it is of the same order of magnitude (36–38). Theta pinches provide very high plasma densities, but the electron temperature is also very high. Furthermore, these devices require complicated switching mechanisms for pulsed power operation (39; 40). There are a variety of other types of plasma sources such as plasma tunnels and arcjets, but due to ease of use concerns, availability of materials and cost, they were not considered for these experiments.

Based on the above comparisons, a helicon source was chosen to simulate the plasma number densities that occur during atmospheric re-entry. The advantages of helicon sources are summarized below.

- High density: as shown in Table 3.2
- High efficiency: helicon discharges produce more plasma at a given input than other RF or DC discharges (41)
- Finite, low magnetic field: helicon sources require less magnetic field than plasma sources with comparable number densities. For example an ECR source needs about 875 G compared with a helicon source needing around 200 - 400 G (37).
- No internal parts: the antenna and magnets all lie outside of the vacuum chamber. This eases operation as well as eliminating the possibility of contamination

by the electrodes

- Remote operation: the plasma can detach from the magnetic field lines (41). This is desirable since a large magnetic field will be used for the plasma amelioration system, and interactions between the magnetic field required to achieve helicon mode and the one required for the ReComm system are unwanted.

Although this last point is subject to debate, the important factor is that that the strength of the magnetic field from the helicon source magnets is negligible in the region where the plasma mitigation system is to be located.

3.2 Helicon Source Theory

Helicon sources consist of a DC axial magnetic field and an RF electric field. The electric field is created by an antenna surrounding a dielectric tube. The helicon waves are basically bounded whistler waves. Whistler waves were first observed during World War I when soldiers spying on the enemy heard tones lasting several seconds descending in frequency from several kHz down to only a few Hz (36). When the waves are bounded inside a dielectric cylinder, they become partly electrostatic, as opposed to the completely electromagnetic nature of whistler waves (42). Early helicon experiments were done in solid state physics, but experiments on helicon waves were first carried out in a gaseous plasma in the 1960s by Lehane and Thonemann (43). It wasn't until Boswell (44; 45) discovered that helicons were unusually efficient in producing plasma that interest in the subject expanded. Boswell's initial helicon plasmas were created with a background pressure of 1.5 mtorr of argon and a "double-saddle" style antenna (44). Since then, extensive research has been done on helicon sources and the mechanism that makes them so efficient at producing plasma (the absorption of RF energy is more than 1000 times faster than what is theoretically predicted due to collisions alone). Wave interactions from Landau damping (42) to Trivelpiece-Gould mode coupling (46) have been credited for the high efficiency of helicon sources. For this work, only the fact that helicon sources produce a very dense, very uniform plasma is important. Thus, only a short overview of the theory behind helicon source operation will be given before going into a detailed description of the PEPL helicon source.

Helicon waves are right-handed, circularly polarized waves bounded by an insulating cylinder (47). The dispersion relation for a whistler wave is

$$\frac{c^2k^2}{\omega^2} = 1 - \frac{\omega_p^2}{\omega\left(\omega - \omega_c \cos\theta\right)} \tag{3.1}$$

where θ is the angle of k relative to $\mathbf{B}$ (48) and ω_c is the electron gyrofrequency. When the driving frequency, ω is sufficiently small (such as 13.56 MHz), then the first term of the denominator on the right hand side of the equation and the 1 can be neglected. This results in the following

$$\frac{c^2k^2}{\omega^2} = \frac{\omega_p^2}{\omega\omega_c \cos\theta} \tag{3.2}$$

In the above approximation, the guiding-center motion of the electrons is carrying the oscillating current in the wave (48).

When the plasma becomes confined, the square of the total wave number becomes the sum of its parallel and perpendicular parts (49).

$$k^2 = k_\perp^2 + k_\parallel^2 \tag{3.3}$$

In Equation 3.3, $k_\perp$ is set by the boundary conditions of the system, and $k_\parallel/k = \cos\theta$ (48). For a cylinder aligned along $\mathbf{B}$ with radius r_h, the lowest radial mode results in the dispersion relation for a helicon wave (50).

$$k_{\|}\sqrt{k_{\|}^2 + k_{\perp}^2} = \frac{\mu_o n_e e \omega}{B_o} \approx \frac{3.83 k_{\|}}{r_h} \tag{3.4}$$

where μ_o is the permeability of vacuum, and 3.83 results from the first zero of the Bessel function $J_1(k_{\perp} r)$ (42). Presumably, the optimum value of $\omega/k_{\|}$ is set by the Landau damping mechanism, so the dispersion relation shows that the helicon resonance requires that nr_h/B also be a constant (where n is the plasma number density). Therefore, each given radius of a helicon source will have a number density that varies linearly with B. In addition, for a given density, the required axial magnetic field should vary linearly with the tube radius. The dispersion relation also shows that the RF frequency is trivial, so long as $k_{\|}$ is adjusted to give the correct value of $\omega/k_{\|}$ (37; 48). Thus, a smaller operating frequency requires a larger antenna radius, r_h.

3.3 PEPL Helicon Source Design

A variety of options go into designing a helicon source. The DC magnetic field strength, antenna shape, radius and length and operating frequency all must be decided upon. Despite the many options, all helicon sources have the same basic setup. An RF power supply provides an oscillating voltage to an antenna via a matching network. The matching network is present to ensure that the downstream impedence is the same as what is expected by the RF power supply (usually 50 Ω or 75 Ω). Changes in the pressure, magnetic field, RF power and RF frequency alter the plasma and thus affect the load impedance of the antenna (49). Therefore, a tunable matching network is required to compensate for any change in the impedance and to minimize reflection of RF power back to the power supply. In addition to the RF components of the helicon source, an axial DC magnetic field is required. Usually, this is done by using a DC power supply with a series of electromagnets, but recent activity has shown that using permanent magnets can be successful as well (51).

For the PEPL helicon source, the tube radius, and thus the antenna radius, was decided upon based on the 14-cm-diameter size of an available port on the Cathode Test Facility (CTF) vacuum chamber described in Chapter 5. The large diameter of the helicon source was desirable for maintaining a constant density in the region downstream of the source as well as for other possible experiments to be done with the source (52). The length of the cylinder was chosen due to limitations of the area in which the helicon source was to be built. Because of the aforementioned reasons, a 15-cm-diameter by 40-cm-long quartz tube was purchased. A nozzle on one end provided a means for argon injection and a flange on the other end allowed for attachment to the CTF via a rubber O-ring. The tube can be seen in Figure 3.1.

The original antenna design (single loop, m = 0 mode) was also chosen based on possible future experiments to be done with the source (52). Previous work had shown that the use of an m = 0 mode antenna is capable of entering into helicon mode (53; 54). Figure 3.1 shows the original antenna design. Initially RG-8

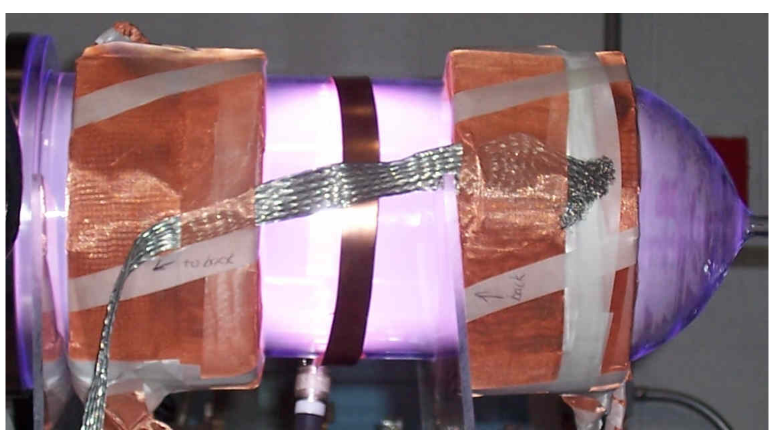

Figure 3.1: Photograph of the helicon source first attempt. The antenna was a m = 0 mode, and the magnets were wound by hand at PEPL.

coaxial cables with HN-connectors were used to connect the antenna to the matching network and the matching network to the RF power supply. The power supply was a PlasmaTherm 13.56-MHz, 2.5-kW RF supply. The supply was chosen because it was already present in the laboratory, and the most common frequency used for helicon sources is 13.56 MHz. The original matching network had two variable capacitors and an inductor.

The magnetic field was produced by two custom made solenoids that were capable of reaching a peak axial magnetic field of about 250 G. Two magnets were used to take advantage of a Helmholtz coil configuration. They were wrapped with copper mesh to shield the wire from RF interference. The silver-colored strap crossing above the antenna and between the two magnets in Figure 3.1 is a tin-coated copper strap used for grounding purposes.

This original design had many flaws resulting from the design requirements and the equipment used. Although the m = 0 mode antenna is capable of achieving helicon mode, it is more difficult to reach resonance with such an antenna (51). For a first attempt at a helicon source, an antenna with a more easily excitable resonance mode, such as m = 1 or m = -1 modes, would have been a better choice. Furthermore, the original matching network was not tuned for the type of load that a helicon source creates. This resulted in minimum reflected power levels of over 70% of the input power. After speaking with experts in matching networks (conversations with Manitou Systems Inc.) and looking at design specifications for matching networks (Costa and Charles of the Australia National University (ANU) design paper), it was realized that the original matching network was designed for a different type of load than that seen with a helicon source. Another flaw in the initial setup came from the magnetic circuit. The original magnet design had a diameter that was too small to fit an antenna between the magnet and the quartz tube. Also, the original power supply used to produce the DC magnetic field was very susceptible to RF interference and would thus either shut itself down or burn out.

A second design iteration was based on a helicon source setup that is in use at ANU called WOMBAT (49; 55; 56). The updated design had the following modifications:

1. New pi-style, water-cooled, 5-kW matching network purchased from Manitou Systems Inc.: See Figure 3.2 for a photograph of the matching network and Figure 3.6 for a sketch of the matching network circuit. The new matching network had silver plated copper straps to make internal connections, and a slot where a copper strap attached to the antenna can attach directly to the variable inductor. The transmission lines from the RF power supply to the matching network remained RG-8 coaxial cables with HN connectors.

2. New antenna design: See Figure 3.3 for a photograph of the double saddle/Boswell-style antenna designed for the updated helicon source. The length of the antenna was chosen because of a combination of previous experiments (49; 57) and the length of the quartz tube. The Boswell-type antenna was chosen to be 30.5 cm long.

3. New magnets: Different magnets were used with a larger inner diameter. This allowed the antenna to be placed between the magnets and the quartz tube. In addition, the new magnets were already encased in a metal shroud to provide shielding against RF radiation. Three magnets were placed equidistance from each other to provide a constant magnetic field along the centerline of the helicon source. Figure 3.4 shows the axial magnetic field strength of the helicon

magnets, and Figure 3.7 shows how the magnets were spaced.

4. New DC power supply for the magnets: A Lambda EMI-EMS 40 V, 60 A DC power supply was used for supplying current to the electromagnets. The new power supply proved immune to RF interference because of the solid state materials used to produce the current.

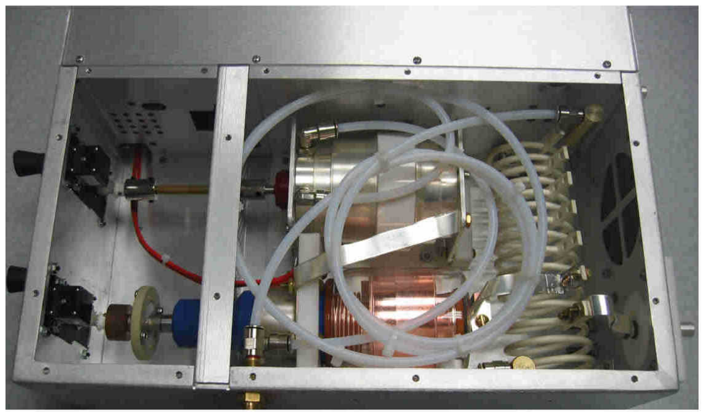

Figure 3.2: Photograph of the pi-style matching network. It was purchased from Manitou Systems Inc. and used with the PEPL helicon source.

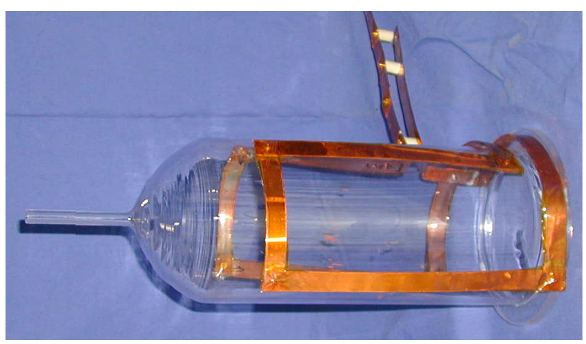

Figure 3.3: Photograph of the Boswell-type antenna. The antenna is wrapped around the quartz tube used in the helicon source.

The updated setup provided a better system, but there were still some issues that prevented reliable operation and testing. One of the improvements was decreased reflected power levels. With the new setup, the maximum reflected power level was

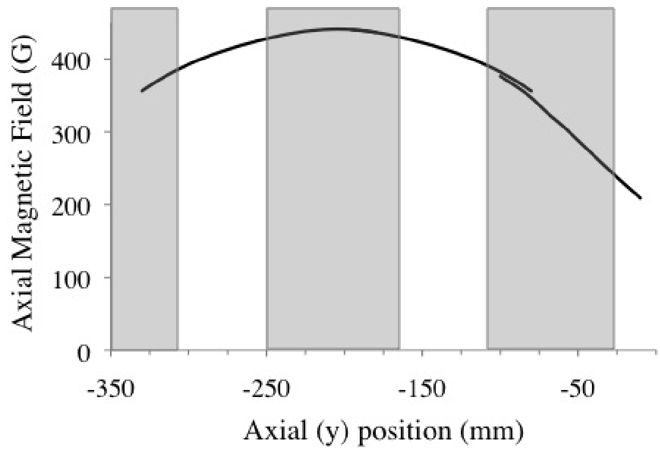

Figure 3.4: Axial (y-direction) magnetic field strength along the helicon centerline. The discontinuity in the plot is due to the fact that the Hall probe required repositioning between measurements.

only 5%. This increase in the power coupled to the plasma resulted in achieving the desired helicon mode of operation (see Section 6.1).

Despite achieving helicon mode, there were still issues with the operation of the updated helicon source. The decrease in reflected power meant that more RF energy was traveling through the system and being coupled to the plasma. However, the system was not properly grounded, resulting in arcing both inside of and outside of the vacuum chamber. In addition, there was no Faraday cage surrounding the RF system (RF power supply, matching network and helicon antenna), resulting in RF interference on diagnostic sensors and computers throughout PEPL.

Furthermore, the Boswell-type antenna was a very complex shape with places where the copper would overlap itself. Thus, spacers were required to keep the antenna from touching itself where the overlap occurred, as can be seen in Figure 3.3. The ceramic spacers were held in place by screws, creating many sharp edges and corners on the antenna. Arcs developed between the antenna and the magnets, creating holes in the mica insulation that was supposed to shield the antenna from the metal casing of the magnets. Thus, the antenna would touch the magnets and the RF power would be coupled to them instead of to the plasma.

The following improvements were required for the final iteration of the PEPL helicon source.

1. Simpler choice of antenna

2. Proper grounding to prevent arcing and RF interference on the ground lines

3. Faraday cage surrounding the RF components to prevent RF radiation

3.4 PEPL Helicon Source Final Setup

The final design for the helicon source was not necessarily the most efficient system but was a combination of safety, convenience, ease of use and efficiency. The final system consisted of a half wavelength double helix antenna, machined from a single copper plate and held together with rivets and silver solder. The antenna is shown in Figure 3.5. The double-helix, half-wavelength antenna was chosen because it is an easier shape to construct and maintain than that of the Boswell-type antenna,

Figure 3.5: Photograph of the double-helix, half-wavelength antenna.

and it still couples the RF energy to the plasma as efficiently (49). The length of the antenna was kept the same as that of the previously used Boswell-type antenna.

The antenna was connected with copper strips to the Manitou Systems Inc. matching network, and RG-8 coaxial cables with HN-connectors were still used to connect the RF power supply to the matching network. This electrical setup is shown in Figure 3.6. The DC magnetic field was maintained with the same three magnets

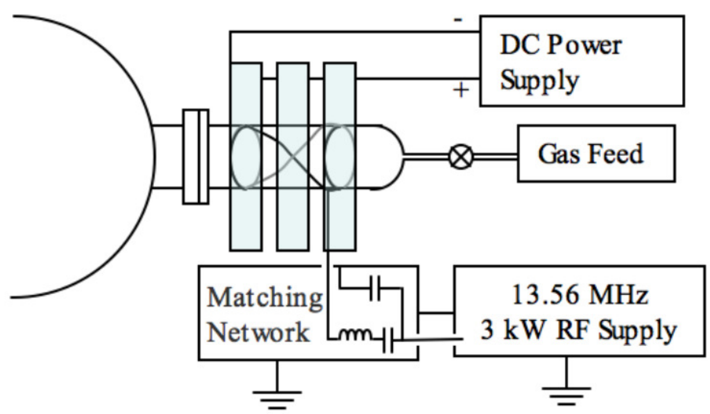

Figure 3.6: Electrical layout of the PEPL helicon source. The pi-style matching network is also shown.

and power supply used in version two of the PEPL helicon source. Figure 3.7 shows the final setup of the source.

In order to maintain proper grounding, the entire setup was isolated from the facility ground except for the RF power supply ground line. The reason for this was so that all RF power would complete the circuit and return to where it began in the RF power supply. Then, in order to ensure that the ground line at the PEPL facility was not corrupted, that line was tied to the water pipes and building structure. A variety of other equipment were attached to the CTF, including power supplies and measurement equipment required for the diagnostic probes, vacuum pumps and pressure transducers. In order to keep RF power from traveling along

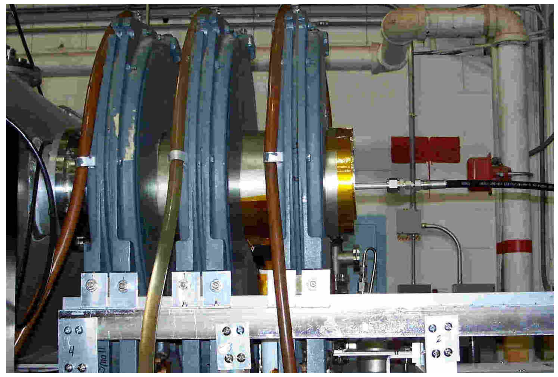

(a)

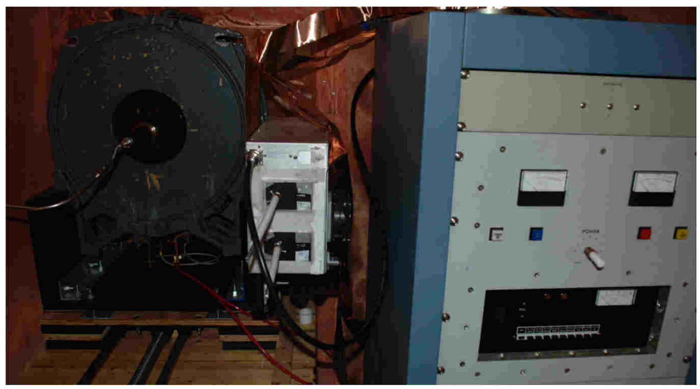

(b)

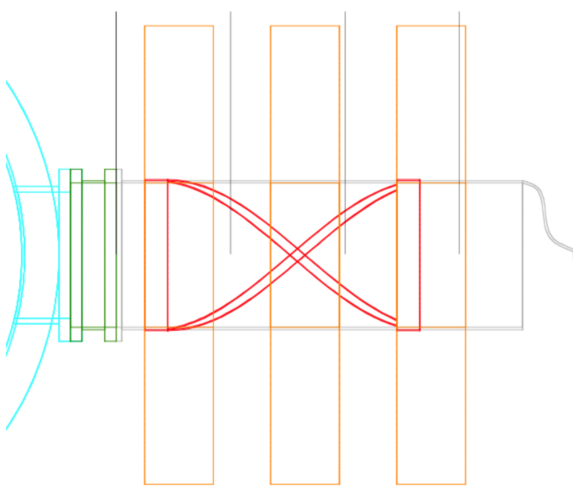

(c)

Figure 3.7: Photographs and schematic of the final version of the PEPL helicon source. (a) From the side, the magnets, mica insulation between the magnets and antenna, gas feed hose and quartz tube nozzle can be seen. (b) From the front, the matching network, power supply, magnets, quartz tube, gas feed line and Faraday cage can be seen. (c) Schematic drawing of the PEPL helicon source, showing the antenna (red), magnets (orange) and quartz tube (gray).

the transmission and power lines of this equipment, low pass filters and RF power blocks were utilized on all lines.

The final update to the plasma source was the addition of a Faraday cage surrounding the RF components of the system. The cage was made up of copper mesh that is specially designed to block radiation at 13.56 MHz. The cage prevented any extraneous radiation from affecting equipment in the laboratory by enclosing the RF power supply, matching network, helical antenna, magnets, and the DC power supply. The cage remained closed while the RF power supply was operating, so there were feedthroughs to control the settings on the matching network and RF power supply. The DC power supply was set to a constant value, so it could be turned on and then left alone for the duration of testing.

3.5 Summary

This chapter explained how the plasma source used for simulating an atmospheric re-entry plasma was chosen. It was decided that a helicon source would be used because of the following, which are demonstrated in Chapter 6:

- Spatially uniform plasma number density in the downstream region
- High plasma number density in the downstream region
- Low electron temperature in the downstream region
- Ease of building and availability of the components

A short section about the theory behind helicon source operation was included. Then, the design, setup and troubleshooting of the PEPL helicon source were presented.

The goal of this chapter is for the reader to understand the reasoning behind using a helicon source to simulate the plasma number density during atmospheric re-entry. In addition, a small section about how helicon sources work was included. Finally, the design and re-design process for developing the final version of the PEPL helicon source should be well understood, including issues with RF radiation and grounding, antenna and magnet design, matching issues, and the final layout of the PEPL helicon source.

CHAPTER 4

Plasma Mitigation System

Communications blackout amelioration research and experiments on laboratory plasmas have indicated that the use of a magnetic field can lower the plasma density because the electrons become trapped by the magnetic field lines (58; 59) . However, the effects of such a magnetic field on the plasma density in a re-entry plasma sheath have not yet been studied in depth. In addition, an applied electric field perpendicular to the magnetic field could lead to some interesting behavior. The $E \times B$ drift of the plasma may further decrease the plasma density below that which occurs from only an applied magnetic field. Ion acceleration by the electrodes could itself significantly lower the number density. This chapter discusses an idea for the plasma manipulation system used in this dissertation and an introduction to the computer simulation work that inspired the ReComm system. In addition, the development and various components of the mitigation system are discussed.

4.1 ReComm System Theory of Operation

Crossed electric and magnetic fields were used for the communications blackout amelioration system. This idea has previously shown promise in modeling work with plasma density reductions up to a factor of 2 being seen (60). The method provides two means for lowering the plasma density:

1. The formation of an electrostatic sheath that is stabilized by a magnetic field (60), and
2. The $E \times B$ drift.

4.1.1 Electrostatic Sheath

The initial idea behind using crossed electric and magnetic fields to lower the plasma density was quite simple. A negative electric field would create an electrostatic sheath that will repel electrons. Since electron mobility and oscillation is the primary cause of radio wave attenuation in plasma, this devoid of electrons will allow the electromagnetic waves to pass. However, this process will also cause the sheath to become thinner, facilitating electrical breakdown and allowing arcs between the electrodes. Thus, a magnetic field is added to expand the sheath thickness. Recent studies have shown that strong magnetic fields can stabilize a high voltage sheath by preventing the thinning of that sheath in a flowing plasma (18). In addition, the electrons will become caught by the magnetic field lines and their motion will be restricted. Since ions are much more massive than electrons, they will not be affected as significantly by the magnetic field. The reduced plasma density in the region where the ions are accelerated and the electrons are directed away from by the magnetic field should create a “window” in the re-entry plasma sheath through which radio signals can pass as shown in Figure 4.1.

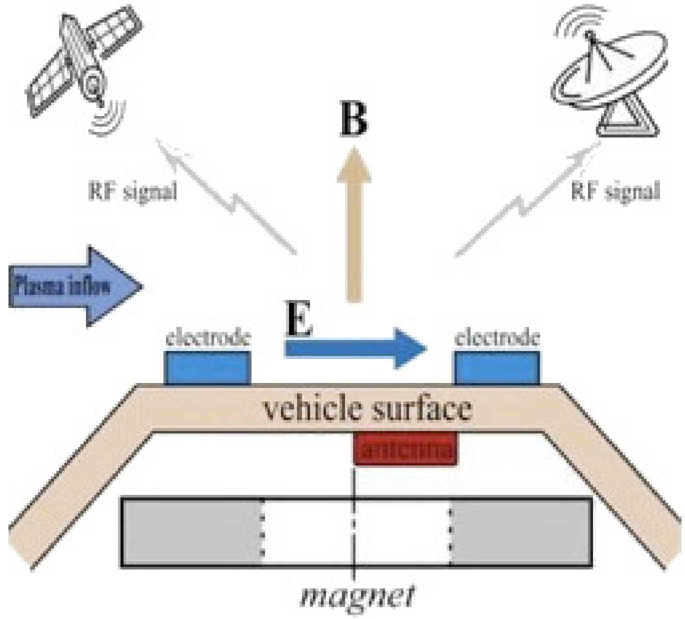

Figure 4.1: Plasma Mitigation Concept. Sketch of the crossed electric and magnetic fields used for the communications blackout amelioration system.

4.1.2 E $\times$ B Drift

A general motion of the plasma should occur in the direction of the $E \times B$ drift. The equation of motion for crossed electric and magnetic fields is given by Equation 4.1 (6).

$$m\frac{dv}{dt} = e(\mathbf{E} + \mathbf{v} \times \mathbf{B}) \tag{4.1}$$

where $\mathbf{E}$, $\mathbf{B}$ and $\mathbf{v}$ are the electric field, magnetic field and velocity vectors, respectively. Assume that an electric field exists along the y-axis ($\mathbf{E}\hat{y}$) and a magnetic field exists along the z-axis ($\mathbf{B}\hat{z}$). The magnetic field itself will cause a moving charged particle to orbit about the z-axis, and the addition of the electric field will cause the guiding center of the circular motion to move along the x-axis according to the right-hand-rule. Chen describes the motion of the guiding center analytically as follows (6). The components of Equation 4.1 are:

$$\frac{dv_z}{dt} = \frac{eE_z}{m} \tag{4.2}$$

$$\frac{dv_x}{dt} = 0 \mp \omega_c v_y \tag{4.3}$$

$$\frac{dv_y}{dt} = \frac{e}{m} E_y \pm \omega_c v_x \tag{4.4}$$

Differentiating Equations 4.3 and 4.4 for constant E gives:

$$\ddot{v}_x = \mp \omega_c \left(\frac{e}{m} E_y \pm \omega_c v_y \right) = -\omega_c^2 \left(\frac{E_y}{B} + v_y \right) \tag{4.5}$$

$$\ddot{v}_y = -\omega_c^2 v_y \tag{4.6}$$

where $\ddot{v}_x$ and $\ddot{v}_y$ are accelerations. The solutions to the homogenous parts of Equations 4.5 and 4.6 are in the form of:

$$v_{x,y} = v_\perp \exp\left(\pm i\omega_c t + i\delta_{x,y} \right) \tag{4.7}$$

This results in the following system:

$$v_x = \pm i v_\perp \exp\left(i\omega_c t \right) - \frac{E_y}{B} \tag{4.8}$$

$$v_y = v_\perp \exp\left(i\omega_c t \right) \tag{4.9}$$

where there is a Larmor motion of the particles about the magnetic field lines but with a superimposed drift velocity, v_{gc}, in the negative x-direction. A general equation for the motion of the guiding center is described by Chen in Equation 4.10 (6).

$$\mathbf{v}_{\perp,gc} = \mathbf{E} \times \mathbf{B}/B^2 \tag{4.10}$$

This is shown graphically in Figure 4.2.

Thus, if an antenna were placed within the crossed electric and magnetic fields, the $E \times B$ drift would cause the plasma to move in a direction orthogonal to the fields. Once again, the density would be lowered due to the conservation of charge. It must be noted that for this effect to be meaningful, the velocity of the guiding center must be greater than the thermal velocity of the plasma.

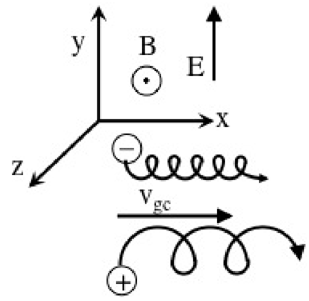

Figure 4.2: Particle motion in an $E \times B$ field. The velocity of the guiding center is known as the $E \times B$ drift

4.2 Concurrent Computer Simulation Work

In order to study the expected $E \times B$ effect on the plasma, complex computer simulation work was performed by Kim (61) concurrently with the experimental work presented in this dissertation. A two-dimensional steady-state fluid model, shown in Equations 4.11 through 4.13 was used to describe the motion of the plasma in the $E \times B$ field.

$$\nabla \cdot (\mathbf{V}_i n) = 0 \tag{4.11}$$

$$m_i n(\mathbf{V}_i \cdot \nabla \mathbf{V}_i) = en(\mathbf{E} + \mathbf{V}_i \times \mathbf{B}) - m_i n \nu_c \mathbf{V}_i \tag{4.12}$$

$$0 = -en(\mathbf{E} + \mathbf{V}_e \times \mathbf{B}) - k_B T_e \nabla n - m_e n \nu_e (\mathbf{V}_e - \mathbf{V}_i) \tag{4.13}$$

where V_i is the ion velocity, V_e is the electron velocity, ν_c is the combined ion-neutral and ion-electron collision frequency, ν_e is the combined electron-ion and electron-neutral collision frequency and T_e is the electron temperature in eV. Additionally, the current density, j, is a vector in the two-dimensional case. Thus, conservation of current density requires consideration.

$$\nabla \cdot \mathbf{j} = 0 \tag{4.14}$$

Assuming that the $E \times B$ drift is in the x-direction and that the applied magnetic field is in the z-direction ($B = B_z$), the $E \times B$ drift will not generate any current (i.e. j_x is negligible). The reason for this is that the electron and ion gyroradii are sufficiently small compared with the dimensions of the ReComm system. Therefore, the current density in component form is described by Equations 4.15 and 4.16.

$$j_y = \sigma \left(E_y + \frac{k_B T_e}{e} \frac{\partial \ln(n)}{\partial z} - V_x B_z \right) \tag{4.15}$$

$$j_z = \sigma \left(E_z + \frac{k_B T_e}{e} \frac{\partial \ln(n)}{\partial z} \right) \tag{4.16}$$

where σ is the electron conductivity and k_B is Boltzmann's constant. The drift velocity in the $E \times B$ direction is (6; 61)

$$V_x = -V_y \frac{\omega_e}{\nu_e} = -V_y \beta_e \tag{4.17}$$

where β_e is the Hall parameter. The Hall parameter is the ratio of the electron gyrofrequency to the electron-heavy particle collision frequency, ν, and can be found using Equation 4.18 (62).

$$\beta_e = \frac{eB}{m_e \nu} \tag{4.18}$$

Since the Coulomb logarithm is only weakly dependent on the number density of the plasma, the electron collision frequency can be expressed as a function of the number density.

$$\nu_e = \mathrm{f}(n) \tag{4.19}$$

By combining Equations 4.14 through 4.19, an expression for the potential distribution, ϕ, can be obtained (61).

$$\begin{aligned} &\frac{1}{1+\beta_e^2} \frac{\partial^2 \phi}{\partial x^2} + \frac{\partial^2 \phi}{\partial z^2} + \left(\frac{2\beta_e^2}{(1+\beta_e^2)^2} \frac{\partial \ln n}{\partial x} \right) \frac{\partial \phi}{\partial x} - T_e \frac{1}{n} \frac{\partial^2 n}{\partial z^2} \\ &+ T_e \left(\frac{\partial \ln n}{\partial z} \right)^2 - \frac{2\beta_e^2}{(1+\beta_e^2)^2} T_e \left(\frac{\partial \ln n}{\partial x} \right)^2 \\ &- \frac{T_e}{1+\beta_e^2} \frac{1}{n} \frac{\partial^2 n}{\partial z^2} + \frac{T_e}{1+\beta_e^2} \left(\frac{\partial \ln n}{\partial x} \right)^2 = 0 \end{aligned} \tag{4.20}$$

The potential distribution function was solved numerically with an iterative scheme. The calculated electric field was then used to solve the ion transport equations shown in 4.11 and 4.12 above. Using the finite volume method to solve the transport equations, the plasma number density and velocity distribution were found, as they are coefficients in the potential distribution function. Comparisons between the experimental and computer simulation results are presented in Chapter 7.

4.3 ReComm System Setup

As previously mentioned, the ReComm system consisted of crossed electric and magnetic fields. Overall, the system was composed of a large electromagnet, that generated the very strong vertical (z-direction) magnetic field, and two electrodes that generated the electric field. A schematic drawing of the ReComm system is shown in Figure 4.3.

The magnetic field was created using a custom designed water-cooled electro-

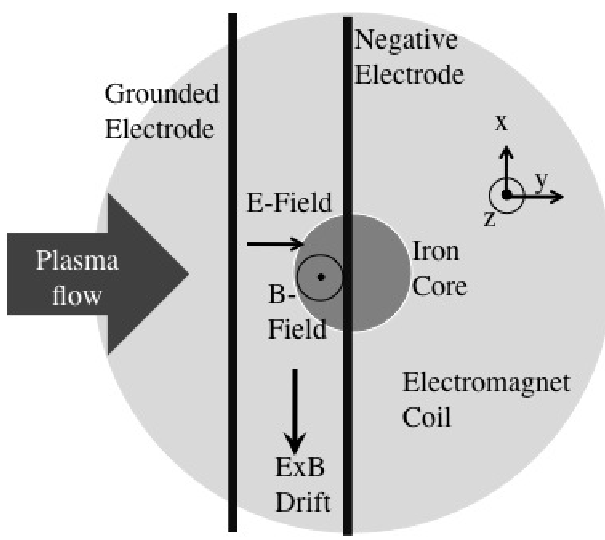

Figure 4.3: Schematic drawing of the ReComm systme. the electromagnet, electrodes and indicated axis directions used throughout this dissertation are shown.

magnet. The magnet consisted of 1/8-inch-diameter copper tubing wrapped around an iron core and set atop an iron base. Copper tubing was used for the windings because the magnet required water cooling while in a vacuum. Otherwise, the coils would heat up, increasing their resistivity. The power supply available for use was already operating at peak voltage, so the resistance of the lines needed to be minimized. The iron core and base helped to boost the strength of the magnetic field as well as created a very uniform field in the region directly above the iron core. The peak magnetic field in the vertical (z) direction reached up to 2000 G, and Table 4.1 shows maximum measured B_z as a function of input current from the ReComm magnet power supply.

Input Current (A)	Peak B_z (G)
0	0
150	925
225	1385
300	1850
325	2000

Table 4.1: Maximum ReComm system vertical magnetic field strength for various input currents.

The further away from the region directly above the iron core, the more divergent the magnetic field became. Figure 4.4 is a plot of the y-z magnetic field vectors with the directions and relative strengths. This plot shows how the magnetic field diverged away from the iron core in the y-z plane downstream of the helicon source centerline. For this experimental setup, $x = 0$, $z = 0$ is at the radial centerline of the helicon source and $y = 0$ is located where the helicon source flange attaches to the vacuum chamber. The setup is discussed further in Chapter 5.

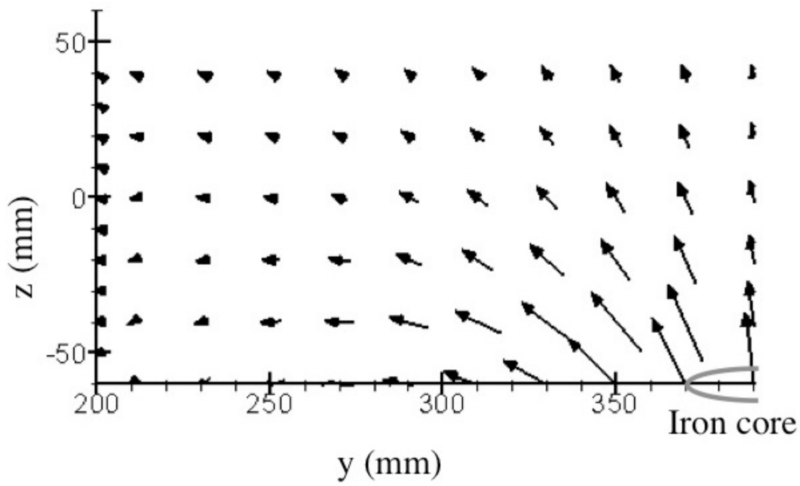

Figure 4.4: ReComm system magnetic field vector plot. The y-z ReComm system magnetic field vectors with the directions and relative strengths are shown. The center of the iron core is at $y = 390$ mm and it extends back to $y = 350$ mm, as indicated by the circle on the plot.

Due to the geometry of the experiment and the diagnostic probes, the closest achievable distance to the surface of the ReComm system was 10 mm. Figure 4.5 shows the z-component of the magnetic field along the plane directly above the ReComm system surface when the magnet was operating at maximum input power. During ReComm system operation, the peak z-component of the magnetic field was varied from 0 G to 2000 G, allowing measurement of the decreased plasma density as a function of magnetic field strength.

Since the axial magnetic field of the helicon source plays an integral role in achieving helicon mode operation, it was important to ensure that the field produced by the ReComm system magnet did not affect the field required for the helicon source. The entire system of magnets was modeled using a software package called MagNet. The package allows for 3-dimensional modeling of magnetic fields. Figure 4.6 shows the peak axial magnetic field along the helicon centerline as a function of the y-position and the driving current of the ReComm system magnet. The figure shows

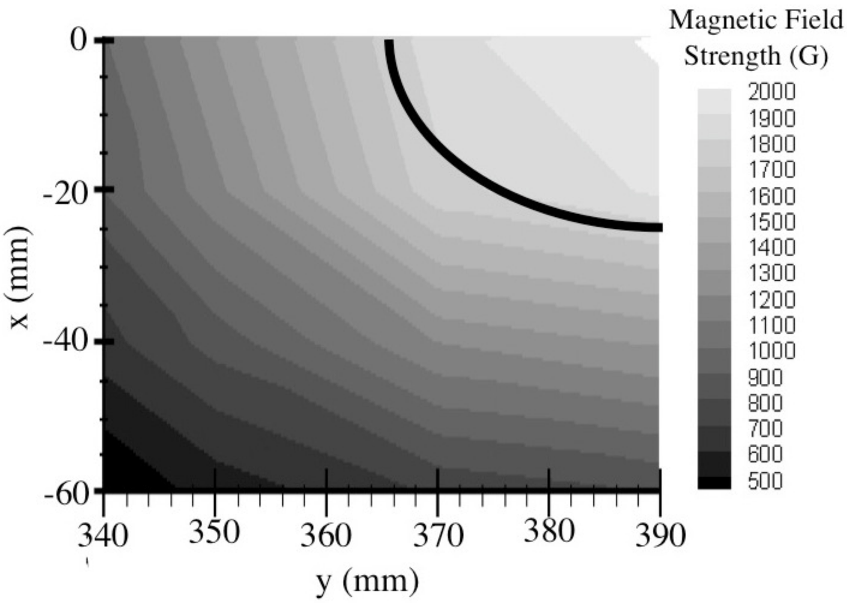

Figure 4.5: ReComm system peak B_z. Data from the plot were measured along the z-plane directly above the surface of the ReComm system. The location of the iron core of the magnet is indicated by the white oval.

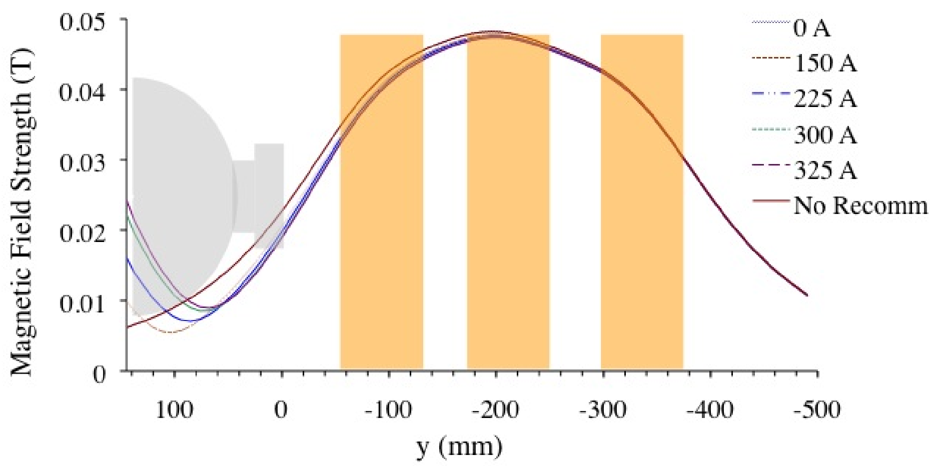

Figure 4.6: Modeled ReComm and helicon source magnetic fields. Peak axial (y) magnetic field along the helicon centerline as a function of the y-position and the current driving the ReComm system magnet.

that the ReComm system magnetic field changes the shape of the helicon source magnetic field by less than one percent. The difference between the cases of 0 A on the magnet and “No ReComm” is that the iron core and base plate had residual magnetic fields. In order to further examine whether the ReComm system magnetic field changed the shape of the helicon source magnetic field, contour plots of B_y as a function of x and z-positions were produced from the MagNet model for the case of no ReComm system magnetic field and maximum ReComm system magnetic field. These plots are shown in Figure 4.7. Again, the residual magnetic field is seen in the

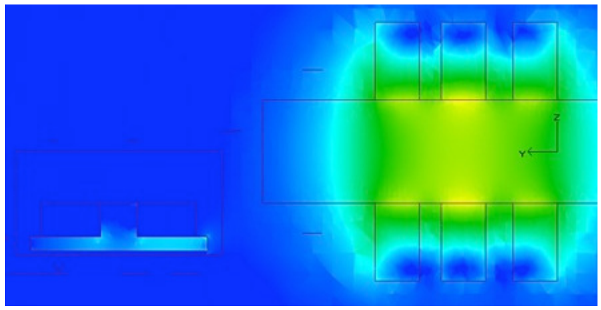

(a)

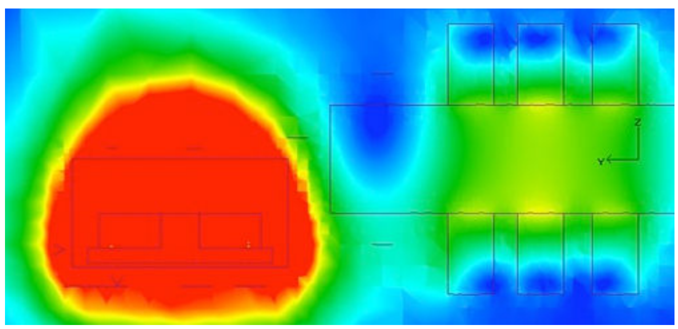

(b)

Figure 4.7: Contour plots of the total magnetic field strength for no ReComm system magnetic field and peak ReComm system magnetic field. Total magnetic field strength is shown as a function of x and z-position along the $y = 0$ mm axis for two ReComm system magnet operating conditions: (a) no ReComm system magnetic field and (b) maximum ReComm system magnetic field.

iron core and base of the ReComm magnet. Once more, the ReComm system magnetic field had little effect on the helicon source magnetic field, even when operating at peak magnetic field strength.

Mounted atop the electromagnet was a 6.3-mm-thick mica sheet. This sheet served two purposes: (1) to create a dielectric barrier between the plasma and the electromagnet; and (2) to simulate the dielectric surface of an atmospheric re-entry vehicle. Without the mica barrier, the plasma, which was at a 50-V-potential, would have arced to any sharp points or edges on the electromagnet. Furthermore, atmospheric re-entry vehicles must withstand incredibly harsh conditions including massive heat loads. Dielectric ceramics are among the few materials viable for re-entry shielding (63).

The electrodes were made up of 0.32-cm-diameter stainless steel rods that ran parallel to each other and the x-axis a distance of 4 cm apart. The electrodes were set into the mica sheet so that only half of the diameter protruded above the sheet. The reason for being set into the sheet was to help with survivability during re-entry. In addition, the electrodes may need to be manufactured out of molybdenum or titanium if stainless steel does not last. The electrodes were covered with dielectric tape so that only 10-cm-lengths near the iron core of the magnet were exposed. The anode, the electrode closest to the plasma source, was set to ground, and the electrode further downstream, the cathode, was set to a negative potential (V_c) that varied between 0 and -250 V. It was decided to set up the electrodes as a grounded anode and a negative cathode to ensure that the ions would be accelerated by a negative electric field. With the electric and magnetic fields as described, the $E \times B$ drift was in the negative x-direction, as shown in Figure 4.3. Figure 4.8 is a photo of the final ReComm system setup with the magnet, mica sheet and stainless steel electrodes.

Due to the nature of the setup and the fact the the operating pressure of the system was at the bottom of the Paschen curve (64), without the presence of a sufficiently strong magnetic field, the electrodes arced to each other and to other metal edges and corners inside the vacuum chamber. Thus, operation with only an electric field was not possible. The maximum possible cathode voltage was a function

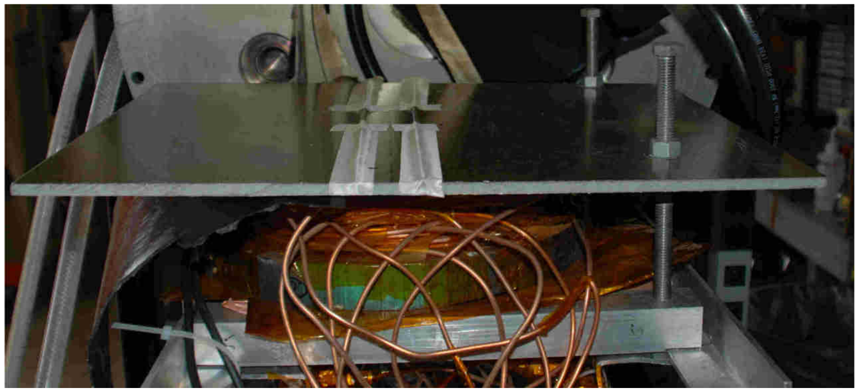

Figure 4.8: Photograph of the ReComm system. The magnet, mica sheet and electrodes are shown.

of the ReComm system magnetic field strength. Table 4.2 shows the maximum voltage applied to the cathode for each magnetic field operating condition.

Peak B_z (G)	Maximum Operating Potential (V)	Average Electric Field (V/m)
0	0	0
925	-100	2500
1385	-100	2500
1850	-250	6250
2000	-250	6250

Table 4.2: Maximum possible potential difference between the electrodes.

4.4 Summary

This chapter presented the concept behind the blackout amelioration system developed for this dissertation. The $E \times B$ field was introduced, and a simple explanation of the theory behind the $E \times B$ drift was included. Concurrent work was performed to computationally simulate the ReComm system, and that work was briefly described here.

An extensive section about the setup of the ReComm system included details about how the magnetic field and electric field were produced. In addition, the magnetic field properties were given and it was determined that the ReComm system magnetic field did not adversely affect the helicon source magnetic field. Finally, a discussion about how the ReComm system could not operate without the presence of its magnetic field was included.

CHAPTER 5

Facilities, Diagnostics and Analysis Techniques

Chapter 5 includes a description and layout of the experimental facilities. In addition the diagnostic tools and their analysis techniques used for measuring ion number density, plasma frequency, signal attenuation and ion energy distribution functions are discussed.

5.1 Cathode Test Facility (CTF)

All testing was performed in the Cathode Test Facility (CTF) at PEPL at the University of Michigan. The CTF is a 0.6-m-diameter by 2.44-m-long aluminum-walled vacuum chamber shown in Figure 5.1. Initially, rough vacuum is reached and maintained with a 25-cfm Edwards XDS35i dry-scroll pump. Once 50 mtorr is reached, the roughing pump is valved off and shut down, and the cryopump is started. The CVI model CGR 411-LS cryopump is attached to the rear of the chamber (bottom left of Figure 5.1). It can evacuate the CTF to a base pressure of 3×10^{-7} torr in about 4 hours. The chamber pressure is monitored by three pressure gauges:

- an MKS series 345 Pirani gauge and MKS model 937 gauge controller

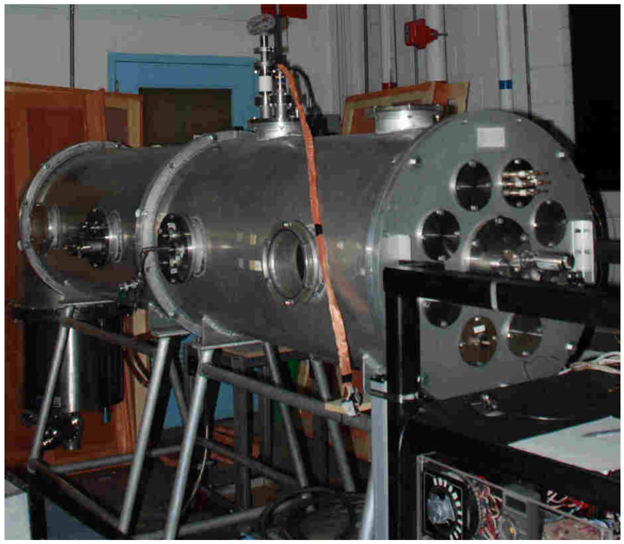

Figure 5.1: Photograph of the Cathode Test Facility.

- an MKS series 909 combined Pirani and hot cathode gauge with a MKS model 900 pressure transducer controller

- a hot cathode gauge with a model Varian LR88590 gauge controller

During testing, the chamber pressure was maintained at 0.6 ± 0.05 mtorr with an argon gas feed. Pressure measurements from the gauges, P_1, are corrected using the known base pressure with air, P_b, and a correction factor for the gas present in the chamber ($C_f = 1.2$ for argon) according to Equation 5.1.

$$P_c = \frac{P_1 - P_b}{C_f} + P_b \tag{5.1}$$

The argon gas was fed into the CTF via a needle valve attached to a hose, which itself was attached to the nozzle of the quartz tube. Since maintaining a fixed background pressure, and thus the plasma number density, was the goal of this research, controlling the mass flow rate was unnecessary. For a fixed setting of the needle valve, the background pressure remained constant to within ± 0.05 mtorr.

Inside the vacuum chamber were three high precision linear tables. These tables, along with an external motion controller allowed for three dimensional motion of probes without requiring access to the inside of the vacuum chamber.

5.2 Experimental Layout

Figures 5.2a and 5.2b show the experimental layout. The quartz tube of the helicon source was connected via a rubber O-ring to a 14.5-cm-diameter port located on the side of the CTF. Argon gas was fed into the CTF through the helicon source

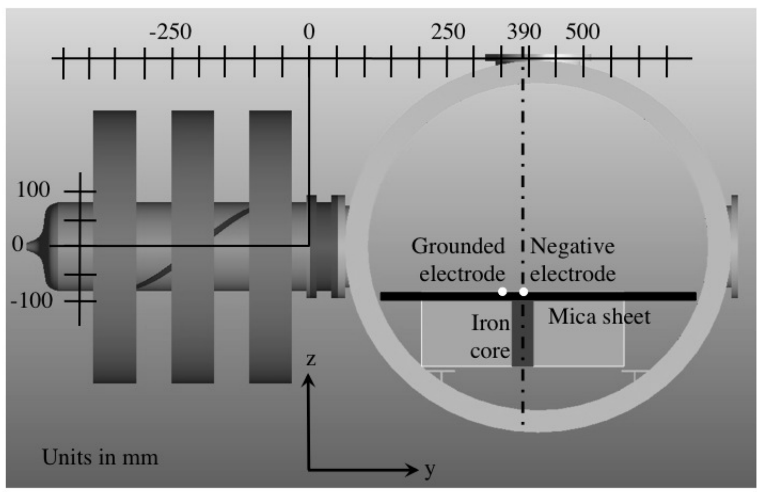

(a)

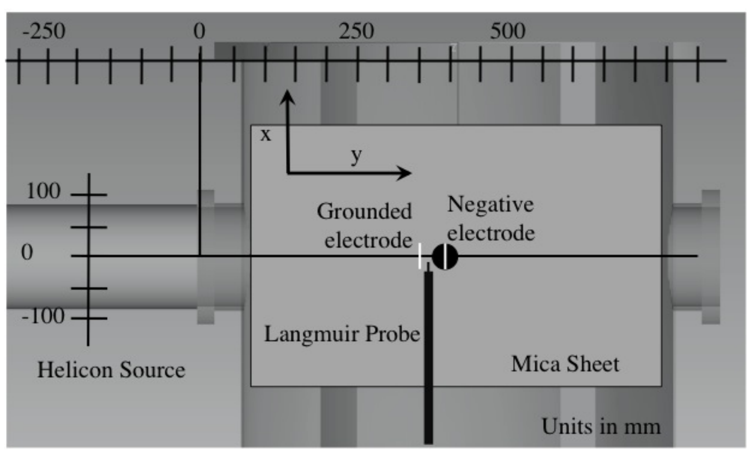

(b)

Figure 5.2: Experimental layout. The PEPL helicon source and ReComm system are shown from (a) the radial (x) direction and (b) looking down upon the mica surface from the vertical (z) direction. In both figures, the (0,0,0) measurement point is indicated along with the location of the mica sheet, when it was present.

from a nozzle on the end of the quartz tube. Figure 5.2a shows the antenna and the magnets that makeup the helicon source.

For the following sets of experiments, only diagnostic probes and three linear tables were present inside the vacuum chamber:

- Confirming helicon mode operating (Section 6.1)
- Characterizing plasma downstream of helicon source (Section 6.2)
- Measuring the ion energy (Section 6.3)

All other testing was done with the ReComm system present downstream of the helicon source, as shown in Figure 5.2, with the location of the magnet, iron core, electrodes and mica sheet indicated. The ReComm system was located such that its upper surface sat directly below the helicon source port at a vertical (z) position of -80 mm.

Each set of experiments occurred in different locations, both inside and downstream of the helicon source. For all experiments, the same set of coordinates were used, and those are indicated in Figure 5.2. The x and z origins were located in the radial center of the helicon source, and the y origin was located in the plane where the quartz tube attached to the vacuum chamber. Further details about testing locations are in Table 5.1.

5.3 Diagnostic Tools

A variety of diagnostics were used for characterizing the plasma and evaluating the ReComm system. These tools include two RF compensated single Langmuir

Test	Diagnostic	Radial (x) boundaries (mm)	Axial (y) boundaries (mm)	Vertical (z) boundaries (mm)
Helicon Confirmation	Langmuir Probe	-60 - 60	-100 and -150	0
Characterization - No ReComm System	Langmuir Probe	-50 - 50	180 - 340	-60 - 0
Characterization - ReComm System Present	Langmuir Probe	-50 - 40	180 - 340	-60 - 0
Helicon IEDF	RPA	0	40 - 240	0
Density Reduction	Langmuir Probe	-40 - 0	350 - 390	-70 and -75
Plasma Frequency	Hairpin Resonance Probe	0	350 - 400	-75
Antenna Response	S2-1 Probe	0	350 - 400	-75 (lower antenna location)

Table 5.1: Diagnostic probe testing locations.

probes to measure ion number density, electron temperature and plasma potential. In addition, a hairpin resonance probe was used to measure the plasma frequency, a signal attenuation probe with two antennas spaced 1 cm apart was used to measure signal attenuation levels and a retarding potential analyzer (RPA) was used to measure the ion energy distribution function (IEDF) of the plasma exiting the helicon source. The signal attenuation is referred to as an S2-1 probe because it measures the power of the signal received by second antenna that was emitted by the first antenna. Table 5.2 shows the important dimensions of the four types of probes used in these experiments.

Probe	Tip/wire diameter (mm)	Length (mm)	Width/diameter separation (mm)	Grid Separation (mm)
Hiden Langmuir probe	0.15	1.78	—	—
PEPL Langmuir probe	0.13	0.787	—	—
Hairpin resonance probe	2.0	37	13	—
S2-1 probe			2.5	
PEPL RPA	—	—	50	1.7
MRPAv1	—	—	21	0.71
MRPAv2	—	—	19	0.5

Table 5.2: Important probe dimensions.

5.3.1 Single Cylindrical Langmuir Probe

The single Langmuir probe is the most basic plasma diagnostic tool. It was first applied by its namesake, Irving Langmuir and his collaborators in 1926 (65; 66). The probe consists, most basically, of a conducting tip, and current to the probe is measured as a function of applied voltage. This results in a current vs. voltage characteristic (I-V curve) from which the number density, electron temperature, floating potential and plasma potential can be determined. A representative I-V curve is shown in Figure 5.3. Langmuir probe characteristics are divided into three regions. The point at which zero net current is collected by the probe is called the floating potential, V_f, and it is about 25 V for the experiments done in this dissertation. At voltages well below the floating potential, the probe is in the ion saturation region (Region 1), and it repels electrons. As the probe voltage increases, the electrons become capable of overcoming the potential difference, and the current to the probe increases as well. This is referred to as the electron retarding region of the character-

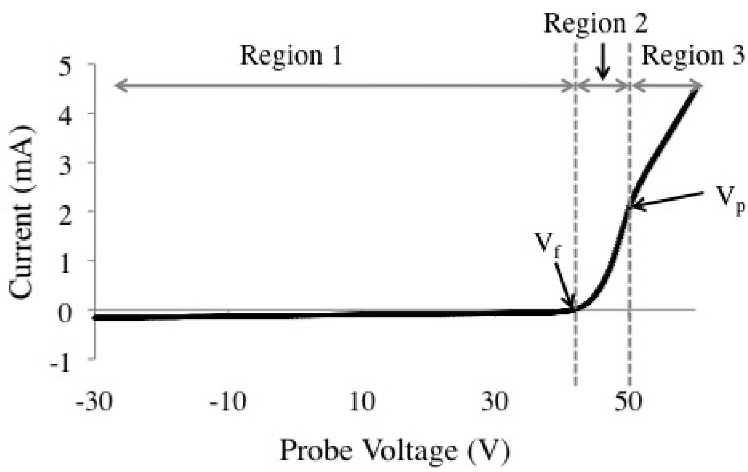

Figure 5.3: Langmuir probe I-V characteristic example.

istic and is shown as Region 2 on Figure 5.3. In Region 3, bias potentials are greater than the plasma potential, V_p, and the probe only collects electron current. This is called the electron saturation region (67).

Although the basic principle of the Langmuir probe is simple, interpreting the I-V curve can be difficult and complicated. There are effects from RF interference, multiple operating regimes, effects from flowing plasmas and magnetic fields and expanding sheath effects that must be considered.

5.3.1.1 Radio Frequency Compensation and Probe Tips

Two Langmuir probes were used for these experiments. An RF compensated probe based on a design by Sudit, *et al.* (68) was developed at PEPL and used in conjunction with an RPA for the IEDF measurements. A commercial RF compensated Langmuir probe from the Hiden Corporation was used for all other measurements. The probe for the IEDF measurements was built because the Hiden Langmuir probe was not long enough to reach the desired region of testing upstream inside the helicon source with the RPA present as well.

The Hiden Langmuir probe contains an inductor to compensate for the RF frequency of 13.56 MHz, using the inherent capacitance of the inductor to create a low-pass filter. The solid black line in Figure 5.4 shows how the output amplitude

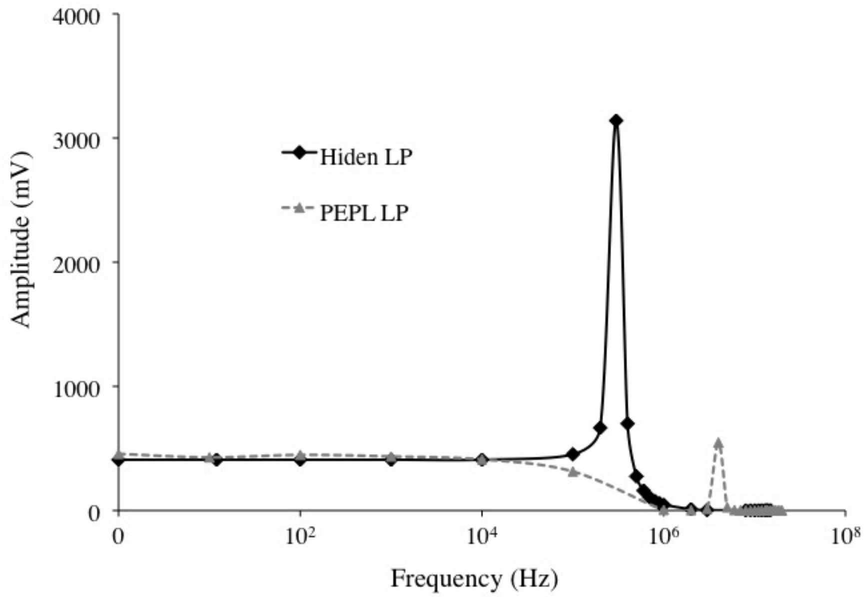

Figure 5.4: RF compensation of the Langmuir probes. The output amplitude as a function of input frequency for a constant 440-mV input amplitude. The black solid line is the signal response for the Hiden Langmuir probe and the gray dashed line is the response for the Langmuir probe built at PEPL.

varies as a function of input frequency for the Hiden Langmuir probe. A constant 440-mV amplitude was provided to the probe tip, and the resulting signal was measured as a function of the input frequency. For signals with frequencies less than 0.1 MHz, the signal passed unchanged. Between 0.1 MHz and 0.4 MHz, the signal was amplified; however, since no signals in that frequency range were expected, the response is satisfactory. Above 0.4 MHz, the signal was almost completely attenuated. Therefore, any RF pickup on the Langmuir probe from the 13.56 MHz power supply was removed from the system

Furthermore, the Hiden Langmuir probe had a graphite compensation electrode surrounding the probe tip. Figure 5.5 is a photograph of the probe tip from the

Figure 5.5: Hiden Langmuir probe tip

Hiden system. The Langmuir probe tip itself was a 1.78-mm-long by 0.15-mm-diameter tungsten electrode that was oriented parallel to the body of the Langmuir probe, as seen in Figure 5.5.

For the Langmuir probe built at PEPL, the RF compensation circuit was more complicated. It consisted of four inductors in series: two for filtering 13.56 MHz and two for filtering 27.12 MHz. The gray dashed line in Figure 5.4 shows the frequency response for this series of inductors. The response is similar to that found with the Hiden probe, but the signal response decreased at about 0.1 MHz, then increased to a peak at about 4.5 MHz and finally dropped off. Again, since no signals were expected around 4.5 MHz, the frequency response is acceptable.

The probe tip for the PEPL Langmuir probe was connected in series with the inductors and in parallel with a capacitor and a compensation electrode. The compensation electrode was a coil of tungsten wire surrounding the alumina tube that held the probe tip. A photograph of the probe tip is shown in Figure 5.6a and a schematic of it is shown in Figure 5.6b. The tungsten probe tip itself was a 0.787-mm-long by 0.13-mm-diameter tungsten electrode orientated perpendicular to the body of the Langmuir probe.

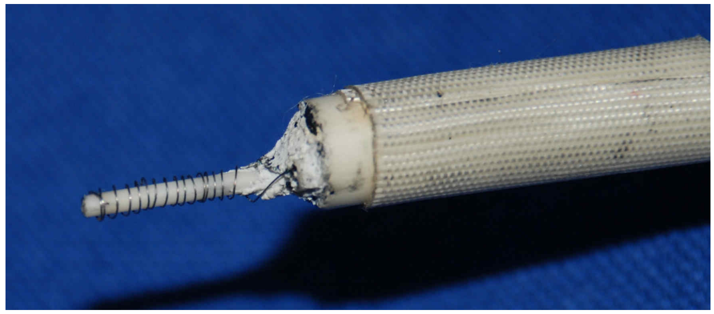

(a)

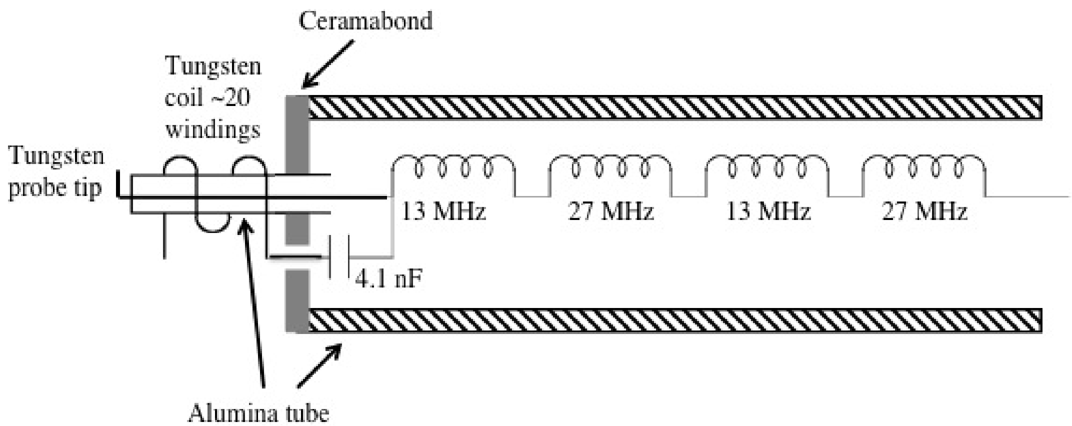

(b)

Figure 5.6: PEPL Langmuir Probe tip. (a) Photograph, (b) schematic drawing.

5.3.1.2 Langmuir Probe Theory of Operation

Langmuir probe operation is divided into different operating regimes by two non-dimensional parameters. The first is the Knudsen number (K_n), which relates the ion/electron mean free path, λ_{MFP} (the distance over which there is a good probability for a collision to occur (6)), to the probe radius, r_p.

$$K_n = \frac{\lambda_{MFP}}{r_p} \tag{5.2}$$

This results in a relative measurement of the number of ion/electron collisions compared to the length scale of the probe, giving insight into whether the probe is in the collisionless or continuum plasma regime. If the Knudsen number is much greater than one, as it was for these experiments, it is safe to assume the probe is operating in the collisionless regime (67).

The second parameter for determining the operating regime of a Langmuir probe is the ratio of the probe radius-to-Debye length. The Debye length, λ_D is a measure of the sheath thickness (6), and thus, it can be used to determine the sheath regime of operation.

$$\lambda_D = \sqrt{\frac{k_B T_e \epsilon_o}{n_e e^2}} \tag{5.3}$$

When $r_p/\lambda_D < 3$, the orbital motion limited (OML) method for analysis is appropriate to use (69). During OML operation, sheath dimensions are important, and the orbits of particles entering the sheath must be considered since not all particles that enter the sheath are collected by the probe. This regime is analyzed using techniques developed by Laframboise (70; 71) that assume a cylindrical probe is immersed in a cold, collisionless, stationary plasma. Therefore, the sheath dimensions are assumed to increase as the probe bias increases, affecting the collected ion current.

When $r_p/\lambda_D > 10$, the thin sheath method for Langmuir probe analysis is appropriate (69). In the thin sheath regime, the flux of the particles entering the sheath can be calculated without considering the details of particle orbits in the sheath (65; 67; 69; 72). In between the two regimes, a transitional approach is used. Because the number density varied greatly in these experiments, the Langmuir probe analysis regime ranged from the OML regime to the thin sheath regime, and in many cases, fell between the two.

5.3.1.3 Langmuir Probe Data Acquisition

The commercial Langmuir probe system from the Hiden Corporation consists of data acquisition software and a controller box that were used with both Langmuir probes during the experiments. The Hiden controller box produces a varying voltage and measures the plasma response via an internal ammeter. At the end of each voltage sweep, the Langmuir probe voltage was increased to 80 V for one second in order to clean the probe tip. Software provided by the Hiden corporation uses a serial port on the computer to set the voltage range and store the collected current data. Raw Langmuir probe data were stored as I-V curves, and then smoothed via a seven-point-box-smoothing spline prior to analysis. The smoothing was done by the Hiden software to eliminate any 13.56-MHz noise that may have been picked up by the transmission lines, therefore facilitating the ion number density calculation. Figure 5.7 shows a representative sample of the raw Langmuir probe data and the result of smoothing those data. After smoothing the I-V curves, the data were exported to Matlab for analysis.

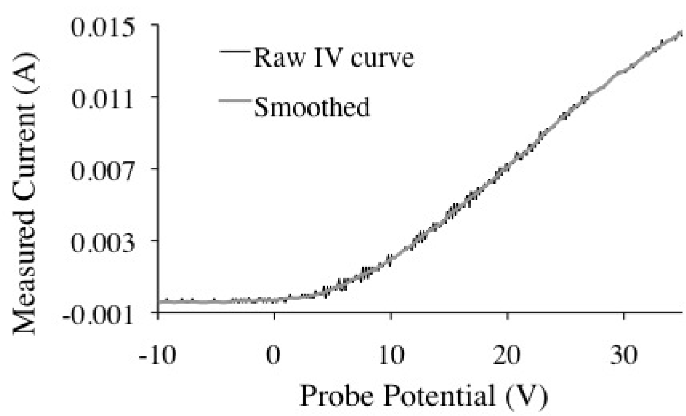

Figure 5.7: Smoothed Langmuir probe I-V curve and its corresponding raw I-V curve.

5.3.1.4 Langmuir Probe Data Analysis

For each data point, three I-V curves were measured. Upon importing the smoothed data into Matlab, the three curves were averaged. For each data point, the following analysis method was used. (A flow chart of this method can be found in Appendix A.) First, the floating potential was found as the point where the collected current is zero. Based on the floating potential, a range of voltages was chosen in order to fit a line to the ion saturation region. For example, if the floating potential was 0 V, the ion saturation curve was fit to the portion of the I-V curve between -40 V and -10 V. If the floating potential was 30 V, the ion saturation curve was fit to the portion of the I-V curve between -10 V and 20 V. The line was extrapolated to the full range of bias voltages, and this ion current was subtracted from the smoothed, averaged I-V curve.

Initially, the OML regime was assumed. The ion number density for a cylindrical probe operating in the OML regime is determined from the slope of the ion current squared versus the bias voltage (69; 71; 73).

$$n_{i,OML} = -\frac{1}{A_p}\sqrt{\left(\frac{d(I_i^2)}{dV}\right)\frac{2\pi M_i}{1.27e^3}} \tag{5.4}$$

where A_p is the surface area of the Langmuir probe tip and M_i is the mass of an ion.

For the remainder of the analysis, the new I-V curve, with the ion saturation portion of the curve removed, was used. The Maxwellian electron temperature (in eV) was found from the inverse slope of the natural log of the electron current versus the probe voltage in the electron retarding region of the I-V curve.

$$T_e = \frac{V_2 - V_1}{\ln\left(I_2/I_1\right)} \tag{5.5}$$

The electron temperature calculation is the same for both the OML regime and the thin sheath regime.

With the electron temperature, the ion number density can be calculated using the thin sheath method. The ion saturation current was assumed to be the average of the data previously used for creating the ion saturation regime curve. This ion saturation current, I_{sat}, along with the electron temperature and the Bohm approximation for the ion velocity (6; 65; 69; 74; 75) allow for calculation of the ion number density from Equation 5.6.

$$n_{i,thin} = \frac{I_{sat}}{0.61 A_s e}\sqrt{\frac{M_i}{T_e}} \tag{5.6}$$

A_s is the electrode collection area, which depends on the sheath surrounding the probe tip. The sheath thickness is a function of the Debye length, and therefore is dependent on the electron temperature and the number density. Initially, the collection area was considered to be the electrode surface area, and an ion number density was determined from Equation 5.6. Then, assuming quasineutrality ($n_e \approx n_i$), the Debye length was found using Equation 5.3. The sheath thickness (76; 77) and corresponding sheath area (67) were then calculated according to:

$$\delta = 1.02\lambda_D \left[\left(-\frac{1}{2}\ln\left(\frac{m}{M_i}\right)\right)^{\frac{1}{2}} - \frac{1}{\sqrt{2}}\right]^{\frac{1}{2}} \left[\left(-\frac{1}{2}\ln\left(\frac{m}{M_i}\right)\right)^{\frac{1}{2}} + \sqrt{2}\right] \tag{5.7}$$

$$A_s = A_p\left(1 + \frac{\delta}{r_p}\right) \tag{5.8}$$

The thin sheath ion number density was then recalculated using the new collection area. This iterative process was repeated until convergence to a final ion number density occurred. The new number density accounts for sheath expansion and represents a slight departure from the traditional thin sheath analysis (26; 78).

Once both the OML and thin sheath ion number densities were found, their respective Debye lengths were calculated. Then the ratio of Debye length-to-probe radius was found and the operation regime determined. Often, the data fell into either the OML regime or the thin sheath regime; however, sometimes the ratio was between 3 and 10, placing the Langmuir probe in a transitional regime. In order to determine the ion number density for these cases, a weighted average, based on the probe radius-to-Debye length ratio, was used. This method gives smooth transition between the various regimes. The analysis techniques presented here have been well documented by several other researchers (26; 65; 67; 69; 72; 73; 78–82).

Once the electron temperature and ion number density were determined, the plasma potential was calculated. Usually, the plasma potential could be read from the I-V curve as the knee between the electron retarding region and electron saturation region of the characteristic. However, for many of the data points in this investigation, the Hiden ammeter used to collect current reached saturation prior to entering the electron saturation region of the I-V curve. Figure 5.8 shows a normalized Langmuir probe trace that did not reach saturation and a normalized trace that did. The saturation sometimes occurred because more current was being collected by

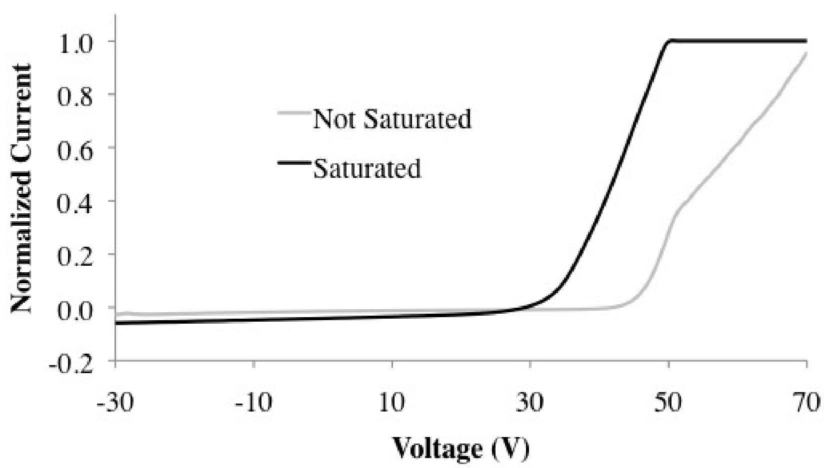

Figure 5.8: Example os a saturated and an unsaturated I-V curve.

the probe at locations closer to the exit of the helicon source than at locations further downstream. In order to keep signal saturation from occurring, the gain of the Hiden system needed to be changed so that the current limit of the ammeter would not be reached. However, since changing the gain would have decreased the accuracy of the measurements in the ion saturation region, and the ion density measurements were the key parameter for this dissertation, the gain remained set to where it was ideal for measurements in the ion saturation regime. In addition, the signal saturation could have been avoided by using multiple sizes of probe tips during testing. This would create more error in the measurements as changing the probe tip during testing would be a variation in the experimental parameters. Since finding the plasma potential was a secondary goal of this investigation, the same probe tip was used throughout testing, and plasma potential was calculated using Equation 5.9 for the assuming quasineutral plasma and cylindrical probe collisionless sheath theory (33).

$$V_p = \ln\left(\sqrt{\frac{m_e}{m_i}}\right) k_B T_e + V_f \tag{5.9}$$

5.3.1.5 Environmental Effects

A variety of environmental considerations must be taken into account when analyzing Langmuir probe data. End effects must be considered when using a cylindrical Langmuir probe submersed in a flowing plasma (73). However, since the helicon plasma source used for this research is of low ion energy (less than 50 V as shown in Section 6.3), end effects have been neglected.

When a Langmuir probe is aligned parallel to the electric field, the I-V curve can become distorted. This distortion is a rounding of the knee of the I-V curve between the electron retarding region and the electron saturation region (83). Since this mostly affects the plasma potential and electron saturation current, there is little effect on the electron temperature and ion number density. Therefore, the effect was neglected in these analyses.

A strong magnetic field can also alter the I-V curve of a cylindrical Langmuir probe. Once again, the electron saturation region is most affected by magnetic field effects (84–86). This is because ions are much more massive than electrons, so the electrons are more likely to be trapped in magnetic field lines. This occurs when the electron cyclotron radius (2.19) is of the same magnitude as the probe radius. When this happens, the electrons cannot cross the magnetic field lines without collisions. Then the probe sheath structure can become affected, causing the electron saturation current to be reduced. Once again, since the analyses used in this investigation relied on the ion saturation region and the electron temperature, this effect was neglected.

When the ReComm System operated at a peak magnetic field of 2000 G, the ion cyclotron radius was still an order of magnitude larger than the Langmuir probe radius. However, at these very high magnetic fields, the electron retarding region of the curve is also suppressed. This lowers the slope in Region 2, resulting in a larger electron temperature. During ReComm system operation, the Langmuir probe traces all fell within the OML operation regime. Therefore, calculation of the ion number density is independent of the electron temperature and is still valid. In addition, the effect of a magnetic field on a cylindrical Langmuir probe is minimized when the probe is oriented perpendicular to the magnetic field lines (67). This was the case for the experiments done while the ReComm system was operating.

Beyond trapping electrons, magnetic fields can also cause an anisotropy in the electron energy distribution function (EEDF), which causes an additional effect on the electron temperature calculation. This effect can be considered small if the ratio of the magnetic field strength-to-vessel pressure (B/p_o) is less than 2.5×10^6 G/torr (83; 87). Given that the operating pressure was 0.6×10^{-3} torr in the region downstream of the helicon source, when the ReComm System was operating at more than 1500 G, the anisotropy effects must be accounted for in the electron temperature calculations. However, the ultimate goal of this research was to measure the density reduction when the ReComm system was in operation. As previously mentioned, the Langmuir probe was operating in the OML regime during ReComm system testing, so the electron temperature was not used in the ion number density calculation.

For the Langmuir probe measurements done inside the helicon source, the Langmuir probe was orientated parallel to the magnetic field lines. In addition, the probe was operating in either the thin sheath or transitional regime, requiring the electron temperature to calculate the ion number density. Therefore, it was important to ensure that an anisotropy did not develop in the electron retarding region. For a magnetic field of about 450 G and a pressure of 0.6×10^{-3} torr, the ratio $B/p_o = 7.5 \times 10^5$, which is below the threshold value given earlier. In addition, the Hall parameter, β was calculated to be around 50.

5.3.1.6 Error Analysis

Traditionally, Langmuir probe error estimates are around 50% for the number density and 20% for the electron temperature (67; 88). Although these errors are high when looking at absolute values for the ion number density and electron temperature, the relative error between measurements using the same experimental setup is considerably lower (89). In addition, comparisons with hairpin resonance probe measurements show that the relative changes in ion number density when the ReComm system was operating correlate well with the reduction in plasma frequency. This increases confidence that the Langmuir probe analysis was accurate.

5.3.2 Hairpin Resonance Probe

Microwave resonator probes provide a resonant structure from which the relative dielectric constant of the surrounding medium can be determined (90). When the resonator is placed in a plasma, its resonant frequency shifts from the characteristic resonant frequency of the probe when it is in a vacuum (91). The plasma frequency can be determined from these resonant frequency shifts.

The simplest microwave resonant probe is an open, quarter wavelength, parallel-wire transmission line that is short-circuited at one end. This design is referred to as a hairpin resonant probe due to its resemblance to a hairpin. The hairpin resonator used in these experiments is shown in Figure 5.9. This design was based on one

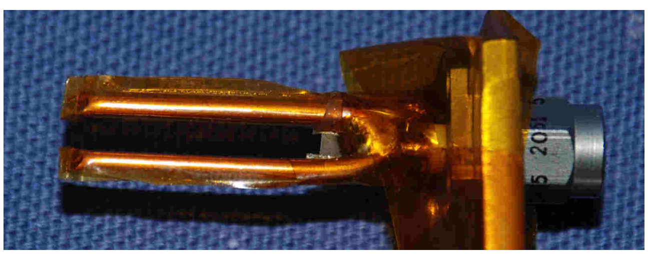

(a)

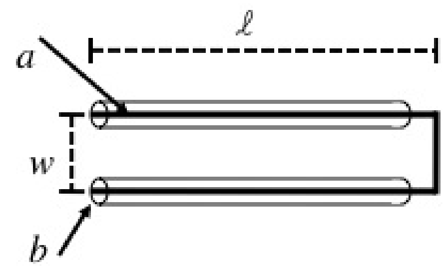

(b)

Figure 5.9: Hairpin resonance probe photograph (a) and schematic (b). a is the wire radius, b is the thickness of the space-charge sheath, w is the probe width and ℓ is the probe length.

introduced by Stenzel in the 1970's (92). The probe width, length and wire radius were: w = 13 mm, ℓ = 57 mm and a = 1.0 mm, respectively. A low-amplitude, time-varying current was driven in the probe by an Agilent E5071C, ENA series 9 kHz - 8.5 GHz network analyzer over a range of frequencies. The power was directly connected to the hairpin probe by a coaxial cable. Reflected power was observed using the same network analyzer to determine the resonant frequency shift of the probe, f_r (93). The resonant frequency is measured as the frequency at which the reflected power is at a minimum. Figure 5.10 is a schematic of the layout of the hairpin probe and the network analyzer, and Figure 5.11 shows a sample trace from the hairpin probe.

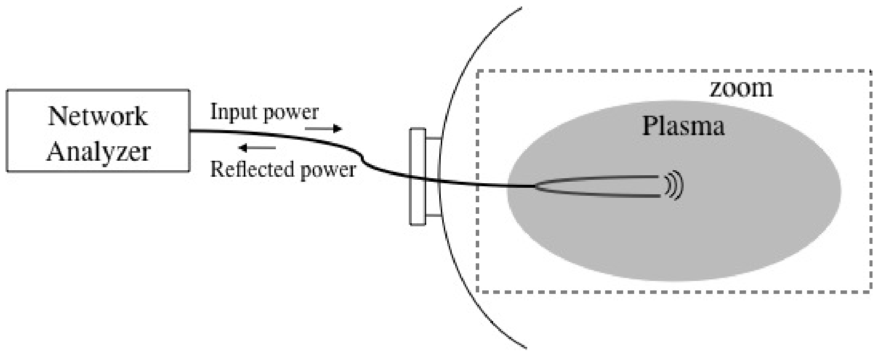

Figure 5.10: Hairpin probe layout.

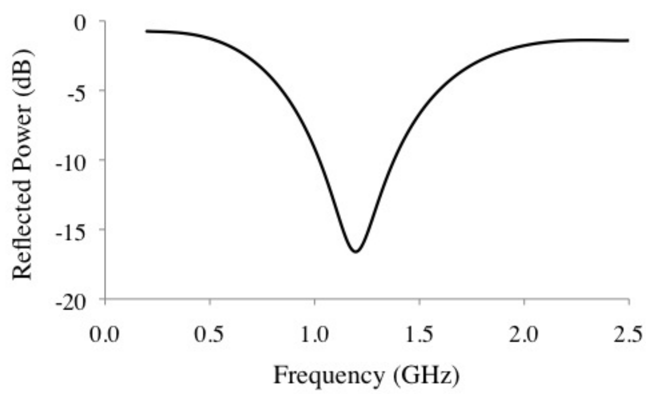

Figure 5.11: Sample reflected power trace from the hairpin probe. The minimum of the curve represents the resonant frequency of the probe.

The hairpin probe resonant frequency is simply a function of the probe length, ℓ, and the relative dielectric constant of the medium, ϵ.

$$f_r = \frac{c}{4\ell\sqrt{\epsilon}} \tag{5.10}$$

In vacuum, the relative dielectric constant is unity, and the corresponding resonant frequency can be calculated from the following

$$f_o = c/4\ell \tag{5.11}$$

The actual measured vacuum resonant frequencies for the probe ranged between 1.15 GHz and 1.8 GHz depending on the location of the hairpin probe. A vacuum resonance frequency was found for each individual operating location within the chamber to account for the differences. The dielectric constant can be found from the cold plasma dispersion relation as a function of the plasma frequency (f_p), the electron cyclotron frequency (f_c) and the hairpin probe resonant frequency (f_r) (6; 91; 94).

$$\epsilon = \left(1 - \frac{f_p^2}{f^2} \frac{f_r^2 - f_p^2}{f_r^2 - \left(f_p^2 + f_c^2\right)}\right)^{\frac{1}{2}} \tag{5.12}$$

The above equation is also the dielectric constant response to the extraordinary wave. The extraordinary wave propagates perpendicular to the magnetic field and affects the motion of electrons (thus the electron cyclotron frequency in Equation 5.12).

For a weakly magnetized plasma, the dispersion relation simplifies to the following general expression for the ordinary wave.

$$\epsilon = 1 - \frac{f_p^2}{f_r^2} \tag{5.13}$$

which is the dielectric constant response to the ordinary wave. In order to determine whether the 2000-G-magnetic field affected the operation of the hairpin resonant probe, the dielectric constant was plotted as a function of frequency for the ordinary wave and the extraordinary wave. As shown in Figure 5.12, the dielectric response of the plasma to extraordinary wave propagation is unity at the vacuum resonant frequency of the hairpin probe (between 1.2 and 1.8 GHz). Thus, only the ordinary wave accounts for the shift in the dielectric constant. Therefore, Equation 5.13 can be used to calculate the plasma frequency as long as $f_r > f_p$. The frequency components are related as:

$$f_r^2 = f_o^2 + f_p^2 \tag{5.14}$$

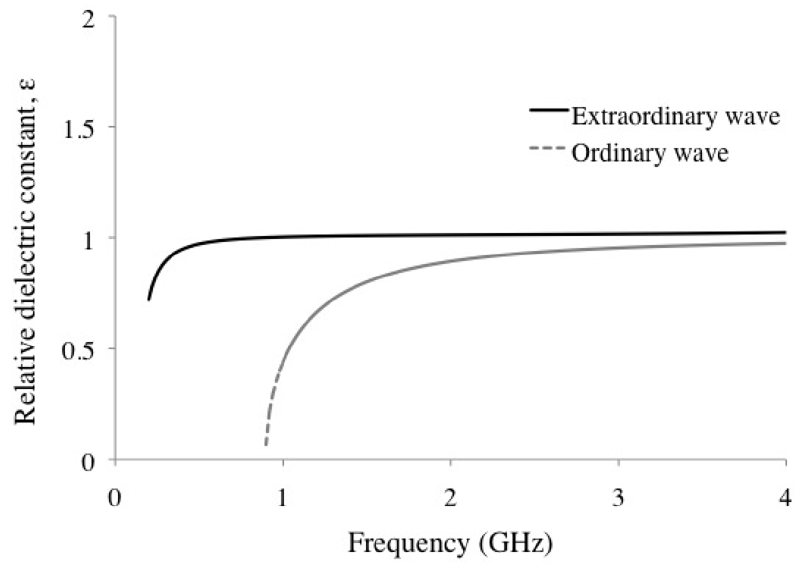

Figure 5.12: Dielectric constant, ϵ, response to the ordinary and extraordinary waves.

where f_o is the measured resonant frequency of the probe at the given operating condition and f_p is the plasma frequency.

The above is an idealized model and assumes that the volume between the prongs of the hairpin probe is just the physical distance between the wires. In actuality, a space-charge sheath devoid of electrons forms around the probe wires. This phenomenon causes an underestimation of the plasma frequency since the volume between the probe wires when measuring the vacuum resonant frequency is less than the "probe volume" with the space-charge sheath present. Correcting for this electron-free sheath requires that Equation 5.14 be written in terms of a corrected plasma frequency, $f_p^{\prime 2}$, and a sheath correction factor, ζ_c (95).

$$f_r^2 = f_o^2 + \zeta_c f_p^2 \tag{5.15}$$

Piejak, *et al.* derived an expression for the sheath correction factor, assuming that the hairpin width is much larger than both the wire radius and the the sheath radius

(b shown in Figure 5.9b above) (90).

$$\zeta_c = 1 - \frac{f_o^2}{f_r^2} \frac{\ln\left(\frac{b}{a}\right)}{\ln\left(\frac{w}{a}\right)} \tag{5.16}$$

However, the probe width is usually not significantly larger than the sheath radius. For these experiments, the probe width was only about four times the wire radius, and thus, the sheath radius was likely to be a significant percentage of the hairpin width. This must be accounted for, and the following equation for the sheath correction factor was used (90).

$$\zeta_c = 1 - \frac{f_o^2}{f_r^2} \frac{\left[\ln\left(\frac{w-a}{w-b}\right) + \ln\left(\frac{b}{a}\right)\right]}{\ln\left(\frac{w-a}{a}\right)} \tag{5.17}$$

In order to apply the sheath correction factor, an appropriate model for the sheath needs to be used in order to determine the sheath radius. For this investigation the sheath radius was assumed to extend out one electron Debye length from the radius of the probe wire ($b = a + \lambda_D$). As discussed in Section 5.3.1.4, an iterative process was used to determine the sheath radius, which was initially assumed to be the probe radius. Using that initial assumption, a plasma frequency, and thus an electron number density was found. Then, the Debye length for that plasma density was calculated and added to the wire radius for a new sheath radius. This process was repeated until the method converged upon a solution.

Sources of error in hairpin resonance probe measurements need to be addressed. First, the assumption that the probe is similar to a transmission line leads to the assumption that the electric field has no gradient along the length of the hairpin probe. This assumption makes finding the plasma frequency straightforward, but numerical models of hairpin probes used elsewhere in the literature show a two order of magnitude variation in the electric field along the probe length (96). This means that any spatial variation in the plasma frequency is compounded by the nonuniform distribution of the electric field along the length of the hairpin probe (95). Another source of error for these experiments lies with the network analyzer used to produce the varying signal on the hairpin probe. The frequency resolution was limited to 10 MHz, so the plasma frequency could only be measured to within $\pm$ 5 MHz. The available frequency range was 200 MHz up to 8 GHz, due to RF and DC filters required for protecting the equipment from RF radiation and DC arcs from the plasma. Finally, the width of the hairpin resonant probe limited the spatial resolution available for these experiments.

5.3.3 Signal Attenuation Probe

The signal attenuation (S2-1) probe consisted of two monopole antennas, separated by 2.5 cm (Figure 5.13). The separation distance was chosen because data gathered during the RAM-C experiments show the thickness of the plasma layer to be about 2 cm (14; 15). This probe provided a direct measurement of the level

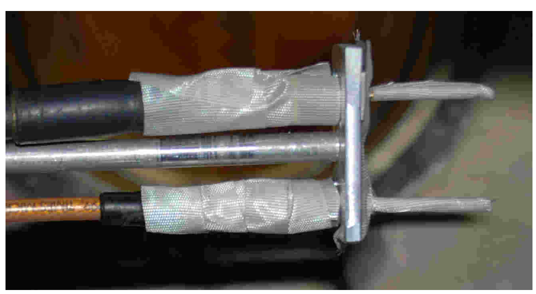

Figure 5.13: Photograph of the S2-1 probe.

of signal attenuation by the plasma. In order to do this, a network analyzer (the same one used previously with the hairpin probe) produced a low-power, frequency-varying signal to the antenna closest to the mica surface and recorded the relative attenuation of the signal on the second antenna. This layout is shown in Figure 5.14.

The frequency response was normalized to the frequency response found in vacuum so as to remove the antenna response from the results.

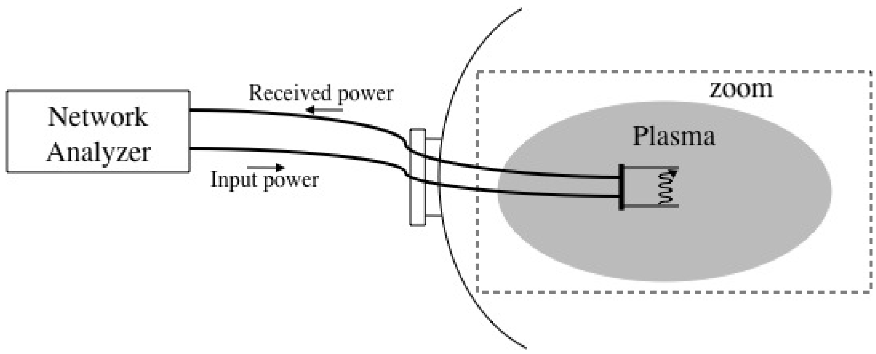

Figure 5.14: S2-1 probe layout.

The same network analyzer was used for the S2-1 probe measurements as was used for the hairpin resonance probe measurements. Thus, the frequency response resolution is 10 MHz with a frequency range of 200 MHz to 8 GHz.

One issue with setting the two monopole antennas only 2 cm apart was the possibility of picking up other types of near-field waves that would usually be attenuated by the atmosphere and distance traveled. One such wave that was expected to be observed was the evanescent wave. Figure 5.15 shows an actual sample trace from the S2-1 probe and a representative trace without the evanescent wave. A An evanescent wave (or a slow decoy pattern wave) travels with a velocity less than the characteristic velocity of the medium, and is attenuated in an exponential manner. The attenuation of the evanescent wave is due to the boundary conditions, not to signal loss in the medium (97). Thus, as long as the emitting and receiving antennas are close enough such that the wave does not dissipate within the separation distance, the signal will be picked up by the receiving antenna.

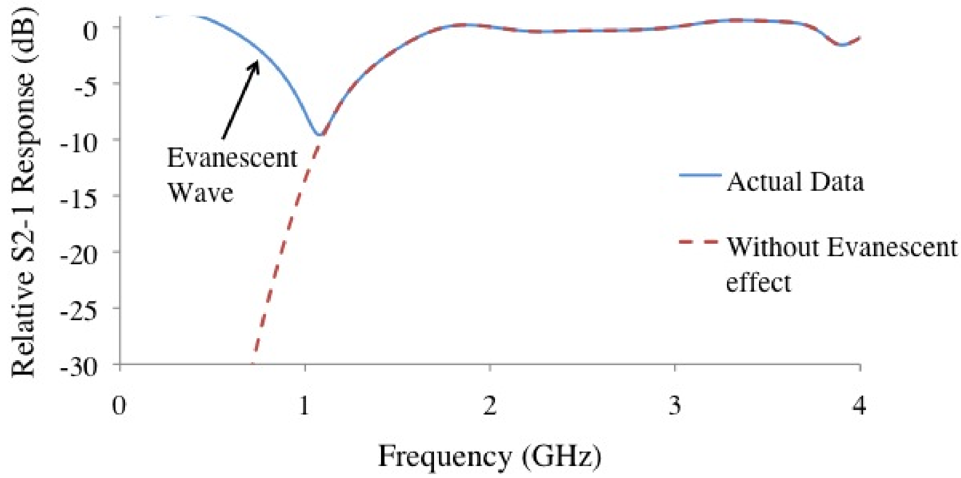

Figure 5.15: Example S2-1 trace.

5.3.4 Retarding Potential Analyzer

The retarding potential analyzer (RPA) is a diagnostic that uses a series of grids to determine the ion energy distribution function (IEDF) (67). This is done by filtering ions on the basis of kinetic energy. For this work, the RPA was used to measure the energy of the ions leaving the helicon source. A secondary desire was to determine whether the PEPL helicon source had a current-free electron double layer at the helicon exit, as do many helicon sources (56; 98; 99). For these reasons, a variety of RPAs were designed and tested for this dissertation. The details of each RPA are below in Sections 5.3.4.4 - 5.3.4.6.

In most cases, an RPA consists of four grids and a collector, as shown in the schematic in Figure 5.16. The first (neutralizing) grid is floating and serves to minimize the plasma perturbations (100). The second grid (electron repelling) is biased negatively so that the plasma born electrons are repelled. The third grid (ion retarding) has a varying bias voltage applied to it. This serves to filter the ions such that only those with an energy-to-charge ratio greater than the bias voltage can pass. The

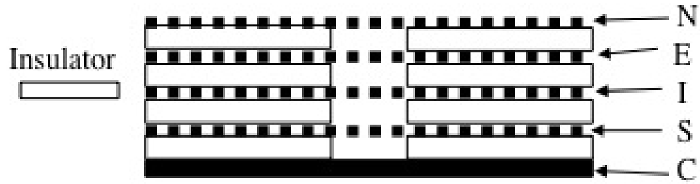

Figure 5.16: RPA schematic drawing. Basic RPA with the four grids (N = neutralizing grid, E = electron repelling grid, I = ion retarding grid, S = electron suppression grid), spacers and collector (C).

fourth grid is an optional electron suppression grid, and it serves to suppress secondary electrons produced when the high-energy ions collide with the ion retarding grid or the collector.

The key parameter in designing an RPA is the grid spacing between the electron repelling and the ion retarding grids. The grids must be close enough together to avoid space-charge limitations. This occurs when, as positively or negatively charged species are removed from the flow, additional charge builds up between the grids, creating a potential hill. If this potential hill increases to the point where it is greater than the applied voltage, then the operation of the RPA will change, resulting in a lowering of the collected current (or saturation of the space charge limited flow). The relationship between the grid spacing, x, and the potential difference between the grids, V_d, is given in Equation 5.18.

$$\frac{x}{\lambda_D} = 1.02 \left(\frac{eV_d}{k_B T_e} \right)^{\frac{3}{4}} \tag{5.18}$$

The voltage on the electron repelling grid is usually set to: $V_{rep}(V) = 3T_e(eV)$. This ensures that essentially all of the plasma born electrons are repelled. Thus, the spacing between the ion retarding grid and the electron repelling grid should be set to satisfy the condition (67):

$$x < 4\lambda_D \tag{5.19}$$

For a plasma with number densities and temperatures in the range found downstream of the helicon source this spacing is approximately 0.1 mm.

A Keithley 2410 source meter was used to drive the voltage on the ion retarding grid from 0 V to 100 V, and a picoammeter measured the current to the collector plate. Both instruments required low pass filters on the transmission lines to remove RF radiation from the DC signal. A LabView VI communicated with the Keithley 2410 to produce voltage and recorded the measurements from the picoammeter. The voltages to the electron repelling (-60 V) and electron suppression (-11.5 V) grids were provided by batteries. The constant voltage provided by a battery pack was ideal for this situation because it is not affected by RF radiation. The RPA potential diagram is shown in Figure 5.17a where the voltages are referenced to the facility ground.

5.3.4.1 RPA Data Analysis

Because the RPA acts as a filter with a characteristic transfer function, it must first be calibrated in order to allow for proper data analysis (101). Thus, all RPAs were first tested using an ion gun to ensure correct calibration. A description of the ion gun and calibration process is in Section 5.3.4.2

The RPA current-voltage characteristic was recorded by a LabView VI. For each location/operating condition, three current-voltage traces were recorded and averaged. Then the data were processed using a 7-point-box smoothing spline (102) in order to remove any RF noise picked up by the transmission lines upstream of the low pass filters. The derivative of the current-voltage characteristic is proportional to the IEDF, as shown in Equation 5.20

$$\frac{dI}{dV} = -\frac{e^2 Z_i^2 n_i A_c}{m_i} f(V) \propto -f(V) \tag{5.20}$$

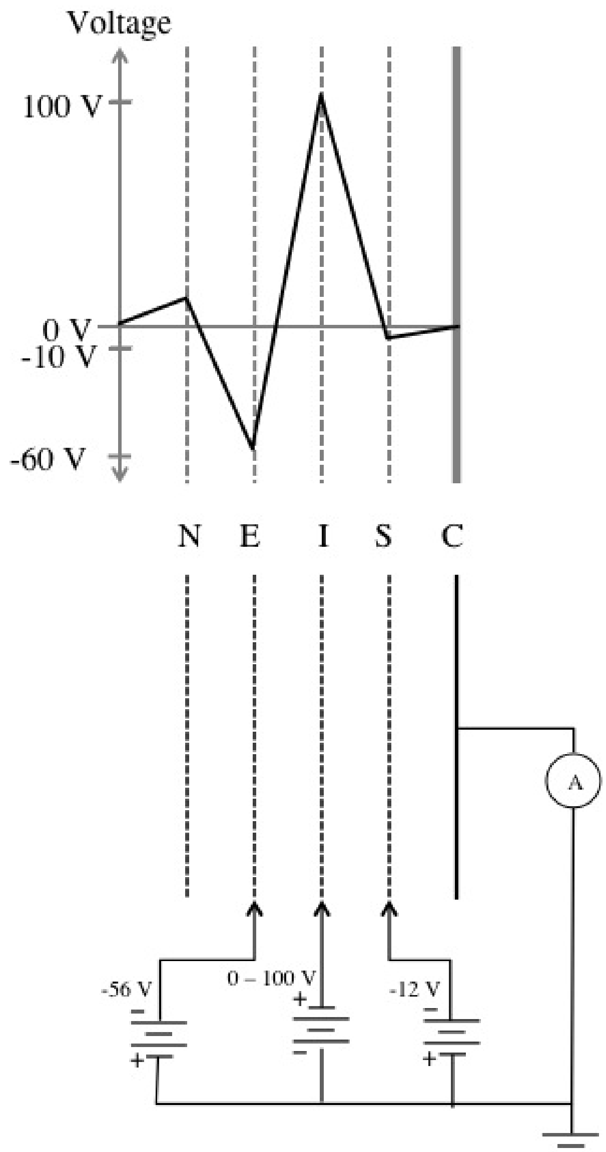

Figure 5.17: Potential (a) and circuit (b) diagram for a four grid RPA. N = neutralizing grid, E = electron repelling grid, I = ion retarding grid, S = electron suppression grid, C = collector plate, and A indicates a picoammeter used to measure current to the collector.

where the IEDF is a function of the charge on an electron (e), the charge state of the ions (Z_i), the ion number density, the area of the collector (A_c) and the mass of an ion. Thus, the IEDF was found by taking the derivative of the collected current with respect to the applied voltage using a central difference method. It was then normalized to unity in order to facilitate comparisons with other IEDFs. The

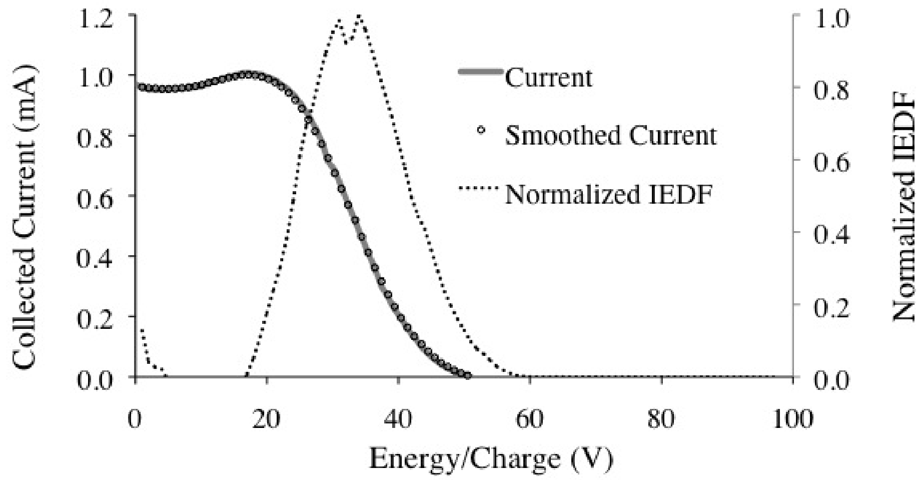

Figure 5.18: Sample of a current vs. voltage sweep from an RPA. Its respective smoothed curve and normalized IEDF are shown.

potential at which the peak of the distribution function occurs indicates the most probable ion voltage, V_{mp}. Figure 5.18 shows an example current vs. voltage sweep, the result of smoothing the curve and the normalized IEDF.

Since the ion retarding grid voltage was applied with respect to facility ground, the ion energy-per-charge distribution function must be corrected for the plasma potential as follows:

$$V_a = V_{mp} + V_p \tag{5.21}$$

where V_a is the actual measured voltage. The plasma potential was measured with the PEPL built Langmuir probe described in Section 5.3.1. The probe was positioned such that its measurements were made in the same location as the RPA measurements.

5.3.4.2 RPA Verification with a Gridded Ion Source

In order to ensure that the RPA analysis resulted in the correct value for the most probable ion voltage, it was tested using a Commonwealth 3-cm-diameter gridded ion source. The ion source was capable of producing ions with 1500 V of beam energy. For the purposes here, the ions were accelerated to 300 V. In each case, the measured most probable energy of the ions should have equaled the beam voltage applied to the ions plus the plasma potential (measured with a Langmuir probe). Figure 5.19 shows a representative RPA current-voltage characteristic downstream of the ion gun and its resulting IEDF. The IEDF showed a most probable ion energy

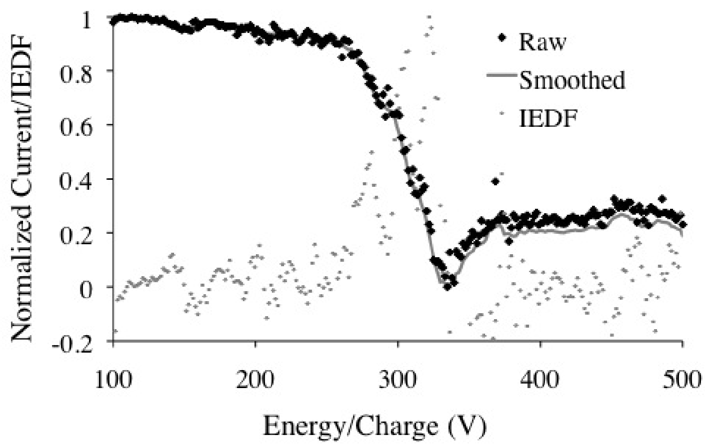

Figure 5.19: Normalized RPA curve measured downstream of an ion gun. The raw current-voltage characteristic, corresponding smoothed characteristic and IEDF are shown to confirm V_{mp} measurements.

of about 325 V, but the plasma potential was measured to be 30 V. Thus, the actual most probable voltage was measured to be 295 V. This is within the expected limits of the accuracy of the ion gun, proving that the RPA was working as expected.

5.3.4.3 RPA Error Analysis

As shown in the previous section, the uncertainty in the measured most probable voltage from the RPA is ±5 V. In addition to the uncertainty, errors can come from having an insufficient voltage applied to either the electron repelling grid or the electron suppression grid. When the retarding potential becomes larger than the maximum ion kinetic energy, the collected current should go to zero. However, in the absence of an applied potential on the electron-repelling grid, or when that potential is too low to repel all electrons, ionization caused by electron-neutral collisions occurs in the analyzer (103). This results in a parasitic current flowing into the collector at higher retarding energies. When there is insufficient bias voltage applied to the electron suppression grid, or when the grid is not present, the secondary electrons emitted by collisions with the collector are free to oscillate along the analyzer axis. This causes a slight increase in the collected current around the region of zero ion energy (103). Both of these phenomena are shown clearly in Figure 5.20.

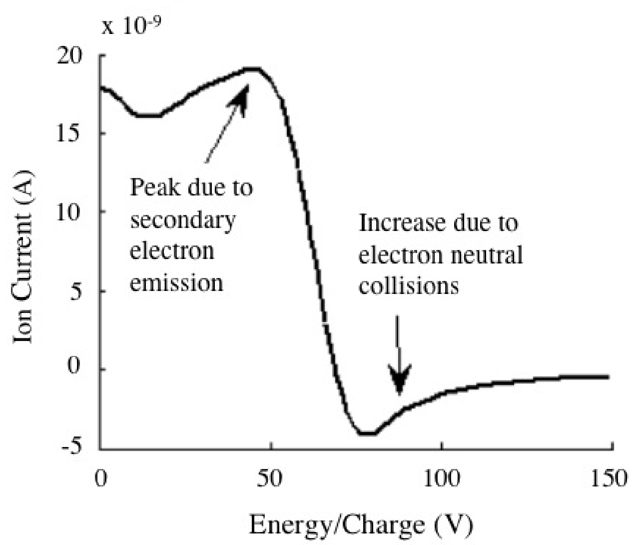

Figure 5.20: Example of errors associated with RPAs. Sample current-voltage characteristic with obvious errors due to insufficient bias voltage applied to the electron repelling grid and the electron suppression grid.

5.3.4.4 PEPL RPA

Original RPA testing was performed with the PEPL RPA, a 3-cm-diameter analyzer designed by Dr. James Haas of AFRL (27), and improved upon by Dr. Jesse

Linnell while at PEPL (26). The outer body of the RPA was constructed of 316 stainless steel tubing and was grounded to the facility. A macor sleeve was placed inside the body and macor washers were used to insulate the grids from the outer body, each other and the collector. The grids were identical and cut from a 316 stainless steel, photochemically machined sheet with 0.127-mm-thickness. The grid openings were 0.2794 mm (0.011 in) in diameter, and the grid open area fraction was 38%. Each macor washer was machined to the correct thickness in order to provide proper separation for operation downstream of a Hall thruster. The electrical connections were accomplished by spot welding stainless steel wire to each grid and to the collector. The wires were routed along the inner edge of the macor sleeve and through the rear of the RPA body. The collector was a tungsten-coated stainless steel disc. The tungsten coating reduced the secondary electron emission from the collector since the PEPL RPA did not have an electron suppression grid. Everything was held together by placing a spring behind the collector and compressing it with a back plate. Figure 5.21a is a photograph of the PEPL RPA, and Figure 5.21b is a schematic drawing.

Some issues arose when testing the PEPL RPA on the helicon source. The PEPL RPA was over 50 mm in diameter. Inserting this upstream in the helicon source caused significant perturbation of the plume. Thus, a smaller diameter probe was desired. Another issue with the PEPL RPA was that there was no electron suppression grid. With the small currents collected downstream of the helicon source, the current added due to the secondary electron emission made a significant contribution to the overall current. In addition, the separation distance between the electron repelling grid and the ion suppression grid was 1.7 mm. This relates to a maximum number density of only 10^{15} m^{-3}. In the upstream region of helicon sources, the

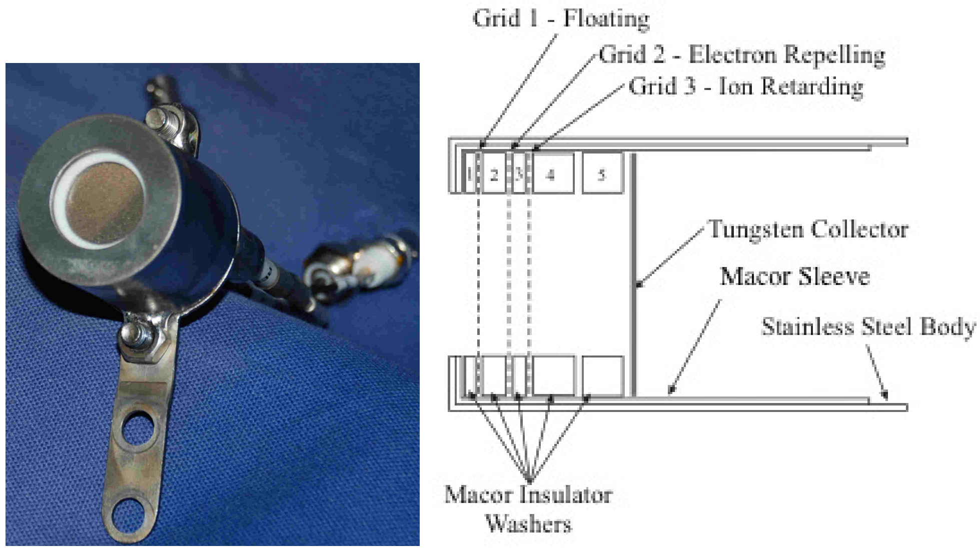

(a) (b)

Figure 5.21: PEPL RPA Photograph (a) and schematic (b).

number density can reach up to 10^{20} m^{-3} (37; 45; 104), and in the region of interest just downstream of the PEPL helicon source exit, the density was up to 10^{18} m^{-3}. Given these densities, the grid spacing between the electron repelling and ion retarding grids should be no more than 0.1 mm. So, in order to make the PEPL RPA function correctly downstream of the helicon source, a series of floating grids were added on the front of the analyzer in order to decrease the density of the plasma entering the RPA. This is not desirable as the more grids that are added to the front of the probe, the more chance there is of changing the plasma properties. Then, the properties of the plasma entering the probe would not be representative of those found in the bulk plasma.

5.3.4.5 Micro RPA Version 1

Because of the limitations of the PEPL RPA, designs were considered for a smaller, "Micro RPA" (MRPA). Two iterations of design were done because the first was not successful. The initial design was based on one previously used at ANU in Canberra (105). Figure 5.22a shows a photograph of the MRPAv1, and Figure 5.22b is a schematic of the 4-grid design. The analyzer was housed inside a stainless

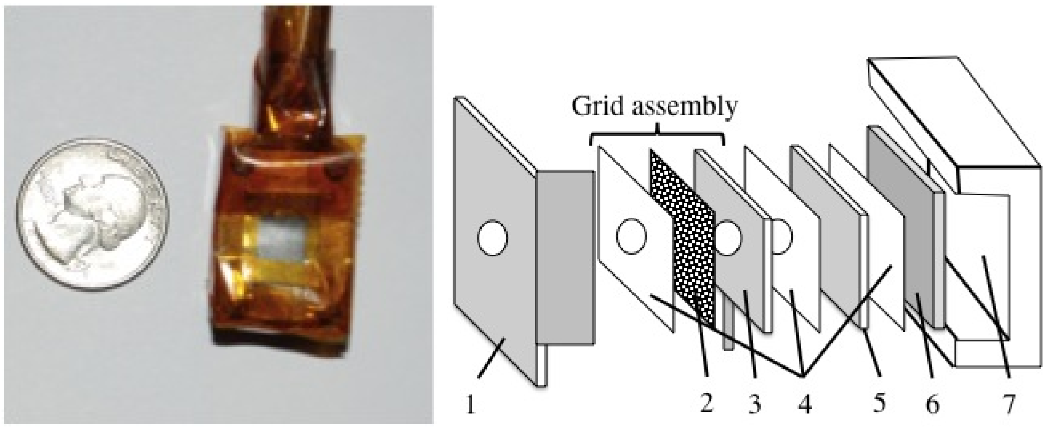

(a) (b)

Figure 5.22: Micro RPA version 1 photograph (a) and schematic (b). In (b), 1 = analyzer lid, 2 = stainless steel mesh, 3 = copper tab, 4 = mica sheet insulator, 5 = nickel collector plate, 6 = base plate and 7 = analyzer casing. There were a total of four grid assemblies stacked one on top of the other.

steel case that was 21 mm x 13.75 mm x 26.5 mm, and a 9.75-mm-diameter stainless steel tube enclosed the electrical connections for the grids. The housing lid had two sides, creating a partial box and ensuring that the only ions entering the analyzer were those entering through the front orifice. The same grid material was used for the MRPAv1 grids as was used for the PEPL RPA. Each grid consisted of stainless steel mesh, a copper plate that provided a means of charging the mesh and a mica sheet for insulation. All three of these were glued together using a high temperature conducting epoxy. The resulting space between grids was 0.71 mm. This is still larger than four times the expected Debye length (0.1 mm), so an attenuating grid was added to the front of the MRPA in order to lower the density inside the analyzer. Although undesirable, the use of only one attenuation grid for the MRPA vs. multiple grids for the PEPL RPA was an improvement. Electrical connections were made via tabs on the copper plates that extend out of the MRPA housing. The collector was made of nickel plate. The grid assembly was stacked inside of and clamped to the housing lid, which was then bolted to the remainder of the housing.

Issues with the MRPAv1 included the difficulty of assembling the analyzer. The grids in an RPA require some amount of alignment in order to allow ions with sufficient energy to pass. Aligning the grids in the MRPAv1 was exceedingly difficult. The sleeve design of the PEPL RPA allowed for placing the grids and looking through a microscope, if necessary, to align them. However, since the MRPAv1 does not have a sleeve to hold the grids in place during assembly (refer to the schematic drawing in 5.22b), they needed to be aligned before being placed into the housing. In addition, the mica sheeting used for insulation was flimsy and would flake away, causing shorts between the grids. The tube protecting the electronics and providing support came from the side of the analyzer, resulting in a silhouette of the probe that was much larger than just the face of the analyzer.

5.3.4.6 Micro RPA Version 2

In order to create a functioning RPA with small enough separation between the electron repelling grid and the ion retarding grid, an analyzer was designed that utilized the benefits of the two previous RPA's. The Micro RPA version 2 (MRPAv2) is shown in Figure 5.23a, and a schematic drawing is in Figure 5.23b. The MRPAv2 had only a 19-mm-diameter casing, giving it an even smaller silhouette than the previous version. In addition, the stainless steel tube protecting the transmission lines came from the back of the analyzer, further reducing the amount of the probe exposed to plasma. The MRPAv2 had four grids like the MRPAv1, but it was

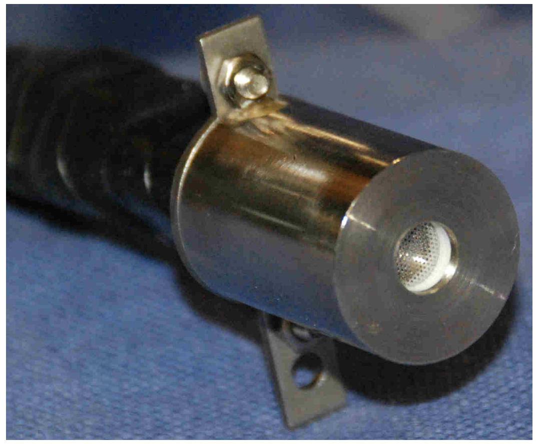

(a)

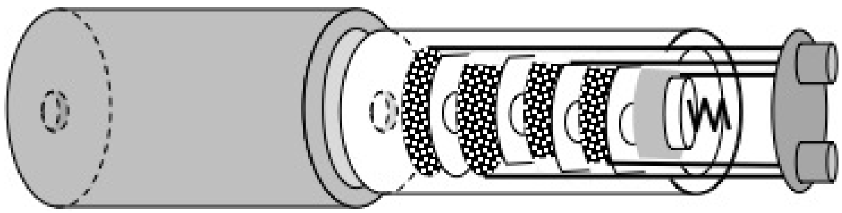

(b)

Figure 5.23: Micro RPA version 2 photograph (a) and schematic (b).

constructed in a manner similar to the PEPL RPA. The body was machined from a 316 stainless steel tube. Inside the body was a macor sleeve within which everything was stacked. Macor washers making up the insulators were machined as thin as possible: 0.5-mm-thick. The four grids were machined from the same 316 stainless steel photochemically machined mesh as used for the previous two iterations of the RPA. The electrical connections were identical to those found in the PEPL RPA, and the collector was a nickel plate, as it was in the MRPAv1. There was a macor disc, and then a spring which compressed the whole assembly together. This iteration of the RPA performed the best, but the spacing between the electron repelling and ion retarding grids was still larger than the expected $4\lambda_D$ in the areas closer to the helicon source exit. Therefore, there may have been errors due to the space-charge limitations. The results are shown and discussed in Section 6.3.

5.4 Summary

This chapter began with a description of the laboratory facilities used for this dissertation. Then, the experimental layout was discussed. It is important that the reader understand the layout of the helicon source and where the ReComm system was within that layout. For this reason, a table with the relevant testing locations was included.

Next, the variety of diagnostic tools and their analysis techniques were presented. Langmuir probes were used to measure ion number density, electron temperature and plasma potential data. A hairpin probe was used to gather information about the plasma frequency. An S2-1 probe connected to a network analyzer measured the actual attenuation of a signal being transmitted through the plasma. Finally, an RPA was used to measure the IEDF at the exit of the helicon source. The reader should have gained an understanding of the analysis techniques and the assumptions used on the data sets for each diagnostic.

CHAPTER 6

Helicon Source Characterization

Before determining whether or not the ReComm system could successfully reduce the plasma density, the helicon source required characterization. First, helicon mode operation was confirmed. Then, the ion number density, electron temperature and plasma potential were measured in the downstream region with the Hiden Langmuir probe when the chamber was vacant and when the ReComm system was present downstream of the helicon source (but not operating). Finally, the ion energy distribution function and plasma potential at the helicon source exit were measured. The results of the above measurements are presented in this chapter. Additional characterization of the downstream region of the helicon source was done with a residual gas analyzer (RGA), and the details of this diagnostic and the results are in Appendix B. The testing matrices for all experiments are shown in Appendix C.

6.1 Helicon Mode Confirmation

There are various methods for confirming helicon mode operation. These range from simply viewing a change in the plasma to complex measurements with magnetic flux probes (106). For the purposes of this research, helicon mode was confirmed by measuring the ion number density as a function of magnetic field strength and input power (36; 45). A Langmuir probe was inserted upstream into the helicon source at a fixed location along the source centerline at y = -100 mm for the first set of experiments. Then, the Langmuir probe was moved further upstream to the y = -150 mm location, and while remaining at z = 0 mm, the probe was moved in the x-direction to measure the ion number density as a function of radial location and input power. These locations were chosen since they were both inside the quartz tube, and therefore where the greatest density was expected to occur. In addition, the change in the y-locations is due to the limitations of the linear tables.

Helicon mode operation was verified for the operating conditions that were used in these experiments:

- input power = 1500 W at 13.56 MHz
- reflected power ∼10% of input power
- peak y-magnetic field strength (B_y) = 450 G along the helicon centerline
- downstream pressure = 0.6 mtorr argon.

Figure 6.1a shows the three "density jumps" that are consistent with the capacitive, inductive and helicon modes of operation (45). These "jumps" become obvious at B_y = 290 G, and they are even more prominent when B_y = 440 G. For all data points in Figure 6.1b, the helicon magnetic field remained fixed at B_y = 440 G, while the x-location of the probe varied. The plot shows a peak in density at the center (x = 0 mm) of the quartz tube when the input power is sufficient for helicon mode operation. Also shown is the volcano-like structure of the radial density profile at lower input power. This structure is consistent with capacitively coupled and inductively coupled modes of operation (37; 107; 108).

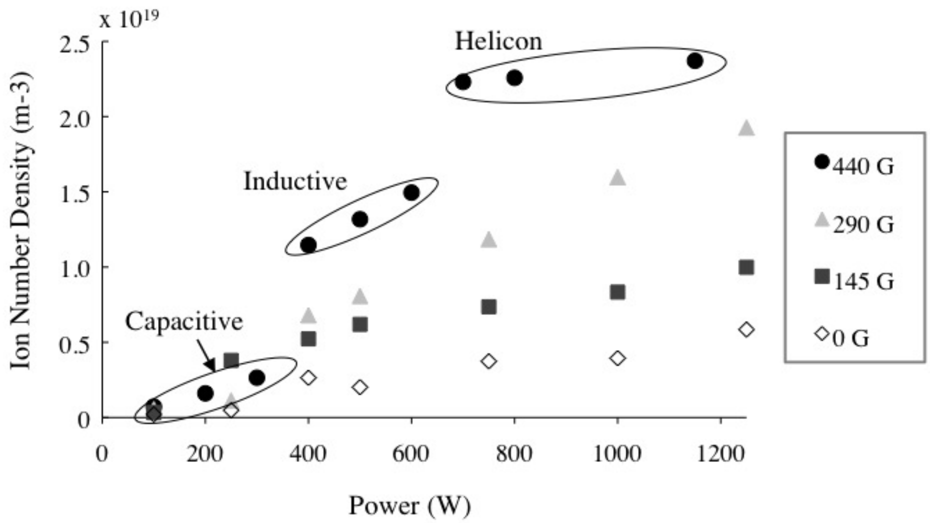

(a)

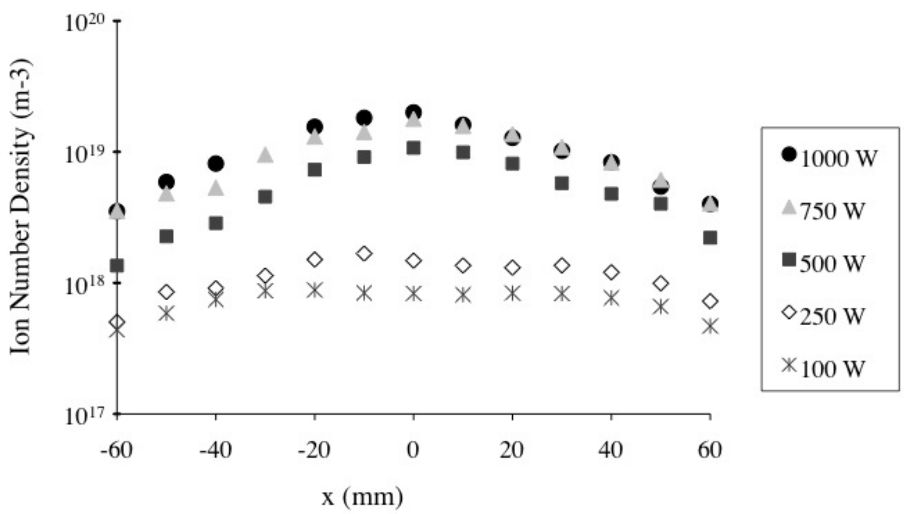

(b)

Figure 6.1: Verification of helicon mode operation. (a) Ion number density inside the helicon source as a function of input power and magnetic field for x = 0 mm, y = -100 mm and z = 0 mm. (b) Ion number density as a function of x-position and input power for B_y = 440 G, z = 0 mm and y = -150 mm.

When an argon plasma is operating in helicon mode, the core of the cylinder changes to a blue color from the usual purple color. Although this is not a quantifiable method for confirming helicon mode operation, it is a good rule of thumb to follow. Figure 6.2 shows the helicon source operating in (a) inductively coupled mode and (b) helicon mode.

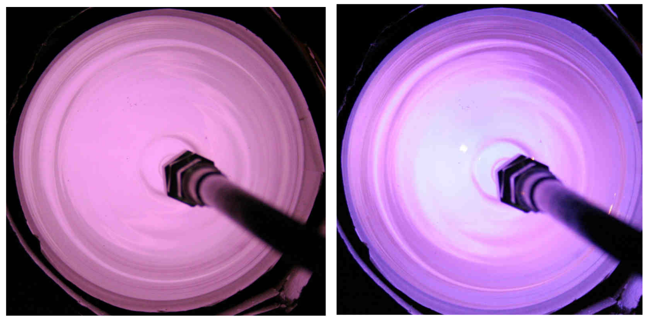

(a) (b)

Figure 6.2: Photographs of the helicon mode confirmation. The rule of thumb is that when the plasma source goes from having a dim, purple core (a) to a bright blue core (b), the source has jumped from the lower inductively coupled mode up to helicon mode.

6.2 Downstream Plasma Characterization

After confirming that the helicon source was producing its maximum number density by operating in helicon mode, the characteristics of the plasma in the vacuum chamber downstream of the helicon source needed to be determined. Initially, the vacuum chamber was empty downstream of the source, except for the Hiden Langmuir probe. Then, the ReComm system was placed in the chamber, while remaining powered off, to see how the addition of the mitigation system body itself changed the plasma parameters.

6.2.1 Plasma Characterization with an Empty Vacuum Chamber

Ion number density and electron temperature were found from the Langmuir probe I-V curves. Then the plasma potential was calculated. The results are presented in Figures 6.4 - 6.6 as functions of x and y- positions for three planes along the z-axis:

- the helicon centerline: $z = 0$ mm
- $z =$ -30 mm
- $z =$ -60 mm

Data were measured in a full 3D map of the downstream area, and the remaining data are presented in Appendix D. The x, y and z-axis labels are consistent with those shown before in Figure 5.2. The area in the x and y plane where the testing occurred is indicated in Figure 6.3.

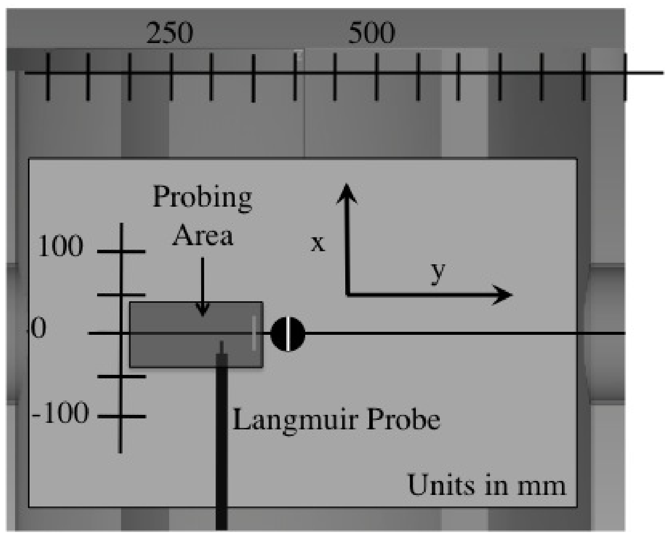

Figure 6.3: Helicon source characterization testing locations.

With no body present, ion number densities ranged from 1.7×10^{17} m^{-3} to 3.3×10^{17} m^{-3}. These number density values are representative of re-entry plasma densities found at altitudes ranging from 60 km to 70 km (Section 2.2). The highest densities were found nearest to the helicon source exit plane at the $z = 0$ mm position in the positive x-region (Figure 6.4a). The higher densities in the positive x-region were expected due to the nature of the experimental setup. There was a flange in the y-z plane along $x = 305$ mm and only empty chamber in the negative x-direction, as previously shown in Figure 5.2b. In addition, the ion number density decreased with

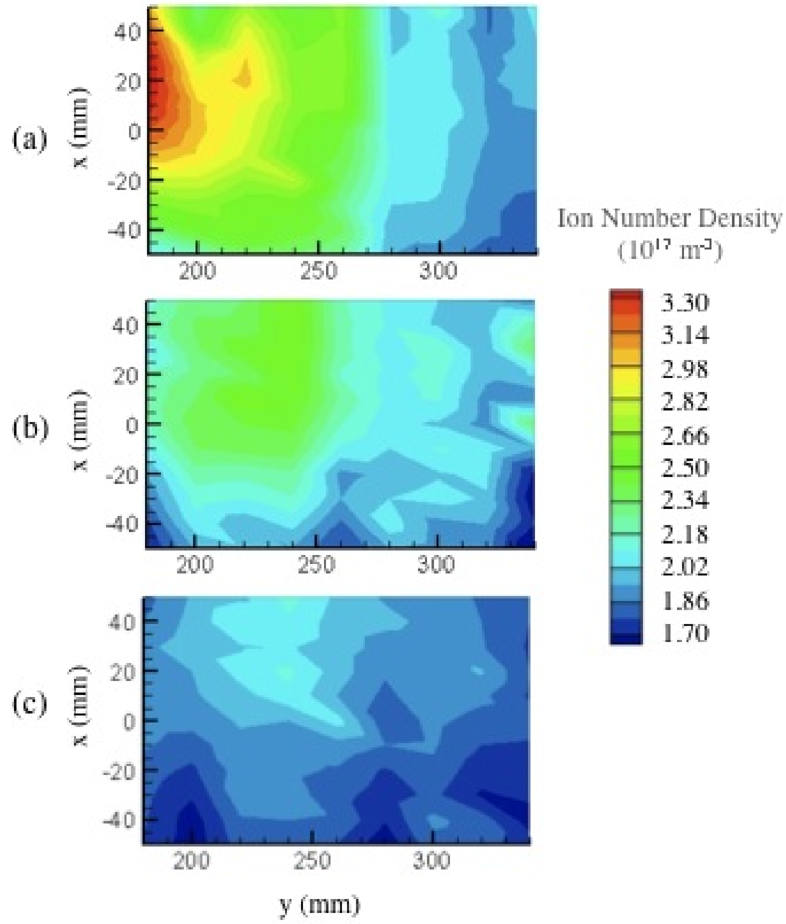

Figure 6.4: Ion number density downstream - empty chamber. (a) z = 0 mm, (b) z = -30 mm and (c) z = -60 mm.

increasing y-position along the $z = 0$ mm plane (Figure 6.4a), but the density became more independent of the downstream y-location for the lower z-planes (Figures 6.4b and 6.4c).

When there was no body present downstream of the helicon source, the electron temperature ranged from 1.5 eV to 6.2 eV for the region of interest in these experiments (Figure 6.5). Based on previous experiments done inside and immediately downstream of helicon sources these values were expected (57); however, they are higher than those measured during the RAM-C experiments. This temperature difference (in some cases as high as 6 eV) is acceptable since number density matching

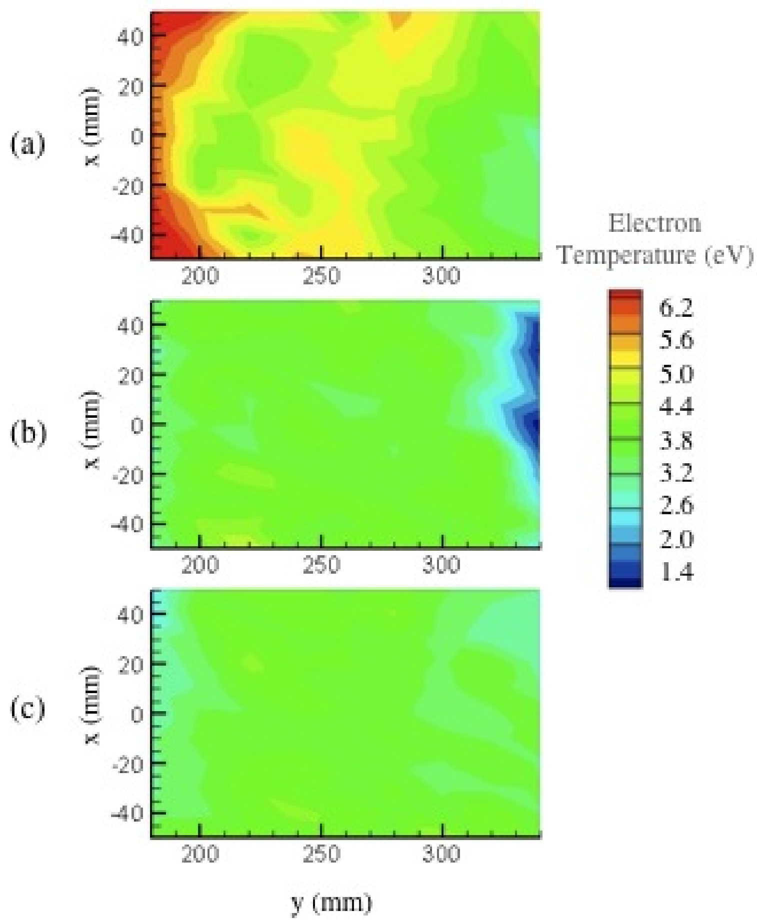

Figure 6.5: Electron temperature downstream - empty chamber. (a) z = 0 mm, (b) z = -30 mm and (c) z = -60 mm.

was the primary concern of the research. The goal with regards to the electron temperature was to ensure that it was of a similar order of magnitude to that found during atmospheric re-entry.

In general, the electron temperature of the plasma was not strongly correlated to downstream position. However, there does appear to have been a warm core along the plane that contains z = 0 mm (Figure 6.5a), and the plasma cooled further below that plane.

Plasma potential was calculated to ensure complete understanding of the plasma characteristics downstream of the helicon source. Figure 6.6 shows how it varied as

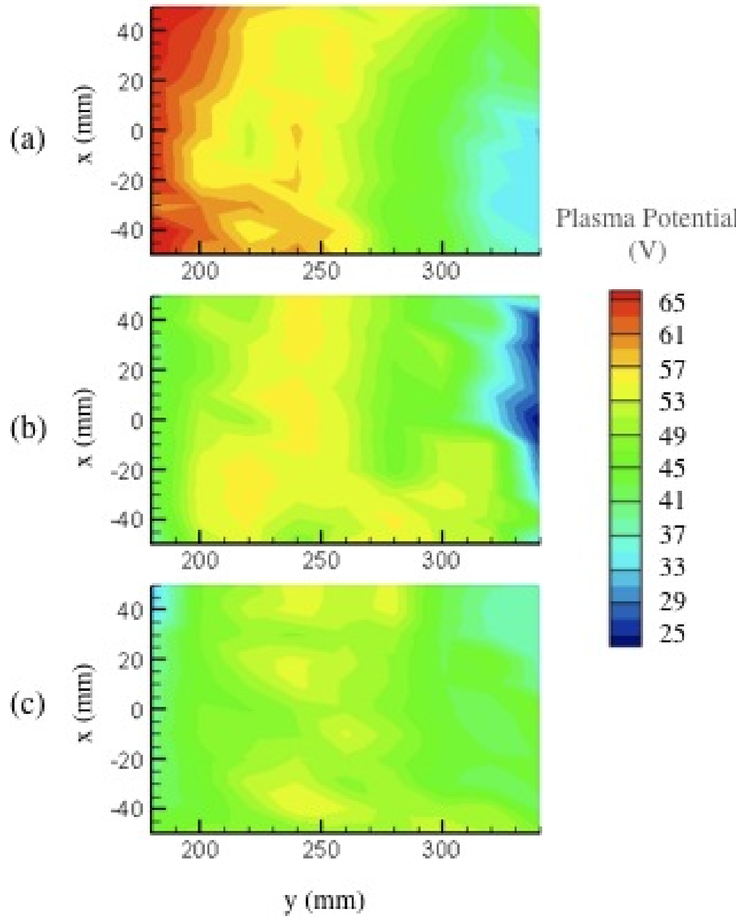

Figure 6.6: Plasma potential downstream - empty chamber. (a) z = 0 mm, (b) z = -30 mm and (c) z = -60 mm.

a function of downstream location. The plasma potential was lower further downstream of the helicon source, but the decrease in potential was not consistent with what would have been expected from the Boltzmann relation (6). This relation suggests that the plasma potential should be related to the number density by Equation 6.1.

$$n = n_o \exp\left(\frac{eV_p}{kT_e}\right) \tag{6.1}$$

where n_o is a reference number density and the electron temperature is in Kelvin. If the Boltzmann relation were applied to the measured number density and plasma potential from these experiments, the electron temperature would have to be around

60 eV.

6.2.2 Plasma Characterization with ReComm System Downstream

The next step was to determine how the addition of the ReComm system body in the region downstream of the helicon source would affect the plasma parameters. It was expected that the ion number density would decrease because of the presence of a large surface with which ions and electrons could collide and neutralize. The electron temperature was expected to decrease with the addition of the very large cold surface downstream. The plasma potential was also expected to decrease slightly with the addition of the ReComm system due to the possibility of the mica sheet charging up and emitting electrons. Figures 6.7, 6.9 and 6.11 show contour maps of the Langmuir probe results from the same locations as shown in Section 6.2.1 but with the addition of a body downstream. Furthermore, Appendix D shows data from the remaining z-planes not shown below.

The addition of the ReComm system downstream of the helicon source did, in fact, cause a decrease in the ion number density by a factor of 2.5. Figure 6.8 is added for clarity, and it shows the ion number density as a function of y-position for the same z-positions given earlier along the $x = 0$ mm axis for both the empty chamber case and the case with the ReComm system downstream. As was the case with an empty chamber downstream, the ion number density was highest nearest to the helicon exit plane, at $z = 0$ in the positive x-region (Figure 6.7a). The addition of a body downstream however, caused the ion number density to be dependent on the y-position for all z-planes. The density range found with a body present downstream of the helicon source (5.0×10^{16} m^{-3} to 1.3×10^{17} m^{-3}) is representative of that

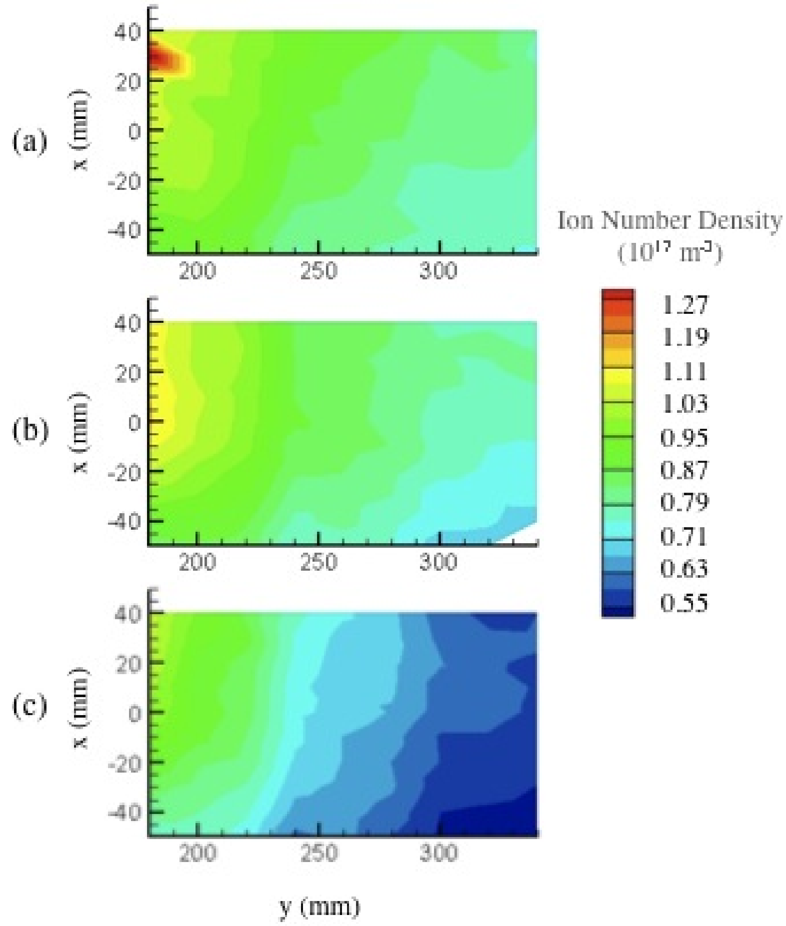

Figure 6.7: Ion number density downstream - ReComm system present. (a) z = 0 mm, (b) z = -30 mm and (c) z = -60 mm.

found at altitudes ranging from 70 km to 80 km during atmospheric re-entry of the RAM-C vehicle.

Electron temperature also dropped with the addition of the ReComm system body downstream of the helicon source. Temperatures ranged from 1.2 eV up to 4.8 eV, lowering the peak measured electron temperature by about 20%. This decrease in temperature means that the simulated temperature was even closer to that found during atmospheric re-entry. The presence of the ReComm system also caused the warm core seen in Figure 6.5a to disappear. This results in a more uniform temperature of the bulk plasma downstream of helicon source. Based on the error analysis

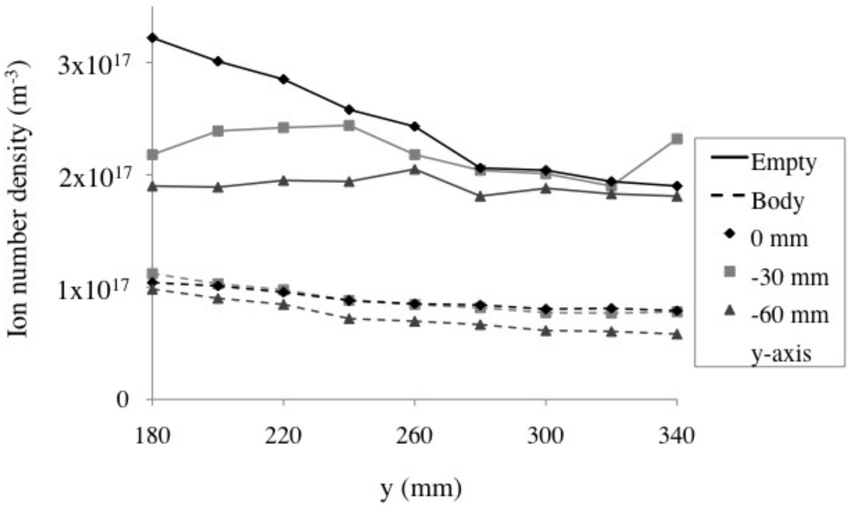

Figure 6.8: Ion number density downstream - comparison with and without ReComm system. Data are presented along the x-axis for three z-positions: z = 0 mm, z = -30 mm and z = -60 mm.

given in Section 5.3.1.6, the temperatures, except for those found with an empty chamber along the centerline, are within similar. Figure 6.10 is added to aid in comparing the electron temperatures measured with and without the presence of the ReComm system downstream of the helicon source.

The decrease in the plasma potential that occurred further downstream of the helicon source was still present when the ReComm system was added. Also, the magnitude of the decrease in plasma potential still could not be explained by the Boltzmann relation. The peak plasma potential decreased with the addition of the ReComm system from about 65 V to 55 V. As mentioned previously, this decrease was expected due to the possibility of the mica sheet releasing secondary electrons when it became charged. Once again, Figure 6.12 is shown to help make comparisons between the two cases. Once again, however, the measurements for plasma potential all fall within the the error estimates for each other.

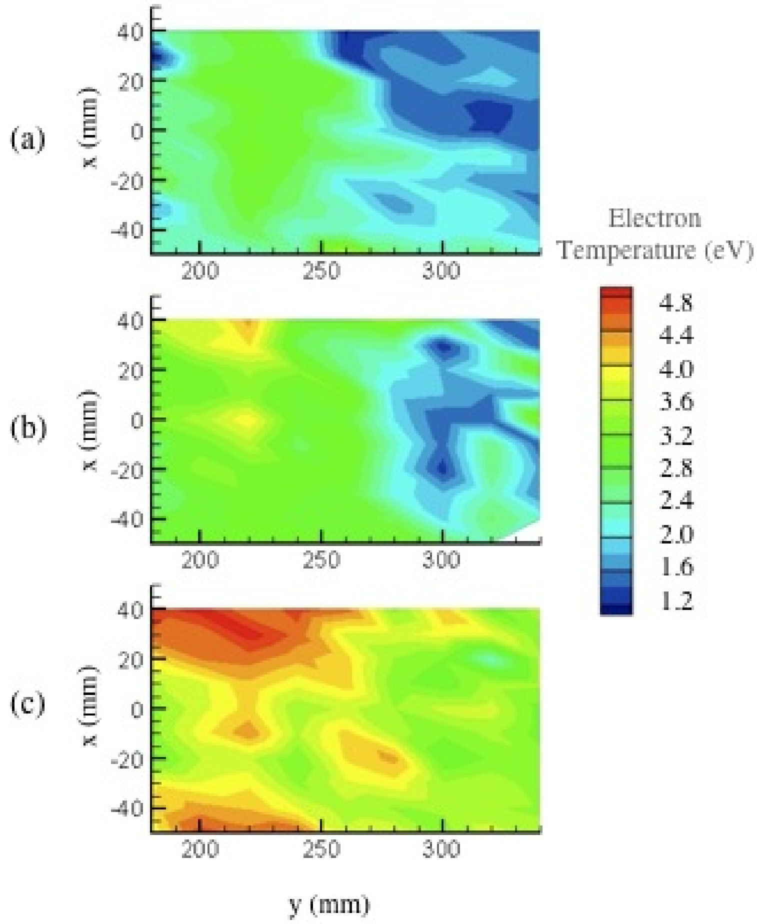

Figure 6.9: Electron temperature downstream - ReComm system present. (a) z = 0 mm, (b) z = -30 mm and (c) z = -60 mm.

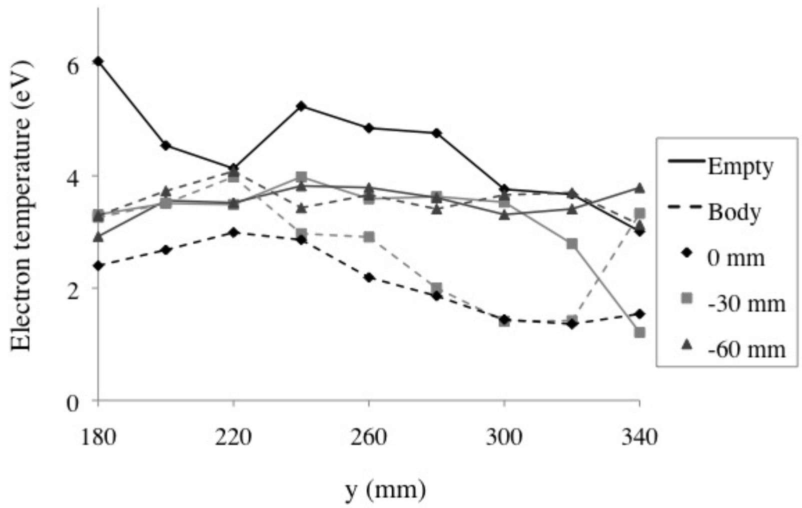

Figure 6.10: Electron temperature downstream - comparison with and without ReComm system. Data are presented along the x-axis for three z-positions: z = 0 mm, z = -30 mm and z = -60 mm.

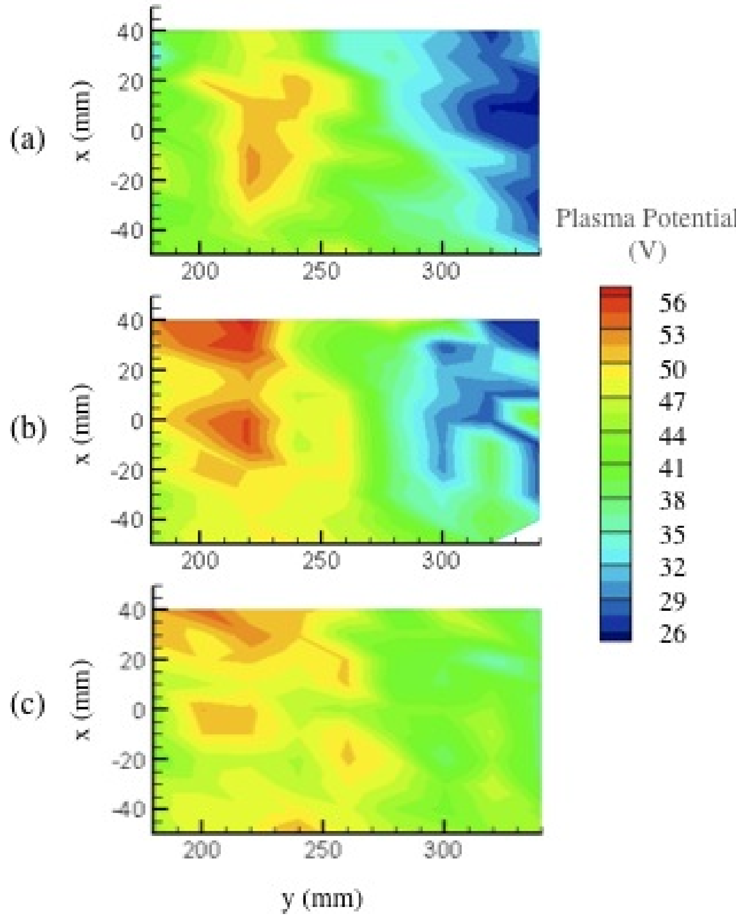

Figure 6.11: Plasma potential downstream - ReComm system present. (a) z = 0 mm, (b) z = -30 mm and (c) z = -60 mm.

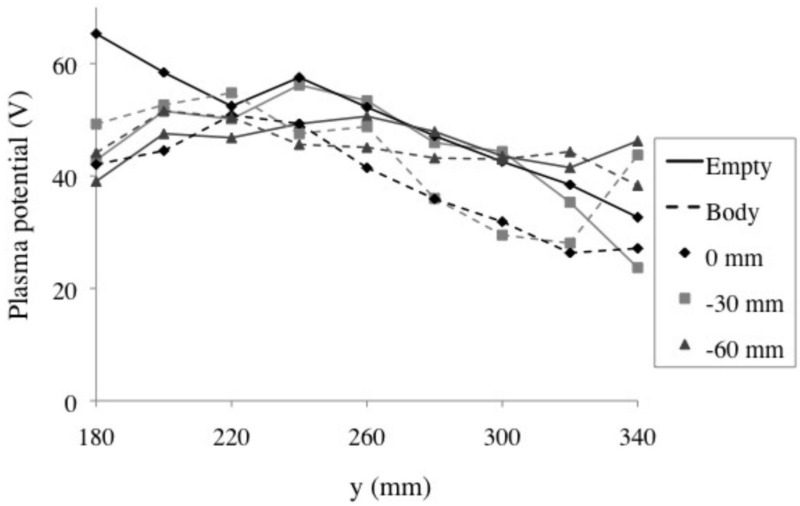

Figure 6.12: Plasma potential downstream - comparison with and without ReComm system. Data are presented along the x-axis for three z-positions: z = 0 mm, z = -30 mm and z = -60 mm.

6.3 Ion Energy Distribution Function

It was shown earlier that matching the velocity of the ions flowing over a hypersonic vehicle was not important for the purposes of this research. However, knowing the energy distribution function of the ions exiting the helicon source gives more insight into the downstream characteristics of the plasma. Thus, the MRPAv2 was used to find the most probable voltage of the ions at various y-locations downstream of the helicon source. In addition, the current-free electron double layer that is often seen downstream of helicon sources was studied briefly. All measurements were taken along the centerline of the helicon source (z = 0 mm and x = 0 mm) between y = 40 mm and y = 240 mm.

For positions further upstream (y < 170 mm), the most probable ion voltage could not be obtained because the RPA was not properly functioning. The plasma number density in that region was too high for the MRPAv2, and the separation distance between the electron repelling grid and the ion retarding grid was too large.

In addition, at the densities found in this area (between 10^{18} m^{-3} and 10^{19} m^{-3}), the size of the grid aperture may even be too large, therefore allowing all ions to pass. The further downstream, the lower the plasma number density became, thereby allowing the MRPAv2 to work properly. In addition to the RPA measurements, a Langmuir probe was utilized to measure the plasma potential. The potentials found by reading the Langmuir probe traces are similar to those found using Equation 5.9. This lends confidence to the results presented in the previous sections. Figure 6.13 shows the results of RPA testing with the MRPAv2 downstream of the helicon source as well as plasma potential measurements from the PEPL Langmuir probe.

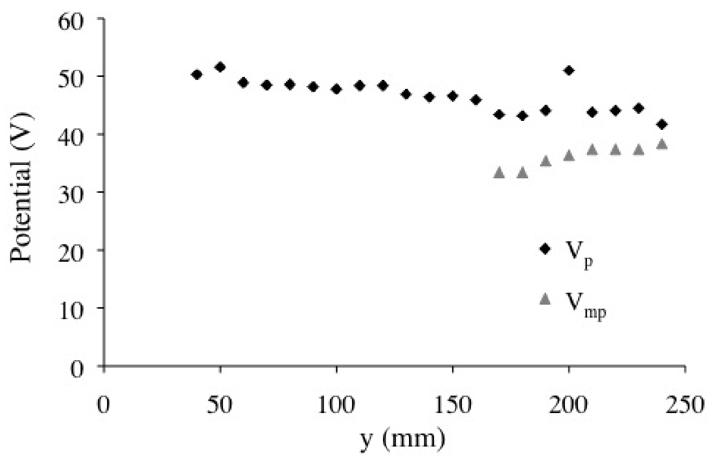

Figure 6.13: Plasma potential and most probable ion voltage.

These results are prior to subtraction of the plasma potential from the most probable ion voltage. The findings show that plasma potential was greater than the measured most probable voltage. This would result in a negative ion voltage (which is not possible) were Equation 5.21 to be applied. This result can be explained by the following. Usually the voltage applied to the retarding grid of an RPA is applied with respect to facility ground. Thus, the measured most probable voltage must be corrected for the plasma potential since the directed energy of the ions is the difference between the plasma potential and the potential of the ions with respect to ground. Due to the grounding scheme of the experimental setup used for this dissertation, the MRPAv2 was grounded with respect to the CTF, and the CTF was isolated from ground via RF filters and chokes. Therefore, the CTF was floating at the potential of the plasma that was filling it. The result being that the most probable ion voltage measurement had already been compensated for the plasma potential and Equation 5.21 is no longer required. In order for the above explanation to be true, the Langmuir probe would still need to be grounded to the facility ground. Otherwise, if the Langmuir probe were also referenced to the CTF, then the plasma potential would be measured as zero. Since the commercial Hiden Langmuir probe system uses its own grounding scheme and method for RF compensation, the probe was isolated from the CTF and referenced to facility ground.

Since the most probable ion voltage was similar to the values found for the plasma potential, the directed energy of the ions was essentially zero. Therefore, the ions only had thermal energy, and moved downstream at the drift velocity. Once again, the velocity of the ions was not a key factor in this work, so the result is acceptable.

Another reason for measuring the IEDF as a function of the axial position was to determine whether a current-free electron double layer existed downstream of the PEPL helicon source. Double layers in plasma consist of two parallel charge sheets with opposite charge which results in a sharp change in voltage. A significant effort has recently been devoted to the study of double layers in the region downstream of helicon sources (56; 98; 109). Double layers are generally formed from DC discharges with an abrupt change in diameter, but the RF discharge of a helicon source with an abrupt change in diameter will also produce one if the conditions are correct. The double layer usually forms within 150 mm of the location where the change in diameter occurs. Therefore, if a double layer were present in the PEPL helicon source, it would be seen somewhere between $y = 100$ mm and $y = 250$ mm. As seen in Figure 6.6, the plasma potential was continuous as a function of the axial position without any discontinuities. The location of the current-free double layer would have been indicated by a discontinuous decrease in the plasma potential as a function of increasing axial position (109). Since this discontinuity was not seen, it was determined that a current-free double layer was not present in the PEPL helicon source with the operating conditions used in this dissertation.

6.4 Summary

In this chapter, data were presented that confirmed the plasma source was operating in helicon mode with the same operating conditions as those used for the remaining experiments. Then, the plasma downstream of the helicon source was characterized with an empty vacuum chamber and with the ReComm system present (but turned off). The results showed that the ion number density of the plasma inside the vacuum chamber represented density found during atmospheric re-entry at altitudes ranging from 60 - 70 km when the chamber was empty. When the ReComm system was present, the plasma density was representative of that found at altitudes ranging from 65 - 75 km. In addition, data showed that the electron temperature ranged from 1 - 6 eV, and the plasma potential ranged from 25 - 65 V. In general, it was found that the ion number density, electron temperature and plasma potential all decreased as a result of adding the ReComm system downstream.

In addition to the characterization of the downstream plasma, ion energy distribution functions were measured as a function of downstream location. The most probable ion voltage and the corresponding plasma potential were presented. The plasma potential was found to be greater than the ion voltage, and an explanation for the discrepancy was discussed. The ions were found to have very little or no directed energy, leaving them with only a thermal energy. Finally the current-free electron double layer often found downstream of helicon sources was not measured in the PEPL helicon source with the conditions used for this dissertation.

CHAPTER 7

ReComm System Effect

This chapter discusses the effect of the ReComm system on the plasma downstream of the helicon source. Langmuir probe data were used to measure the change in density for various magnetic and electric field conditions as a function of downstream location. Density variation was found by first subtracting the ion number density measured when the ReComm system was operating, $n_{i,R/C}$, from the density measured when the ReComm system was turned off, $n_{i,o}$. This resulted in the amount that the density was reduced. Then, that value was divided by $n_{i,o}$, and the percent reduction was found by multiplying the ratio by 100.

$$\% \text{ reduction} = \frac{n_{i,o} - n_{i,R/C}}{n_{i,o}} * 100 \tag{7.1}$$

Plasma frequency was determined from the data gathered with the hairpin resonance probe using the methods outlined in Chapter 5. Signal strength was measured as a function of input signal frequency. The resulting signal response was normalized by the vacuum S2-1 response ($S_{2-1,o}$) and converted to dB.

$$\text{Relative dB} = 10 * \log_{10}\left(\frac{S_{2-1}}{S_{2-1,o}}\right) \tag{7.2}$$

The experimental results were then compared with results from computer simulations of the ReComm effect. As previously mentioned, the ReComm system was operated with only the magnetic field, and with both the magnetic and electric fields; however, it was not operated with only the electric field. Figure 7.1 shows the magnetic field strength at the two planes where data were taken: z = -70 mm and z = -75 mm.

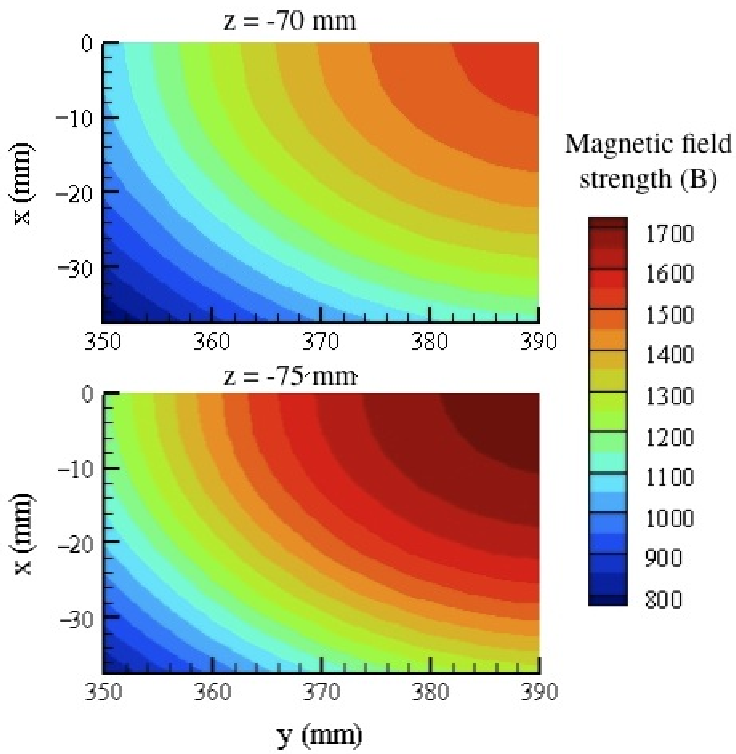

Figure 7.1: B_z along the two planes where plasma mitigation data were found, z = -70 mm and z = -75 mm.

7.1 Density Reduction

Density reduction was found as a function of x and y-positions and for various ReComm system operating conditions in x-y planes along the z = -70 mm and z = -75 mm axes (15 mm and 10 mm above the mica surface, respectively). These two testing locations are referred to as the z_{high} condition (z = -70 mm) and the z_{low} condition (z = -75 mm). In Figures 7.2 - 7.7 the black curves represent the quarter circle where data overlap the location of the iron core of the magnet, and the black lines on either side of the plots indicate the locations of the electrodes. Recall that the anode was located at $y = 350$ mm, and the cathode was located at $y = 390$ mm.

Figures 7.2 (z_{high} condition) and 7.3 (z_{low} condition) show the density reduction when the peak magnetic field from the ReComm system in the z-direction (B_z) is 925 G with (a) no applied potential and with (b) a -100 V applied potential. As expected, the application of an $E \times B$ field caused a reduction in the plasma density where

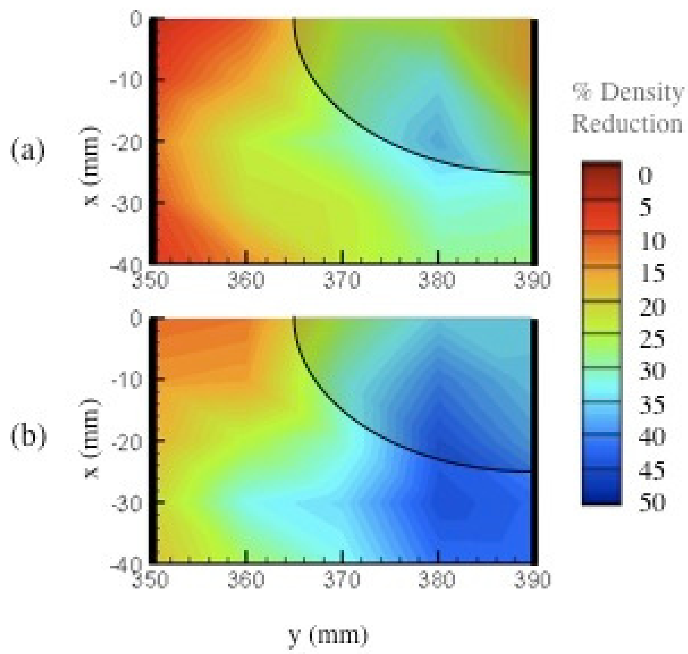

Figure 7.2: Percent density reduction for 925 G peak magnetic field at z = -70 mm. (a) V_c = 0 V and (b) V_c = -100 V.

the area of greatest reduction occurred over the iron core of the magnet, nearest the cathode. For both the z_{high} and z_{low} conditions with the ReComm system magnet operating at about half its maximum value, the peak density reduction was 50% with only the magnetic field turned on. It was unexpected that the magnetic field itself would contribute greatly to the density reduction.

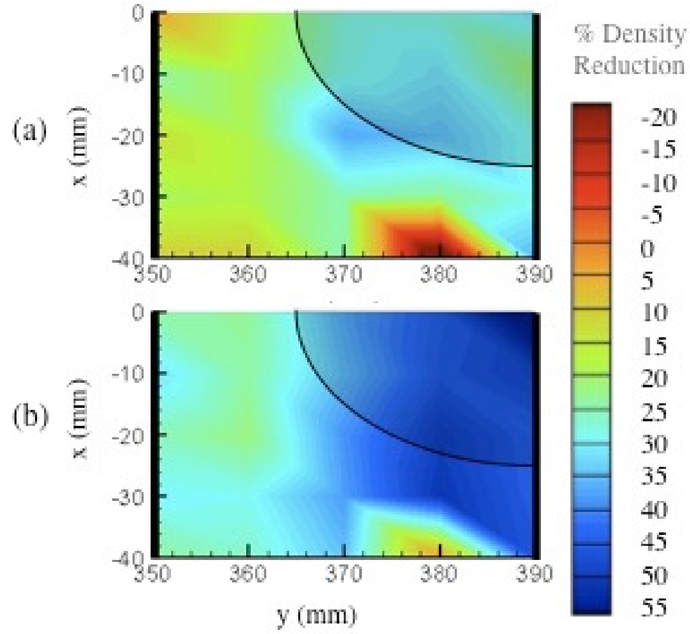

Figure 7.3: Percent density reduction for 925 G peak magnetic field at z = -75 mm. (a) V_c = 0 V and (b) V_c = -100 V.

The addition of the electric field served not only to increase the area of peak density reduction for the z_{high} condition, but it also further increased the density reduction to 55% for the z_{low} condition. The fact that the plasma was more affected by the addition of the electric field closer to the mica surface (and thus closer to the electrodes) was not surprising since the electric field was stronger along that plane. However, it was unexpected that the electric field would have such little effect on the plasma further from the mica sheet. One possibility is that the electric field was not sufficiently strong to cause any significant additional density reduction. For every testing condition axial plots were produced to aid in data comparison. The plots are shown in Appendix E.

Figures 7.4 (z_{high} condition) and 7.5 (z_{low} condition) show density reduction when (B_z) was increased to 1385 G with (a) V_c = 0 V and (b) V_c = -100 V. Again, the

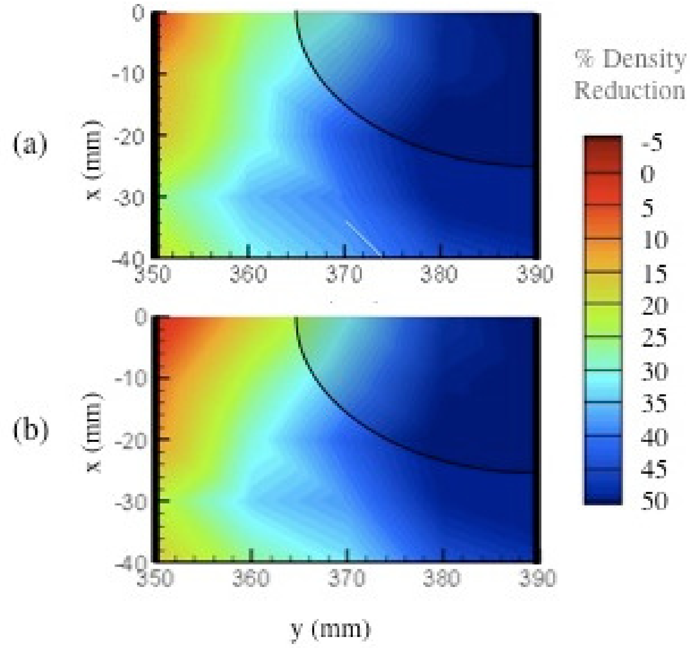

Figure 7.4: Percent density reduction for 1385 B Peak magnetic field at z = -70 mm. (a) V_c = 0 V and (b) V_c = -100 V.

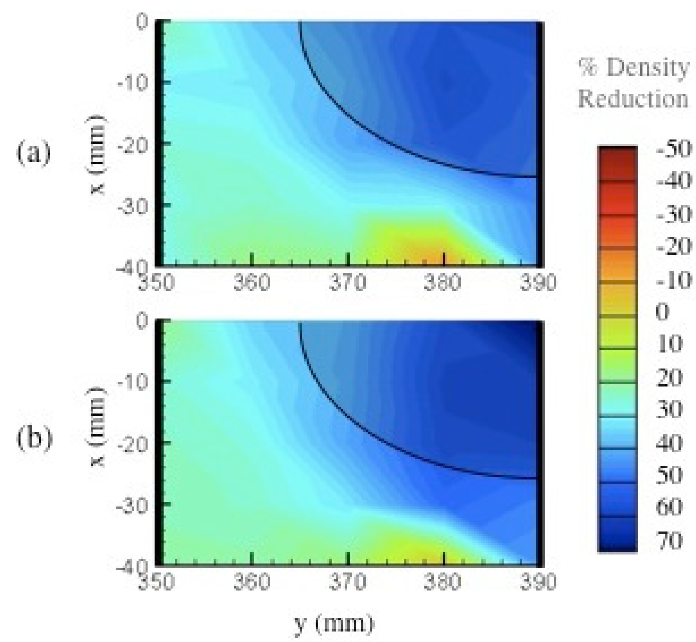

Figure 7.5: Percent density reduction for 1385 G peak magnetic field at z = -75. (a) V_c = 0 V and (b) V_c = -100 V.

region of greatest density reduction occurred in the area above the iron core and near the cathode. The larger magnetic field caused an increase in the size of the region where the 50% peak density reduction occurred for the z_{high} condition, but it also increased the amount of density reduction from 50% to 70% for the z_{low} condition. As before, the magnetic field alone caused significant density reduction in the plasma, but in this case, the addition of the -100-V potential applied to the cathode did not further increase the density reduction for either condition.

In order to investigate whether a stronger electric field would provide more density reduction, the magnetic field strength needed to be increased further so that arcs would not develop between the electrodes. Figures 7.6 and 7.7 show the density reduction as a function of x and y-positions for peak B_z = 1850 G. In this case, three potential differences between the electrodes were investigated: (a) V_c = 0 V, (b) V_c = -100 V and (c) V_c = -250 V.

Once again, the increased magnetic field caused a greater density reduction than that found with B_z = 1385 G, and the addition of a -100 V potential difference increased the area where the maximum density reduction occurred. In this case, the peak reduction was 60% for the z_{high} condition and 80% z_{low} condition. Increasing the potential difference to -250 V neither increased the size of the reduction window, nor did it increase the density reduction itself. In actuality, the increase in voltage caused the area of maximum density reduction to shrink, and outside the region directly above the iron core of the magnet, the ion number density actually increased (negative density reduction). One possible explanation for this is that the stronger potential difference between the electrodes caused further breakdown of the argon gas, and the magnetic field was not strong enough to prevent the DC breakdown.

Originally, Langmuir probe testing had been done with peak B_z = 2000 G, but the resulting IV curves were not useable. After analyzing the data using the methods discussed in Section 5.3.1, the ion number densities were found to be more than

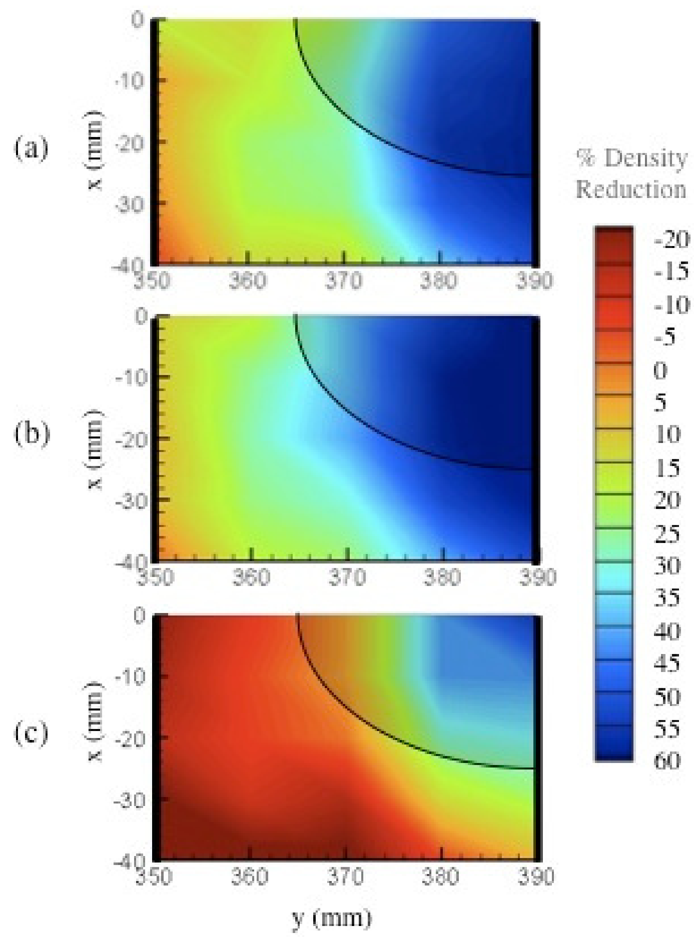

Figure 7.6: Percent density reduction for 1850 G peak magnetic field at z = -70 mm. (a) V_c = 0 V, (b) V_c = -100 V (c) V_c = -250 V.

an order of magnitude larger than those found with similar conditions but a lower magnetic field strength. Due to this irregularity, the Langmuir probe data for B_z = 2000 G were not used in this dissertation. Possible explanations for the variation in the data include magnetic field effects on the Langmuir probe that were not previously accounted for at those strong magnetic fields and irregularities in the operation of the helicon source and matching network, resulting in increased power coupling to the plasma.

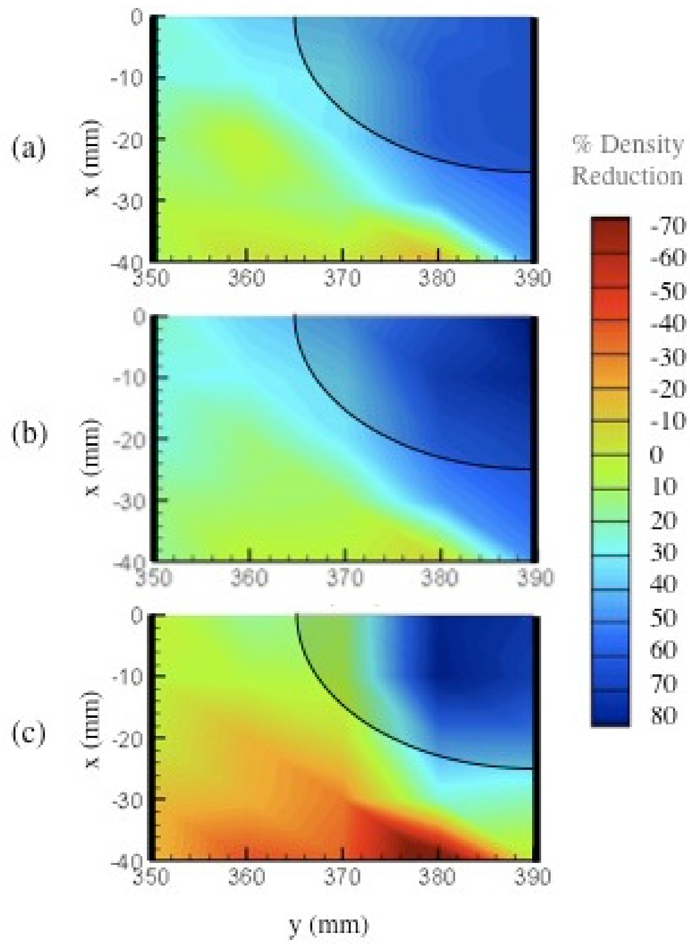

Figure 7.7: Percent density reduction for 1850 G peak magnetic field at z = -75 mm. (a) V_c = 0 V, (b) V_c = -100 V and (c) V_c = -250 V.

7.2 Plasma Frequency

Hairpin resonance probe measurements were conducted along the x-y plane at z = -75 mm for three ReComm system operating conditions:

- B_z = 0 G, V_c = 0 V
- B_z = 2000 G, V_c = 0 V
- B_z = 2000 G, V_c = -250 V

The hairpin probe was designed to operate with B_z = 2000 G, as was shown in Figure 5.12, so any irregularities, as were possibly seen with the Langmuir probe, were neither expected, nor observed with this probe. Figure 7.8 shows the plasma frequency as a function of y-position for the three conditions mentioned above. Due to the nature of the probe (it was 57 mm long) the measured frequency is considered an integration over the area in the x-direction. Therefore, data are only presented at one x-position where the center of the probe moved along the x = 0 mm, z = -75 mm line. Indicated on the plot are the locations of the electrodes (vertical lines at y = 350 mm and y = 390 mm) and the iron core of the magnet (shaded grey region at the bottom of the plot).

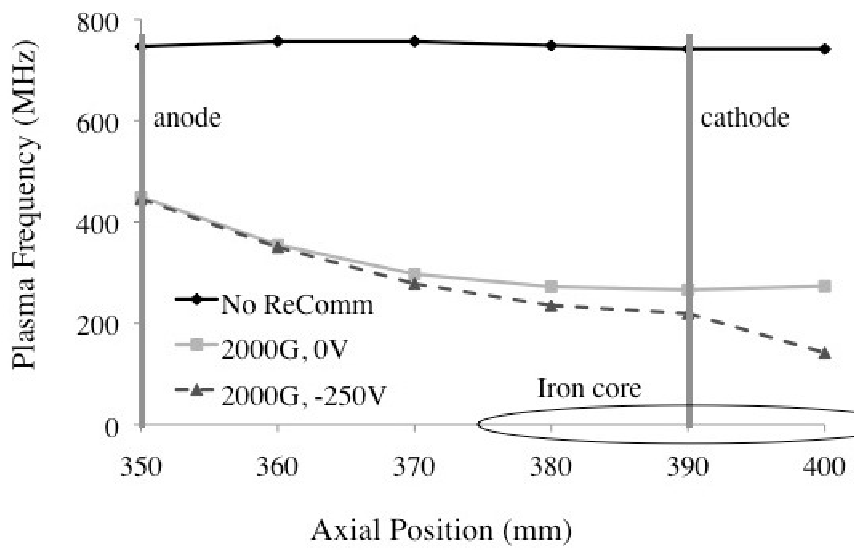

Figure 7.8: Plasma frequency for 2000 G peak magnetic field at z = -75 mm and x = 0 mm. Data presented are from three operating conditions: B_z = 0 G, V_c = 0 V (solid black line with diamonds), B_z = 2000 G, V_c = 0 V (solid grey line with squares) and B_z = 2000 G, V_c = -250 V (dashed line with triangles).

The plasma frequency dropped significantly when the ReComm System magnetic field was turned on, causing a frequency reduction of up to 65% of that found without the ReComm system operating. The addition of the electric field further lowered the plasma frequency to 80% of the original value. This increase in the frequency reduction only occurred near the cathode.

This level of frequency reduction is within error estimates of the density reduction data measured with the Langmuir probe when the ReComm system was operating at B_z = 1850 G and V_c = -100 V. Given that the maximum density reduction along the line where z = -75 mm and x = 0 mm is 80%, the maximum plasma frequency reduction (based on Equation 2.12) should be 64%. The frequency reduction measured by the hairpin probe at the same position and with no voltage applied to the cathode was 65%. That reduction increased to 80% with an applied -250 V potential difference. The larger frequency reduction was expected since the magnetic field was greater when the hairpin probe was being used. This correlation also provides confidence that both the Langmuir probe and the hairpin probe were properly functioning.

7.3 Signal Attenuation

Signal attenuation measurements were conducted with a network analyzer via an S2-1 probe. The signal attenuation data were measured as a function of input signal frequency for downstream locations varying from directly above the anode (y = 350 mm) to 10 mm downstream of the cathode (y = 400 mm). The probe was centered above the x = 0 mm axis and remained at a constant vertical location where the lower antenna was at z = -75 mm. Signal attenuation was measured for the same ReComm system operating conditions as were used with the hairpin probe:

- No ReComm system operating: B_z = 0 G, V_c = 0 V
- B_z = 2000 G, V_c = 0 V
- B_z = 2000 G, V_c = -250 V

The relative S2-1 signal response had little attenuation at the lower frequency limit of the network analyzer. As the frequency of the input signal increased, the response decreased to a minimum value that corresponds to the plasma frequency measurements found with the hairpin probe in the previous section. Figure 7.9 shows how the frequency at which minimum signal response occurred during two different periods of S2-1 testing corresponds with the plasma frequency data obtained for similar operating conditions with the hairpin probe. The minimum values from the signal response curves during the first set of experiments (trial 1 in Figure 7.9) were consistently higher than the plasma frequencies measured with the hairpin probe. On the other hand, the minimum values of the signal response curves from the second set of experiments (trial 2 in Figure 7.9) closely correspond with the hairpin probe plasma frequencies. A possible explanation for the discrepancy is that the helicon source and matching network were better tuned for the trial 2 data.

Figures 7.10 to 7.13 show the relative S2-1 response in dB as a function of the signal input frequency from the network analyzer for various y-positions. The peak in the signal response at the lower frequencies (below 5 GHz) was most likely due to the evanescent wave that was expected to be observed. Evanescent waves may still be able to transmit between the antennas below the plasma frequency because the distance between them is at most 5% of a wavelength (at the ~1 GHz plasma frequency) (6).

In general, turning on the magnetic field significantly reduced the frequency at which communications could pass with minimal signal attenuation (less than -2 dB). The level of frequency reduction was greater in the region closer to the center of the magnet, toward the cathode (Figure 7.13). Adding the potential drop across the electrodes further reduced the plasma frequency, but in this case, the most reduction

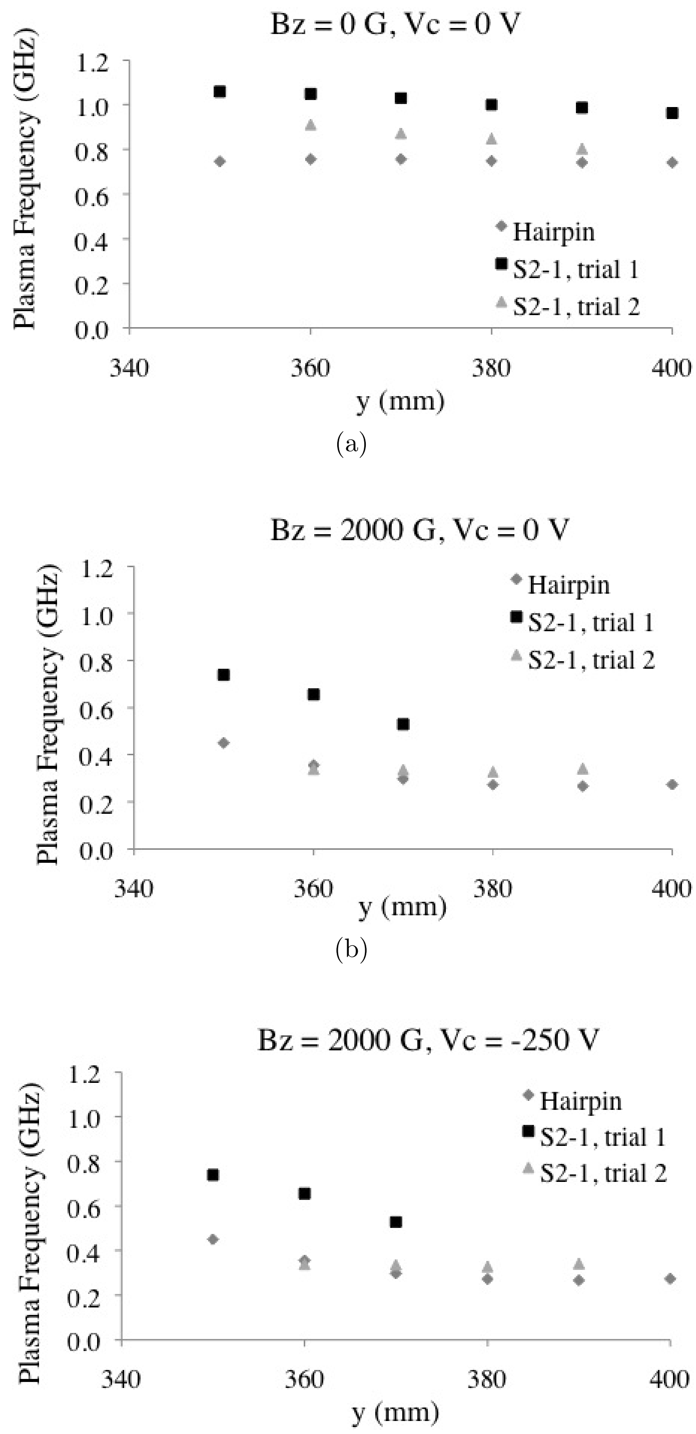

(a)

(b)

(c)

Figure 7.9: Comparison of plasma frequency measurements from the hairpin probe and the minimum of the S2-1 response curve. Three ReComm system operating conditions were used: (a) B_z = 0 G, V_c = 0 V (b) B_z = 2000 G, V_c = 0 V and (c) B_z = 2000 G, V_c = -250 V.

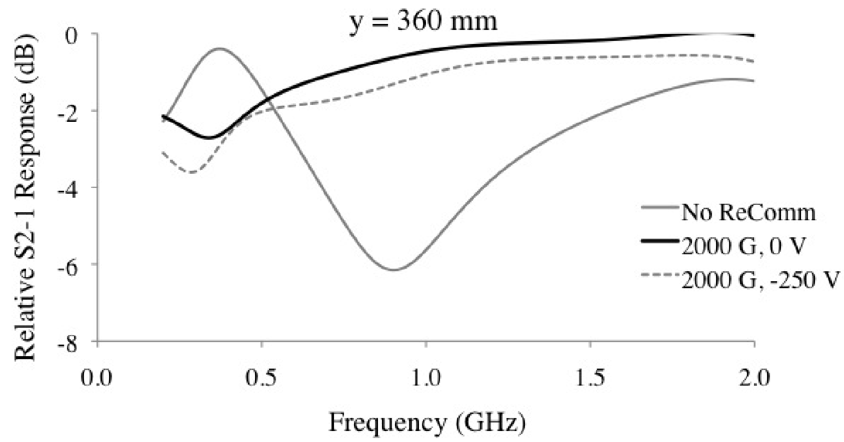

Figure 7.10: Relative S2-1 response as a function of signal input frequency at $x = 0$ mm, $y = 360$ mm and $z = -75$ mm (trial 2).

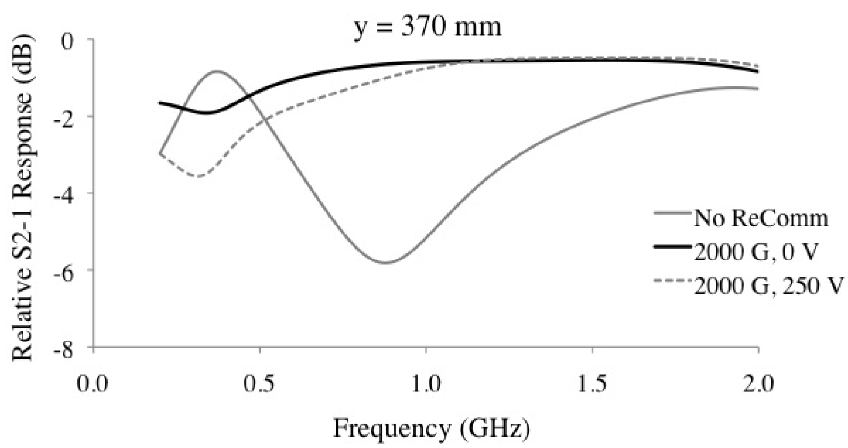

Figure 7.11: Relative S2-1 response as a function of signal input frequency at $x = 0$ mm, $y = 370$ mm and $z = -75$ mm (trial 2).

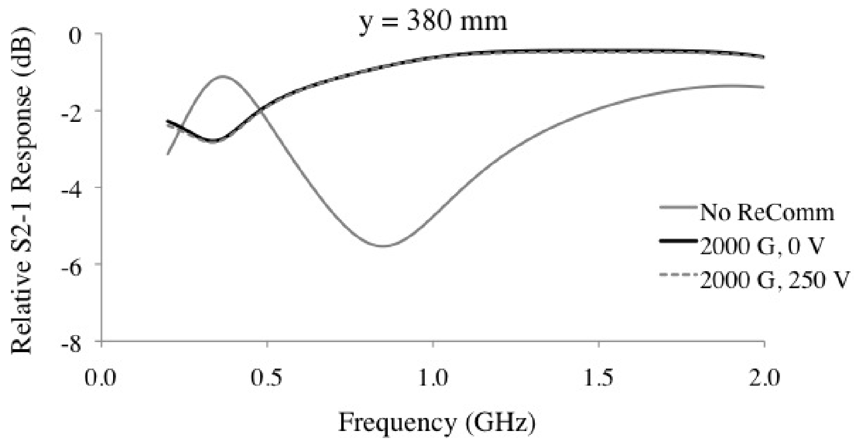

Figure 7.12: Relative S2-1 response as a function of signal input frequency at $x = 0$ mm, $y = 380$ mm and $z =$ -75 mm (trial 2).

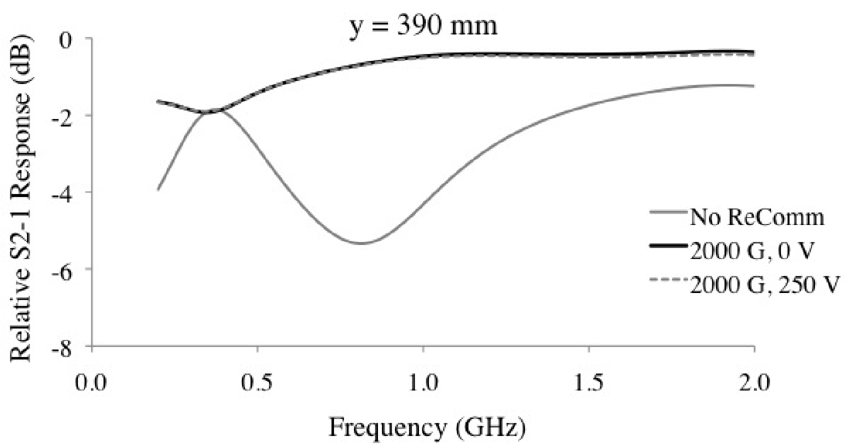

Figure 7.13: Relative S2-1 response as a function of signal input frequency at $x = 0$ mm, $y = 390$ mm (above the cathode) and $z =$ -75 mm (trial 2).

occurred nearer the anode, which was unexpected. The initial experiments done with the S2-1 probe (trial 1) show that the addition of a potential drop across the electrodes should cause a reduction in the plasma frequency nearer the cathode, as was similarly observed with the Langmuir probe density reduction data and the hairpin probe plasma frequency data. Figures 7.14 through 7.19 show the S2-1 response curves from the initial set of data for varying y-positions.

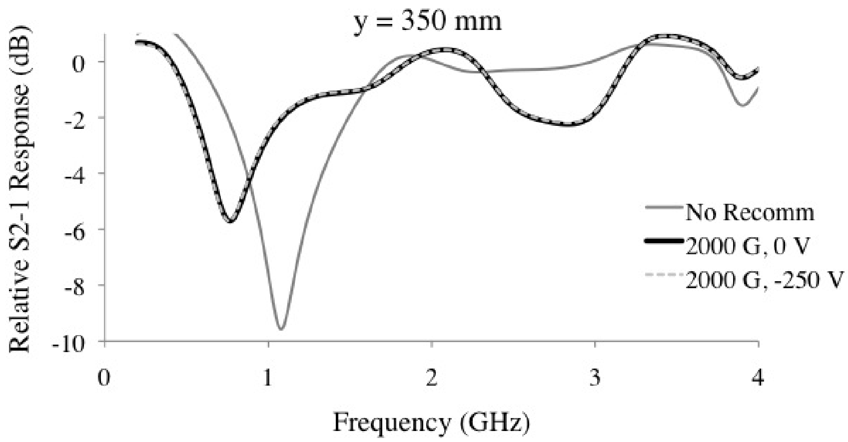

Figure 7.14: Relative S2-1 response as a function of signal input frequency at $x = 0$ mm, $y = 350$ mm (above the anode) and $z =$ -75 mm (trial 1).

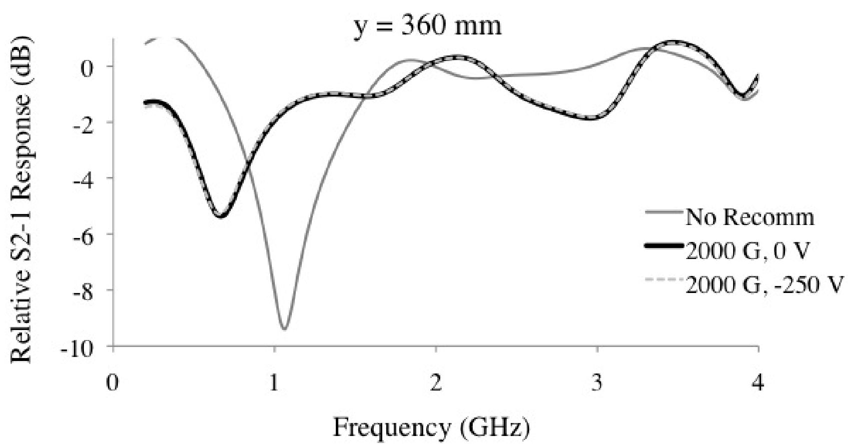

Figure 7.15: Relative S2-1 response as a function of signal input frequency at $x = 0$ mm, $y = 360$ mm and $z =$ -75 mm (trial 1).

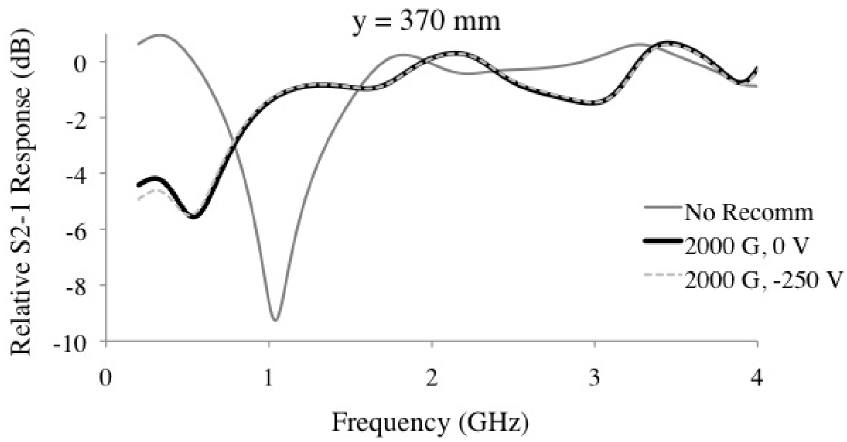

Figure 7.16: Relative S2-1 response as a function of signal input frequency at $x = 0$ mm, $y = 370$ mm and $z =$ -75 mm (trial 1).

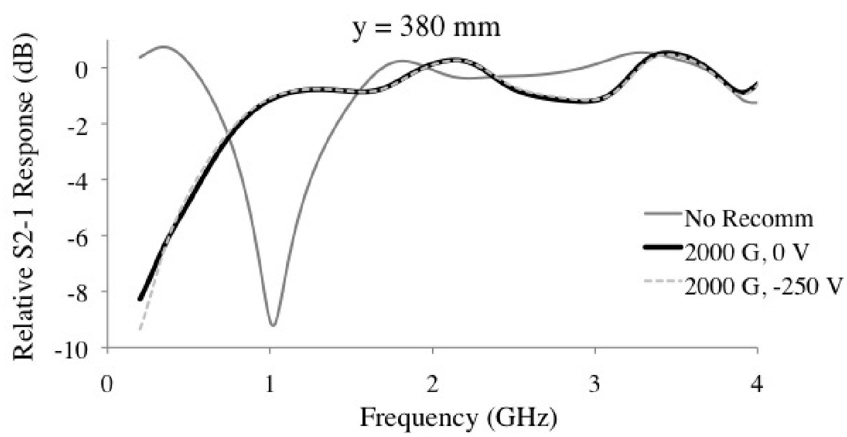

Figure 7.17: Relative S2-1 response as a function of signal input frequency at $x = 0$ mm, $y = 380$ mm and $z =$ -75 mm (trial 1).

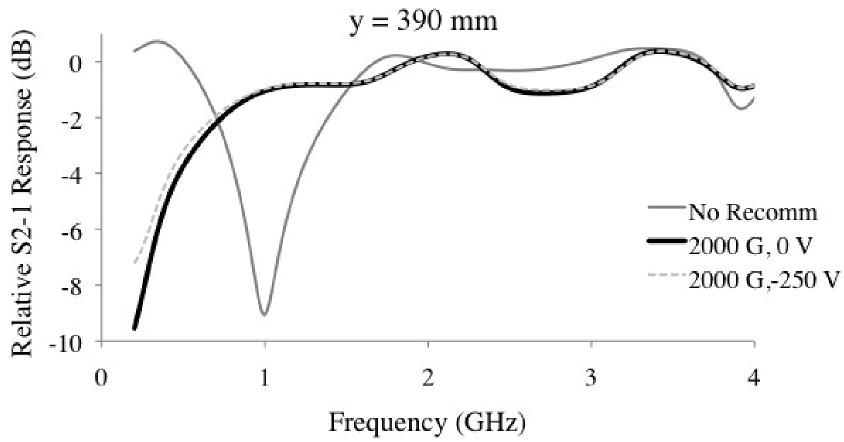

Figure 7.18: Relative S2-1 response as a function of signal input frequency at $x = 0$ mm, $y = 390$ mm (above the cathode) and $z =$ -75 mm (trial 1).

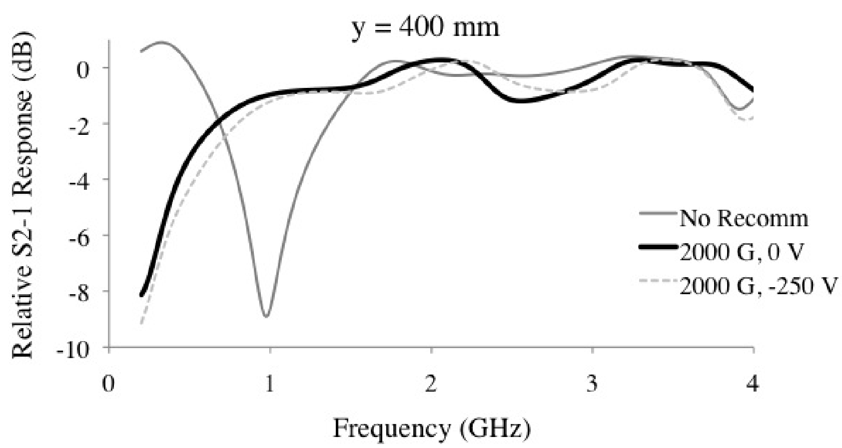

Figure 7.19: Relative S2-1 response as a function of signal input frequency at $x = 0$ mm, $y = 400$ mm and $z =$ -75 mm (trial 1).

7.4 Comparison with Simulation Data

The experimental results discussed in the previous sections were compared to computer simulation results of the ReComm system effect on a plasma sheath. Table 7.1 shows the operating conditions used for the computer simulations that produced Figures 7.20 through 7.22, as well as the operating conditions used for the experi-

Parameter	Value	
	Simulation	Experiment
Pressure (mtorr)	1.0	0.6
Electrode gap (mm)	40	40
Applied Cathode voltages (V)	-20 to -1500	0, -100 and -250
Peak Magnetic field strengths (G)	200 to 3000	925 to 2000
Distance above "spacecraft" surface (mm)	0, 20 and 40	100 to 15
Location of iron core centerline	Centered between electrodes	Below cathode

Table 7.1: Differences between simulation and experimental operating conditions.

ments. The figures in this section are courtesy of Kim (110). In the results from the computer simulations, the x-axis is the same as the y-axis in the experiments. Another difference between the simulation results and the results for density reduction presented here is the method by which the results are displayed. For the work in this dissertation, the density reduction is the percent that the density is reduced by the application of the ReComm system. For the simulations, the results were presented as a density reduction ratio. This ratio is the the number density when the ReComm system was operating divided by the number density when the ReComm system was off.

$$\text{Density Reduction} = \frac{n_{i,R/C}}{n_{i,o}} \tag{7.3}$$

Thus, for the simulation figures, the lower the density reduction ratio, the better the ReComm system was performing. One last difference between the experimental setup and the computer simulation setup is that during the experiments, the electromagnet was centered under the cathode, while for the simulations, it was centered between the anode and cathode.

Figure 7.20 shows the density reduction as a function of the y-position for various locations above the ReComm system (as mentioned previously, the plot shows the y-axis as the x-axis). The magnetic field strength was 700 G, with a background pressure of 1.0 mtorr and -800 V applied to the cathode. Similar to the experimental

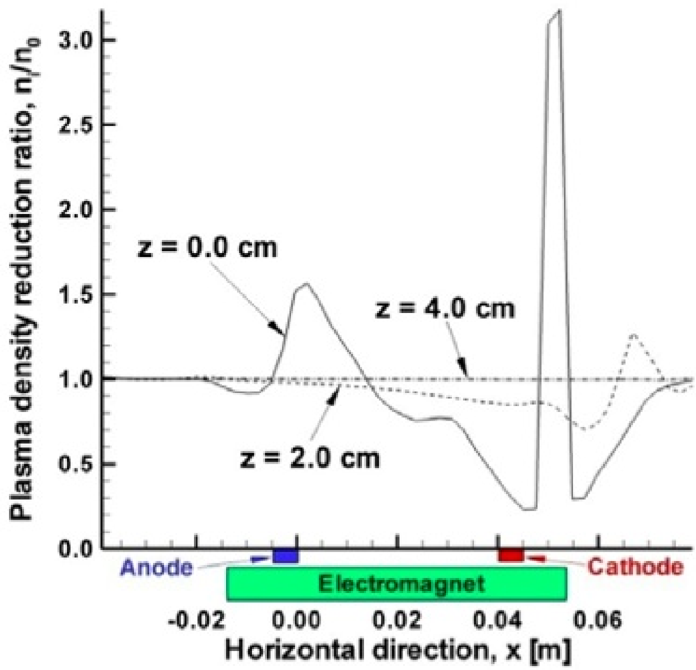

Figure 7.20: Simulation results: density reduction as a function of y and z-positions. The following operating conditions were used to produce these results: x = 0 mm, B_z = 700 G, p = 1.0 mtorr and V_c = -800 V (110).

results, the simulations show that the region of greatest density reduction was in the area nearest the cathode. The density was reduced a maximum of about 70% directly above the surface of the ReComm system where reduction was expected to be at a maximum. For the case 20-mm-above the surface, the reduction only reached 20%. This correlates well with the experimental results as the magnetic field was not strong for this case. In addition, at this high potential with only 700 G, the density in the region upstream of the cathode increased (density reduction greater than 1 in this case), which also follows the trends found experimentally (Figures 7.6 and 7.7).

Figure 7.21 shows simulation results for density reduction as a function of magnetic field strength and y-position for a z-position *directly* above the ReComm system surface. These results agree well with the experimental data in that as the magnetic field was increased, the density reduction became stronger. However, the simulation shows that the reduction occurred only in an area directly above the cathode. Experimental results show that the area of density reduction extended upstream a couple of centimeters.

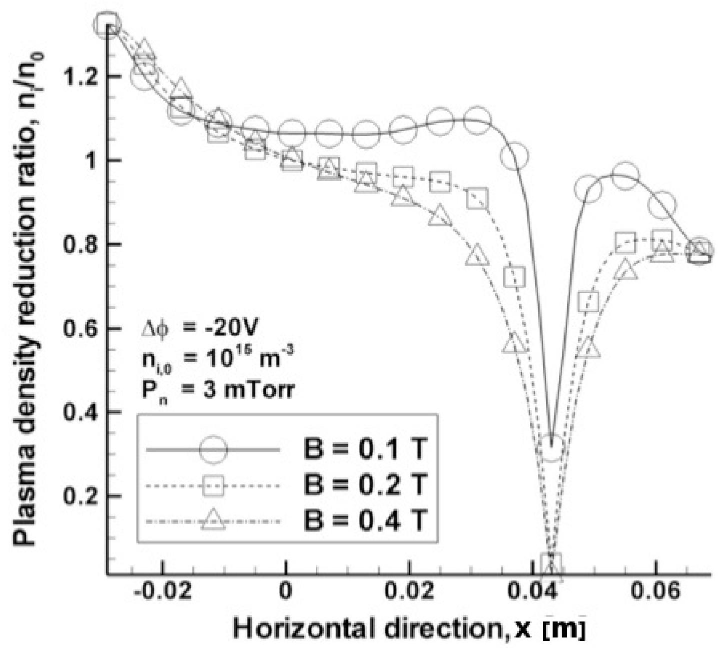

Figure 7.21: Simulation results: density reduction as a function of y-position and magnetic field. Three magnetic field strengths are simulated *directly* above the ReComm system surface (110).

Figure 7.22 shows the density reduction as a function of the potential applied to the cathode, V_c, for a neutral pressure of 1 mtorr and a magnetic field strength of 700 G. The data were taken at the equivalent experimental positions of y = 390 mm and z = -85 mm (*directly* above the cathode). When there was very little potential applied to the cathode (V_c = -20 V), the density was reduced by about 65%. The results of these simulations are different from the experimental results as they show an increased reduction in density as the potential was further increased. However, during the experiments the voltage applied to the cathode could not exceed -100 V

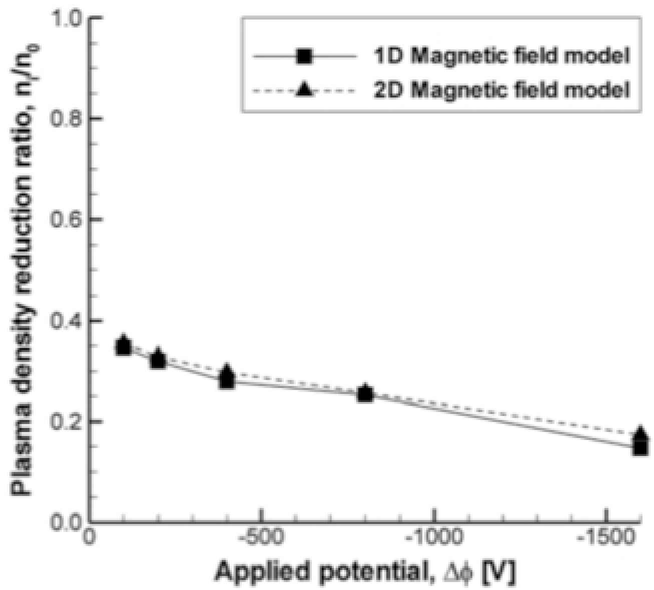

Figure 7.22: Simulation results: density reduction as a function of cathode potential. The following parameters were used to develop this plot: z = -85 mm (*directly* above the ReComm system surface), y = 390 mm, B_z = 700 G and p = 1.0 mtorr (110).

without arcs occurring for the lowest magnetic field setting that was tested (B_z = 925 G). Had the electrodes been able to sustain a higher potential difference between them, a further decrease in number density may have been observed experimentally, but this is not likely since the higher potential applied to the cathode when B_z = 1850 G lowered the density reduction.

Overall, the trends found from the computer simulation data agree with those found from the experimental data. As the magnetic field was increased, the amount of density reduction increased. In addition, the application of a potential drop across the electrodes further decreased the plasma number density, but the computer simulation of the ReComm system over-predicted its effect on the plasma. In addition, the simulation did not account for the additional DC breakdown in the plasma due to higher potential differences between the electrodes.

7.5 Electric Field Effects

Originally, it was thought that $E \times B$ drift would contribute significantly to the density reduction. However, the results from the Langmuir probe, the hairpin probe and the S2-1 probe show differently. These all show that when the electric field was added, the only change in the plasma occurred near the cathode. This indicates that the potential drop between the electrodes was not steady as was expected, but rather consisted of distinct jumps, as shown in Figure 7.23. Although this behavior was not

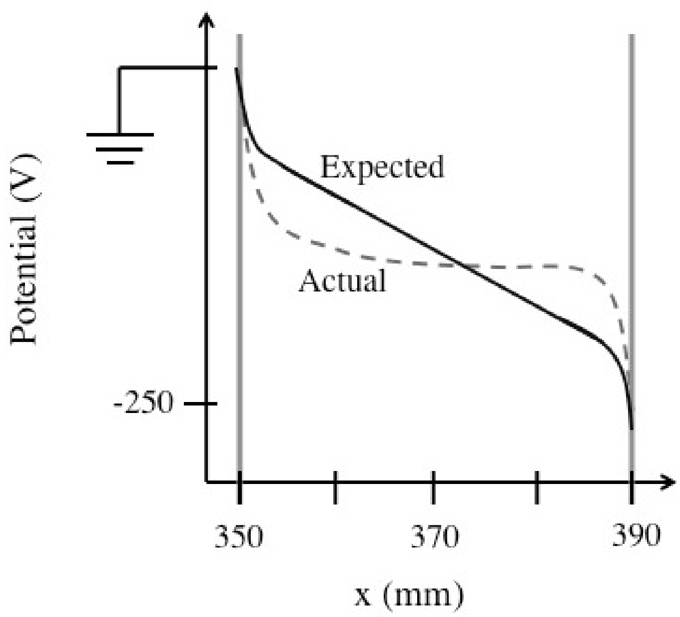

Figure 7.23: Expected vs. actual potential drop between the electrodes.

expected, it is consistent with the plasma density. At the plasma number densities present in these experiments, the potential sheaths will be very thin, as shown in Figure 7.23. Therefore, the data show that when the electric field is applied, the increased density reduction is due to the electrostatic sheath present, not the $E \times B$ effect.

7.6 Summary

This chapter began with a brief discussion of the various methods for determining whether or not the ReComm system was effective. Next, results from the Langmuir probe, hairpin probe and S1-2 probe were presented. The density reduction from the Langmuir probe showed that the magnetic field alone significantly lowered the ion number density of the plasma. As the magnetic field strength increased, the ion number density decreased. The addition of the electric field mostly served to increase the area in which the density reduction occurred. In the locations closer to the surface of the ReComm system, the electric field slightly increased the amount of density reduction. However, if the electric field was too high, the amount of density reduction would decrease, and in some locations, the ion number density would actually increase. This was explained by a DC discharge occurring between the electrodes. The data from the hairpin resonance probe showed that the plasma frequency decreased when the ReComm system was turned on. The level of frequency reduction measured was expected based on the data found with the Langmuir probe. Furthermore, the frequency reduction was also similar to that found with the S2-1 signal attenuation measurements.

In addition to the amount of density reduction, the “shape” of the reduced plasma density was presented. The density/frequency reduction was greatest in the region closest to the iron core of the magnet. When the electric field was turned on, any further increase in the density reduction was in the region nearest to the cathode.

The only exception to this was in one set of the S2-1 signal attenuation experiments.

Data from the computer simulation work done concurrently to this dissertation work was compared with the experimental data. The overall trends of the simulation results agreed with the trends found experimentally, but the magnitudes of the density reduction were different. Also, the simulations showed that the electric field should have had a larger effect on the density than was actually observed.

CHAPTER 8

ReComm System Magnetic Field Effects

An unexpected result of the ReComm system experiments was that the magnetic field alone contributed greatly to the density reduction. This chapter contains an explanation for the discrepancy in the measured data compared with what was expected. In some cases, the density was reduced by 70% without any applied electric field. It was expected that with only a magnet field, the electrons would be caught in orbits around the field lines and move only in a vertical direction above the region where an antenna would be located. This would lead to an increase in the plasma number density in the region directly above the magnet. However, this idea was based on the key assumption that the magnetic field was only in one direction ($B = B_z$) and that it was uniform.

For the setup used during these experiments, the ReComm magnet was a solenoid with an iron base and core. This design resulted in a divergent, non-spatially-uniform magnetic field, as shown in Figures 4.4 and 4.5, thus annulling the key assumption stated above. In order to understand how a divergent, non-uniform magnetic field would affect the plasma, the equations for how magnetic fields interact with plasma were studied. Then, the ReComm system was modeled with the physics package COMSOL.

8.1 Plasmadynamics in a Non-Uniform Magnetic Field

The equations of motion for a particle acted on by electric and magnetic fields are given as functions of the Lorentz force (Equation 8.1) and the Lagrangian velocity (Equation 8.2) (33).

$$m\frac{d\mathbf{v}}{dt} = q[\mathbf{E}(\mathbf{r}, t) + \mathbf{v} \times \mathbf{B}(\mathbf{r}, t)] \tag{8.1}$$

$$\frac{d\mathbf{r}}{dt} = \mathbf{v}(t) \tag{8.2}$$

The above equations cannot be solved for the general case, but for the special case of a constant magnetic field $\mathbf{B} = \hat{z}B_0$ with no electric field, the components of Equation 8.1 simplify to:

$$m\frac{dv_x}{dt} = qv_yB_0 \tag{8.3}$$

$$m\frac{dv_y}{dt} = -qv_xB_0 \tag{8.4}$$

$$m\frac{dv_z}{dt} = 0 \tag{8.5}$$

Combining Equations 8.3 and 8.4 and then differentiating Equations 8.3, 8.4 and 8.5 gives the following system of equations for the particle velocity.

$$v_x = v_{\perp 0}\cos(\omega_c t + \varphi_0) \tag{8.6}$$

$$v_y = -v_{\perp 0}\sin(\omega_c t + \varphi_0) \tag{8.7}$$

$$v_z = v_{z0} \tag{8.8}$$

where $v_{\perp 0}$ is the speed perpendicular to $\mathbf{B}_0$ and φ_o is an arbitrary phase.

The particle position can be obtained by integrating Equation 8.2.

$$x = r_c\sin(\omega_c t + \varphi_0) + (x_0 - r_c\sin\varphi_0) \tag{8.9}$$

$$y = r_c\sin(\omega_c t + \varphi_0) + (y_0 - r_c\cos\varphi_0) \tag{8.10}$$

$$z = z_0 + v_{z0}t \tag{8.11}$$

where r_c is the gyration radius, defined by

$$r_c = \frac{v_{\perp 0}}{|\omega_c|} \tag{8.12}$$

The results of Equations 8.6 through 8.11 are that the particle has a circular motion, orbiting in a direction perpendicular to the magnetic field lines. The frequency of the orbit is ω_c and the radius is r_c. The particle moves along a guiding center of the orbit with

$$x_{gc} = x_0 \tag{8.13}$$

$$y_{gc} = y_0 \tag{8.14}$$

$$z_{gc} = z_0 + v_{z0}t \tag{8.15}$$

This is the outcome that was expected during ReComm system operation with only a magnetic field. However, the results obtained from the experiments do not correspond with the analytical solution shown above. Thus, the motion of a particle in a non-uniform magnetic field needed to be studied. When the electron gyroradius is much smaller than the length scale of the magnetic field variation, the particle motion can be split into the fast gyromotion of the electrons orbiting about the field lines and the slow drift of the guiding center (33). This assumption is valid with respect to the ReComm system. In order to separate the motion, the instantaneous particle position must be split into a guiding center (r_g) and a gyroradius (r_c) about that center, along with the accompanying velocity.

$$\mathbf{r} = \mathbf{r}_g(t) + \mathbf{r}_c(t) \tag{8.16}$$

$$\mathbf{v} = \mathbf{v}_g + \mathbf{v}_c \tag{8.17}$$

The magnetic field near the guiding center is expanded to

$$\mathbf{B}(\mathbf{r}) = \mathbf{B}_0(\mathbf{r}) + (\mathbf{r}_c \cdot \nabla)\mathbf{B}(\mathbf{r}) \tag{8.18}$$

Given the earlier approximation, that the gyroradius is much smaller than the length scale of the magnetic field variation, the rapidly rotating terms average to zero when the motion is averaged over a gyroperiod. This results in an equation for the drift motion (33).

$$m\frac{d\mathbf{v}_g}{dt} = \mathbf{F}_{ext} + q\mathbf{v}_g \times \mathbf{B} - \frac{\frac{1}{2}mv_\perp^2}{B_0}\nabla B \tag{8.19}$$

where $\mathbf{F}_{ext}$ includes all the external forces, $B_0 = |\mathbf{B}_0|$ and $v_\perp = |\mathbf{v}_c|$

Now, consider the case where the magnetic field lines are curved in the x-z plane. Then, $\partial B_x/\partial z$ is a function of the radius of curvature (R) of the magnetic field lines. (33).

$$\frac{1}{R} = -\frac{1}{B_z}\frac{\partial B_x}{\partial z} \tag{8.20}$$

The centrifugal force acting on a particle is given by

$$\mathbf{F}_R = \frac{mv_z^2}{R} \tag{8.21}$$

By combining the centrifugal force with the expression for the radius of curvature, an equation for the drift velocity of the guiding center due to the magnetic field line curvature can be found (33).

$$\mathbf{v}_R = \frac{2W_z}{qB_z^2}\frac{\partial B_z}{\partial z}\hat{y} \tag{8.22}$$

where W_z is the kinetic energy in the z-direction. The ions and electrons drift in opposite directions, perpendicular to both the curvature force and $\mathbf{B}$, giving rise to a net current. Looking back at Figure 4.4, if the motion of the electrons were in a direction perpendicular to $\mathbf{B}$, they would be deflected away from the region near an antenna.

8.2 COMSOL Modeling of ReComm System

In order to visualize the dynamics of the ReComm system, the physics modeling package COMSOL was used to model its electric and magnetic fields. Then the particle tracing feature of the program was used to study how the electrons respond to the fields. First, a simple model of a uniform magnetic field oriented orthogonal to a straight electric field was modeled to ensure that the tracing program was properly modeling the fields. Then, a comprehensive model needed to be built of the entire ReComm system. Figure 8.1 shows the solid frame model as well as the generated mesh used for solving the electrostatic and magnetostatic fields of the ReComm system.

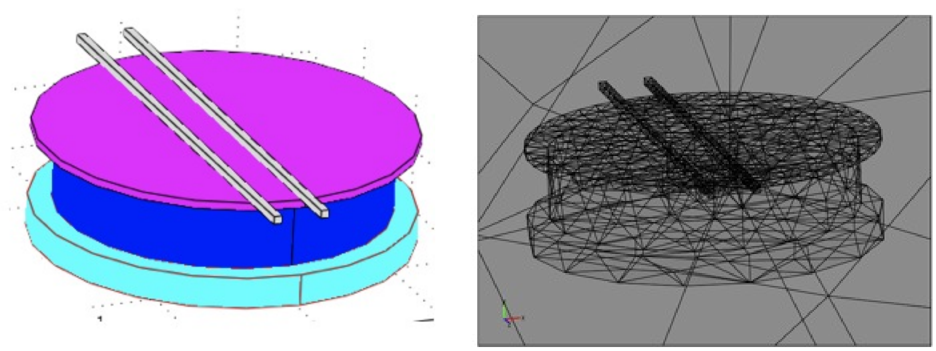

(a) (b)

Figure 8.1: Solid frame model (a) and generated mesh (b) for ReComm COMSOL modeling.

The model was solved for the magnetic and electric fields present in the system when 325 A were flowing through the ReComm system electromagnet and -250 V were applied to the cathode. Figure 8.2 shows the electric field and the potential map, and Figure 8.3 shows the magnetic field. All of these plots were generated by COMSOL. The COMSOL magnetic field is very similar to that generated by the electrostatic solver MagNet and measured with a Hall probe (Section 4.3). This

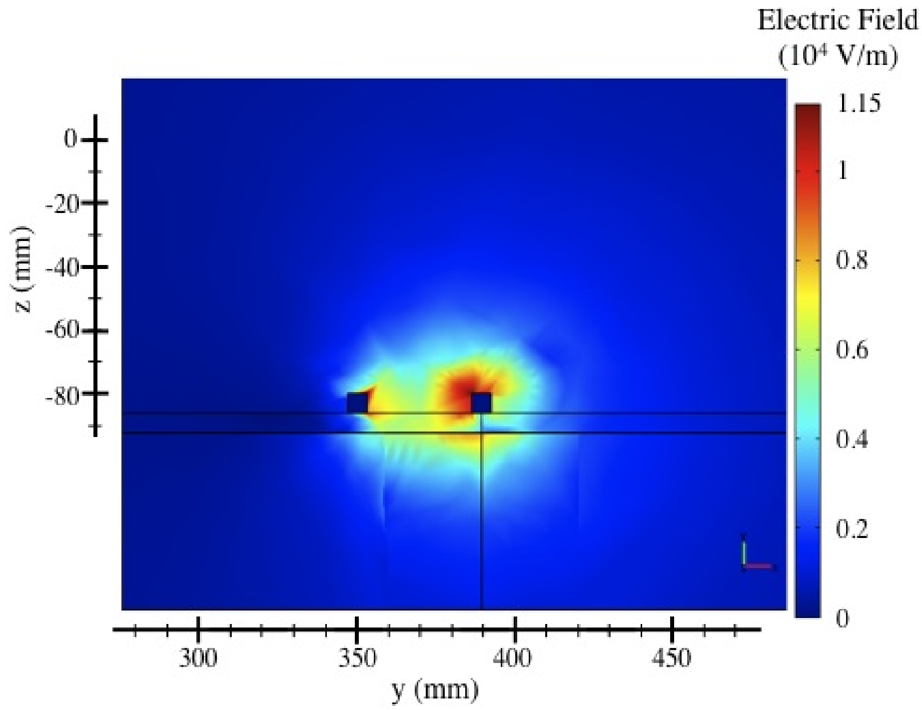

(a)

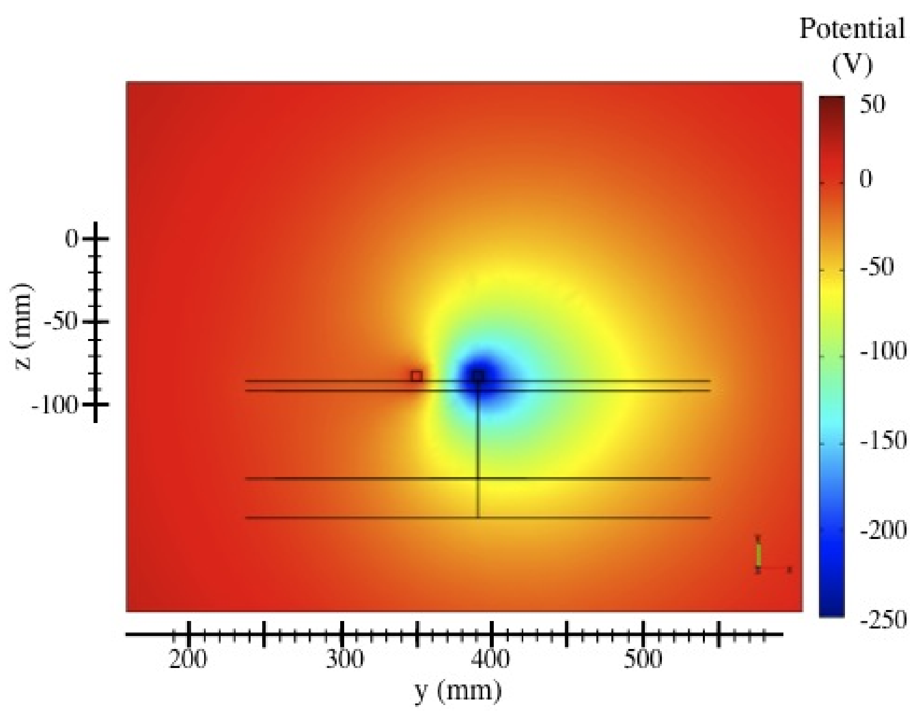

(b)

Figure 8.2: Electric field (a) and potential map (b) modeled by COMSOL when V_c = -250 V.

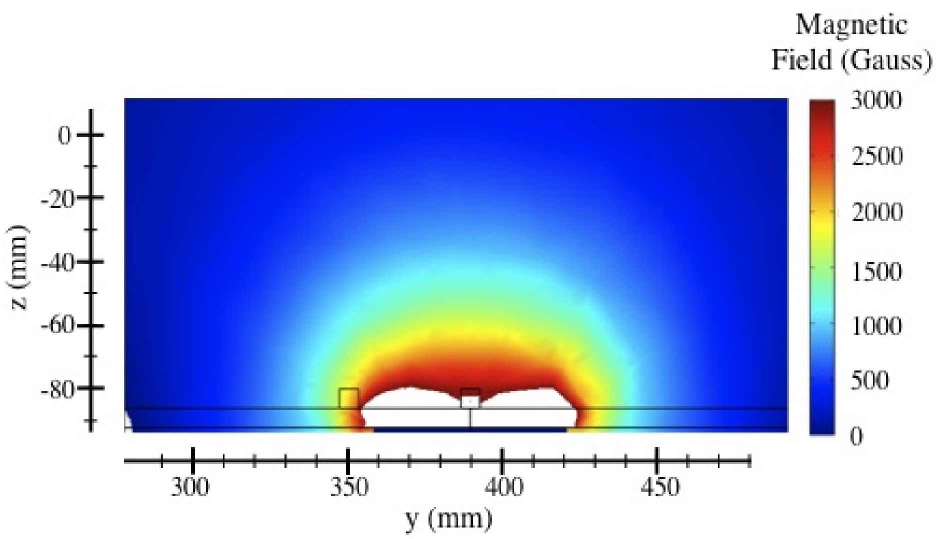

(a)

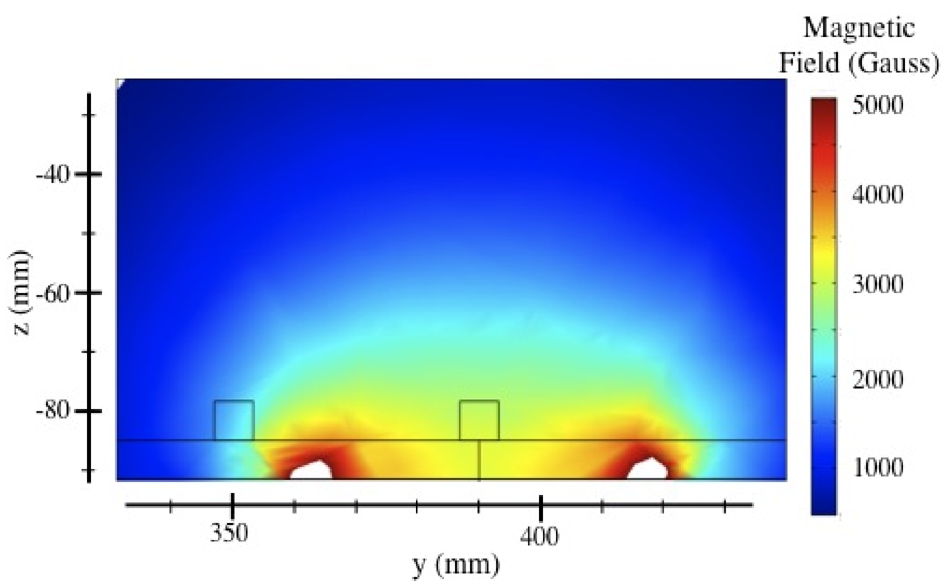

(b)

Figure 8.3: Magnetic field modeled by COMSOL. The maximum current is pushed through the coils. (b) is a closer, more detailed picture of the magnetic field directly above the iron core. The white space is where the contour plot saturated.

lends confidence to the ability of the COMSOL system to model field lines.

Once the magnetic and electric fields were modeled, the particle tracing feature of COMSOL was utilized to study how the electrons behaved in the presence of the fields. Table 8.1 shows the various initial conditions used for launching the electrons and the corresponding figures in which the electron traces appear. The initial conditions include the y and z locations, as well as the electron temperature and the corresponding thermal velocity. The velocity is calculated using the following (62):

$$V_{TH} = \sqrt{\frac{k_B T_e}{m_e}} \tag{8.23}$$

For all particle tracing figures (Figure 8.9 through Figure 8.4), the electrons were launched from a line along the x-axis at 1-cm-intervals across the ReComm system. In addition, the traces were created with (a) B_z = 2000 G, V_c = 0 V and with (b) B_z = 2000 G and V_c = -250 V.

	Particle Start Location			
Figure	y (mm)	z (mm)	Temperature (eV)	Velocity (m/s)
Figure 8.4	315	-75	0.5	296,000
Figure 8.5	315	-65	0.5	296,000
Figure 8.6	315	-75	5	937,000
Figure 8.7	315	-65	5	937,000
Figure 8.8	340	-75	0.5	296,000
Figure 8.9	340	-65	0.5	296,000
Figure 8.10	340	-75	5	937,000
Figure 8.11	340	-65	5	937,000

Table 8.1: Summary of electron initial conditions for particle tracing using the COMSOL.

Figures 8.4a and 8.4b show traces of electrons that began with an initial velocity of 296,000 m/s at y = 315 mm and z = -75 mm with (a) only the magnetic field present and (b) both the magnetic field and the electric field present. The electron traces show that when only the magnetic field was present, the particles never entered the area where the electric field could have affected them. The electrons immediately became trapped in the B-field lines, and were directed away from the ReComm

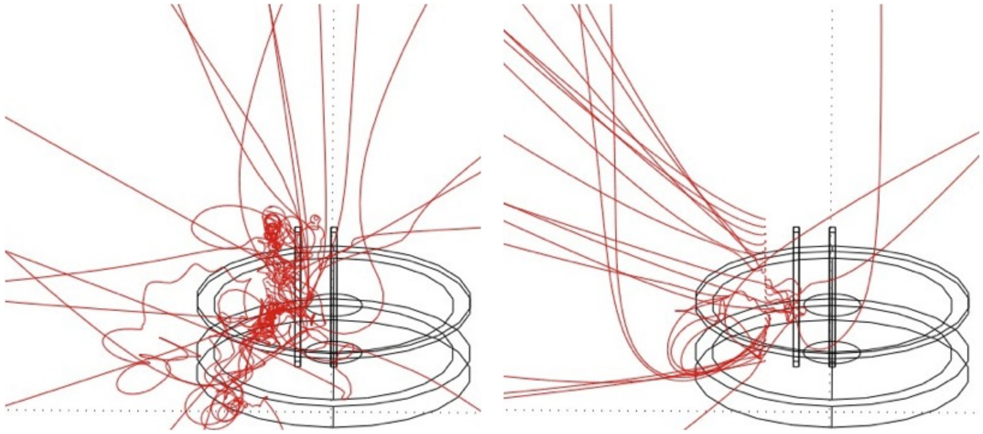

(a) (b)

Figure 8.4: Electron particle tracing using COMSOL for (a) B_z = 2000 G, V_c = 0 V and (b) B_z = 2000 G, V_c = -250 V for the initial conditions: y = 315 mm, z = -75 mm and $v_{i,y}$ = 296,000 m/s.

system. This is due to the divergent nature of the magnetic field lines. Because of this, there was a build up of positive charge between the electrodes, and the ions would tend to move away from that area as well. The electrons did become trapped by the magnetic field, but this occurred before even crossing the anode. This explains why only the magnetic field was necessary for significant density reduction. The addition of the electric field caused the electrons to move away from the region of interest more uniformly, and the electrons no longer were trapped by the magnetic field. However, the region in the center of the magnet, above the iron core is devoid of electrons for both the case with the electric field and that without the electric field.

Figure 8.5 shows the electron traces for the same conditions as in Figure 8.4, but for z = -65 mm. The purpose of this was to determine whether launching the electrons further from the electrode would show any significant changes between the case without an electric field (Figure 8.5a) and the case with an electric field (Figure 8.5b). However, the expected difference between the two cases was not obvious. The traces looked very similar to those found previously with the electrons launched from z = -75 mm.

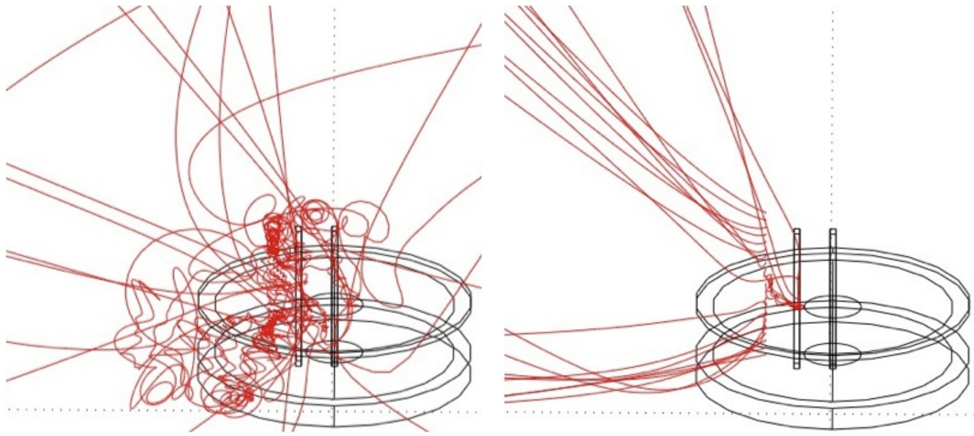

(a) (b)

Figure 8.5: Electron particle tracing using COMSOL for (a) B_z = 2000 G, V_c = 0 V and (b) B_z = 2000 G, V_c = -250 V for the initial conditions: y = 315 mm, z = -65 mm and $v_{i,y}$ = 296,000 m/s.

Increasing the velocity of the electrons should allow them to penetrate further into the magnetic field. Therefore, the initial velocity was increased to 937,000 m/s (the thermal velocity at T_e = 5 eV). Figures 8.6 and 8.7 show electron traces for the same initial electron positions as Figures 8.4 and 8.5, respectively. Although the electrons did travel further downstream, the magnetic field was successful at keeping the majority of them from lingering over the iron core of the magnet. Once again, the addition of the electric field made the electrons travel in a more uniform direction away from the region around the ReComm system magnet centerline. There were fewer electrons over the iron core of the magnet when the electric field was operating as opposed to only the magnetic field with the increased electron thermal velocity.

Finally, all four cases were repeated with the electrons launched from a position closer to the grounded electrode (further downstream at y = 340 mm). The purpose of this was to launch the electrons in a magnetic field that was more uniform than the

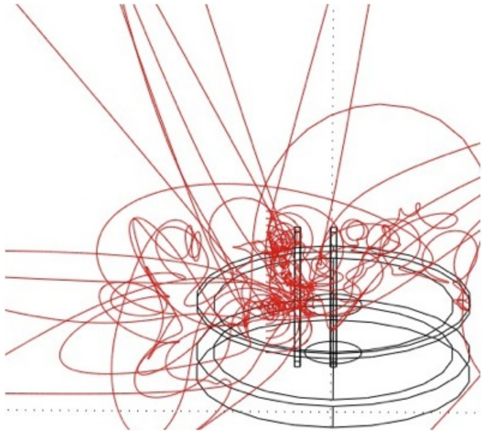

(a)

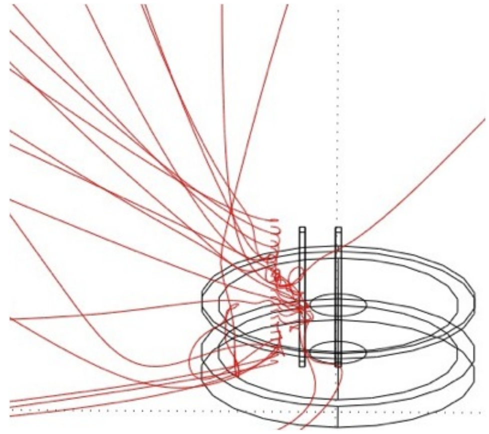

(b)

Figure 8.6: Electron particle tracing using COMSOL for (a) B_z = 2000 G, V_c = 0 V and (b) B_z = 2000 G, V_c = -250 V for the initial conditions: y = 315 mm, z = -75 mm and $v_{i,y}$ = 937,000 m/s.

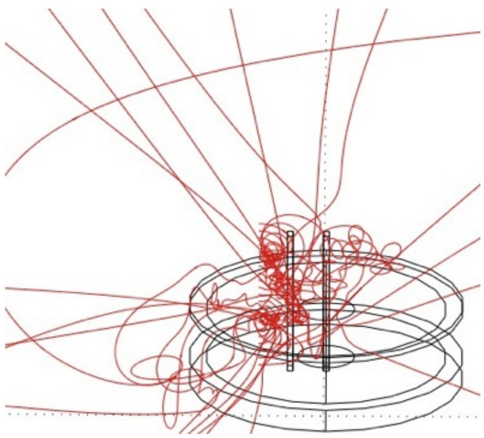

(a)

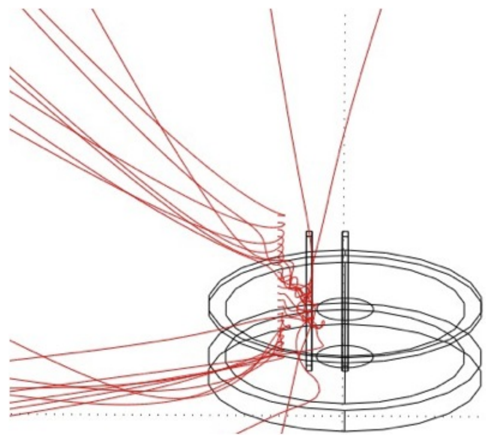

(b)

Figure 8.7: Electron particle tracing using COMSOL for (a) B_z = 2000 G, V_c = 0 V and (b) B_z = 2000 G, V_c = -250 V for the initial conditions: y = 315 mm, z = -65 mm and $v_{i,y}$ = 937,000 m/s.

one found further from the magnet centerline. The hope being that by initializing the electrons further downstream, the ReComm system would demonstrate the originally expected behavior. Figures 8.8 through 8.11 show the results of those traces.

When the electrons were launched closer to the anode, they demonstrated more of the behavior that was originally expected from the ReComm system. When only the magnet field was operating (part a of the figures), the electrons were orbiting about guiding centers above the core of the magnet. This was especially obvious when the electrons were launched with the higher velocity. When the electric field was added, the electrons were immediately directed away from the magnet centerline. In the experiments, however, the electrons were not launched from y = 340 mm, rather they were born back in the helicon source at $y < 0$.

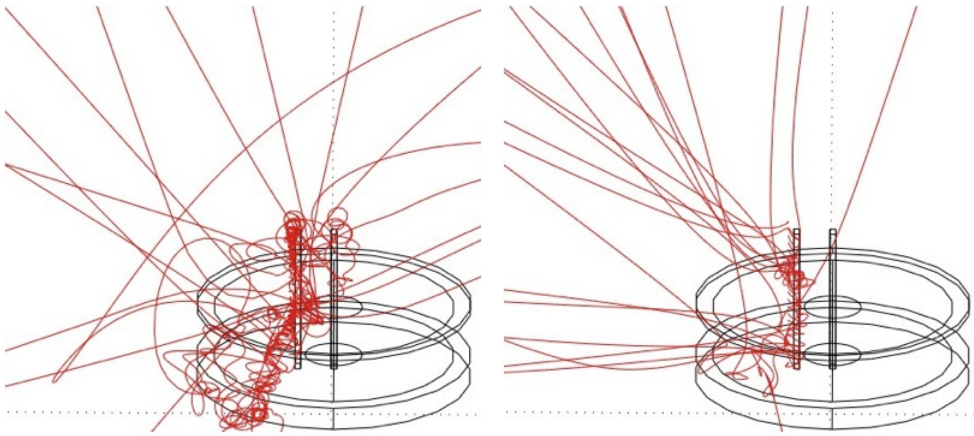

(a) (b)

Figure 8.8: Electron particle tracing using COMSOL for (a) B_z = 2000 G, V_c = 0 V and (b) B_z = 2000 G, V_c = -250 V for the initial conditions: y = 340 mm, z = -75 mm and $v_{i,y}$ = 296,000 m/s.

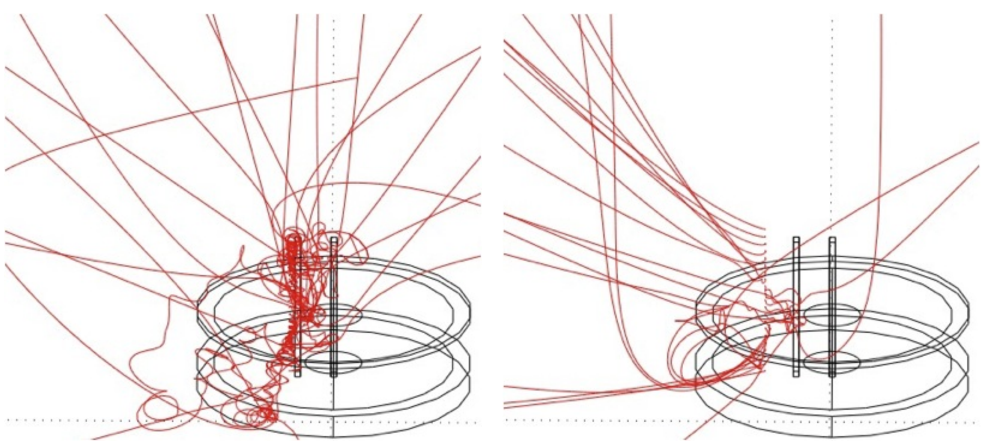

(a) (b)

Figure 8.9: Electron particle tracing using COMSOL for (a) B_z = 2000 G, V_c = 0 V and (b) B_z = 2000 G, V_c = -250 V for the initial conditions: y = 340 mm, z = -65 mm and $v_{i,y}$ = 296,000 m/s.

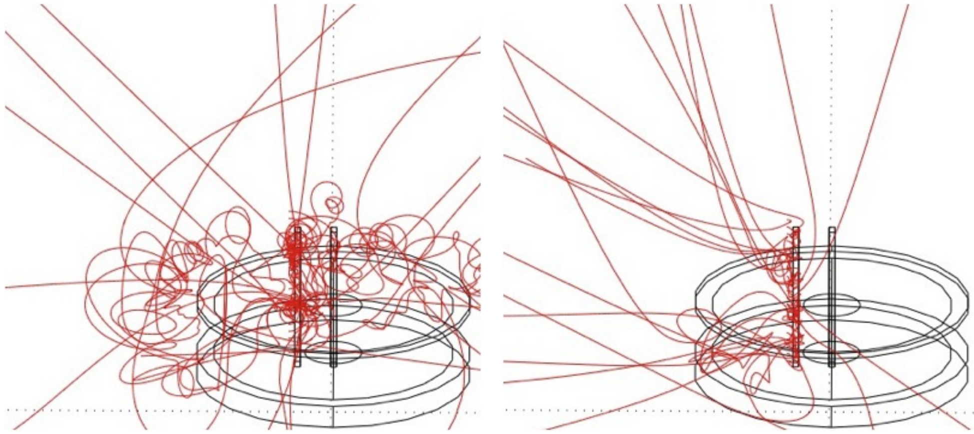

(a) (b)

Figure 8.10: Electron particle tracing using COMSOL for (a) $B_z = 2000$ G, $V_c = 0$ V and (b) $B_z = 2000$ G, $V_c =$ -250 V for the initial conditions: $y = 340$ mm, $z =$ -75 mm and $v_{i,y} = 937{,}000$ m/s.

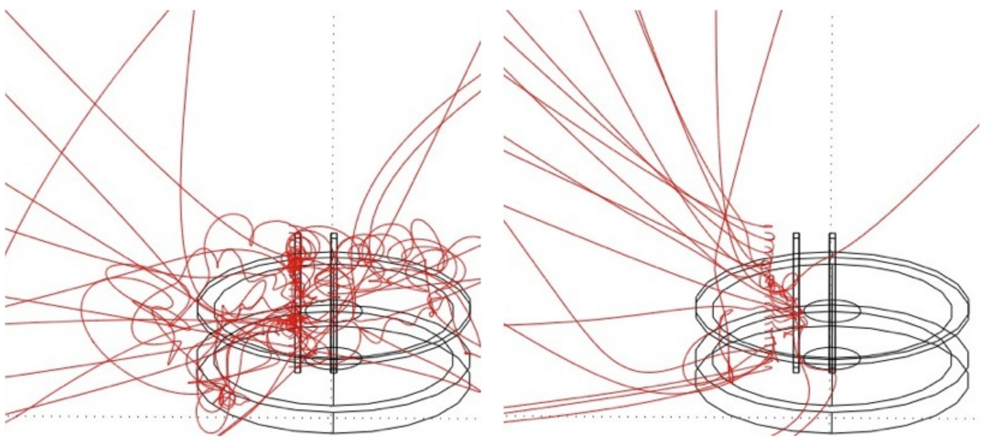

(a) (b)

Figure 8.11: Electron particle tracing using COMSOL for (a) $B_z = 2000$ G, $V_c = 0$ V and (b) $B_z = 2000$ G, $V_c =$ -250 V for the initial conditions: $y = 340$ mm, $z =$ -65 mm and $v_{i,y} = 937{,}000$ m/s.

8.3 Summary

The goal of this chapter was to have the reader understand why the magnetic field of the ReComm system had a large effect on the plasma density without the presence of the electric field. In order to do this, an analytic expression for how plasma reacts to a uniform B-field was developed. Then, the expression was modified for a spatially varying magnetic field, as was present in this work.

In order to gain further understanding of the magnetic field effects on the electrons, the physics modeling package COMSOL was used to create a model of the ReComm system magnetic and electric fields. The particle tracing feature was used to launch electrons at various initial velocities and locations into the fields. Although the magnetic field alone affected the electrons differently than the combination of the electric and magnetic fields, the end result was the same. The region where the density was measured in this dissertation (a volume near and over the iron core of the magnet) was devoid of electrons. Only in the extreme case when the electrons were launched very near to the iron core of the magnet was the expected behavior observed.

CHAPTER 9

Conclusions

The goal of this research was to develop a method for ameliorating the communications blackout phenomenon that occurs during atmospheric re-entry. In the process, a helicon source was developed and characterized at the Plasmadynamics and Electric Propulsion Laboratory at the University of Michigan. Helicon source characterization occurred with a commercially-purchased RF-compensated Langmuir probe from the Hiden Corporation, as well as a retarding potential analyzer and a custom-built Langmuir probe. An electromagnet with two electrodes was used as the system to mitigate the plasma density. This system was called the ***Re***-entry and hypersonic vehicle plasma ***comm***unication (ReComm) system. Density reduction was measured with the Hiden Langmuir probe, plasma frequency was measured with a custom-built hairpin resonance probe and signal attenuation measurements were performed with a network analyzer and a S2-1 probe. The design of the electromagnet resulted in some surprising results that were discussed and explained.

This chapter summarizes the major conclusions and contributions of this dissertation. Then, a system impact study is presented to demonstrate how this idea of crossed electric and magnetic fields could be implemented into a flight model. The system impact study also goes into details about some of the major challenges that would be encountered in producing a flight model. Finally, suggestions for future work are presented.

9.1 Helicon Source Development

A helicon source was identified as the type of plasma source to be used for simulating the plasma number density that occurs during atmospheric re-entry. A variety of plasma sources were examined and researched, and the helicon source proved to have the required combination of plasma properties and ease of construction. During the process of developing the helicon source, two versions were built before a final version succeeded. The final helicon source consisted of three electromagnets evenly spaced around a half-double-helix antenna. The antenna was wrapped around a 15-cm-diameter quartz tube that was attached to the vacuum chamber. Argon gas flowed through a nozzle on one end of the tube such that a constant chamber pressure of 0.6 $\pm$ 0.05 mtorr was maintained. The electromagnets created a uniform magnetic field inside of the antenna. The antenna was connected via a pi-style matching network to a 13.56-MHz RF, 2.5-kW power supply. In order to reduce RF radiation around PEPL, a Faraday cage was built to enclose the entire source. RF noise on the PEPL grounding lines was reduced by isolating all power lines on equipment attached to the CTF from the facility via RF chokes or filters.

9.2 ReComm System Development

The goal of this research was to use an $E \times B$ field to create a "window" that would allow the passage of electromagnetic waves through a plasma sheath. In order to test this, the ReComm system was developed and built. The system consisted of a solenoid electromagnet with an iron base and core to boost the magnetic field strength. In addition, two stainless steel electrodes created an electric field perpendicular to the magnetic field. The original idea required that the magnetic field be uniform and only in the z-direction, but due to the nature of the solenoid, the field was not spatially uniform. In addition, the magnetic field diverged from the z-direction into both the x and y-directions.

9.3 Helicon Source Plasma Properties

Once the helicon source was developed, it required characterization. First, the plasma source was confirmed to be operating in helicon mode based on ion number density profiles as functions of input power, magnetic field strength and radial (x) position. The maximum ion number density inside the helicon source was found to be about 2.5×10^{19} m^{-3}. Next, the plasma downstream of the helicon source was probed with a Langmuir probe and the ion number density, electron temperature and plasma potential were found as functions of the probe position. These measurements were made for two conditions: (1) an empty vacuum chamber and (2) the ReComm system present in the vacuum chamber. A summary of the results is shown in Table 9.1.

The plasma source was also characterized by measuring the ion energy distribution function at various locations downstream of the helicon source. This gave the most probable ion voltage as a function of axial (y) position. These results are also summarized in Table 9.1. Since the entire vacuum chamber was at the plasma potential, and the retarding potential analyzer was grounded to the chamber, the

Langmuir Probe	Empty Chamber	ReComm Present
Ion Number Density (m^{-3})	1.7 - 3.3$\times 10^{17}$	0.55 - 1.27$\times 10^{17}$
Electron Temperature (eV)	1.4 - 6.2	1.2 - 4.8
Plasma Potential (V)	25 - 65	26 - 56
Retarding Potential Analyzer		
Most Probable Ion Voltage (V)	40 - 45	—
Plasma Potential (V)	40 - 50	—

Table 9.1: Helicon source characterization summary

most probable ion voltage did not require correction by the plasma potential. The results show that the ions had essentially no directed energy and relied solely on the drift velocity to move downstream. Finally, it was determined that the commonly observed current-free electron double layer was not present in the PEPL source for the operating conditions used in this dissertation.

9.4 ReComm System Effect

Table 9.2 summarizes the results from the experiments conducted with the ReComm system operating downstream of the helicon source. The ReComm system caused a decrease in the plasma density and a similar decrease in the plasma frequency. The area where the ReComm system had the most impact was near the cathode, above the iron core of the magnet (Figure 9.1).

The data obtained from the experiments were compared with those obtained from computer simulations of the ReComm system. Overall, the simulations agreed with the trends seen during ReComm system operation, but they differed with respect to the magnitudes. In addition, the large density reduction seen with only the ReComm

Maximum % Density Reduction - Langmuir Probe - z = -70 mm			
	Peak B_z		
V_c	925 G	1385 G	1850 G
0 V	40%	50%	60%
-100 V	45%	50%	60%
-250 V	—	—	50%
	z = -75 mm		
0 V	35%	60%	70%
-100 V	50%	65%	80%
-250 V	—	—	80%

Maximum % Plasma Frequency Reduction - z = -75 mm, B_z = 2000 G		
	Probe Type	
V_c	Hairpin Resonance Probe	S2-1 Probe
0 V	60%	63%
-250 V	78%	75%

Signal Attenuation at 1 GHz - S2-1 Probe		
	Peak B_z	
V_c	0 G	2000 G
0 V	-9 dB	-1 dB
-250 V	—	-1 dB

Table 9.2: ReComm system results summary.

system magnetic field operating was not demonstrated in the computer simulations. Thus, further investigation was required.

The ReComm system electric and magnetic fields were modeled with the COMSOL physics package. Using the electrostatics and magnetostatics solvers, traces of electron trajectories as functions of the magnetic field only and of the magnetic field coupled with the electric field were created. The tracing was performed for various initial electron positions and velocities. It was shown that the divergent magnetic field produced by the ReComm system magnet trapped and diverted the electrons

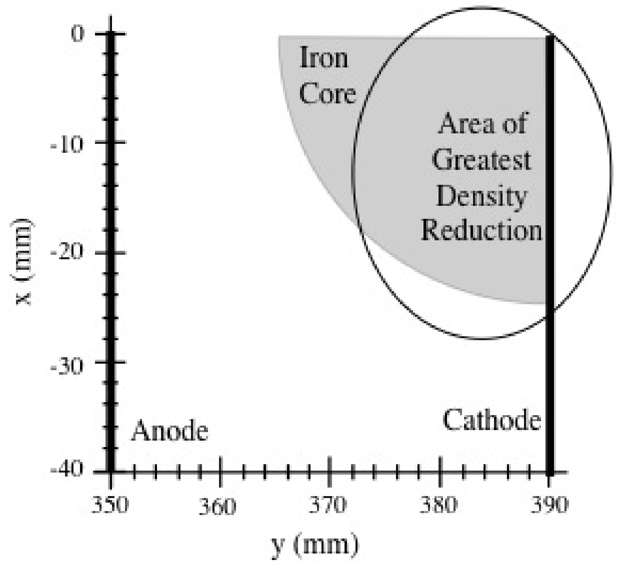

Figure 9.1: Diagram showing region of greatest ReComm system effect.

before they encountered the electric field. The addition of the electric field more efficiently directed the electrons, but the final result was still a lack of electrons over the iron core of the magnet where an antenna would be located.

9.5 System Impact

The ReComm system has been proven to reduce the plasma number density. However, with its current design, the system would be too inefficient and too heavy to use for flight. This section discusses what would be required to make a system such as this plausible as a flight model. A variety of changes would need to be addressed, including making the system less massive, removing the water cooling requirement and addressing any aerodynamic issues.

The ReComm system, as it was configured for this dissertation took up a large volume and was quite heavy at about 50 kg, not including the mass of the required power supplies. This is not acceptable for a spacecraft where every gram and square centimeter are accounted for, especially considering the cost of launching one kilogram into orbit is approximately \$11,000. In addition, putting that type of mass on only one side of the re-entry vehicle could likely cause the capsule to tumble during re-entry. Therefore, an equal amount of mass would be required on the opposite side of the capsule, or the aerodynamic forces would need to be compensated in some other way in order to offset the mass imbalance leading to more complication in the system. One possible method for lowering the mass of the ReComm system is using thinner wire to create the magnet. This would require a greater number of turns as the resistance of the wire would be greater, but since the wire would be much thinner than the 1/8-in copper tubing used for the current ReComm system setup, it would be acceptable. Another method for creating a smaller, less massive magnet is using an array of permanent magnets. Using permanent magnets would negate the need for a power supply for the electromagnet, further reducing the mass of the system. This idea would require further study in order to determine if a magnetic field that is constantly present would cause other issues with the spacecraft. In addition, the magnets would have to be studied to ensure that they did not lose their magnetism due to the high thermal loads that occur during hypersonic velocities.

The fact that the current ReComm system setup uses water to cool the magnet is something that would not be suitable on an actual flight system. The required water chiller, pump and storage tank would add additional mass to the system. As previously mentioned, keeping the system as light and small as possible should be one of the goals for a flight system. In addition, water cooling the magnet adds additional complication to the re-entry vehicle, which is unacceptable when one of the main reasons for returning to a capsule-style re-entry vehicle is to minimize how complicated the system becomes. Once again, the use of permanent magnets would eliminate the water cooling requirement. Furthermore, a simple redesign of the ReComm system magnet with thinner wire and more turns would lower the current required to produce a sufficiently strong magnetic field, thus reducing the magnet heating.

Aerodynamics are very important to a re-entry vehicle. If there is anything protruding into the flow, it could be ripped off or melted by the extreme frictional forces and heating that occur during hypersonic flow. This would most likely cause the vehicle to begin tumbling, resulting in catastrophic failure of the craft. For this reason, any system added to the external surface of a re-entry or hypersonic vehicle must maintain as low a profile as possible. One solution for this was demonstrated with the ReComm system: the electromagnet was beneath the "spacecraft surface" that was represented by the mica sheet. This is a promising idea, but one would need to ensure that the strong magnetic field under the heat shield did not in any way interfere with the protection the shield is supposed to provide.

9.6 Suggestions for Future Work

The work presented in this dissertation establishes a solid foundation from which future research into using an $E \times B$ field to ameliorate communications blackout can move forward. The following is a summary of work that will expand on the research presented here and lead towards a more flight ready ReComm system.

1. **Different Plasma Source:** Initially, a helicon source was chosen to produce the plasma that simulated the properties found during atmospheric re-entry. The reasoning behind this decision, as presented earlier, was that the scope of this research was to understand how an $E \times B$ field affected the plasma

number density. Since the number density produced by a helicon source is similar to that found during atmospheric re-entry, the helicon source was deemed appropriate. However, further research should be done using a plasma source that more closely matches the flow conditions that are present during atmospheric re-entry, such as a microwave discharge. One such property is the thin sheath of a re-entry plasma. Since the helicon source created a thick, uniform plume downstream that filled the vacuum chamber, the sheath thickness was accounted for by placing the attenuation antennas the same distance apart as the sheath thickness. However, the proximity of the antennas to one another allowed for the propagation of evanescent waves. If the plasma sheath itself were thin, then the antennas could be placed far enough apart so that the extraneous waves would not fully propagate between them. Another big difference between the helicon plasma source and the plasma sheath that exists during atmospheric re-entry is the neutral pressure. The neutral pressure during helicon source operation was only 0.6 mtorr, but during atmospheric re-entry the ambient pressure is at least 75 mtorr. Pressure increases as air moves through a shock, so the pressure in the region where the plasma sheath is present would be significantly higher. This increased neutral pressure would result in more collisions, and thus a decrease in the effectiveness of the magnetic field to contain electrons.

2. **Different Surface Material** Originally mica was used as the "spacecraft surface" material because it is a dielectric ceramic. This is the type of material that usually surrounds an antenna on a re-entry vehicle surface. However, the majority of the re-entry vehicle usually consists of metals and graphite. Future work should include investigations into how the surrounding material affects

the operation of the ReComm system.

3. **Different Gas Species** Testing should be done to determine whether the presence of a reacting species in the plume makes any big differences in the operation of the ReComm system. During an actual atmospheric re-entry, the air dissociates and the oxygen and nitrogen react with each other and other species present. In addition, the species present in the atmosphere have different masses than argon, resulting in a different response to the magnetic field of the ReComm system.

4. **Redesign of ReComm Magnetic Circuit:** The ReComm system magnetic field was not uniform, and it diverged away from the iron core of the magnet. For this reason, the system did not behave as expected. Although significant density reduction was observed with the magnetic field as it was, the circuit should be redesigned so that a constant, uniform magnetic field exists in the region downstream of the plasma source. The reason for this is that understanding exactly how the $E \times B$ field affects the plasma when the fields are orthogonal is important. Some possible methods for redesigning the magnetic circuit include using an array of permanent magnets or a number of solenoids so that the magnetic field is less divergent. Another method for creating a more uniform magnetic field is demonstrated in Hall thrusters and uses magnetic materials to shape the field.

5. **Increased Operating Pressure:** This was touched on above, but increasing the operating pressure of the system will allow for a better simulation of an atmospheric re-entry plasma. A higher pressure surrounding the ReComm system will allow for a stronger electric field to be maintained by the electrodes.

The operating pressure as it was during this dissertation placed the system at the bottom of the Paschen curve. The pressure could have been decreased, but then the neutral pressure would be even lower than what is observed during atmospheric re-entry. The pressure could not be increased because the cryopump would saturate and no longer remove gas from the system, causing the pressure in the vacuum chamber to increase to levels that the helicon source could not sustain. Using a different pump on the system, such as a turbopump, would solve the operating pressure issue. Helicon sources have been shown to operate with pressures up to 5 mtorr, but at higher pressures, helicon mode would no longer be attainable (50; 111).

APPENDICES

APPENDIX A

Langmuir Probe Analysis Flow Chart

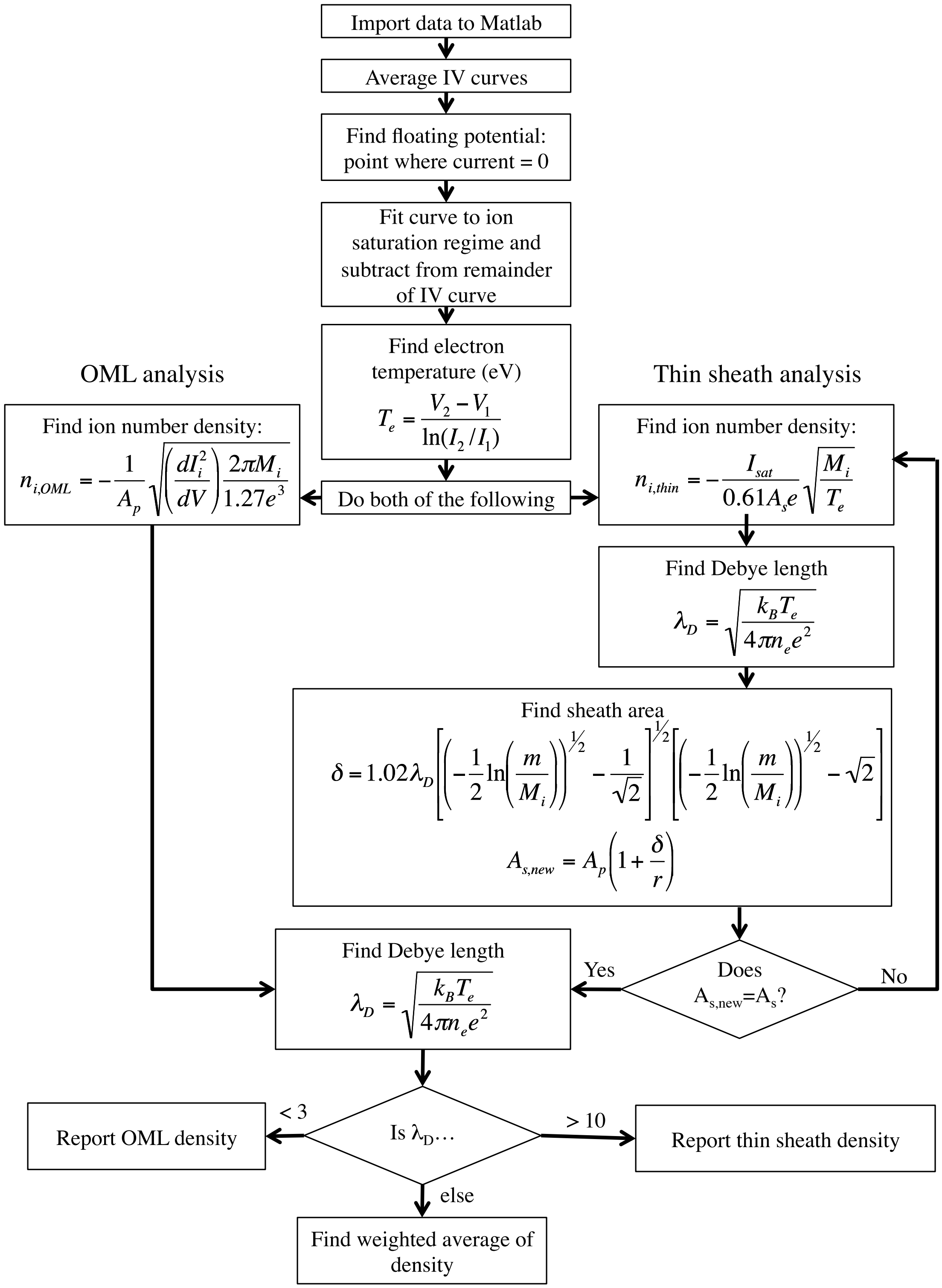
Import data to Matlab
Average IV curves
Find floating potential: point where current = 0
Fit curve to ion saturation regime and subtract from remainder of IV curve
Find electron temperature (eV)
$T_e = \frac{V_2 - V_1}{\ln(I_2/I_1)}$
OML analysis
Thin sheath analysis
Find ion number density:
$n_{i,OML} = -\frac{1}{A_p}\sqrt{\left(\frac{dI_i^2}{dV}\right)\frac{2\pi M_i}{1.27e^3}}$
Do both of the following
Find ion number density:
$n_{i,thin} = -\frac{I_{sat}}{0.61 A_s e}\sqrt{\frac{M_i}{T_e}}$
Find Debye length
$\lambda_D = \sqrt{\frac{k_B T_e}{4\pi n_e e^2}}$
Find sheath area
$\delta = 1.02\lambda_D\left[\left(-\frac{1}{2}\ln\left(\frac{m}{M_i}\right)\right)^{1/2} - \frac{1}{\sqrt{2}}\right]^{1/2}\left[\left(-\frac{1}{2}\ln\left(\frac{m}{M_i}\right)\right)^{1/2} - \sqrt{2}\right]$
$A_{s,new} = A_p\left(1 + \frac{\delta}{r}\right)$
Does $A_{s,new} = A_s$?
Yes
No
Find Debye length
$\lambda_D = \sqrt{\frac{k_B T_e}{4\pi n_e e^2}}$
Is λ_D…
< 3
> 10
else
Report OML density
Report thin sheath density
Find weighted average of density

Figure A.1

APPENDIX B

Residual Gas Analyzer (RGA)

A Residual Gas Analyzer (RGA) was used to determine the composition of the gas downstream of the helicon source. This was done to make sure that there were no unexpected species present in the plume of the helicon plasma while operating with argon. In addition, the helicon source was operated with pure nitrogen and with air.

B.1 RGA Setup

The RGA was a Kurt J. Lesker AccuQuad model SRS RGA-200 and was mounted to a flange on the CTF directly downstream of the helicon source. It was located more than a meter downstream of the source exit and along the same axial centerline ($x = 0$ mm and $z = 0$ mm). To maintain an RGA inlet pressure below the 10^{-4} torr upper limit, an auxiliary turbopump with an attached backing pump was placed on a tee at the RGA entrance. Figure B.1a shows a schematic drawing of the RGA setup and Figure B.1b is a photo of the RGA.

In order to ensure that the turbopump had negligible effect on the gas sample entering the RGA, the conductance of the RGA-to-turbopump path, C_2, needed to

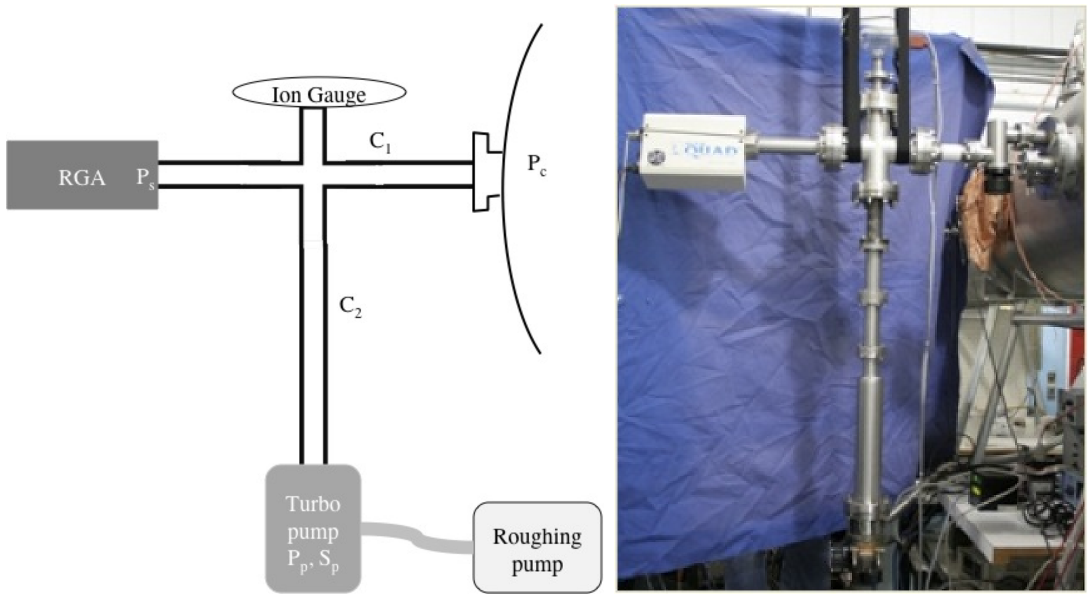

(a) (b)

Figure B.1: Residual gas analyzer setup. (a) is a schematic drawing and (b) is a photograph.

be kept well below the turbopump speed, S_p, such that the pressure of the gas sample was only a function of the pipe conductances (C_1 and C_2) and the chamber pressure (P_c).

$$P_s = \frac{P_c}{1+\left(\frac{C_2}{C_1}\right)\cancelto{C_2<<S_p}{\left(\frac{S_p}{S_p+C_2}\right)}} \tag{B.1}$$

After the gas entered the RGA, it was ionized and the particle mass per unit charge was measured with a channel electron multiplier (CEM).

B.2 RGA Results

The results are presented as molar concentration as a function of helicon source input power for air, nitrogen and argon gas inputs. Without exception, the species concentrations were independent of the input power while the plasma source was operating in helicon mode. Figure B.2 shows the results of RGA testing. As ex-

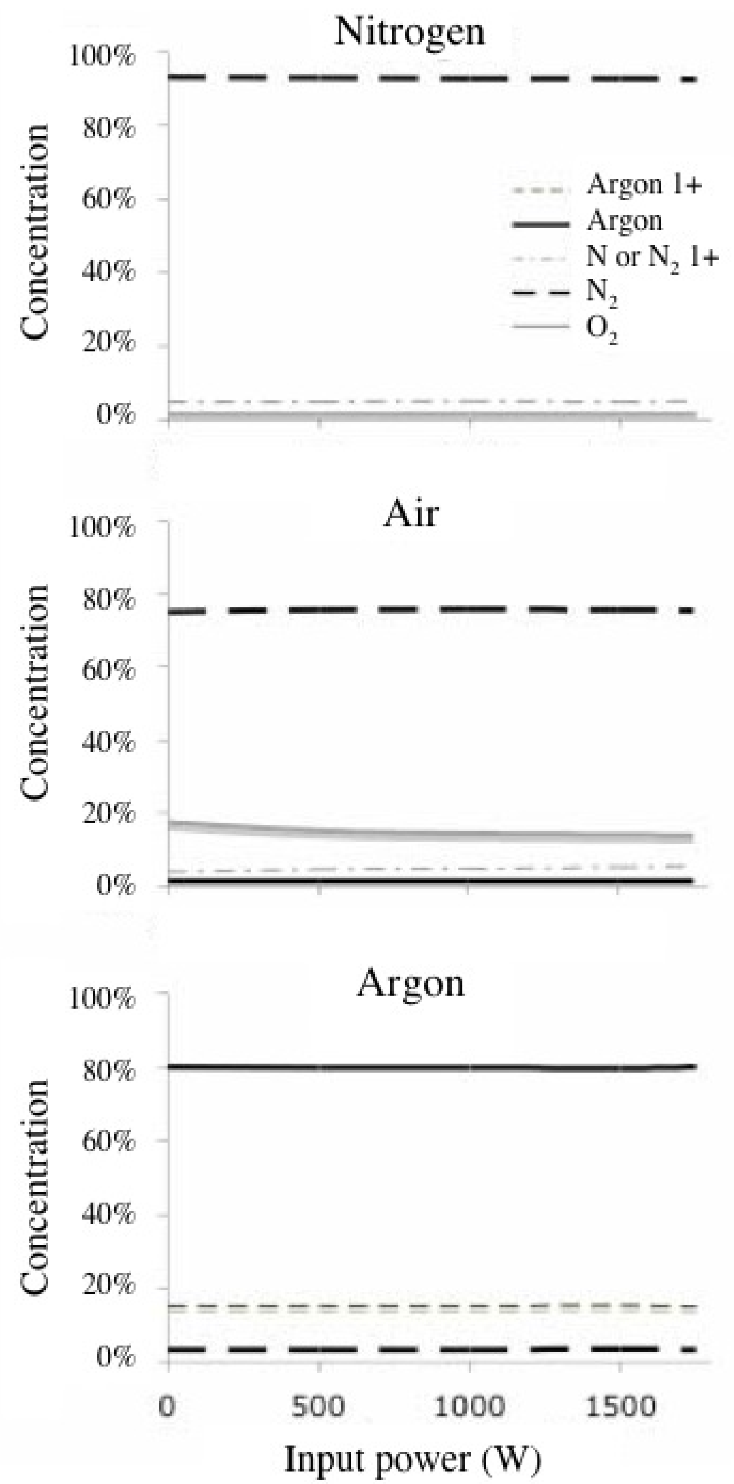

Figure B.2: Species molar concentrations as a function of helicon source input power.

pected, when the nitrogen gas was flowing, there was N_2 and molecular nitrogen (or ionized N_2) present. When the helicon source was operating with air, the dominant gas was again N_2 with significant amounts of O_2. With argon flowing, argon was most prevalent, but ionized argon was also present in significant amounts. This was somewhat surprising so far downstream of the plasma source.

APPENDIX C

Testing Matrices for All Data Points

Table C.1: Testing Matrix for Verifying Helicon Mode

Filename	LP position (mm) Vert	LP position (mm) Axial	LP position (mm) Rad	Power (watts) input	Power (watts) reflected	Matching Network Loading	Matching Network Tuning	Magnets Cur (A)	Magnets Vol (V)	Pressure (mtorr)	notes
P1 0M0	0	-150	0	100	5	137	184	0	0	7	10 mA -60 to 60V
P2 5M0	0	-150	0	250	5	137	184.5	0	0	7	
P4 0M0	0	-150	0	400	5	137	184.5	0	0	7	100 mA arcing to the probe
P5 0M0	0	-150	0	500	5	137	184.5	0	0	7	
P7 5M0	0	-150	0	750	5	137	184.5	0	0	7	
P1 00M0	0	-150	0	1000	5	137	184.5	0	0	7	cryotemp moniter is reading
P1 25M0	0	-150	0	1250	5	140	184.5	0	0	7	incorrectly unplugging it
P1 0M2	0	-150	0	100	5	153	184.5	20.6	1.5	7	10 mA
P2 5M2	0	-150	0	250	5	163	188	20.6	1.5	7	100 mA
P4 0M2	0	-150	0	400	5	163	188	20.6	1.5	7	
P5 0M2	0	-150	0	525	5	165	188	20.6	1.5	7	
P7 5M2	0	-150	0	750	5	165	188	20.6	1.5	7	
P1 00M2	0	-150	0	1000	5	168	190	19.8	1.4	7	
P1 25M2	0	-150	0	1250	5	168	190	20.5	1.5	7	
P1 0M4	0	-150	0	100	5	164.5	1855	40.1	2.9	7	10 mA
P2 5M4	0	-150	0	250	5	164.5	188	40.1	2.9	7	
P4 0M4	0	-150	0	400	5	164.5	188	40	2.9	7	100 mA
P5 0M4	0	-150	0	500	5	164.5	188	40	2.9	7	
P7 5M4	0	-150	0	750	5	170	189	39.6	2.9	7	
P1 00M4	0	-150	0	1000	5	170	189	39.4	29	7	
P1 25M4	0	-150	0	1250	5	170	188	40	2.9	7	
P1 0M6	0	-150	0	100	5	158	184	60.2	4.5	7	10 mA
P2 0M6	0	-150	0	200	5	158	184	60.2	4.5	7	
P3 0M6	0	-150	0	300	5	159	187	60	4.5	7	
P4 0M6	0	-150	0	400	5	168	187.5	60	4.5	7	100 mA
P5 0M6	0	-150	0	500	5	168	184.5	59.7	4.5	7	
P6 0M6	0	-150	0	600	5	168	184.5	59.5	4.5	7	
P7 0M6	0	-150	0	700	5	168	184.5	59.4	4.5	7	
P8 0M6	0	-150	0	800	5	168	184.5	60	4.5	7	
P1 1M6	0	-150	0	1150	5	171	189	60	4.5	7	finicky, would only sit
											at 1150 in that area
											probe saturates out
P2 Rm6	0	-100	-60	250	5	172	189.5	60.1	4.5	7	10 mA
P2 Rm5	0	-100	-50	250	5	172	189.5	60.1	4.5	7	
P2 Rm4	0	-100	-40	250	5	172	189.5	60.1	4.5	7	
P2 Rm3	0	-100	-30	250	5	172	189.5	60.1	4.5	7	
P2 Rm2	0	-100	-20	250	5	172	189.5	60.1	4.5	7	
P2 Rm1	0	-100	-10	250	5	172	189.5	60.1	4.5	7	
P2 R0	0	-100	0	250	5	172	189.5	60	4.5	7	
P2 R1	0	-100	10	250	5	172	189.5	60	4.5	7	
P2 R2	0	-100	20	250	5	172	189.5	60	4.5	7	
P2 R3	0	-100	30	250	5	172	189.5	60	4.5	7	
P2 R4	0	-100	40	250	5	172	189.5	60	4.5	7	
P2 R5	0	-100	50	250	5	172	189.5	60	4.5	7	
P2 R6	0	-100	-60	500	5	172	189.5	60	4.5	7	
P5 Rm6	0	-100	60	250	10	184	190.5	60	4.6	7	100 mA
P5 Rm5	0	-100	-50	500	10	184	190.5	60	4.6	7	
P5 Rm4	0	-100	-40	500	10	184	190.5	60	4.5	7	
P5 Rm3	0	-100	-30	500	10	184	190.5	60	4.5	7	
P5 Rm2	0	-100	-20	500	10	184	190.5	60	4.5	7	
P5 Rm1	0	-100	-10	500	5	184	190.5	60	4.5	7	
P5 R0	0	-100	0	500	5	184	190.5	60	4.5	7	
P5 R1	0	-100	10	500	5	184	190.5	60	4.5	7	
P5 R2	0	-100	20	500	5	184	190.5	60	4.5	7	
P5 R3	0	-100	30	500	10	184	190.5	60	4.5	7	
P5 R4	0	-100	40	500	10	184	190.5	60	4.5	7	
P5 R5	0	-100	50	500	10	184	190.5	60	4.5	7	
P5 R6	0	-100	60	500	10	184	190.5	60	4.5	7	
P7 Rm6	0	-100	-60	750	25	179	192	58.8	4.5	7	100 mA
P7 Rm5	0	-100	-50	750	25	179	192	58.8	4.5	7	
P7 Rm4	0	-100	-40	750	25	179	192	58.8	4.5	7	
P7 Rm3	0	-100	-30	750	25	179	192	58.8	4.5	7	

Filename	LP position (mm) Vert	LP position (mm) Axial	LP position (mm) Rad	Power (watts) input	Power (watts) reflected	Matching Network Loading	Matching Network Tuning	Magnets Cur (A)	Magnets Vol (V)	Pressure (mtorr)	notes
P7 Rm2	0	-100	-20	750	10	179	192	60	4.6	7	
P7 Rm1	0	-100	-10	750	10	179	192	60	4.6	7	
P7 R0	0	-100	0	750	5	179	192	60	4.6	7	
P7 R1	0	-100	10	750	5	179	192	60	4.6	7	
P7 R2	0	-100	20	750	5	179	192	60	4.6	7	
P7 R3	0	-100	30	750	5	179	192	60	4.6	7	
P7 R4	0	-100	40	750	5	179	192	60	4.6	7	
P7 R5	0	-100	50	750	5	179	192	60	4.6	7	
P7 R6	0	-100	60	750	5	179	192	60	4.6	7	
P1 0Rm6	0	-100	6	1000	30	180	192	57.6	4.4	7	100 mA
P1 0Rm5	0	-100	50	1000	30	180	192	57.1	4.4	7	
P1 0Rm4	0	-100	40	1000	30	180	192	57.1	4.4	7	
P1 0Rm3	0	-100	30	1000	10	180	192	60	4.6	7	
P1 0Rm2	0	-100	20	1000	10	180	192	60	4.6	7	
P1 0Rm1	0	-100	10	1000	10	180	192	60	4.6	7	
P1 0R0	0	-100	0	1000	10	180	192	60.1	4.6	7	
P1 0R1	0	-100	-10	1000	10	180	192	60.1	4.6	7	
P1 0R2	0	-100	-20	1000	10	180	192	60.1	4.6	7	
P1 0R3	0	-100	-30	1000	10	180	192	60.1	4.6	7	
P1 0R4	0	-100	-40	1000	10	180	192	60.1	4.6	7	
P1 0R5	0	-100	-50	1000	10	180	192	60.1	4.6	7	
P1 0R6	0	-100	-60	1000	10	180	192	60.1	4.6	7	
P1 Rm6	0	-100	-60	100	5	175	185.5	60.1	4.6	7	10 mA
P1 Rm5	0	-100	-50	100	5	175	185.5	60.1	4.6	7	
P1 Rm4	0	-100	-40	100	5	175	185.5	60.1	4.6	7	
P1 Rm3	0	-100	-30	100	5	175	185.5	60.1	4.6	7	
P1 Rm2	0	-100	-20	100	5	175	185.5	60.1	4.6	7	
P1 Rm1	0	-100	-10	100	5	175	185.5	60.1	4.6	7	
P1 R0	0	-100	0	100	10	175	185.5	60.1	4.6	7	
P1 R1	0	-100	10	100	10	175	185.5	60.1	4.6	7	
P1 R2	0	-100	20	100	10	175	185.5	60.1	4.6	7	
P1 R3	0	-100	30	100	10	175	185.5	60.1	4.6	7	
P1 R4	0	-100	40	100	10	175	185.5	60.1	4.6	7	
P1 R5	0	-100	50	100	10	175	185.5	60.1	4.6	7	
P1 R6	0	-100	60	100	10	175	185.5	60.1	4.6	7	

Table C.2: Testing Matrix for Plasma Characterization: No ReComm System Present Downstream

Filename	Langmuir Probe Position (mm)			Power (W)		Matching Network		Magnet		Pressure	notes
	Vert	Axial	rad	input	reflected	loading	tuning	cur(A)	Vol (V)	(mtorr)	
RAAAVA	0	180	-50	1500	85	197.5	192.5	60.0	4.6	0.7	1 mA
RBAAVA	0	180	-40	1500	75	197.5	192.5	60.0	4.6	0.7	
RCAAVA	0	180	-30	1500	75	197.5	192.5	60.0	4.6	0.7	
RDAAVA	0	180	-20	1500	75	197.5	192.5	60.0	4.6	0.7	
REAAVA	0	180	-10	1500	75	197.5	192.5	60.0	4.6	0.7	
RFAAVA	0	180	0	1500	75	197.5	192.5	60.0	4.6	0.7	
RGAAVA	0	180	10	1500	75	197.5	192.5	60.0	4.6	0.7	
RHAAVA	0	180	20	1500	75	197.5	192.5	60.0	4.6	0.7	
RIAAVA	0	180	30	1500	75	197.5	192.5	60.0	4.6	0.7	
RJAAVA	0	180	40	1500	75	197.5	192.5	60.0	4.6	0.7	
RKAAVA	0	180	50	1500	75	197.5	192.5	60.1	4.6	0.7	break
RAABVA	0	200	-50	1500	85	196.5	192.5	60.0	4.6	0.7	
RBABVA	0	200	-40	1500	85	196.5	192.5	60.0	4.6	0.7	
RCABVA	0	200	-30	1500	85	196.5	192.5	60.0	4.6	0.7	
RDABVA	0	200	-20	1500	90	196.5	192.5	60.0	4.6	0.7	
REABVA	0	200	-10	1500	90	196.5	192.5	60.0	4.6	0.7	
RFABVA	0	200	0	1500	90	196.5	192.5	60.0	4.6	0.7	
RGABVA	0	200	10	1500	90	196.5	192.5	60.0	4.6	0.7	
RHABVA	0	200	20	1500	90	196.5	192.5	60.0	4.6	0.7	
RIABVA	0	200	30	1500	100	196.5	192.5	60.0	4.6	0.7	
RJABVA	0	200	40	1500	100	196.5	192.5	60.0	4.6	0.7	
RKABVA	0	200	50	1500	110	196.5	192.5	60.0	4.6	0.7	
RAACVA	0	220	-50	1500	85	196.5	192.5	60.1	4.7	0.7	
RBACVA	0	220	-40	1500	85	196.5	192.5	60.1	4.7	0.7	
RCACVA	0	220	-30	1500	85	196.5	192.5	60.1	4.7	0.7	
RDACVA	0	220	-20	1500	85	196.5	192.5	60.1	4.7	0.7	
REACVA	0	220	-10	1500	85	196.5	192.5	60.1	4.7	0.7	
RFACVA	0	220	0	1500	85	196.5	192.5	60.1	4.7	0.7	
RGACVA	0	220	10	1500	85	196.5	192.5	60.1	4.7	0.7	
RHACVA	0	220	20	1500	85	196.5	192.5	60.1	4.8	0.7	
RIACVA	0	220	30	1500	85	196.5	192.5	60.1	4.8	0.7	
RJACVA	0	220	40	1500	85	196.5	192.5	60.1	4.8	0.7	
RKACVA	0	220	50	1500	85	196.5	192.5	60.1	4.8	0.7	break
RAADVA	0	240	-50	1500	80	198.5	193.5	60.0	4.8	0.7	
RBADVA	0	240	-40	1500	80	198.5	193.5	60.0	4.8	0.7	
RCADVA	0	240	-30	1500	80	198.5	193.5	60.0	4.8	0.7	
RDADVA	0	240	-20	1500	80	198.5	193.5	60.0	4.8	0.7	
READVA	0	240	-10	1500	80	198.5	193.5	60.0	4.8	0.7	
RFADVA	0	240	0	1500	75	198.5	193.5	60.0	4.8	0.7	
RGADVA	0	240	10	1500	75	198.5	193.5	60.0	4.8	0.7	
RHADVA	0	240	20	1500	80	198.5	193.5	60.0	4.8	0.7	
RIADVA	0	240	30	1500	80	198.5	193.5	60.0	4.8	0.7	
RJADVA.	0	240	40	1500	80	198.5	193.5	60.0	4.8	0.7	
RKADVA	0	240	50	1500	80	198.5	193.5	60.0	4.8	0.7	
RAAEVA	0	260	-50	1500	80	198.5	193.5	60.1	4.8	0.7	
RBAEVA	0	260	-40	1500	80	198.5	193.5	60.1	4.8	0.7	
RCAEVA	0	260	-30	1500	75	198.5	193.5	60.1	4.8	0.7	
RDAEVA	0	260	-20	1500	75	198.5	193.5	60.1	4.8	0.7	
REAEVA	0	260	-10	1500	75	198.5	193.5	60.1	4.8	0.7	
RFAEVA	0	260	0	1500	75	198.5	193.5	60.1	4.8	0.7	
RGAEVA	0	260	10	1500	75	198.5	193.5	60.1	4.8	0.7	
RHAEVA	0	260	20	1500	75	198.5	193.5	60.1	4.8	0.7	
RIAEVA	0	260	30	1500	75	198.5	193.5	60.1	4.8	0.7	
RJAEVA	0	260	40	1500	75	198.5	193.5	60.1	4.8	0.7	
RKAEVA	0	260	50	1500	75	198.5	193.5	60.1	4.8	0.7	break
RAAFVA	0	280	-50	1500	90	198.5	192.5	60.1	4.9	0.7	
RBAFVA	0	280	-40	1500	90	198.5	192.5	60.1	4.9	0.7	
RCAFVA	0	280	-30	1500	90	198.5	192.5	60.1	4.9	0.7	
RDAFVA	0	280	-20	1500	90	198.5	192.5	60.1	4.9	0.7	
REAFVA	0	280	-10	1500	90	198.5	192.5	60.1	4.9	0.7	
RFAFVA	0	280	0	1500	90	198.5	192.5	60.1	4.9	0.7	
RGAFVA	0	280	10	1500	90	198.5	192.5	60.1	4.9	0.7	
RHAFVA	0	280	20	1500	90	198.5	192.5	60.1	4.8	0.7	
RIAFVA	0	280	30	1500	90	198.5	192.5	60.1	4.8	0.7	
RJAFVA	0	280	40	1500	90	198.5	192.5	60.1	4.8	0.7	
RKAFVA	0	280	50	1500	90	198.5	192.5	60.1	4.8	0.7	
RAAGVA	0	300	-50	1500	90	198.5	192.5	60.1	4.9	0.7	
RBAGVA	0	300	-40	1500	90	198.5	192.5	60.1	4.9	0.7	
RCAGVA	0	300	-30	1500	90	198.5	192.5	60.1	4.9	0.7	
RDAGVA	0	300	-20	1500	90	198.5	192.5	60.1	4.9	0.7	
REAGVA	0	300	-10	1500	90	198.5	192.5	60.1	4.9	0.7	
RFAGVA	0	300	0	1500	90	198.5	192.5	60.1	4.9	0.7	
RGAGVA	0	300	10	1500	85	198.5	192.5	60.1	4.9	0.7	
RHAGVA	0	300	20	1500	85	198.5	192.5	60.1	4.9	0.7	
RIAGVA	0	300	30	1500	85	198.5	192.5	60.1	4.9	0.7	
RJAGVA	0	300	40	1500	85	198.5	192.5	60.1	4.9	0.7	
RKAGVA	0	300	50	1500	85	198.5	192.5	60.1	4.9	0.7	break
RAAHVA	0	320	-50	1500	95	198.5	194	60.1	4.9	0.7	
RBAHVA	0	320	-40	1500	95	198.5	194	60.1	4.9	0.7	
RCAHVA	0	320	-30	1500	95	198.5	194	60.1	4.9	0.7	
RDAHVA	0	320	-20	1500	95	198.5	194	60.1	4.9	0.7	
REAHVA	0	320	-10	1500	95	198.5	194	60.1	4.8	0.7	
RFAHVA	0	320	0	1500	95	198.5	194	60.1	4.8	0.7	
RGAHVA	0	320	10	1500	95	198.5	194	60.1	4.8	0.7	
RHAHVA	0	320	20	1500	95	198.5	194	60.1	4.8	0.7	
RIAHVA	0	320	30	1500	95	198.5	194	60.1	4.8	0.7	
RJAHVA	0	320	40	1500	95	198.5	194	60.1	4.8	0.7	
RKAHVA	0	320	50	1500	95	198.5	194	60.0	4.8	0.7	
RAAIVA	0	340	-50	1500	95	198.5	194	60.1	4.9	0.7	
RBAIVA	0	340	-40	1500	95	198.5	194	60.1	4.9	0.7	
RCAIVA	0	340	-30	1500	95	198.5	194	60.1	4.9	0.7	
RDAIVA	0	340	-20	1500	90	198.5	194	60.1	4.9	0.7	
REAIVA	0	340	-10	1500	90	198.5	194	60.1	4.9	0.7	
RFAIVA	0	340	0	1500	90	198.5	194	60.1	4.9	0.7	
RGAIVA	0	340	10	1500	90	198.5	194	60.1	4.9	0.7	
RHAIVA	0	340	20	1500	90	198.5	194	60.1	4.9	0.7	
RIAIVA	0	340	30	1500	90	198.5	194	60.1	4.9	0.7	
RJAIVA	0	340	40	1500	90	198.5	194	60.1	4.9	0.7	
RKAIVA	0	340	50	1500	90	198.5	194	60.1	4.9	0.7	big break
RAAAVB	-10	180	-50	1500	100	198.5	193.5	60.1	4.9	0.7	
RBAAVB	-10	180	-40	1500	100	198.5	193.5	60.1	4.9	0.7	
RCAAVB	-10	180	-30	1500	100	198.5	193.5	60.1	4.9	0.7	
RKABVB	-10	200	50	1500	100	198.5	193.5	60.1	4.9	0.7	
RAACVB	-10	220	-50	1500	100	198.5	193.5	60.1	4.9	0.7	
RBACVB	-10	220	-40	1500	100	198.5	193.5	60.1	4.9	0.7	
RCACVB	-10	220	-30	1500	100	198.5	193.5	60.1	4.9	0.7	
RDACVB	-10	220	-20	1500	100	198.5	193.5	60.1	4.9	0.7	
REACVB	-10	220	-10	1500	100	198.5	193.5	60.1	4.9	0.7	
RFACVB	-10	220	0	1500	100	198.5	193.5	60.1	4.9	0.7	
RGACVB	-10	220	10	1500	100	198.5	193.5	60.1	4.9	0.7	
RHACVB	-10	220	20	1500	100	198.5	193.5	60.1	4.9	0.7	
RIACVB	-10	220	30	1500	100	198.5	193.5	60.1	4.9	0.7	
RJACVB	-10	220	40	1500	100	198.5	193.5	60.1	4.9	0.7	
RKACVB	-10	220	50	1500	100	198.5	193.5	60.1	4.9	0.7	break
RAADVB	-10	240	-50	1500	100	198.5	193.5	60.0	4.9	0.7	
RBADVB	-10	240	-40	1500	100	198.5	193.5	60.0	4.9	0.7	
RCADVB	-10	240	-30	1500	100	198.5	193.5	60.0	4.9	0.7	
RDADVB	-10	240	-20	1500	100	198.5	193.5	60.0	4.9	0.7	
READVB	-10	240	-10	1500	100	198.5	193.5	60.0	4.9	0.7	
RFADVB	-10	240	0	1500	100	198.5	193.5	60.0	4.9	0.7	
RGADVB	-10	240	10	1500	100	198.5	193.5	60.0	4.9	0.7	arcing
RHADVB	-10	240	20	1550	160	198.5	193.5	53.2	4.3	0.7	and sparking

Filename	Langmuir Probe Position (mm)			Power (W)		Matching Network		Magnet		Pressure	notes
	Vert	Axial	rad	input	reflected	loading	tuning	cur(A)	Vd (V)	(mtorr)	
RIADVB	-10	240	30	1550	160	198.5	193.5	53.2	4.3	0.7	between
RJADVB	-10	240	40	1550	160	198.5	193.5	53.2	4.3	0.7	the power
RKADVB	-10	240	50	1550	160	198.5	193.5	53.2	4.3	0.7	supply chasse
RAAEVB	-10	260	-50	1500	110	198.5	193.5	60.0	4.9	0.7	and faraday
RBAEVB	-10	260	-40	1500	110	198.5	193.5	60.0	4.9	0.7	cage
RCAEVB	-10	260	-30	1500	110	198.5	193.5	60.0	4.9	0.7	
RDAEVB	-10	260	-20	1500	110	198.5	193.5	60.0	4.9	0.7	
REAEVB	-10	260	-10	1500	110	198.5	193.5	60.0	4.9	0.7	
RFAEVB	-10	260	0	1500	110	198.5	193.5	60.0	4.9	0.7	
RGAEVB	-10	260	10	1500	110	198.5	193.5	60.0	4.9	0.7	
RHAEVB	-10	260	20	1500	110	198.5	193.5	60.0	4.9	0.7	
RIAEVB	-10	260	30	1500	110	198.5	193.5	60.0	4.9	0.7	
RJAEVB	-10	260	40	1500	110	198.5	193.5	60.0	4.9	0.7	
RKAEVB	-10	260	50	1500	110	198.5	193.5	60.0	4.9	0.7	
RAAFVB	-10	280	-50	1500	110	198.5	193.5	60.0	4.9	0.7	
RBAFVB	-10	280	-40	1500	110	198.5	193.5	60.0	4.9	0.7	
RCAFVB	-10	280	-30	1500	110	198.5	193.5	60.0	4.9	0.7	
RDAFVB	-10	280	-20	1500	110	198.5	193.5	60.0	4.9	0.7	
REAFVB	-10	280	-10	1500	110	198.5	193.5	60.0	4.9	0.7	
RFAFVB	-10	280	0	1500	110	198.5	193.5	60.0	4.9	0.7	
RGAFVB	-10	280	10	1500	110	198.5	193.5	60.0	4.9	0.7	
RHAFVB	-10	280	20	1500	110	198.5	193.5	60.0	4.9	0.7	
RIAFVB	-10	280	30	1500	110	198.5	193.5	60.0	4.9	0.7	
RJAFVB	-10	280	40	1500	110	198.5	193.5	60.0	4.9	0.7	
RKAFVB	-10	280	50	1500	110	198.5	193.5	60.0	4.9	0.7	
RAAGVB	-10	300	-50	1500	120	198.5	193.5	60.0	4.9	0.7	
RBAGVB	-10	300	-40	1500	120	198.5	193.5	60.0	4.9	0.7	
RCAGVB	-10	300	-30	1500	120	198.5	193.5	60.0	4.9	0.7	
RDAGVB	-10	300	-20	1500	120	198.5	193.5	60.0	4.9	0.7	
REAGVB	-10	300	-10	1500	120	198.5	193.5	60.0	4.9	0.7	
RFAGVB	-10	300	0	1500	120	198.5	193.5	60.0	4.9	0.7	
RGAGVB	-10	300	10	1500	110	198.5	193.5	60.0	4.9	0.7	
RHAGVB	-10	300	20	1500	110	198.5	193.5	60.0	4.9	0.7	
RIAGVB	-10	300	30	1500	110	198.5	193.5	60.0	4.9	0.7	
RJAGVB	-10	300	40	1500	110	198.5	193.5	60.0	4.9	0.7	
RKAGVB	-10	300	50	1500	110	198.5	193.5	60.0	4.9	0.7	
RAAHVB	-10	320	-50	1500	110	198.5	193.5	60.0	4.9	0.7	
RBAHVB	-10	320	-40	1500	110	198.5	193.5	60.0	4.9	0.7	
RCAHVB	-10	320	-30	1500	110	198.5	193.5	60.0	4.9	0.7	
RDAHVB	-10	320	-20	1500	110	198.5	193.5	60.0	4.9	0.7	
REAHVB	-10	320	-10	1500	110	198.5	193.5	60.0	4.9	0.7	
RFAHVB	-10	320	0	1500	110	198.5	193.5	60.0	4.9	0.7	
RGAHVB	-10	320	10	1500	110	198.5	193.5	60.0	4.9	0.7	helicon does
RHAHVB	-10	320	20	1500	110	198.5	193.5	60.0	4.9	0.7	not like
RIAHVB	-10	320	30	1500	110	198.5	193.5	60.0	4.9	0.7	this point
RJAHVB	-10	320	40	1500	110	198.5	193.5	60.0	4.9	0.7	very sparky
RKAHVB	-10	320	50	1500	110	198.5	193.5	60.0	4.9	0.7	
RAAIVB	-10	340	-50	1500	110	198.5	193.5	60.0	5	0.7	
RBAIVB	-10	340	-40	1500	110	198.5	193.5	60.0	5	0.7	
RCAIVB	-10	340	-30	1500	110	198.5	193.5	60.0	5	0.7	
RDAIVB	-10	340	-20	1500	110	198.5	193.5	60.0	5	0.7	
REAIVB	-10	340	-10	1500	110	198.5	193.5	60.0	5	0.7	
RFAIVB	-10	340	0	1500	110	198.5	193.5	60.0	5	0.7	
RGAIVB	-10	340	10	1500	110	198.5	193.5	60.0	5	0.7	
RHAIVB	-10	340	20	1500	110	198.5	193.5	60.0	5	0.7	
RIAIVB	-10	340	30	1500	110	198.5	193.5	60.0	5	0.7	
RJAIVB	-10	340	40	1500	110	198.5	193.5	60.0	5	0.7	
RKAIVB	-10	340	50	1500	110	198.5	193.5	60.0	5	0.7	
RAAAVC	-20	180	-50	1500	110	195.5	193.5	60.2	4.6	0.7	4/13/08
RBAAVC	-20	180	-40	1500	110	195.5	193.5	60.2	4.6	0.7	
RCAAVC	-20	180	-30	1500	110	195.5	193.5	60.1	4.6	0.7	

Filename	Langmuir Probe Position (mm)			Power (W)		Matching Network		Magnet		Pressure	notes
	Vert	Axial	rad	input	reflected	loading	tuning	cur(A)	Vd (V)	(mtorr)	
RDAAVC	-20	180	-20	1500	110	195.5	193.5	60.1	4.6	0.7	
REAAVC	-20	180	-10	1500	110	195.5	193.5	60.1	4.6	0.7	
RFAAVC	-20	180	0	1500	110	195.5	193.5	60.1	4.6	0.7	
RGAAVC	-20	180	10	1500	110	195.5	193.5	60.1	4.6	0.7	
RHAAVC	-20	180	20	1500	110	195.5	193.5	60.1	4.6	0.7	
RIAAVC	-20	180	30	1500	110	195.5	193.5	60.1	4.6	0.7	
RJAAVC	-20	180	40	1500	110	195.5	193.5	60.1	4.6	0.7	
RKAAVC	-20	180	50	1500	110	195.5	193.5	60.1	4.6	0.7	
RAABVC	-20	200	-50	1500	110	195.5	193.5	60.1	4.6	0.7	
RBABVC	-20	200	-40	1500	110	195.5	193.5	60.1	4.6	0.7	
RCABVC	-20	200	-30	1500	110	195.5	193.5	60.1	4.6	0.7	
RDABVC	-20	200	-20	1500	110	195.5	193.5	60.1	4.6	0.7	
REABVC	-20	200	-10	1500	110	195.5	193.5	60.1	4.6	0.7	
RFABVC	-20	200	0	1500	110	195.5	193.5	60.1	4.6	0.7	
RGABVC	-20	200	10	1500	110	195.5	193.5	60.1	4.6	0.7	
RHABVC	-20	200	20	1500	110	195.5	193.5	60.1	4.6	0.7	
RIABVC	-20	200	30	1500	110	195.5	193.5	60.1	4.6	0.7	
RJABVC	-20	200	40	1500	110	195.5	193.5	60.1	4.6	0.7	
RKABVC	-20	200	50	1500	110	195.5	193.5	60.1	4.6	0.7	
RAACVC	-20	220	-50	1500	100	195.5	193.5	60.1	4.6	0.7	
RBACVC	-20	220	-40	1500	100	195.5	193.5	60.1	4.6	0.7	
RCACVC	-20	220	-30	1500	100	195.5	193.5	60.1	4.6	0.7	
RDACVC	-20	220	-20	1500	100	195.5	193.5	60.1	4.6	0.7	
REACVC	-20	220	-10	1500	100	195.5	193.5	60.1	4.6	0.7	
RFACVC	-20	220	0	1500	100	195.5	193.5	60.1	4.6	0.7	
RGACVC	-20	220	10	1500	100	195.5	193.5	60.1	4.6	0.7	
RHACVC	-20	220	20	1500	100	195.5	193.5	60.1	4.6	0.7	
RIACVC	-20	220	30	1500	100	195.5	193.5	60.1	4.6	0.7	
RJACVC	-20	220	40	1500	100	195.5	193.5	60.1	4.6	0.7	
RKACVC	-20	220	50	1500	100	195.5	193.5	60.1	4.6	0.7	break
RAADVC	-20	240	-50	1500	110	197	193	60.1	4.8	0.7	
RBADVC	-20	240	-40	1500	110	197	193	60.1	4.8	0.7	
RCADVC	-20	240	-30	1500	110	197	193	60.1	4.8	0.7	
RDADVC	-20	240	-20	1500	110	197	193	60.1	4.8	0.7	
READVC	-20	240	-10	1500	110	197	193	60.1	4.8	0.7	
RFADVC	-20	240	0	1500	110	197	193	60.1	4.8	0.7	
RGADVC	-20	240	10	1500	110	197	193	60.1	4.8	0.7	
RHADVC	-20	240	20	1500	110	197	193	60.1	4.8	0.7	
RIADVC	-20	240	30	1500	110	197	193	60.1	4.8	0.7	
RJADVC	-20	240	40	1500	110	197	193	60.1	4.8	0.7	
RKADVC	-20	240	50	1500	110	197	193	60.1	4.8	0.7	
RAAEVC	-20	260	-50	1500	110	197	193	60.1	4.8	0.7	
RBAEVC	-20	260	-40	1500	110	197	193	60.1	4.8	0.7	
RCAEVC	-20	260	-30	1500	110	197	193	60.1	4.8	0.7	
RDAEVC	-20	260	-20	1500	110	197	193	60.1	4.8	0.7	
REAEVC	-20	260	-10	1500	110	197	193	60.1	4.8	0.7	
RFAEVC	-20	260	0	1500	100	197	193	60.1	4.8	0.7	
RGAEVC	-20	260	10	1500	100	197	193	60.1	4.8	0.7	
RHAEVC	-20	260	20	1500	100	197	193	60.1	4.8	0.7	
RIAEVC	-20	260	30	1500	100	197	193	60.1	4.8	0.7	
RJAEVC	-20	260	40	1500	100	197	193	60.1	4.8	0.7	
RKAEVC	-20	260	50	1500	110	197	193	60.1	4.8	0.7	
RAAFVC	-20	280	-50	1500	100	197	193	60.1	4.8	0.7	
RBAFVC	-20	280	-40	1500	100	197	193	60.1	4.8	0.7	
RCAFVC	-20	280	-30	1500	100	197	193	60.1	4.8	0.7	
RDAFVC	-20	280	-20	1500	100	197	193	60.1	4.8	0.7	
REAFVC	-20	280	-10	1500	100	197	193	60.1	4.8	0.7	
RFAFVC	-20	280	0	1500	110	197	193	60.1	4.8	0.7	
RGAFVC	-20	280	10	1500	110	197	193	60.1	4.8	0.7	
RHAFVC	-20	280	20	1500	100	197	193	60.1	4.8	0.7	
RIAFVC	-20	280	30	1500	100	197	193	60.1	4.8	0.7	

Filename	Langmuir Probe Position (mm)			Power (W)		Matching Network		Magnet		Pressure	notes
	Vert	Axial	rad	input	reflected	loading	tuning	cur(A)	Vol (V)	(mtorr)	
RJAFVC	-20	280	40	1500	110	197	193	60.1	4.8	0.7	
RKAFVC	-20	280	50	1500	110	197	193	60.1	4.8	0.7	break
RAAGVC	-20	300	-50	1500	120	198.5	193.5	60.1	4.8	0.7	
RBAGVC	-20	300	-40	1500	120	198.5	193.5	60.1	4.8	0.7	
RCAGVC	-20	300	-30	1500	120	198.5	193.5	60.1	4.8	0.7	
RDAGVC	-20	300	-20	1500	120	198.5	193.5	60.1	4.8	0.7	
REAGVC	-20	300	-10	1500	120	198.5	193.5	60.1	4.8	0.7	
RFAGVC	-20	300	0	1500	120	198.5	193.5	60.1	4.8	0.7	
RGAGVC	-20	300	10	1500	120	198.5	193.5	60.1	4.8	0.7	
RHAGVC	-20	300	20	1500	120	198.5	193.5	60.1	4.8	0.7	
RIAGVC	-20	300	30	1500	110	198.5	193.5	60.1	4.8	0.7	
RJAGVC	-20	300	40	1500	110	198.5	193.5	60.1	4.8	0.7	
RKAGVC	-20	300	50	1500	110	198.5	193.5	60.1	4.8	0.7	
RAAHVC	-20	320	-50	1500	110	198.5	193.5	60.1	4.9	0.7	skip
RBAHVC	-20	320	-40	1500	110	198.5	193.5	60.1	4.9	0.7	
RCAHVC	-20	320	-30	1500	110	198.5	193.5	60.1	4.9	0.7	
RDAHVC	-20	320	-20	1500	110	198.5	193.5	60.1	4.9	0.7	
REAHVC	-20	320	-10	1500	110	198.5	193.5	60.1	4.9	0.7	
RFAHVC	-20	320	0	1500	110	198.5	193.5	60.1	4.9	0.7	
RGAHVC	-20	320	10	1500	110	198.5	193.5	60.1	4.9	0.7	
RHAHVC	-20	320	20	1500	110	198.5	193.5	60.1	4.9	0.7	
RIAHVC	-20	320	30	1500	110	198.5	193.5	60.1	4.9	0.7	
RJAHVC	-20	320	40	1500	110	198.5	193.5	60.1	4.9	0.7	
RKAHVC	-20	320	50	1500	110	198.5	193.5	60.1	4.9	0.7	
RAAIVC	-20	340	-50	1500	110	198.5	193.5	60.1	5	0.7	
RBAIVC	-20	340	-40	1500	110	198.5	193.5	60.1	5	0.7	
RCAIVC	-20	340	-30	1500	110	198.5	193.5	60.1	5	0.7	
RDAIVC	-20	340	-20	1500	110	198.5	193.5	60.1	5	0.7	
REAIVC	-20	340	-10	1500	110	198.5	193.5	60.1	5	0.7	
RFAIVC	-20	340	0	1500	110	198.5	193.5	60.1	5	0.7	
RGAIVC	-20	340	10	1500	110	198.5	193.5	60.1	5	0.7	
RHAIVC	-20	340	20	1500	110	198.5	193.5	60.1	5	0.7	
RIAIVC	-20	340	30	1500	110	198.5	193.5	60.1	5	0.7	
RJAIVC	-20	340	40	1500	110	198.5	193.5	60.1	5	0.7	
RKAIVC	-20	340	50	1500	110	198.5	193.5	60.1	5	0.7	big break
RAAAVD	-30	180	-50	1500	120	197.5	193.5	60.2	4.7	0.7	
RBAAVD	-30	180	-40	1500	120	197.5	193.5	60.2	4.7	0.7	
RCAAVD	-30	180	-30	1500	120	197.5	193.5	60.2	4.7	0.7	
RDAAVD	-30	180	-20	1500	120	197.5	193.5	60.2	4.7	0.7	
REAAVD	-30	180	-10	1500	120	197.5	193.5	60.2	4.7	0.7	
RFAAVD	-30	180	0	1500	120	197.5	193.5	60.2	4.7	0.7	
RGAAVD	-30	180	10	1500	120	197.5	193.5	60.2	4.7	0.7	
RHAAVD	-30	180	20	1500	120	197.5	193.5	60.2	4.7	0.7	
RIAAVD	-30	180	30	1500	120	197.5	193.5	60.2	4.7	0.7	
RJAAVD	-30	180	40	1500	120	197.5	193.5	60.1	4.8	0.7	
RKAAVD	-30	180	50	1500	120	197.5	193.5	60.1	4.8	0.7	
RAABVD	-30	200	-50	1500	110	197.5	193.5	60.1	4.8	0.7	
RBABVD	-30	200	-40	1500	110	197.5	193.5	60.1	4.8	0.7	
RCABVD	-30	200	-30	1500	110	197.5	193.5	60.1	4.8	0.7	
RDABVD	-30	200	-20	1500	110	197.5	193.5	60.1	4.8	0.7	
REABVD	-30	200	-10	1500	110	197.5	193.5	60.1	4.8	0.7	
RFABVD	-30	200	0	1500	110	197.5	193.5	60.1	4.8	0.7	
RGABVD	-30	200	10	1500	120	197.5	193.5	60.1	4.8	0.7	
RHABVD	-30	200	20	1500	120	197.5	193.5	60.1	4.8	0.7	
RIABVD	-30	200	30	1500	120	197.5	193.5	60.1	4.8	0.7	
RJABVD	-30	200	40	1500	120	197.5	193.5	60.1	4.8	0.7	
RKABVD	-30	200	50	1500	120	197.5	193.5	60.1	4.8	0.7	
RAACVD	-30	220	-50	1500	110	197.5	193.5	60.1	4.9	0.7	
RBACVD	-30	220	-40	1500	110	197.5	193.5	60.1	4.9	0.7	
RCACVD	-30	220	-30	1500	110	197.5	193.5	60.1	4.9	0.7	
RDACVD	-30	220	-20	1500	110	197.5	193.5	60.1	4.9	0.7	

Filename	Langmuir Probe Position (mm)			Power (W)		Matching Network		Magnet		Pressure	notes
	Vert	Axial	rad	input	reflected	loading	tuning	cur(A)	Vol (V)	(mtorr)	
REACVD	-30	220	-10	1500	110	197.5	193.5	60.1	4.9	0.7	
RFACVD	-30	220	0	1500	110	197.5	193.5	60.1	4.9	0.7	
RGACVD	-30	220	10	1500	110	197.5	193.5	60.1	4.9	0.7	
RHACVD	-30	220	20	1500	110	197.5	193.5	60.1	4.9	0.7	
RIACVD	-30	220	30	1500	110	197.5	193.5	60.1	4.9	0.7	
RJACVD	-30	220	40	1500	110	197.5	193.5	60.1	4.9	0.7	
RKACVD	-30	220	50	1500	110	197.5	193.5	60.1	4.9	0.7	
RAADVD	-30	240	-50	1500	110	197.5	193.5	60.1	5	0.7	
RBADVD	-30	240	-40	1500	110	197.5	193.5	60.1	5	0.7	
RCADVD	-30	240	-30	1500	110	197.5	193.5	60.1	5	0.7	
RDADVD	-30	240	-20	1500	110	197.5	193.5	60.1	5	0.7	
READVD	-30	240	-10	1500	110	197.5	193.5	60.1	5	0.7	
RFADVD	-30	240	0	1500	110	197.5	193.5	60.1	5	0.7	
RGADVD	-30	240	10	1500	110	197.5	193.5	60.1	5	0.7	
RHADVD	-30	240	20	1500	110	197.5	193.5	60.1	5	0.7	
RIADVD	-30	240	30	1500	110	197.5	193.5	60.1	5	0.7	
RJADVD	-30	240	40	1500	110	197.5	193.5	60.1	5	0.7	
RKADVD	-30	240	50	1500	110	197.5	193.5	60.1	5	0.7	break
RAAEVD	-30	260	-50	1500	120	198.5	193.5	60.1	4.9	0.7	
RBAEVD	-30	260	-40	1500	120	198.5	193.5	60.1	4.9	0.7	
RCAEVD	-30	260	-30	1500	120	198.5	193.5	60.1	4.9	0.7	
RDAEVD	-30	260	-20	1500	120	198.5	193.5	60.1	4.9	0.7	
REAEVD	-30	260	-10	1500	110	198.5	193.5	60.1	4.9	0.7	
RFAEVD	-30	260	0	1500	110	198.5	193.5	60.1	4.9	0.7	
RGAEVD	-30	260	10	1500	110	198.5	193.5	60.1	4.9	0.7	
RHAEVD	-30	260	20	1500	110	198.5	193.5	60.1	4.9	0.7	
RIAEVD	-30	260	30	1500	120	198.5	193.5	60.1	4.9	0.7	
RJAEVD	-30	260	40	1500	120	198.5	193.5	60.1	4.9	0.7	
RKAEVD	-30	260	50	1500	120	198.5	193.5	60.1	4.9	0.7	
RAAFVD	-30	280	-50	1500	120	198.5	193.5	60.1	5.2	0.7	
RBAFVD	-30	280	-40	1500	120	198.5	193.5	60.1	5.2	0.7	
RCAFVD	-30	280	-30	1500	110	198.5	193.5	60.1	5	0.7	
RDAFVD	-30	280	-20	1500	110	198.5	193.5	60.1	5	0.7	
REAFVD	-30	280	-10	1500	110	198.5	193.5	60.1	5	0.7	
RFAFVD	-30	280	0	1500	110	198.5	193.5	60.1	5	0.7	
RGAFVD	-30	280	10	1500	110	198.5	193.5	60.1	5	0.7	
RHAFVD	-30	280	20	1500	110	198.5	193.5	60.1	5	0.7	
RIAFVD	-30	280	30	1500	110	198.5	193.5	60.1	5	0.7	
RJAFVD	-30	280	40	1500	110	198.5	193.5	60.1	5	0.7	
RKAFVD	-30	280	50	1500	120	198.5	193.5	60.1	4.9	0.7	
RAAGVD	-30	300	-50	1500	110	198.5	193.5	60.1	5.2	0.7	
RBAGVD	-30	300	-40	1500	110	198.5	193.5	60.1	5.2	0.7	
RCAGVD	-30	300	-30	1500	110	198.5	193.5	60.1	5.2	0.7	
RDAGVD	-30	300	-20	1500	110	198.5	193.5	60.1	5.2	0.7	
REAGVD	-30	300	-10	1500	110	198.5	193.5	60.1	5.2	0.7	
RFAGVD	-30	300	0	1500	110	198.5	193.5	60.1	5.2	0.7	
RGAGVD	-30	300	10	1500	110	198.5	193.5	60.1	5.2	0.7	
RHAGVD	-30	300	20	1500	110	198.5	193.5	60.1	5.2	0.7	
RIAGVD	-30	300	30	1500	110	198.5	193.5	60.1	5.2	0.7	
RJAGVD	-30	300	40	1500	110	198.5	193.5	60.1	5.2	0.7	
RKAGVD	-30	300	50	1500	110	198.5	193.5	60.1	5.2	0.7	
RAAHVD	-30	320	-50	1500	110	198.5	193.5	60.1	5.3	0.7	
RBAHVD	-30	320	-40	1500	110	198.5	193.5	60.1	5.3	0.7	
RCAHVD	-30	320	-30	1500	110	198.5	193.5	60.1	5.3	0.7	
RDAHVD	-30	320	-20	1500	110	198.5	193.5	60.1	5.2	0.7	
REAHVD	-30	320	-10	1500	110	198.5	193.5	60.1	5.2	0.7	
RFAHVD	-30	320	0	1500	110	198.5	193.5	60.1	5.2	0.7	
RGAHVD	-30	320	10	1500	110	198.5	193.5	60.1	5.2	0.7	
RHAHVD	-30	320	20	1500	110	198.5	193.5	60.1	5.2	0.7	
RIAHVD	-30	320	30	1500	110	198.5	193.5	60.1	5.2	0.7	
RJAHVD	-30	320	40	1500	110	198.5	193.5	60.1	5.2	0.7	

Filename	Langmuir Probe Position (mm)			Power (W)		Matching Network		Magnet		Pressure	notes
	Vert	Axial	rad	input	reflected	loading	tuning	cur (A)	Vol (V)	(mtorr)	
RKAHVD	-30	320	50	1500	110	198.5	193.5	60.1	5.2	0.7	break
RAAIVD	-30	340	-50	1500	120	198.5	193	60.1	4.9	0.7	
RBAIVD	-30	340	-40	1500	120	198.5	193	60.1	5	0.7	
RCAIVD	-30	340	-30	1500	120	198.5	193	60.1	5	0.7	
RDAIVD	-30	340	-20	1500	120	198.5	193	60.1	5	0.7	
REAIVD	-30	340	-10	1500	120	198.5	193	60.1	5	0.7	
RFAIVD	-30	340	0	1500	120	198.5	193	60.1	5	0.7	
RGAIVD	-30	340	10	1500	120	198.5	193	60.1	5	0.7	
RHAIVD	-30	340	20	1500	110	198.5	193	60.1	5	0.7	
RIAIVD	-30	340	30	1500	110	198.5	193	60.1	5	0.7	
RJAIVD	-30	340	40	1500	110	198.5	193	60.1	5	0.7	
RKAIVD	-30	340	50	1500	110	198.5	193	60.1	5	0.7	
RAAAVE	-40	180	-50	1500	120	198.5	193	60.1	5.3	0.7	
RBAAVE	-40	180	-40	1500	120	198.5	193	60.1	5.3	0.7	
RCAAVE	-40	180	-30	1500	120	198.5	193	60.1	5.3	0.7	
RDAAVE	-40	180	-20	1500	120	198.5	193	60.1	5.3	0.7	
REAAVE	-40	180	-10	1500	120	198.5	193	60.1	5.2	0.7	
RFAAVE	-40	180	0	1500	120	198.5	193	60.1	5.2	0.7	
RGAAVE	-40	180	10	1500	120	198.5	193	60.1	5.2	0.7	
RHAAVE	-40	180	20	1500	120	198.5	193	60.1	5.2	0.7	
RIAAVE	-40	180	30	1500	120	198.5	193	60.1	5.1	0.7	
RJAAVE	-40	180	40	1500	120	198.5	193	60.1	5.1	0.7	
RKAAVE	-40	180	50	1500	120	198.5	193	60.1	5.1	0.7	
RAABVE	-40	200	-50	1500	120	198.5	193	60.1	5.3	0.7	
RBABVE	-40	200	-40	1500	120	198.5	193	60.1	5.3	0.7	
RCABVE	-40	200	-30	1500	120	198.5	193	60.1	5.3	0.7	
RDABVE	-40	200	-20	1500	110	198.5	193	60.1	5.3	0.7	
REABVE	-40	200	-10	1500	110	198.5	193	60.1	5.3	0.7	
RFABVE	-40	200	0	1500	110	198.5	193	60.1	5.3	0.7	
RGABVE	-40	200	10	1500	110	198.5	193	60.1	5.3	0.7	
RHABVE	-40	200	20	1500	110	198.5	193	60.1	5.3	0.7	
RIABVE	-40	200	30	1500	110	198.5	193	60.1	5.3	0.7	
RJABVE	-40	200	40	1500	120	198.5	193	60.1	5.3	0.7	
RKABVE	-40	200	50	1500	120	198.5	193	60.1	5.3	0.7	
RAACVE	-40	220	-50	1500	110	198.5	193	60.1	5.3	0.7	
RBACVE	-40	220	-40	1500	110	198.5	193	60.1	5.3	0.7	
RCACVE	-40	220	-30	1500	110	198.5	193	60.1	5.3	0.7	
RDACVE	-40	220	-20	1500	110	198.5	193	60.1	5.3	0.7	
REACVE	-40	220	-1	1500	110	198.5	193	60.1	5.3	0.7	
RFACVE	-40	220	0	1500	110	198.5	193	60.1	5.3	0.7	
RGACVE	40	220	10	1500	110	198.5	193	60.1	5.3	0.7	
RHACVE	-40	220	20	1500	110	198.5	193	60.1	5.3	0.7	
RIACVE	-40	220	30	1500	110	198.5	193	60.1	5.3	0.7	
RJACVE	-40	220	40	1500	110	198.5	193	60.1	5.3	0.7	
RKACVE	-40	220	50	1500	110	198.5	193	60.1	5.3	0.7	break
RAADVE	-40	240	-50	1500	120	198.5	193	60.1	5	0.7	
RBADVE	-40	240	-40	1500	120	198.5	193	60.1	5	0.7	
RCADVE	-40	240	-30	1500	120	198.5	193	60.1	5	0.7	
RDADVE	-40	240	-20	1500	120	198.5	193	60.1	5.1	0.7	
READVE	-40	240	-10	1500	120	198.5	193	60.1	5.1	0.7	
RFADVE	-40	240	0	1500	120	198.5	193	60.1	5.1	0.7	
RGADVE	-40	240	10	1500	120	198.5	193	60.1	5.1	0.7	
RHADVE	-40	240	20	1500	120	198.5	193	60.1	5.2	0.7	
RIADVE	-40	240	30	1500	120	198.5	193	60.1	5.2	0.7	
RJADVE	-40	240	40	1500	120	198.5	193	60.1	5.2	0.7	
RKADVE	-40	240	50	1500	120	198.5	193	60.1	5.2	0.7	
RAAEVE	-40	260	-50	1500	120	198.5	193	60.1	5.2	0.7	
RBAEVE	-40	260	-40	1500	110	198.5	193	60.1	5.2	0.7	
RCAEVE	-40	260	-30	1500	110	198.5	193	60.1	5.2	0.7	
RDAEVE	-40	260	-20	1500	110	198.5	193	60.1	5.2	0.7	
REAEVE	-40	260	-10	1500	110	198.5	193	60.1	5.2	0.7	

Filename	Langmuir Probe Position (mm)			Power (W)		Matching Network		Magnet		Pressure	notes
	Vert	Axial	rad	input	reflected	loading	tuning	cur (A)	Vol (V)	(mtorr)	
RFAEVE	-40	260	0	1500	110	198.5	193	60.1	5.2	0.7	
RGAEVE	-40	260	10	1500	110	198.5	193	60.1	5.3	0.7	
RHAEVE	-40	260	20	1500	110	198.5	193	60.1	5.3	0.7	
RIAEVE	-40	260	30	1500	110	198.5	193	60.1	5.3	0.7	
RJAEVE	-40	260	40	1500	110	198.5	193	60.1	5.3	0.7	
RKAEVE	-40	260	50	1500	120	198.5	193	60.1	5.2	0.7	
RAAFVE	-40	280	-50	1500	110	198.5	193	60.1	5.3	0.7	
RBAFVE	-40	280	-40	1500	110	198.5	193	60.1	5.3	0.7	
RCAFVE	-40	280	-30	1500	110	198.5	193	60.1	5.3	0.7	
RDAFVE	-40	280	-20	1500	110	198.5	193	60.1	5.3	0.7	
REAFVE	-40	280	-10	1500	110	198.5	193	60.1	5.3	0.7	
RFAFVE	-40	280	0	1500	110	198.5	193	60.1	5.3	0.7	
RGAFVE	-40	280	10	1500	110	198.5	193	60.1	5.3	0.7	
RHAFVE	-40	280	20	1500	110	198.5	193	60.1	5.3	0.7	
RIAFVE	-40	280	30	1500	110	198.5	193	60.1	5.3	0.7	
RJAFVE	-40	280	40	1500	110	198.5	193	60.1	5.3	0.7	
RKAFVE	-40	280	50	1500	110	198.5	193	60.1	5.3	0.7	
RAAGVE	-40	300	-50	1500	110	198.5	193	60.1	5.4	0.7	
RBAGVE	-40	300	-40	1500	110	198.5	193	60.1	5.4	0.7	
RCAGVE	-40	300	-30	1500	110	198.5	193	60.1	5.4	0.7	
RDAGVE	-40	300	-20	1500	110	198.5	193	60.1	5.4	0.7	
REAGVE	-40	300	-10	1500	110	198.5	193	60.1	5.4	0.7	
RFAGVE	-40	300	0	1500	110	198.5	193	60.1	5.4	0.7	
RGAGVE	-40	300	10	1500	110	198.5	193	60.1	5.4	0.7	
RHAGVE	-40	300	20	1500	110	198.5	193	60.1	5.4	0.7	
RIAGVE	-40	300	30	1500	110	198.5	193	60.1	5.3	0.7	
RJAGVE	-40	300	40	1500	110	198.5	193	60.1	5.3	0.7	
RKAGVE	-40	300	50	1500	110	198.5	193	60.1	5.3	0.7	break
RAAHVE	-40	320	-50	1500	120	198.5	193.5	60.1	5.1	0.7	
RBAHVE	-40	320	-40	1500	120	198.5	193.5	60.1	5.1	0.7	
RCAHVE	-40	320	-30	1500	120	198.5	193.5	60.1	5.2	0.7	
RDAHVE	-40	320	-20	1500	120	198.5	193.5	60.1	5.2	0.7	
REAHVE	-40	320	-10	1500	120	198.5	193.5	60.1	5.2	0.7	
RFAHVE	-40	320	0	1500	110	198.5	193.5	60.1	5.2	0.7	
RGAHVE	-40	320	10	1500	110	198.5	193.5	60.1	5.2	0.7	
RHAHVE	-40	320	20	1500	110	198.5	193.5	60.1	5.3	0.7	
RIAHVE	-40	320	30	1500	110	198.5	193.5	60.1	5.3	0.7	
RJAHVE	-40	320	40	1500	110	198.5	193.5	60.1	5.3	0.7	
RKAHVE	-40	320	50	1500	110	198.5	193.5	60.1	5.3	0.7	
RAAIVE	-40	340	-50	1500	110	198.5	193.5	60.1	5.4	0.7	
RBAIVE	-40	340	-40	1500	110	198.5	193.5	60.1	5.4	0.7	
RCAIVE	-40	340	-30	1500	110	198.5	193.5	60.1	5.4	0.7	
RDAIVE	-40	340	-20	1500	110	198.5	193.5	60.1	5.4	0.7	
REAIVE	-40	340	-10	1500	110	198.5	193.5	60.1	5.4	0.7	
RFAIVE	-40	340	0	1500	110	198.5	193.5	60.1	5.4	0.7	
RGAIVE	-40	340	10	1500	110	198.5	193.5	60.1	5.4	0.7	
RHAIVE	-40	340	20	1500	110	198.5	193.5	60.1	5.4	0.7	
RIAIVE	-40	340	30	1500	110	198.5	193.5	60.1	5.3	0.7	
RJAIVE	-40	340	40	1500	110	198.5	193.5	60.1	5.3	0.7	
RKAIVE	-40	340	50	1500	110	198.5	193.5	60.1	5.3	0.7	break for day 4-14-08
RAAAVF	-50	180	-50	1500	110	198.5	193.5	60.2	5	0.7	
RBAAVF	-50	180	-40	1500	110	198.5	193.5	60.2	5.1	0.7	
RCAAVF	-50	180	-30	1500	110	198.5	193.5	60.2	5.1	0.7	
RDAAVF	-50	180	-20	1500	110	198.5	193.5	60.2	5.1	0.7	
REAAVF	-50	180	-10	1500	110	198.5	193.5	60.2	5.1	0.7	
RFAAVF	-50	180	0	1500	110	198.5	193.5	60.2	5.1	0.7	
RGAAVF	-50	180	10	1500	110	198.5	193.5	60.2	5.1	0.7	
RHAAVF	-50	180	20	1500	100	198.5	193.5	60.2	5.1	0.7	
RIAAVF	-50	180	30	1500	100	198.5	193.5	60.2	5.1	0.7	
RJAAVF	-50	180	40	1500	100	198.5	193.5	60.2	5.1	0.7	
RKAAVF	-50	180	50	1500	100	198.5	193.5	60.2	5.1	0.7	

Filename	Langmuir Probe Position (mm)			Power (W)		Matching Network		Magnet		Pressure	notes
	Vert	Axial	rad	input	reflected	loading	tuning	cur(A)	Vol (V)	(mtorr)	
RAABVF	-50	200	-50	1500	100	198.5	193.5	60.1	5	0.7	
RBABVF	-50	200	-40	1500	100	198.5	193.5	60.1	5	0.7	
RCABVF	-50	200	-30	1500	100	198.5	193.5	60.1	5	0.7	
RDABVF	-50	200	-20	1500	100	198.5	193.5	60.1	5	0.7	
REABVF	-50	200	-10	1500	100	198.5	193.5	60.1	5	0.7	
RFABVF	-50	200	0	1500	100	198.5	193.5	60.1	5	0.7	
RGABVF	-50	200	10	1500	100	198.5	193.5	60.2	5.1	0.7	
RHABVF	-50	200	20	1500	100	198.5	193.5	60.2	5.1	0.7	
RIABVF	-50	200	30	1500	100	198.5	193.5	60.2	5.1	0.7	
RJABVF	-50	200	40	1500	100	198.5	193.5	60.2	5.1	0.7	
RKABVF	-50	200	50	1500	100	198.5	193.5	60.2	5.1	0.7	
RAACVF	-50	220	-50	1500	100	198.5	193.5	60.1	5	0.7	
RBACVF	-50	220	-40	1500	100	198.5	193.5	60.1	5	0.7	
RCACVF	-50	220	-30	1500	100	198.5	193.5	60.1	5	0.7	
RDACVF	-50	220	-20	1500	100	198.5	193.5	60.1	5	0.7	
REACVF	-50	220	-10	1500	100	198.5	193.5	60.1	5.1	0.7	
RFACVF	-50	220	0	1500	100	198.5	193.5	60.1	5.1	0.7	
RGACVF	-50	220	10	1500	100	198.5	193.5	60.1	5.1	0.7	
RHACVF	-50	220	20	1500	90	198.5	193.5	60.1	5.2	0.7	
RIACVF	-50	220	30	1500	90	198.5	193.5	60.1	5.2	0.7	
RJACVF	-50	220	40	1500	90	198.5	193.5	60.1	5.2	0.7	
RKACVF	-50	220	50	1500	90	198.5	193.5	60.1	5.2	0.7	
RAADVF	-50	240	-50	1500	90	198.5	193.5	60.1	5.2	0.7	
RBADVF	-50	240	-40	1500	90	198.5	193.5	60.1	5.2	0.7	
RCADVF	-50	240	-30	1500	90	198.5	193.5	60.1	5.2	0.7	
RDADVF	-50	240	-20	1500	90	198.5	193.5	60.1	5.2	0.7	
READVF	-50	240	-10	1500	90	198.5	193.5	60.1	5.2	0.7	
RFADVF	-50	240	0	1500	90	198.5	193.5	60.1	5.2	0.7	
RGADVF	-50	240	10	1500	90	198.5	193.5	60.1	5.2	0.7	
RHADVF	-50	240	20	1500	90	198.5	193.5	60.1	5.2	0.7	
RIADVF	-50	240	30	1500	90	198.5	193.5	60.1	5.2	0.7	
RJADVF	-50	240	40	1500	90	198.5	193.5	60.1	5.2	0.7	
RKADVF	-50	240	50	1500	90	198.5	193.5	60.1	5.2	0.7	break
RAAEVF	-50	260	-50	1500	110	198.5	193.5	60.1	4.9	0.7	
RBAEVF	-50	260	-40	1500	100	198.5	193.5	60.1	4.9	0.7	
RCAEVF	-50	260	-30	1500	100	198.5	193.5	60.1	4.9	0.7	
RDAEVF	-50	260	-20	1500	100	198.5	193.5	60.1	4.9	0.7	
REAEVF	-50	260	-10	1500	100	198.5	193.5	60.2	5.1	0.7	
RFAEVF	-50	260	0	1500	100	198.5	193.5	60.2	5.1	0.7	
RGAEVF	-50	260	10	1500	100	198.5	193.5	60.1	5.1	0.7	
RHAEVF	-50	260	20	1500	100	198.5	193.5	60.1	5.1	0.7	
RIAEVF	-50	260	30	1500	100	198.5	193.5	60.1	5.1	0.7	
RJAEVF	-50	260	40	1500	100	198.5	193.5	60.1	5.2	0.7	
RKAEVF	-50	260	50	1500	100	198.5	193.5	60.1	5.2	0.7	
RAAFVF	-50	280	-50	1500	100	198.5	193.5	60.1	5.2	0.7	
RBAFVF	-50	280	-40	1500	100	198.5	193.5	60.1	5.2	0.7	
RCAFVF	-50	280	-30	1500	100	198.5	193.5	60.1	5.2	0.7	
RDAFVF	-50	280	-20	1500	100	198.5	193.5	60.1	5.2	0.7	
REAFVF	-50	280	-10	1500	100	198.5	193.5	60.1	5.2	0.7	
RFAFVF	-50	280	0	1500	100	198.5	193.5	60.1	5.2	0.7	
RGAFVF	-50	280	10	1500	100	198.5	193.5	60.1	5.2	0.7	
RHAFVF	-50	280	20	1500	100	198.5	193.5	60.1	5.2	0.7	
RIAFVF	-50	280	30	1500	100	198.5	193.5	60.1	5.2	0.7	
RJAFVF	-50	280	40	1500	100	198.5	193.5	60.1	5.2	0.7	
RKAFVF	-50	280	50	1500	100	198.5	193.5	60.1	5.2	0.7	
RAAGVF	-50	300	-50	1500	100	198.5	193.5	60.1	5.2	0.7	
RBAGVF	-50	300	-40	1500	100	198.5	193.5	60.1	5.2	0.7	
RCAGVF	-50	300	-30	1500	100	198.5	193.5	60.1	5.2	0.7	
RDAGVF	-50	300	-20	1500	100	198.5	193.5	60.1	5.2	0.7	
REAGVF	-50	300	-10	1500	100	198.5	193.5	60.1	5.2	0.7	
RFAGVF	-50	300	0	1500	100	198.5	193.5	60.1	5.2	0.7	

Filename	Langmuir Probe Position (mm)			Power (W)		Matching Network		Magnet		Pressure	notes
	Vert	Axial	rad	input	reflected	loading	tuning	cur(A)	Vol (V)	(mtorr)	
RGAGVF	-50	300	10	1500	100	198.5	193.5	60.1	5.2	0.7	
RHAGVF	-50	300	20	1500	100	198.5	193.5	60.1	5.2	0.7	
RIAGVF	-50	300	30	1500	100	198.5	193.5	60.1	5.2	0.7	
RJAGVF	-50	300	40	1500	100	198.5	193.5	60.1	5.2	0.7	
RKAGVF	-50	300	50	1500	100	198.5	193.5	60.1	5.2	0.7	
RAAHVF	-50	320	-50	1500	95	198.5	193.5	60.1	5.3	0.7	
RBAHVF	-50	320	-40	1500	95	198.5	193.5	60.1	5.3	0.7	
RCAHVF	-50	320	-30	1500	95	198.5	193.5	60.1	5.3	0.7	
RDAHVF	-50	320	-20	1500	95	198.5	193.5	60.1	5.3	0.7	
REAHVF	-50	320	-10	1500	95	198.5	193.5	60.1	5.3	0.7	
RFAHVF	-50	320	0	1500	95	198.5	193.5	60.1	5.2	0.7	
RGAHVF	-50	320	10	1500	95	198.5	193.5	60.1	5.2	0.7	
RHAHVF	-50	320	20	1500	95	198.5	193.5	60.1	5.2	0.7	
RIAHVF	-50	320	30	1500	95	198.5	193.5	60.1	5.2	0.7	
RJAHVF	-50	320	40	1500	95	198.5	193.5	60.1	5.2	0.7	
RKAHVF	-50	320	50	1500	95	198.5	193.5	60.1	5.2	0.7	break
RAAIVF	-50	340	-50	1500	110	198.5	193.5	60.0	4.9	0.7	
RBAIVF	-50	340	-40	1500	110	198.5	193.5	60.1	4.9	0.7	
RCAIVF	-50	340	-30	1500	110	198.5	193.5	60.1	4.9	0.7	
RDAIVF	-50	340	-20	1500	110	198.5	193.5	60.1	4.9	0.7	
REAIVF	-50	340	-10	1500	110	198.5	193.5	60.1	5	0.7	
RFAIVF	-50	340	0	1500	110	198.5	193.5	60.1	5	0.7	
RGAIVF	-50	340	10	1500	110	198.5	193.5	60.1	5.1	0.7	
RHAIVF	-50	340	20	1500	110	198.5	193.5	60.1	5.1	0.7	
RIAIVF	-50	340	30	1500	100	198.5	193.5	60.1	5.1	0.7	
RJAIVF	-50	340	40	1500	100	198.5	193.5	60.1	5.1	0.7	
RKAIVF	-50	340	50	1500	100	198.5	193.5	60.1	5.1	0.7	
RAAIVG	-60	340	-50	1500	100	198.5	193.5	60.1	5.3	0.7	
RBAIVG	-60	340	-40	1500	100	198.5	193.5	60.1	5.2	0.7	
RCAIVG	-60	340	-30	1500	100	198.5	193.5	60.1	5.2	0.7	
RDAIVG	-60	340	-20	1500	100	198.5	193.5	60.1	5.2	0.7	
REAIVG	-60	340	-10	1500	100	198.5	193.5	60.1	5.3	0.7	
RFAIVG	-60	340	0	1500	100	198.5	193.5	60.1	5.3	0.7	
RGAIVG	-60	340	10	1500	100	198.5	193.5	60.1	5.3	0.7	
RHAIVG	-60	340	20	1500	100	198.5	193.5	60.1	5.3	0.7	
RIAIVG	-60	340	30	1500	100	198.5	193.5	60.1	5.3	0.7	
RJAIVG	-60	340	40	1500	100	198.5	193.5	60.1	5.3	0.7	
RKAIVG	-60	340	50	1500	100	198.5	193.5	60.1	5.3	0.7	
RAAHVG	-60	320	-50	1500	100	198.5	193.5	60.1	5.3	0.7	
RBAHVG	-60	320	-40	1500	100	198.5	193.5	60.1	5.3	0.7	
RCAHVG	-60	320	-30	1500	100	198.5	193.5	60.1	5.3	0.7	
RDAHVG	-60	320	-20	1500	100	198.5	193.5	60.1	5.3	0.7	
REAHVG	-60	320	-10	1500	100	198.5	193.5	60.1	5.3	0.7	
RFAHVG	-60	320	0	1500	100	198.5	193.5	60.1	5.3	0.7	
RGAHVG	-60	320	10	1500	100	198.5	193.5	60.1	5.3	0.7	
RHAHVG	-60	320	20	1500	100	198.5	193.5	60.1	5.3	0.7	
RIAHVG	-60	320	30	1500	100	198.5	193.5	60.1	5.3	0.7	
RJAHVG	-60	320	40	1500	100	198.5	193.5	60.1	5.3	0.7	
RKAHVG	-60	320	50	1500	100	198.5	193.5	60.1	5.3	0.7	
RAAGVG	-60	300	-50	1500	100	198.5	193.5	60.0	5.4	0.7	
RBAGVG	-60	300	-40	1500	100	198.5	193.5	60.0	5.4	0.7	
RCAGVG	-60	300	-30	1500	100	198.5	193.5	60.0	5.4	0.7	
RDAGVG	-60	300	-20	1500	100	198.5	193.5	60.0	5.4	0.7	
REAGVG	-60	300	-10	1500	100	198.5	193.5	60.0	5.4	0.7	
RFAGVG	-60	300	0	1500	100	198.5	193.5	60.0	5.4	0.7	
RGAGVG	-60	300	10	1500	100	198.5	193.5	60.0	5.4	0.7	
RHAGVG	-60	300	20	1500	100	198.5	193.5	60.1	5.3	0.7	
RIAGVG	-60	300	30	1500	100	198.5	193.5	60.1	5.3	0.7	
RJAGVG	-60	300	40	1500	100	198.5	193.5	60.1	5.3	0.7	
RKAGVG	-60	300	50	1500	100	198.5	193.5	60.1	5.3	0.7	break
RAAPVG	-60	280	-50	1500	120	198.5	193.5	60.1	4.8	0.7	

Filename	Langmuir Probe Position (mm)			Power (W)		Matching Network		Magnet		Pressure	notes
	Vert	Axial	rad	input	reflected	loading	tuning	cur (A)	Vol (V)	(mtorr)	
RBAFVG	-60	280	-40	1500	120	198.5	193.5	60.1	4.8	0.7	
RCAFVG	-60	280	-30	1500	110	198.5	193.5	60.1	4.8	0.7	
RDAFVG	-60	280	-20	1500	110	198.5	193.5	60.1	4.8	0.7	
REAFVG	-60	280	-10	1500	110	198.5	193.5	60.1	4.9	0.7	
RFAFVG	-60	280	0	1500	110	198.5	193.5	60.1	4.9	0.7	
RGAFVG	-60	280	10	1500	110	198.5	193.5	60.1	4.9	0.7	
RHAFVG	-60	280	20	1500	110	198.5	193.5	60.1	4.9	0.7	
RIAFVG	-60	280	30	1500	110	198.5	193.5	60.1	4.9	0.7	
RJAFVG	-60	280	40	1500	110	198.5	193.5	60.1	4.9	0.7	
RKAFVG	-60	280	50	1500	110	198.5	193.5	60.1	4.9	0.7	
RAAEVG	-60	260	-50	1500	110	198.5	193.5	60.1	5	0.7	
RBAEVG	-60	260	-40	1500	110	198.5	193.5	60.1	5	0.7	
RCAEVG	-60	260	-30	1500	110	198.5	193.5	60.1	5	0.7	
RDAEVG	-60	260	-20	1500	110	198.5	193.5	60.1	5	0.7	matching
REAEVG	-60	260	-10	1500	110	198.5	193.5	60.1	5	0.7	network
RFAEVG	-60	260	0	1500	110	198.5	193.5	60.1	5	0.7	water on
RGAEVG	-60	260	10	1500	110	198.5	193.5	60.1	5	0.7	
RHAEVG	-60	260	20	1500	110	198.5	193.5	60.1	5	0.7	
RIAEVG	-60	260	30	1500	110	198.5	193.5	60.1	5	0.7	
RJAEVG	-60	260	40	1500	110	198.5	193.5	60.1	4.9	0.7	
RKAEVG	-60	260	50	1500	110	198.5	193.5	60.1	4.9	0.7	
RAADVG	-60	240	-50	1500	110	198.5	193.5	60.1	5	0.7	
RBADVG	-60	240	-40	1500	110	198.5	193.5	60.1	5	0.7	
RCADVG	-60	240	-30	1500	110	198.5	193.5	60.1	5	0.7	
RDADVG	-60	240	-20	1500	110	198.5	193.5	60.1	5	0.7	
READVG	-60	240	-10	1500	110	198.5	193.5	60.1	5.1	0.7	
RFADVG	-60	240	0	1500	110	198.5	193.5	60.1	5.1	0.7	
RGADVG	-60	240	10	1500	110	198.5	193.5	60.1	5.1	0.7	
RHADVG	-60	240	20	1500	110	198.5	193.5	60.0	5.1	0.7	
RIADVG	-60	240	30	1500	110	198.5	193.5	60.0	5.1	0.7	
RJADVG	-60	240	40	1500	110	198.5	193.5	60.0	5.1	0.7	
RKADVG	-60	240	50	1500	110	198.5	193.5	60.0	5.1	0.7	
RAACVG	-60	220	-50	1500	110	198.5	193.5	60.0	5.1	0.7	
RBACVG	-60	220	-40	1500	110	198.5	193.5	60.0	5.1	0.7	
RCACVG	-60	220	-30	1500	110	198.5	193.5	60.0	5.1	0.7	
RDACVG	-60	220	-20	1500	110	198.5	193.5	60.0	5.1	0.7	
REACVG	-60	220	-10	1500	110	198.5	193.5	60.0	5.1	0.7	
RFACVG	-60	220	0	1500	110	198.5	193.5	60.0	5.1	0.7	
RGACVG	-60	220	10	1500	110	198.5	193.5	60.0	5.1	0.7	
RHACVG	-60	220	20	1500	110	198.5	193.5	60.0	5.1	0.7	
RIACVG	-60	220	30	1500	110	198.5	193.5	60.0	5.1	0.7	
RJACVG	-60	220	40	1500	110	198.5	193.5	60.0	5.1	0.7	
RKACVG	-60	220	50	1500	110	198.5	193.5	60.0	5.1	0.7	break
RAABVG	-60	200	-50	1500	120	198.5	193.5	60.1	5	0.7	
RBABVG	-60	200	-40	1500	120	198.5	193.5	60.1	5	0.7	
RCABVG	-60	200	-30	1500	120	198.5	193.5	60.1	5	0.7	
RDABVG	-60	200	-20	1500	120	198.5	193.5	60.1	5	0.7	
REABVG	-60	200	-10	1500	110	198.5	193.5	60.1	5	0.7	
RFABVG	-60	200	0	1500	110	198.5	193.5	60.1	5	0.7	
RGABVG	-60	200	10	1500	110	198.5	193.5	60.1	5	0.7	
RHABVG	-60	200	20	1500	110	198.5	193.5	60.1	5	0.7	
RIABVG	-60	200	30	1500	110	198.5	193.5	60.1	5	0.7	
RJABVG	-60	200	40	1500	110	198.5	193.5	60.1	5	0.7	
RKABVG	-60	200	50	1500	110	198.5	193.5	60.1	5	0.7	
RAAAVG	-60	180	-50	1500	110	198.5	193.5	60.1	5.2	0.7	
RBAAVG	-60	180	-40	1500	110	198.5	193.5	60.1	5.2	0.7	
RCAAVG	-60	180	-30	1500	110	198.5	193.5	60.1	5.2	0.7	
RDAAVG	-60	180	-20	1500	110	198.5	193.5	60.1	5.2	0.7	
REAAVG	-60	180	-10	1500	110	198.5	193.5	60.1	5.1	0.7	
RFAAVG	-60	180	0	1500	110	198.5	193.5	60.1	5.1	0.7	
RGAAVG	-60	180	10	1500	110	198.5	193.5	60.1	5.1	0.7	

Filename	Langmuir Probe Position (mm)			Power (W)		Matching Network		Magnet		Pressure	notes
	Vert	Axial	rad	input	reflected	loading	tuning	cur (A)	Vol (V)	(mtorr)	
RHAAVG	-60	180	20	1500	110	198.5	193.5	60.1	5.1	0.7	
RIAAVG	-60	180	30	1500	110	198.5	193.5	60.1	5.1	0.7	
RJAAVG	-60	180	40	1500	110	198.5	193.5	60.1	5.1	0.7	
RKAAVG	-60	180	50	1500	110	198.5	193.5	60.1	5.1	0.7	
RAAAVH	-70	180	-50	1500	110	198.5	193.5	60.1	5.2	0.7	
RBAAVH	-70	180	-40	1500	110	198.5	193.5	60.1	5.2	0.7	
RCAAVH	-70	180	-30	1500	110	198.5	193.5	60.1	5.2	0.7	
RDAAVH	-70	180	-20	1500	110	198.5	193.5	60.0	5.2	0.7	
REAAVH	-70	180	-10	1500	110	198.5	193.5	60.0	5.2	0.7	
RFAAVH	-70	180	0	1500	110	198.5	193.5	60.0	5.2	0.7	
RGAAVH	-70	180	10	1500	110	198.5	193.5	60.0	5.2	0.7	
RHAAVH	-70	180	20	1500	110	198.5	193.5	60.0	5.2	0.7	
RIAAVH	-70	180	30	1500	110	198.5	193.5	60.0	5.3	0.7	
RJAAVH	-70	180	40	1500	110	198.5	193.5	60.0	5.3	0.7	
RKAAVH	-70	180	50	1500	110	198.5	193.5	60.0	5.3	0.7	
RAABVH	-70	200	-50	1500	110	198.5	193.5	60.0	5.3	0.7	
RBABVH	-70	200	-40	1500	110	198.5	193.5	60.0	5.3	0.7	
RCABVH	-70	200	-30	1500	110	198.5	193.5	60.0	5.3	0.7	
RDABVH	-70	200	-20	1500	110	198.5	193.5	60.0	5.3	0.7	
REABVH	-70	200	-10	1500	110	198.5	193.5	60.0	5.3	0.7	
RFABVH	-70	200	0	1500	110	198.5	193.5	60.0	5.3	0.7	
RGABVH	-70	200	10	1500	110	198.5	193.5	60.0	5.3	0.7	
RHABVH	-70	200	20	1500	110	198.5	193.5	60.0	5.3	0.7	
RIABVH	-70	200	30	1500	110	198.5	193.5	60.0	5.3	0.7	
RJABVH	-70	200	40	1500	110	198.5	193.5	60.0	5.3	0.7	
RKABVH	-70	200	50	1500	110	198.5	193.5	60.0	5.3	0.7	break
RAACVH	-70	220	-50	1500	110	198.5	193.5	60.1	5.1	0.7	
RBACVH	-70	220	-40	1500	110	198.5	193.5	60.1	5.1	0.7	
RCACVH	-70	220	-30	1500	110	198.5	193.5	60.1	5.1	0.7	
RDACVH	-70	220	-20	1500	110	198.5	193.5	60.1	5.1	0.7	
REACVH	-70	220	-10	1500	110	198.5	193.5	60.1	5.1	0.7	
RFACVH	-70	220	0	1500	110	198.5	193.5	60.1	5.1	0.7	
RGACVH	-70	220	10	1500	110	198.5	193.5	60.1	5.1	0.7	
RHACVH	-70	220	20	1500	110	198.5	193.5	60.1	5.1	0.7	
RIACVH	-70	220	30	1500	110	198.5	193.5	60.1	5.1	0.7	
RJACVH	-70	220	40	1500	110	198.5	193.5	60.1	5.1	0.7	
RKACVH	-70	220	50	1500	110	198.5	193.5	60.1	5.1	0.7	
RAADVH	-70	240	-50	1500	110	198.5	193.5	60.1	5.2	0.7	
RBADVH	-70	240	-40	1500	110	198.5	193.5	60.1	5.2	0.7	
RCADVH	-70	240	-30	1500	110	198.5	193.5	60.1	5.2	0.7	
RDADVH	-70	240	-20	1500	110	198.5	193.5	60.1	5.2	0.7	
READVH	-70	240	-10	1500	110	198.5	193.5	60.1	5.2	0.7	
RFADVH	-70	240	0	1500	110	198.5	193.5	60.1	5.2	0.7	
RGADVH	-70	240	10	1500	110	198.5	193.5	60.1	5.2	0.7	
RHADVH	-70	240	20	1500	110	198.5	193.5	60.1	5.2	0.7	
RIADVH	-70	240	30	1500	110	198.5	193.5	60.1	5.2	0.7	
RJADVH	-70	240	40	1500	110	198.5	193.5	60.1	5.1	0.7	
RKADVH	-70	240	50	1500	110	198.5	193.5	60.1	5.1	0.7	
RAAEVH	-70	260	-50	1500	110	198.5	193.5	60.1	5.2	0.7	
RBAEVH	-70	260	-40	1500	110	198.5	193.5	60.1	5.2	0.7	
RCAEVH	-70	260	-30	1500	110	198.5	193.5	60.1	5.2	0.7	
RDAEVH	-70	260	-20	1500	110	198.5	193.5	60.0	5.3	0.7	
REAEVH	-70	260	-10	1500	110	198.5	193.5	60.0	5.3	0.7	
RFAEVH	-70	260	0	1500	110	198.5	193.5	60.0	5.3	0.7	
RGAEVH	-70	260	10	1500	110	198.5	193.5	60.0	5.2	0.7	
RHAEVH	-70	260	20	1500	110	198.5	193.5	60.0	5.2	0.7	
RIAEVH	-70	260	30	1500	110	198.5	193.5	60.0	5.2	0.7	
RJAEVH	-70	260	40	1500	110	198.5	193.5	60.0	5.2	0.7	
RKAEVH	-70	260	50	1500	110	198.5	193.5	60.0	5.2	0.7	
RAAFVH	-70	280	-50	1500	110	198.5	193.5	60.0	5.3	0.7	
RBAFVH	-70	280	-40	1500	110	198.5	193.5	60.0	5.3	0.7	

Filename	Langmuir Probe Position (mm)			Power (W)		Matching Network		Magnet		Pressure	notes
	Vert	Axial	rad	input	reflected	loading	tuning	cur(A)	Vol (V)	(mtorr)	
RCAPVH	-70	280	-30	1500	110	198.5	193.5	60.0	5.3	0.7	
RDAPVH	-70	280	-20	1500	110	198.5	193.5	60.0	5.3	0.7	
REAPVH	-70	280	-10	1500	110	198.5	193.5	60.0	5.3	0.7	
RFAPVH	-70	280	0	1500	110	198.5	193.5	60.0	5.3	0.7	
RGAPVH	-70	280	10	1500	110	198.5	193.5	60.0	5.3	0.7	
RHAPVH	-70	280	20	1500	110	198.5	193.5	60.0	5.3	0.7	
RIAPVH	-70	280	30	1500	110	198.5	193.5	60.0	5.3	0.7	
RJAPVH	-70	280	40	1500	110	198.5	193.5	60.0	5.3	0.7	
RKAPVH	-70	280	50	1500	110	198.5	193.5	60.0	5.3	0.7	break
RAAGVH	-70	300	-50	1500	120	198.5	193.5	60.1	5	0.7	
RBAGVH	-70	300	-40	1500	120	198.5	193.5	60.1	5	0.7	
RCAGVH	-70	300	-30	1500	120	198.5	193.5	60.1	5	0.7	
RDAGVH	-70	300	-20	1500	110	198.5	193.5	60.1	5.1	0.7	
REAGVH	-70	300	-10	1500	110	198.5	193.5	60.1	5.1	0.7	
RFAGVH	-70	300	0	1500	110	198.5	193.5	60.1	5.1	0.7	
RGAGVH	-70	300	10	1500	110	198.5	193.5	60.1	5.2	0.7	
RHAGVH	-70	300	20	1500	110	198.5	193.5	60.1	5.2	0.7	
RIAGVH	-70	300	30	1500	110	198.5	193.5	60.1	5.2	0.7	
RJAGVH	-70	300	40	1500	110	198.5	193.5	60.1	5.2	0.7	
RKAGVH	-70	300	50	1500	110	198.5	193.5	60.1	5.2	0.7	
RAAHVH	-70	320	-50	1500	110	198.5	193.5	60.1	5.2	0.7	
RBAHVH	-70	320	-40	1500	110	198.5	193.5	60.1	5.2	0.7	
RCAHVH	-70	320	-30	1500	110	198.5	193.5	60.1	5.2	0.7	
RDAHVH	-70	320	-20	1500	110	198.5	193.5	60.1	5.2	0.7	
REAHVH	-70	320	-10	1500	110	198.5	193.5	60.1	5.3	0.7	
RFAHVH	-70	320	0	1500	110	198.5	193.5	60.1	5.3	0.7	
RGAHVH	-70	320	10	1500	110	198.5	193.5	60.1	5.2	0.7	
RHAHVH	-70	320	20	1500	110	198.5	193.5	60.1	5.2	0.7	
RIAHVH	-70	320	30	1500	110	198.5	193.5	60.1	5.2	0.7	
RJAHVH	-70	320	40	1500	110	198.5	193.5	60.1	5.2	0.7	
RKAHVH	-70	320	50	1500	110	198.5	193.5	60.1	5.2	0.7	
RAAIVH	-70	340	-50	1500	110	198.5	193.5	60.1	5.3	0.7	
RBAIVH	-70	340	-40	1500	110	198.5	193.5	60.1	5.3	0.7	
RCAIVH	-70	340	-30	1500	110	198.5	193.5	60.1	5.3	0.7	
RDAIVH	-70	340	-20	1500	110	198.5	193.5	60.1	5.3	0.7	
REAIVH	-70	340	-10	1500	110	198.5	193.5	60.1	5.3	0.7	
RFAIVH	-70	340	0	1500	110	198.5	193.5	60.1	5.3	0.7	
RGAIVH	-70	340	10	1500	110	198.5	193.5	60.1	5.4	0.7	
RHAIVH	-70	340	20	1500	110	198.5	193.5	60.1	5.4	0.7	
RIAIVH	-70	340	30	1500	110	198.5	193.5	60.1	5.4	0.7	
RJAIVH	-70	340	40	1500	110	198.5	193.5	60.1	5.3	0.7	
RKAIVH	-70	340	50	1500	110	198.5	193.5	60.1	5.3	0.7	break for day
RAAAVI	-75	180	-50	1500	110	198.5	193.5	60.2	4.9	0.7	4-15-08
RBAAVI	-75	180	-40	1500	110	198.5	193.5	60.2	5	0.7	
RCAAVI	-75	180	-30	1500	110	198.5	193.5	60.2	5	0.7	
RDAAVI	-75	180	-20	1500	110	198.5	193.5	60.2	4.9	0.7	
REAAVI	-75	180	-10	1500	110	198.5	193.5	60.2	4.9	0.7	
RFAAVI	-75	180	0	1500	110	198.5	193.5	60.2	5	0.7	
RGAAVI	-75	180	10	1500	110	198.5	193.5	60.2	5	0.7	
RHAAVI	-75	180	20	1500	110	198.5	193.5	60.2	5	0.7	
RIAAVI	-75	180	30	1500	110	198.5	193.5	60.2	5	0.7	
RJAAVI	-75	180	40	1500	110	198.5	193.5	60.2	5	0.7	
RKAAVI	-75	180	50	1500	110	198.5	193.5	60.2	5	0.7	
RAABVI	-75	200	-50	1500	110	198.5	193.5	60.2	5.1	0.7	
RBABVI	-75	200	-40	1500	110	198.5	193.5	60.2	5.1	0.7	
RCABVI	-75	200	-30	1500	110	198.5	193.5	60.2	5.1	0.7	
RDABVI	-75	200	-20	1500	110	198.5	193.5	60.2	5.1	0.7	
REABVI	-75	200	-10	1500	110	198.5	193.5	60.2	5.1	0.7	
RFABVI	-75	200	0	1500	110	198.5	193.5	60.2	5.1	0.7	
RGABVI	-75	200	10	1500	110	198.5	193.5	60.2	5.1	0.7	
RHABVI	-75	200	20	1500	110	198.5	193.5	60.2	5	0.7	

Filename	Langmuir Probe Position (mm)			Power (W)		Matching Network		Magnet		Pressure	notes
	Vert	Axial	rad	input	reflected	loading	tuning	cur(A)	Vol (V)	(mtorr)	
RIABVI	-75	200	30	1500	110	198.5	193.5	60.2	5	0.7	
RJABVI	-75	200	40	1500	110	198.5	193.5	60.2	5	0.7	
RKABVI	-75	200	50	1500	110	198.5	193.5	60.2	5	0.7	
RAACVI	-75	220	-50	1500	110	198.5	193.5	60.1	5.1	0.7	
RBACVI	-75	220	-40	1500	110	198.5	193.5	60.1	5.1	0.7	
RCACVI	-75	220	-30	1500	110	198.5	193.5	60.1	5.1	0.7	
RDACVI	-75	220	-20	1500	110	198.5	193.5	60.1	5.2	0.7	
REACVI	-75	220	-10	1500	110	198.5	193.5	60.1	5.2	0.7	
RFACVI	-75	220	0	1500	110	198.5	193.5	60.1	5.2	0.7	
RGACVI	-75	220	10	1500	110	198.5	193.5	60.1	5.2	0.7	
RHACVI	-75	220	20	1500	110	198.5	193.5	60.1	5.2	0.7	
RIACVI	-75	220	30	1500	100	198.5	193.5	60.1	5.2	0.7	
RJACVI	-75	220	40	1500	100	198.5	193.5	60.1	5.2	0.7	
RKACVI	-75	220	50	1500	100	198.5	193.5	60.1	5.2	0.7	
RAADVI	-75	240	-50	1500	100	198.5	193.5	60.1	5.3	0.7	
RBADVI	-75	240	-40	1500	100	198.5	193.5	60.1	5.3	0.7	
RCADVI	-75	240	-30	1500	100	198.5	193.5	60.1	5.3	0.7	
RDADVI	-75	240	-20	1500	100	198.5	193.5	60.1	5.3	0.7	
READVI	-75	240	-10	1500	100	198.5	193.5	60.1	5.3	0.7	
RFADVI	-75	240	0	1500	100	198.5	193.5	60.1	5.2	0.7	
RGADVI	-75	240	10	1500	100	198.5	193.5	60.1	5.2	0.7	
RHADVI	-75	240	20	1500	100	198.5	193.5	60.1	5.2	0.7	
RIADVI	-75	240	30	1500	100	198.5	193.5	60.1	5.2	0.7	
RJADVI	-75	240	40	1500	100	198.5	193.5	60.1	5.2	0.7	
RKADVI	-75	240	50	1500	100	198.5	193.5	60.1	5.2	0.7	break
RAAEVI	-75	260	-50	1500	120	198.5	193.5	60.1	4.9	0.7	
RBAEVI	-75	260	-40	1500	120	198.5	193.5	60.1	4.9	0.7	
RCAEVI	-75	260	-30	1500	110	198.5	193.5	60.2	5	0.7	
RDAEVI	-75	260	-20	1500	110	198.5	193.5	60.2	5	0.7	
REAEVI	-75	260	-10	1500	110	198.5	193.5	60.2	5	0.7	
RFAEVI	-75	260	0	1500	110	198.5	193.5	60.2	5.1	0.7	
RGAEVI	-75	260	10	1500	110	198.5	193.5	60.2	5.1	0.7	
RHAEVI	-75	260	20	1500	110	198.5	193.5	60.2	5.1	0.7	
RIAEVI	-75	260	30	1500	110	198.5	193.5	60.2	5.1	0.7	
RJAEVI	-75	260	40	1500	110	198.5	193.5	60.2	5.1	0.7	
RKAEVI	-75	260	50	1500	110	198.5	193.5	60.2	5.1	0.7	
RAAFVI	-75	280	-50	1500	100	198.5	193.5	60.2	5.3	0.7	
RBAFVI	-75	280	-40	1500	100	198.5	193.5	60.2	5.3	0.7	
RCAFVI	-75	280	-30	1500	100	198.5	193.5	60.2	5.3	0.7	
RDAFVI	-75	280	-20	1500	100	198.5	193.5	60.2	5.2	0.7	
REAFVI	-75	280	-10	1500	100	198.5	193.5	60.2	5.2	0.7	
RFAFVI	-75	280	0	1500	100	198.5	193.5	60.2	5.2	0.7	
RGAFVI	-75	280	10	1500	110	198.5	193.5	60.2	5.2	0.7	
RHAFVI	-75	280	20	1500	110	198.5	193.5	60.2	5.2	0.7	
RIAFVI	-75	280	30	1500	110	198.5	193.5	60.2	5.2	0.7	
RJAFVI	-75	280	40	1500	110	198.5	193.5	60.2	5.1	0.7	
RKAFVI	-75	280	50	1500	110	198.5	193.5	60.2	5.1	0.7	
RAAGVI	-75	300	-50	1500	110	198.5	193.5	60.2	5.3	0.7	
RBAGVI	-75	300	-40	1500	110	198.5	193.5	60.2	5.3	0.7	
RCAGVI	-75	300	-30	1500	110	198.5	193.5	60.2	5.3	0.7	
RDAGVI	-75	300	-20	1500	110	198.5	193.5	60.2	5.3	0.7	
REAGVI	-75	300	-10	1500	100	198.5	193.5	60.1	5.3	0.7	
RFAGVI	-75	300	0	1500	100	198.5	193.5	60.1	5.3	0.7	
RGAGVI	-75	300	10	1500	100	198.5	193.5	60.1	5.3	0.7	
RHAGVI	-75	300	20	1500	100	198.5	193.5	60.1	5.3	0.7	
RIAGVI	-75	300	30	1500	100	198.5	193.5	60.1	5.3	0.7	
RJAGVI	-75	300	40	1500	100	198.5	193.5	60.1	5.3	0.7	
RKAGVI	-75	300	50	1500	100	198.5	193.5	60.1	5.3	0.7	
RAAHVI	-75	320	-50	1500	100	198.5	193.5	60.1	5.4	0.7	
RBAHVI	-75	320	-40	1500	100	198.5	193.5	60.1	5.4	0.7	
RCAHVI	-75	320	-30	1500	100	198.5	193.5	60.1	5.4	0.7	

Filename	Langmuir Probe Position (mm)			Power (W)		Matching Network		Magnet		Pressure	notes
	Vert	Axial	rad	input	reflected	loading	tuning	cur(A)	Vol (V)	(mtorr)	
RDAHVI	-75	320	-20	1500	100	198.5	193.5	60.1	5.4	0.7	
REAHVI	-75	320	-10	1500	100	198.5	193.5	60.1	5.4	0.7	
RFAHVI	-75	320	0	1500	100	198.5	193.5	60.1	5.4	0.7	
RGAHVI	-75	320	10	1500	100	198.5	193.5	60.1	5.3	0.7	
RHAHVI	-75	320	20	1500	100	198.5	193.5	60.1	5.3	0.7	
RIAHVI	-75	320	30	1500	100	198.5	193.5	60.1	5.3	0.7	
RJAHVI	-75	320	40	1500	100	198.5	193.5	60.1	5.3	0.7	
RKAHVI	-75	320	50	1500	100	198.5	193.5	60.1	5.3	0.7	
RAAVI	-75	340	-50	1500	110	198.5	193.5	60.0	5.4	0.7	
RBAVI	-75	340	-40	1500	110	198.5	193.5	60.0	5.4	0.7	
RCAVI	-75	340	-30	1500	110	198.5	193.5	60.0	5.4	0.7	
RDAVI	-75	340	-20	1500	110	198.5	193.5	60.0	5.4	0.7	
REAVI	-75	340	-10	1500	110	198.5	193.5	60.0	5.4	0.7	
RFAVI	-75	340	0	1500	110	198.5	193.5	60.0	5.4	0.7	
RGAVI	-75	340	10	1500	110	198.5	193.5	60.0	5.4	0.7	
RHAVI	-75	340	20	1500	110	198.5	193.5	60.0	5.4	0.7	
RIAVI	-75	340	30	1500	110	198.5	193.5	60.0	5.4	0.7	
RJAVI	-75	340	40	1500	110	198.5	193.5	60.0	5.4	0.7	
RKAVI	-75	340	50	1500	110	198.5	193.5	60.0	5.4	0.7	

Table C.3: Testing Matrix for Plasma Characterization: ReComm System Present Downstream

Filename	Langmuir Probe Position (mm)			Power (W)		Matching Network		Magnet		Pressure	notes
	Vert	Axial	rad	Input	reflected	loading	tuning	cur(A)	Vol (V)	(mtorr)	
RAAAVH	-65	180	-50	1550	140	198.8	192.5	60.1	4.6	0.7	1mA gain
RBAAVH	-65	180	-40	1550	140	198.8	192.5	60.1	4.6	0.7	
RCAAVH	-65	180	-30	1550	140	198.8	192.5	60.1	4.6	0.7	
RDAAVH	-65	180	-20	1550	140	198.8	192.5	60.1	4.6	0.7	
REAAVH	-65	180	-10	1550	140	198.8	192.5	60.1	4.6	0.7	
RFAAVH	-65	180	0	1550	140	198.8	192.5	60.1	4.6	0.7	
RGAAVH	-65	180	10	1550	140	198.8	192.5	60.1	4.6	0.7	
RHAAVH	-65	180	20	1550	140	198.8	192.5	60.1	4.6	0.7	
RIAAVH	-65	180	30	1550	140	198.8	192.5	60.1	4.6	0.7	
RJAAVH	-65	180	40	1550	140	198.8	192.5	60.1	4.6	0.7	
RAABVH	-65	200	-50	1550	120	198.5	192.5	60.1	4.6	0.7	
RBABVH	-65	200	-40	1550	120	198.5	192.5	60.1	4.6	0.7	
RCABVH	-65	200	-30	1550	120	198.5	192.5	60.1	4.6	0.7	
RDABVH	-65	200	-20	1550	130	198.5	192.5	60.1	4.6	0.7	
REABVH	-65	200	-10	1550	130	198.5	192.5	60.1	4.6	0.7	
RFABVH	-65	200	0	1550	130	198.5	192.5	60.1	4.6	0.7	
RGABVH	-65	200	10	1550	130	198.5	192.5	60.1	4.6	0.7	
RHABVH	-65	200	20	1550	130	198.5	192.5	60.1	4.6	0.7	
RIABVH	-65	200	30	1550	130	198.5	192.5	60.1	4.6	0.7	
RJABVH	-65	200	40	1550	130	198.5	192.5	60.1	4.6	0.7	
RAACVH	-65	220	-50	1500	110	198.5	192.5	60.1	4.6	0.7	
RBACVH	-65	220	-40	1500	110	198.5	192.5	60.1	4.6	0.7	
RCACVH	-65	220	-30	1500	110	198.5	192.5	60.1	4.6	0.7	
RDACVH	-65	220	-20	1500	110	198.5	192.5	60.1	4.6	0.7	
REACVH	-65	220	-10	1500	110	198.5	192.5	60.1	4.6	0.7	
RFACVH	-65	220	0	1500	110	198.5	192.5	60.1	4.6	0.7	
RGACVH	-65	220	10	1500	110	198.5	192.5	60.1	4.6	0.7	
RHACVH	-65	220	20	1500	110	198.5	192.5	60.1	4.6	0.7	
RIACVH	-65	220	30	1500	110	198.5	192.5	60.1	4.6	0.7	
RJACVH	-65	220	40	1500	110	198.5	192.5	60.1	4.6	0.7	break
RAADVH	-65	240	-50	1500	120	198.5	192.5	60.1	4.6	0.7	
RBADVH	-65	240	-40	1500	120	198.5	192.5	60.1	4.6	0.7	
RCADVH	-65	240	-30	1500	110	198.5	192.5	60.1	4.7	0.7	
RDADVH	-65	240	-20	1500	110	198.5	192.5	60.1	4.7	0.7	
READVH	-65	240	-10	1500	110	198.5	192.5	60.1	4.7	0.7	
RFADVH	-65	240	0	1500	110	198.5	192.5	60.1	4.7	0.7	
RGADVH	-65	240	10	1500	110	198.5	192.5	60.1	4.7	0.7	
RHADVH	-65	240	20	1500	110	198.5	192.5	60.1	4.7	0.7	
RIADVH	-65	240	30	1500	110	198.5	192.5	60.1	4.7	0.7	
RJADVH	-65	240	40	1500	110	198.5	192.5	60.1	4.7	0.7	
RAAEVH	-65	260	-50	1500	110	198.5	192.5	60.1	4.7	0.7	
RBAEVH	-65	260	-40	1500	110	198.5	192.5	60.1	4.7	0.7	
RCAEVH	-65	260	-30	1500	110	198.5	192.5	60.1	4.7	0.7	
RDAEVH	-65	260	-20	1500	110	198.5	192.5	60.1	4.7	0.7	
REAEVH	-65	260	-10	1500	110	198.5	192.5	60.1	4.7	0.7	
RFAEVH	-65	260	0	1500	110	198.5	192.5	60.1	4.7	0.7	
RGAEVH	-65	260	10	1500	110	198.5	192.5	60.1	4.7	0.7	
RHAEVH	-65	260	20	1500	110	198.5	192.5	60.1	4.7	0.7	
RIAEVH	-65	260	30	1500	110	198.5	192.5	60.1	4.7	0.7	
RJAEVH	-65	260	40	1500	110	198.5	192.5	60.1	4.7	0.7	
RAAFVH	-65	280	-50	1500	110	198.5	192.5	60.1	4.7	0.7	
RBAFVH	-65	280	-40	1500	110	198.5	192.5	60.1	4.7	0.7	
RCAFVH	-65	280	-30	1500	110	198.5	192.5	60.1	4.7	0.7	
RDAFVH	-65	280	-20	1500	110	198.5	192.5	60.1	4.7	0.7	
REAFVH	-65	280	-10	1500	110	198.5	192.5	60.1	4.7	0.7	
RFAFVH	-65	280	0	1500	110	198.5	192.5	60.1	4.7	0.7	
RGAFVH	-65	280	10	1500	110	198.5	192.5	60.1	4.7	0.7	
RHAFVH	-65	280	20	1500	110	198.5	192.5	60.1	4.7	0.7	
RIAFVH	-65	280	30	1500	110	198.5	192.5	60.1	4.7	0.7	
RJAFVH	-65	280	40	1500	110	198.5	192.5	60.1	4.7	0.7	break

Filename	Langmuir Probe Position (mm)			Power (W)		Matching Network		Magnet		Pressure	notes
	Vert	Axial	rad	Input	reflected	loading	tuning	cur(A)	Vol (V)	(mtorr)	
RAAGVH	-65	300	-50	1500	120	198.5	192.5	60.1	4.7	0.7	
RBAGVH	-65	300	-40	1500	120	198.5	192.5	60.1	4.7	0.7	
RCAGVH	-65	300	-30	1500	120	198.5	192.5	60.1	4.7	0.7	
RDAGVH	-65	300	-20	1500	120	198.5	192.5	60.1	4.7	0.7	
REAGVH	-65	300	-10	1500	120	198.5	192.5	60.1	4.7	0.7	
RFAGVH	-65	300	0	1500	120	198.5	192.5	60.1	4.7	0.7	
RGAGVH	-65	300	10	1500	120	198.5	192.5	60.1	4.7	0.7	
RHAGVH	-65	300	20	1500	120	198.5	192.5	60.1	4.7	0.7	
RIAGVH	-65	300	30	1500	120	198.5	192.5	60.1	4.7	0.7	
RJAGVH	-65	300	40	1500	120	198.5	192.5	60.1	4.7	0.7	
RAAHVH	-65	320	-50	1500	110	198.5	192.5	60.1	4.8	0.7	
RBAHVH	-65	320	-40	1500	110	198.5	192.5	60.1	4.8	0.7	
RCAHVH	-65	320	-30	1500	110	198.5	192.5	60.1	4.8	0.7	
RDAHVH	-65	320	-20	1500	110	198.5	192.5	60.1	4.8	0.7	
REAHVH	-65	320	-10	1500	120	198.5	192.5	60.1	4.7	0.7	
RFAHVH	-65	320	0	1500	120	198.5	192.5	60.1	4.7	0.7	
RGAHVH	-65	320	10	1500	120	198.5	192.5	60.1	4.7	0.7	
RHAHVH	-65	320	20	1500	120	198.5	192.5	60.1	4.7	0.7	
RIAHVH	-65	320	30	1500	120	198.5	192.5	60.1	4.7	0.7	
RJAHVH	-65	320	40	1500	120	198.5	192.5	60.1	4.7	0.7	
RAAIVH	-65	340	-50	1500	110	198.5	192.5	60.1	4.8	0.7	
RBAIVH	-65	340	-40	1500	110	198.5	192.5	60.1	4.8	0.7	
RCAIVH	-65	340	-30	1500	110	198.5	192.5	60.1	4.8	0.7	
RDAIVH	-65	340	-20	1500	110	198.5	192.5	60.1	4.8	0.7	
REAIVH	-65	340	-10	1500	110	198.5	192.5	60.1	4.8	0.7	
RFAIVH	-65	340	0	1500	110	198.5	192.5	60.1	4.8	0.7	
RGAIVH	-65	340	10	1500	110	198.5	192.5	60.1	4.8	0.7	
RHAIVH	-65	340	20	1500	110	198.5	192.5	60.1	4.8	0.7	
RIAIVH	-65	340	30	1500	110	198.5	192.5	60.1	4.8	0.7	
RJAIVH	-65	340	40	1500	110	198.5	192.5	60.1	4.8	0.7	break
RAAAVG	-60	180	-50	1500	120	198.5	193	60.1	4.8	0.7	
RBAAVG	-60	180	-40	1500	120	198.5	193	60.1	4.8	0.7	
RCAAVG	-60	180	-30	1500	120	198.5	193	60.1	4.8	0.7	
RDAAVG	-60	180	-20	1500	120	198.5	193	60.1	4.8	0.7	
REAAVG	-60	180	-10	1500	120	198.5	193	60.1	4.8	0.7	
RFAAVG	-60	180	0	1500	120	198.5	193	60.1	4.8	0.7	
RGAAVG	-60	180	10	1500	120	198.5	193	60.1	4.8	0.7	
RHAAVG	-60	180	20	1500	120	198.5	193	60.1	4.8	0.7	
RIAAVG	-60	180	30	1500	120	198.5	193	60.1	4.8	0.7	
RJAAVG	-60	180	40	1500	120	198.5	193	60.1	4.8	0.7	
RAABVG	-60	200	-50	1500	120	198.5	193	60.1	4.8	0.7	
RBABVG	-60	200	-40	1500	120	198.5	193	60.1	4.8	0.7	
RCABVG	-60	200	-30	1500	120	198.5	193	60.1	4.8	0.7	
RDABVG	-60	200	-20	1500	120	198.5	193	60.1	4.8	0.7	
REABVG	-60	200	-10	1500	120	198.5	193	60.1	4.8	0.7	
RFABVG	-60	200	0	1500	120	198.5	193	60.1	4.8	0.7	
RGABVG	-60	200	10	1500	120	198.5	193	60.1	4.8	0.7	
RHABVG	-60	200	20	1500	120	198.5	193	60.1	4.8	0.7	
RIABVG	-60	200	30	1500	120	198.5	193	60.1	4.8	0.7	
RJABVG	-60	200	40	1500	120	198.5	193	60.1	4.8	0.7	
RAACVG	-60	220	-50	1500	110	198.5	193	60.1	4.8	0.7	
RBACVG	-60	220	-40	1500	110	198.5	193	60.1	4.8	0.7	
RCACVG	-60	220	-30	1500	110	198.5	193	60.1	4.8	0.7	
RDACVG	-60	220	-20	1500	110	198.5	193	60.1	4.8	0.7	
REACVG	-60	220	-10	1500	110	198.5	193	60.1	4.8	0.7	
RFACVG	-60	220	0	1500	110	198.5	193	60.1	4.8	0.7	
RGACVG	-60	220	10	1500	110	198.5	193	60.1	4.8	0.7	
RHACVG	-60	220	20	1500	110	198.5	193	60.1	4.8	0.7	
RIACVG	-60	220	30	1500	110	198.5	193	60.1	4.8	0.7	
RJACVG	-60	220	40	1500	110	198.5	193	60.1	4.8	0.7	break

Filename	Langmuir Probe Position (mm)			Power (W)		Matching Network		Magnet		Pressure	notes
	Vert	Axial	rad	Input	reflected	loading	tuning	cur(A)	Vol (V)	(mtorr)	
RAADVG	-60	240	-50	1500	120	198.5	194	60.1	4.8	0.7	
RBADVG	-60	240	-40	1500	120	198.5	194	60.1	4.8	0.7	
RCADVG	-60	240	-30	1500	120	198.5	194	60.1	4.8	0.7	
RDADVG	-60	240	-20	1500	120	198.5	194	60.1	4.8	0.7	
READVG	-60	240	-10	1500	120	198.5	194	60.1	4.8	0.7	
RFADVG	-60	240	0	1500	120	198.5	194	60.1	4.8	0.7	
RGADVG	-60	240	10	1500	120	198.5	194	60.1	4.8	0.7	
RHADVG	-60	240	20	1500	120	198.5	194	60.1	4.8	0.7	
RIADVG	-60	240	30	1500	120	198.5	194	60.1	4.8	0.7	
RJADVG	-60	240	40	1500	120	198.5	194	60.1	4.8	0.7	
RAAEVG	-60	260	-50	1500	120	198.5	194	60.1	4.8	0.7	
RBAEVG	-60	260	-40	1500	120	198.5	194	60.1	4.8	0.7	
RCAEVG	-60	260	-30	1500	120	198.5	194	60.1	4.8	0.7	
RDAEVG	-60	260	-20	1500	120	198.5	194	60.1	4.8	0.7	
REAEVG	-60	260	-10	1500	120	198.5	194	60.1	4.8	0.7	
RFAEVG	-60	260	0	1500	120	198.5	194	60.1	4.8	0.7	
RGAEVG	-60	260	10	1500	120	198.5	194	60.1	4.8	0.7	
RHAEVG	-60	260	20	1500	120	198.5	194	60.1	4.8	0.7	
RIAEVG	-60	260	30	1500	120	198.5	194	60.1	4.8	0.7	
RJAEVG	-60	260	40	1500	120	198.5	194	60.1	4.8	0.7	
RAAFVG	-60	280	-50	1500	120	198.5	194	60.1	4.8	0.7	
RBAFVG	-60	260	-40	1500	120	198.5	194	60.1	4.8	0.7	
RCAFVG	-60	280	-30	1500	120	198.5	194	60.1	4.8	0.7	
RDAFVG	-60	280	-20	1500	120	198.5	194	60.1	4.8	0.7	
REAFVG	-60	280	-10	1500	120	198.5	194	60.1	4.8	0.7	
RFAFVG	-60	280	0	1500	120	198.5	194	60.1	4.8	0.7	
RGAFVG	-60	280	10	1500	120	198.5	194	60.1	4.8	0.7	
RHAFVG	-60	280	20	1500	120	198.5	194	60.1	4.8	0.7	
RIAFVG	-60	280	30	1500	120	198.5	194	60.1	4.8	0.7	
RJAFVG	-60	280	40	1500	120	198.5	194	60.1	4.8	0.7	break
RAAGVG	-60	300	-50	1500	125	198.5	193	60.1	4.8	0.7	
RBAGVG	-60	300	-40	1500	125	198.5	193	60.1	4.8	0.7	
RCAGVG	-60	300	-30	1500	125	198.5	193	60.1	4.8	0.7	
RDAGVG	-60	300	-20	1500	125	198.5	193	60.1	4.8	0.7	
REAGVG	-60	300	-10	1500	125	198.5	193	60.1	4.8	0.7	
RFAGVG	-60	300	0	1500	125	198.5	193	60.1	4.8	0.7	
RGAGVG	-60	300	10	1500	125	198.5	193	60.1	4.8	0.7	
RHAGVG	-60	300	20	1500	125	198.5	193	60.1	4.8	0.7	
RIAGVG	-60	300	30	1500	125	198.5	193	60.1	4.8	0.7	
RJAGVG	-60	300	40	1500	125	198.5	193	60.1	4.8	0.7	
RAAHVG	-60	320	-50	1500	125	198.5	193	60.1	4.8	0.7	
RBAHVG	-60	320	-40	1500	125	198.5	193	60.1	4.8	0.7	
RCAHVG	-60	320	-30	1500	125	198.5	193	60.1	4.8	0.7	
RDAHVG	-60	320	-20	1500	125	198.5	193	60.1	4.8	0.7	
REAHVG	-60	320	-10	1500	125	198.5	193	60.1	4.8	0.7	
RFAHVG	-60	320	0	1500	125	198.5	193	60.1	4.8	0.7	
RGAHVG	-60	320	10	1500	125	198.5	193	60.1	4.8	0.7	
RHAHVG	-60	320	20	1500	125	198.5	193	60.1	4.8	0.7	
RIAHVG	-60	320	30	1500	125	198.5	193	60.1	4.8	0.7	
RJAHVG	-60	320	40	1500	125	198.5	193	60.1	4.8	0.7	
RAAIVG	-60	340	-50	1500	125	198.5	193	60.1	4.9	0.7	
RBAIVG	-60	340	-40	1500	125	198.5	193	60.1	4.9	0.7	
RCAIVG	-60	340	-30	1500	125	198.5	193	60.1	4.9	0.7	
RDAIVG	-60	340	-20	1500	125	198.5	193	60.1	4.9	0.7	
REAIVG	-60	340	-10	1500	125	198.5	193	60.1	4.9	0.7	
RFAIVG	-60	340	0	1500	125	198.5	193	60.1	4.9	0.7	
RGAIVG	-60	340	10	1500	120	198.5	193	60.1	4.9	0.7	
RHAIVG	-60	340	20	1500	120	198.5	193	60.1	4.9	0.7	
RIAIVG	-60	340	30	1500	120	198.5	193	60.1	4.9	0.7	
RJAIVG	-60	340	40	1500	120	198.5	193	60.1	4.9	0.7	break

Filename	Langmuir Probe Position (mm)			Power (W)		Matching Network		Magnet		Pressure	notes
	Vert	Axial	rad	Input	reflected	loading	tuning	cur(A)	Vol (V)	(mtorr)	
RAAAVF	-50	180	-50	1550	145	198.5	193	60.1	4.8	0.7	
RBAAVF	-50	180	-40	1550	145	198.5	193	60.1	4.8	0.7	
RCAAVF	-50	180	-30	1550	140	198.5	193	60.1	4.8	0.7	
RDAAVF	-50	180	-20	1550	140	198.5	193	60.1	4.8	0.7	
REAAVF	-50	180	-10	1550	140	198.5	193	60.1	4.9	0.7	
RFAAVF	-50	180	0	1550	140	198.5	193	60.1	4.9	0.7	
RGAAVF	-50	180	10	1550	140	198.5	193	60.1	4.9	0.7	
RHAAVF	-50	180	20	1550	140	198.5	193	60.1	4.9	0.7	
RIAAVF	-50	180	30	1550	140	198.5	193	60.1	4.9	0.7	
RJAAVF	-50	180	40	1550	140	198.5	193	60.1	4.9	0.7	
RAABVF	-50	200	-50	1550	140	198.5	193	60.1	4.9	0.7	
RBABVF	-50	200	-40	1550	140	198.5	193	60.1	4.9	0.7	
RCABVF	-50	200	-30	1550	140	198.5	193	60.1	4.9	0.7	
RDABVF	-50	200	-20	1550	140	198.5	193	60.1	4.9	0.7	
REABVF	-50	200	-10	1550	140	198.5	193	60.1	4.9	0.7	
RFABVF	-50	200	0	1550	140	198.5	193	60.1	4.9	0.7	
RGABVF	-50	200	10	1550	140	198.5	193	60.1	4.9	0.7	
RHABVF	-50	200	20	1550	140	198.5	193	60.1	4.9	0.7	
RIABVF	-50	200	30	1550	140	198.5	193	60.1	4.9	0.7	
RJABVF	-50	200	40	1550	140	198.5	193	60.1	4.9	0.7	
RAACVF	-50	220	-50	1550	135	198.5	193	60.1	4.9	0.7	
RBACVF	-50	220	-40	1550	135	198.5	193	60.1	4.9	0.7	
RCACVF	-50	220	-30	1550	135	198.5	193	60.1	4.9	0.7	
RDACVF	-50	220	-20	1550	135	198.5	193	60.1	4.9	0.7	
REACVF	-50	220	-10	1550	135	198.5	193	60.1	4.9	0.7	
RFACVF	-50	220	0	1550	135	198.5	193	60.1	4.9	0.7	
RGACVF	-50	220	10	1550	135	198.5	193	60.1	4.9	0.7	
RHACVF	-50	220	20	1550	135	198.5	193	60.1	4.9	0.7	
RIACVF	-50	220	30	1550	135	198.5	193	60.1	4.9	0.7	
RJACVF	-50	220	40	1550	135	198.5	193	60.1	4.9	0.7	break
RAADVF	-50	240	-50	1550	150	198.5	193	60.1	4.9	0.7	
RBADVF	-50	240	-40	1550	150	198.5	193	60.1	4.9	0.7	
RCADVF	-50	240	-30	1550	145	198.5	193	60.1	4.9	0.7	
RDADVF	-50	240	-20	1550	145	198.5	193	60.1	4.9	0.7	
READVF	-50	240	-10	1550	145	198.5	193	60.1	4.9	0.7	
RFADVF	-50	240	0	1550	145	198.5	193	60.1	4.9	0.7	
RGADVF	-50	240	10	1550	145	198.5	193	60.1	4.9	0.7	
RHADVF	-50	240	20	1550	145	198.5	193	60.1	4.9	0.7	
RIADVF	-50	240	30	1550	145	198.5	193	60.1	4.9	0.7	
RJADVF	-50	240	40	1550	145	198.5	193	60.1	4.9	0.7	
RAAEVF	-50	260	-50	1550	140	198.5	193	60.1	4.9	0.7	
RBAEVF	-50	260	-40	1550	140	198.5	193	60.1	4.9	0.7	
RCAEVF	-50	260	-30	1550	140	198.5	193	60.1	4.9	0.7	
RDAEVF	-50	260	-20	1550	140	198.5	193	60.1	4.9	0.7	
REAEVF	-50	260	-10	1550	140	198.5	193	60.1	4.9	0.7	
RFAEVF	-50	260	0	1550	140	198.5	193	60.1	4.9	0.7	
RGAEVF	-50	260	10	1550	140	198.5	193	60.1	4.9	0.7	
RHAEVF	-50	260	20	1550	140	198.5	193	60.1	4.9	0.7	
RIAEVF	-50	260	30	1550	140	198.5	193	60.1	4.9	0.7	
RJAEVF	-50	260	40	1550	140	198.5	193	60.1	4.9	0.7	
RAAFVF	-50	280	-50	1550	140	198.5	193	60.1	4.9	0.7	
RBAFVF	-50	280	-40	1550	140	198.5	193	60.1	4.9	0.7	
RCAFVF	-50	280	-30	1550	140	198.5	193	60.1	4.9	0.7	
RDAFVF	-50	280	-20	1550	140	198.5	193	60.1	4.9	0.7	
REAFVF	-50	280	-10	1550	135	198.5	193	60.1	4.9	0.7	
RFAFVF	-50	280	0	1550	135	198.5	193	60.1	4.9	0.7	
RGAFVF	-50	280	10	1550	135	198.5	193	60.1	4.9	0.7	
RHAFVF	-50	280	20	1550	135	198.5	193	60.1	4.9	0.7	
RIAFVF	-50	280	30	1550	135	198.5	193	60.1	4.9	0.7	
RJAFVF	-50	280	40	1550	135	198.5	193	60.1	4.9	0.7	break

Filename	Langmuir Probe Position (mm)			Power (W)		Matching Network		Magnet		Pressure	notes
	Vert	Axial	rad	Input	reflected	loading	tuning	cur(A)	Vol (V)	(mtorr)	
RAAGVF	-50	300	-50	1550	145	198.5	193	60.1	4.8	0.7	
RBAGVF	-50	300	-40	1550	140	198.5	193	60.1	4.8	0.7	
RCAGVF	-50	300	-30	1550	140	198.5	193	60.1	4.8	0.7	
RDAGVF	-50	300	-20	1550	140	198.5	193	60.1	4.8	0.7	
REAGVF	-50	300	-10	1550	140	198.5	193	60.1	4.9	0.7	
RFAGVF	-50	300	0	1550	140	198.5	193	60.1	4.9	0.7	
RGAGVF	-50	300	10	1550	140	198.5	193	60.1	4.9	0.7	
RHAGVF	-50	300	20	1550	140	198.5	193	60.1	4.9	0.7	
RIAGVF	-50	300	30	1550	140	198.5	193	60.1	4.9	0.7	
RJAGVF	-50	300	40	1550	140	198.5	193	60.1	4.9	0.7	
RAAHVF	-50	320	-50	1550	140	198.5	193	60.1	4.9	0.7	
RBAHVF	-50	320	-40	1550	140	198.5	193	60.1	4.9	0.7	
RCAHVF	-50	320	-30	1550	140	198.5	193	60.1	4.9	0.7	
RDAHVF	-50	320	-20	1550	140	198.5	193	60.1	4.9	0.7	
REAHVF	-50	320	-10	1550	140	198.5	193	60.1	4.9	0.7	
RFAHVF	-50	320	0	1550	140	198.5	193	60.1	4.9	0.7	
RGAHVF	-50	320	10	1550	140	198.5	193	60.1	4.9	0.7	
RHAHVF	-50	320	20	1550	140	198.5	193	60.1	4.9	0.7	
RIAHVF	-50	320	30	1550	140	198.5	193	60.1	4.9	0.7	
RJAHVF	-50	320	40	1550	140	198.5	193	60.1	4.9	0.7	
RAAIVF	-50	340	-50	1550	140	198.5	193	60.1	4.9	0.7	
RBAIVF	-50	340	-40	1550	140	198.5	193	60.1	4.9	0.7	
RCAIVF	-50	340	-30	1550	140	198.5	193	60.1	4.9	0.7	
RDAIVF	-50	340	-20	1550	140	198.5	193	60.1	4.9	0.7	
REAIVF	-50	340	-10	1550	140	198.5	193	60.1	4.9	0.7	
RFAIVF	-50	340	0	1550	140	198.5	193	60.1	4.9	0.7	
RGAIVF	-50	340	10	1550	140	198.5	193	60.1	4.9	0.7	
RHAIVF	-50	340	20	1550	140	198.5	193	60.1	4.9	0.7	
RIAIVF	-50	340	30	1550	140	198.5	193	60.1	4.9	0.7	
RJAIVF	-50	340	40	1550	140	198.5	193	60.1	4.9	0.7	break for day
RAAAVE	-40	180	-50	1550	140	198.5	193.5	60.1	4.6	0.7	4/17/08
RBAAVE	-40	180	-40	1550	140	198.5	193.5	60.1	4.6	0.7	
RCAAVE	-40	180	-30	1550	135	198.5	193.5	60.1	4.6	0.7	
RDAAVE	-40	180	-20	1550	135	198.5	193.5	60.1	4.6	0.7	
REAAVE	-40	180	-10	1550	135	198.5	193.5	60.1	4.6	0.7	
RFAAVE	-40	180	0	1550	135	198.5	193.5	60.1	4.6	0.7	
RGAAVE	-40	180	10	1550	135	198.5	193.5	60.1	4.6	0.7	
RHAAVE	-40	180	20	1550	135	198.5	193.5	60.1	4.6	0.7	
RIAAVE	-40	180	30	1550	135	198.5	193.5	60.1	4.6	0.7	
RJAAVE	-40	180	40	1550	135	198.5	193.5	60.1	4.6	0.7	
RAABVE	-40	200	-50	1500	120	198.5	193.5	60.1	4.6	0.7	
RBABVE	-40	200	-40	1500	120	198.5	193.5	60.1	4.6	0.7	
RCABVE	-40	200	-30	1500	120	198.5	193.5	60.1	4.6	0.7	
RDABVE	-40	200	-20	1500	120	198.5	193.5	60.1	4.6	0.7	
REABVE	-40	200	-10	1500	120	198.5	193.5	60.1	4.6	0.7	
RFABVE	-40	200	0	1550	130	198.5	193.5	60.1	4.6	0.7	
RGABVE	-40	200	10	1550	130	198.5	193.5	60.2	4.6	0.7	
RHABVE	-40	200	20	1550	130	198.5	193.5	60.2	4.6	0.7	
RIABVE	-40	200	30	1550	130	198.5	193.5	60.2	4.6	0.7	
RJABVE	-40	200	40	1550	130	198.5	193.5	60.2	4.6	0.7	
RAACVE	-40	220	-50	1500	120	198.5	193.5	60.1	4.7	0.7	
RBACVE	-40	220	-40	1500	120	198.5	193.5	60.1	4.7	0.7	
RCACVE	-40	220	-30	1500	120	198.5	193.5	60.1	4.7	0.7	
RDACVE	-40	220	-20	1500	120	198.5	193.5	60.1	4.7	0.7	
REACVE	-40	220	-10	1500	120	198.5	193.5	60.1	4.7	0.7	
RFACVE	-40	220	0	1500	120	198.5	193.5	60.1	4.7	0.7	
RGACVE	-40	220	10	1500	120	198.5	193.5	60.1	4.7	0.7	
RHACVE	-40	220	20	1500	120	198.5	193.5	60.1	4.7	0.7	
RIACVE	-40	220	30	1500	120	198.5	193.5	60.1	4.7	0.7	
RJACVE	-40	220	40	1500	120	198.5	193.5	60.1	4.7	0.7	break

Filename	Langmuir Probe Position (mm)			Power (W)		Matching Network		Magnet		Pressure	notes
	Vert	Axial	rad	Input	reflected	loading	tuning	cur(A)	Vol (V)	(mtorr)	
RAADVE	-40	240	-50	1550	140	198.5	193.5	60.1	4.7	0.7	
RBADVE	-40	240	-40	1550	140	198.5	193.5	60.1	4.7	0.7	
RCADVE	-40	240	-30	1550	140	198.5	193.5	60.1	4.7	0.7	
RDADVE	-40	240	-20	1550	130	198.5	193.5	60.1	4.7	0.7	
READVE	-40	240	-10	1550	130	198.5	193.5	60.1	4.7	0.7	
RFADVE	-40	240	0	1550	130	198.5	193.5	60.1	4.7	0.7	
RGADVE	-40	240	10	1550	130	198.5	193.5	60.1	4.7	0.7	
RHADVE	-40	240	20	1550	135	198.5	193.5	60.1	4.7	0.7	
RIADVE	-40	240	30	1550	135	198.5	193.5	60.1	4.7	0.7	
RJADVE	-40	240	40	1550	135	198.5	193.5	60.1	4.7	0.7	
RAAEVE	-40	260	-50	1550	130	198.5	193.5	60.1	4.8	0.7	
RBAEVE	-40	260	-40	1550	130	198.5	193.5	60.1	4.8	0.7	
RCAEVE	-40	260	-30	1550	130	198.5	193.5	60.1	4.8	0.7	
RDAEVE	-40	260	-20	1550	130	198.5	193.5	60.1	4.8	0.7	
REAEVE	-40	260	-10	1550	130	198.5	193.5	60.1	4.8	0.7	
RFAEVE	-40	260	0	1550	130	198.5	193.5	60.1	4.8	0.7	
RGAEVE	-40	260	10	1550	130	198.5	193.5	60.1	4.8	0.7	
RHAEVE	-40	260	20	1550	130	198.5	193.5	60.1	4.8	0.7	
RIAEVE	-40	260	30	1550	130	198.5	193.5	60.1	4.8	0.7	
RJAEVE	-40	260	40	1550	130	198.5	193.5	60.1	4.8	0.7	
RAAFVE	-40	280	-50	1550	130	198.5	193.5	60.1	4.8	0.7	
RBAFVE	-40	280	-40	1550	130	198.5	193.5	60.1	4.8	0.7	
RCAFVE	-40	280	-30	1550	130	198.5	193.5	60.1	4.8	0.7	
RDAFVE	-40	280	-20	1500	120	198.5	193.5	60.1	4.8	0.7	
REAFVE	-40	280	-10	1500	120	198.5	193.5	60.1	4.8	0.7	
RFAFVE	-40	280	0	1500	120	198.5	193.5	60.1	4.8	0.7	
RGAFVE	-40	280	10	1500	120	198.5	193.5	60.1	4.8	0.7	
RHAFVE	-40	280	20	1500	120	198.5	193.5	60.1	4.8	0.7	
RIAFVE	-40	280	30	1500	120	198.5	193.5	60.1	4.8	0.7	
RJAFVE	-40	280	40	1500	120	198.5	193.5	60.1	4.8	0.7	break
RAAGVE	-40	300	-50	1550	140	198.5	193.5	60.1	4.8	0.7	
RBAGVE	-40	300	-40	1550	140	198.5	193.5	60.1	4.9	0.7	
RCAGVE	-40	300	-30	1550	140	198.5	193.5	60.1	4.9	0.7	
RDAGVE	-40	300	-20	1550	140	198.5	193.5	60.1	4.9	0.7	
REAGVE	-40	300	-10	1550	140	198.5	193.5	60.1	4.9	0.7	
RFAGVE	-40	300	0	1550	140	198.5	193.5	60.1	4.9	0.7	
RGAGVE	-40	300	10	1550	140	198.5	193.5	60.1	4.9	0.7	
RHAGVE	-40	300	20	1550	140	198.5	193.5	60.1	4.9	0.7	
RIAGVE	-40	300	30	1550	140	198.5	193.5	60.1	4.9	0.7	
RJAGVE	-40	300	40	1550	140	198.5	193.5	60.1	4.9	0.7	
RAAHVE	-40	320	-50	1550	140	198.5	193.5	60.1	4.9	0.7	
RBAHVE	-40	320	-40	1550	140	198.5	193.5	60.1	4.9	0.7	
RCAHVE	-40	320	-30	1550	140	198.5	193.5	60.1	4.9	0.7	
RDAHVE	-40	320	-20	1550	140	198.5	193.5	60.1	4.9	0.7	
REAHVE	-40	320	-10	1550	140	198.5	193.5	60.1	4.9	0.7	
RFAHVE	-40	320	0	1550	140	198.5	193.5	60.1	4.9	0.7	
RGAHVE	-40	320	10	1550	140	198.5	193.5	60.1	4.9	0.7	
RHAHVE	-40	320	20	1550	140	198.5	193.5	60.1	4.9	0.7	
RIAHVE	-40	320	30	1550	140	198.5	193.5	60.1	4.9	0.7	
RJAHVE	-40	320	40	1550	130	198.5	193.5	60.1	4.9	0.7	
RAAIVE	-40	340	-50	1550	130	198.5	193.5	60.1	4.9	0.7	
RBAIVE	-40	340	-40	1550	130	198.5	193.5	60.1	4.9	0.7	
RCAIVE	-40	340	-30	1550	130	198.5	193.5	60.1	4.9	0.7	
RDAIVE	-40	340	-20	1550	130	198.5	193.5	60.1	4.9	0.7	
REAIVE	-40	340	-10	1550	130	198.5	193.5	60.1	4.9	0.7	
RFAIVE	-40	340	0	1550	130	198.5	193.5	60.1	4.9	0.7	
RGAIVE	-40	340	10	1550	130	198.5	193.5	60.1	5	0.7	
RHAIVE	-40	340	20	1550	130	198.5	193.5	60.1	5	0.7	
RIAIVE	-40	340	30	1550	130	198.5	193.5	60.1	5	0.7	
RJAIVE	-40	340	40	1550	130	198.5	193.5	60.1	5	0.7	break

Filename	Langmuir Probe Position (mm)			Power (W)		Matching Network		Magnet		Pressure	notes
	Vert	Axial	rad	input	reflected	loading	tuning	cur(A)	Vol (V)	(mtorr)	
RAAAVD	-30	180	-50	1550	145	198.5	193.5	60.1	4.8	0.7	
RBAAVD	-30	180	-40	1550	145	198.5	193.5	60.1	4.8	0.7	
RCAAVD	-30	180	-30	1550	145	198.5	193.5	60.1	4.8	0.7	
RDAAVD	-30	180	-20	1550	145	198.5	193.5	60.1	4.8	0.7	
REAAVD	-30	180	-10	1550	145	198.5	193.5	60.1	4.8	0.7	
RFAAVD	-30	180	0	1550	145	198.5	193.5	60.1	4.8	0.7	
RGAAVD	-30	180	10	1550	145	198.5	193.5	60.1	4.8	0.7	
RHAAVD	-30	180	20	1550	145	198.5	193.5	60.1	4.8	0.7	
RIAAVD	-30	180	30	1550	145	198.5	193.5	60.1	4.8	0.7	
RJAAVD	-30	180	40	1550	145	198.5	193.5	60.1	4.8	0.7	
RAABVD	-30	200	-50	1550	140	198.5	193.5	60.1	4.9	0.7	
RBABVD	-30	200	-40	1550	140	198.5	193.5	60.1	4.9	0.7	
RCABVD	-30	200	-30	1550	140	198.5	193.5	60.1	4.9	0.7	
RDABVD	-30	200	-20	1550	140	198.5	193.5	60.1	4.9	0.7	
REABVD	-30	200	-10	1550	140	198.5	193.5	60.1	4.9	0.7	
RFABVD	-30	200	0	1550	145	198.5	193.5	60.1	4.8	0.7	
RGABVD	-30	200	10	1550	145	198.5	193.5	60.1	4.8	0.7	
RHABVD	-30	200	20	1550	145	198.5	193.5	60.1	4.8	0.7	
RIABVD	-30	200	30	1550	145	198.5	193.5	60.1	4.8	0.7	
RJABVD	-30	200	40	1550	145	198.5	193.5	60.1	4.8	0.7	
RAACVD	-30	220	-50	1550	145	198.5	193.5	60.1	4.9	0.7	
RBACVD	-30	220	-40	1550	145	198.5	193.5	60.1	4.9	0.7	
RCACVD	-30	220	-30	1550	145	198.5	193.5	60.1	4.9	0.7	
RDACVD	-30	220	-20	1550	145	198.5	193.5	60.1	4.9	0.7	
REACVD	-30	220	-10	1550	145	198.5	193.5	60.1	4.9	0.7	
RFACVD	-30	220	0	1550	140	198.5	193.5	60.1	4.9	0.7	
RGACVD	-30	220	10	1550	140	198.5	193.5	60.1	4.9	0.7	
RHACVD	-30	220	20	1550	140	198.5	193.5	60.1	4.9	0.7	
RIACVD	-30	220	30	1550	140	198.5	193.5	60.1	4.9	0.7	
RJACVD	-30	220	40	1550	140	198.5	193.5	60.1	4.9	0.7	break
RAADVD	-30	240	-50	1550	145	198.5	193.5	60.1	4.8	0.7	
RBADVD	-30	240	-40	1550	145	198.5	193.5	60.1	4.9	0.7	
RCADVD	-30	240	-30	1550	145	198.5	193.5	60.1	4.9	0.7	
RDADVD	-30	240	-20	1550	145	198.5	193.5	60.1	4.9	0.7	
READVD	-30	240	-10	1550	145	198.5	193.5	60.1	4.9	0.7	
RFADVD	-30	240	0	1550	145	198.5	193.5	60.1	4.9	0.7	
RGADVD	-30	240	10	1550	140	198.5	193.5	60.1	4.9	0.7	
RHADVD	-30	240	20	1550	140	198.5	193.5	60.1	4.9	0.7	
RIADVD	-30	240	30	1550	140	198.5	193.5	60.1	4.9	0.7	
RJADVD	-30	240	40	1550	140	198.5	193.5	60.1	4.9	0.7	
RAAEVD	-30	260	-50	1550	140	198.5	193.5	60	5	0.7	
RBAEVD	-30	260	-40	1550	140	198.5	193.5	60	5	0.7	
RCAEVD	-30	260	-30	1550	140	198.5	193.5	60	5	0.7	
RDAEVD	-30	260	-20	1550	140	198.5	193.5	60	5	0.7	
REAEVD	-30	260	-10	1550	140	198.5	193.5	60	5	0.7	
RFAEVD	-30	260	0	1550	140	198.5	193.5	60	5	0.7	
RGAEVD	-30	260	10	1550	140	198.5	193.5	60	5	0.7	
RHAEVD	-30	260	20	1550	140	198.5	193.5	60	5	0.7	
RIAEVD	-30	260	30	1550	140	198.5	193.5	60	5	0.7	
RJAEVD	-30	260	40	1550	140	198.5	193.5	60	5	0.7	
RAAFVD	-30	280	-50	1550	135	198.5	193.5	60	5	0.7	
RBAFVD	-30	280	-40	1550	135	198.5	193.5	60	5	0.7	
RCAFVD	-30	280	-30	1550	135	198.5	193.5	60	5	0.7	
RDAFVD	-30	280	-20	1550	135	198.5	193.5	60	5	0.7	
REAFVD	-30	280	-10	1550	135	198.5	193.5	60	5	0.7	
RFAFVD	-30	280	0	1550	135	198.5	193.5	60	5	0.7	
RGAFVD	-30	280	10	1550	135	198.5	193.5	60	5	0.7	
RHAFVD	-30	280	20	1550	135	198.5	193.5	60	5	0.7	
RIAFVD	-30	280	30	1550	135	198.5	193.5	60	5	0.7	
RJAFVD	-30	280	40	1550	135	198.5	193.5	60	5	0.7	break

Filename	Langmuir Probe Position (mm)			Power (W)		Matching Network		Magnet		Pressure	notes
	Vert	Axial	rad	input	reflected	loading	tuning	cur(A)	Vol (V)	(mtorr)	
RAAGVD	-30	300	-50	1550	150	198.5	193	60	4.9	0.7	
RBAGVD	-30	300	-40	1550	150	198.5	193	60	4.9	0.7	
RCAGVD	-30	300	-30	1550	150	198.5	193	60	4.9	0.7	
RDAGVD	-30	300	-20	1550	150	198.5	193	60	4.9	0.7	
REAGVD	-30	300	-10	1551	150	198.5	193	60	4.9	0.7	
RFAGVD	-30	300	0	1550	145	198.5	193	60	4.9	0.7	
RGAGVD	-30	300	10	1550	145	198.5	193	60	4.9	0.7	
RHAGVD	-30	300	20	1550	145	198.5	193	60.1	5	0.7	
RIAGVD	-30	300	30	1550	145	198.5	193	60.1	5	0.7	
RJAGVD	-30	300	40	1550	145	198.5	193	60.1	5	0.7	
RAAHVD	-30	320	-50	1550	145	198.5	193	60.1	5	0.7	
RBAHVD	-30	320	-40	1550	145	198.5	193	60.1	5	0.7	
RCAHVD	-30	320	-30	1550	145	198.5	193	60.1	5	0.7	
RDAHVD	-30	320	-20	1550	145	198.5	193	60.1	5	0.7	
REAHVD	-30	320	-10	1550	145	198.5	193	60.1	5	0.7	
RFAHVD	-30	320	0	1550	145	198.5	193	60.1	5	0.7	
RGAHVD	-30	320	10	1550	145	198.5	193	60.1	5	0.7	
RHAHVD	-30	320	20	1550	145	198.5	193	60.1	5	0.7	
RIAHVD	-30	320	30	1550	145	198.5	193	60.1	5	0.7	
RJAHVD	-30	320	40	1550	140	198.5	193	60.1	5	0.7	
RAAIVD	-30	340	-50	1550	140	198.5	193.5	60.1	5	0.7	
RBAIVD	-30	340	-40	1550	140	198.5	193.5	60.1	5	0.7	
RCAIVD	-30	340	-30	1550	140	198.5	193.5	60.1	5	0.7	
RDAIVD	-30	340	-20	1550	140	198.5	193.5	60.1	5	0.7	
REAIVD	-30	340	-10	1550	140	198.5	193.5	60.1	5	0.7	
RFAIVD	-30	340	0	1550	140	198.5	193.5	60.1	5	0.7	
RGAIVD	-30	340	10	1550	140	198.5	193.5	60.1	5	0.7	
RHAIVD	-30	340	20	1550	140	198.5	193.5	60.1	5	0.7	
RIAIVD	-30	340	30	1550	140	198.5	193.5	60.1	5	0.7	
RJAIVD	-30	340	40	1550	140	198.5	193.5	60.1	5	0.7	break
RAAAVC	-20	180	-50	1550	150	198.5	193.5	60.1	4.9	0.7	
RBAAVC	-20	180	-40	1550	150	198.5	193.5	60.1	4.9	0.7	
RCAAVC	-20	180	-30	1550	150	198.5	193.5	60.1	4.9	0.7	
RDAAVC	-20	180	-20	1550	150	198.5	193.5	60.1	4.9	0.7	
REAAVC	-20	180	-10	1550	150	198.5	193.5	60.1	4.9	0.7	
RFAAVC	-20	180	0	1550	150	198.5	193.5	60.1	4.9	0.7	
RGAAVC	-20	180	10	1550	150	198.5	193.5	60.1	4.9	0.7	
RHAAVC	-20	180	20	1550	150	198.5	193.5	60.1	5	0.7	
RIAAVC	-20	180	30	1550	150	198.5	193.5	60.1	5	0.7	
RJAAVC	-20	180	40	1550	150	198.5	193.5	60.1	5	0.7	
RAABVC	-20	200	-50	1550	145	198.5	193.5	60.1	5	0.7	
RBABVC	-20	200	-40	1550	145	198.5	193.5	60.1	5	0.7	
RCABVC	-20	200	-30	1550	145	198.5	193.5	60.1	5	0.7	
RDABVC	-20	200	-20	1550	145	198.5	193.5	60.1	5	0.7	
REABVC	-20	200	-10	1550	145	198.5	193.5	60.1	5	0.7	
RFABVC	-20	200	0	1550	145	198.5	193.5	60.1	5	0.7	
RGABVC	-20	200	10	1550	145	198.5	193.5	60.1	5	0.7	
RHABVC	-20	200	20	1550	145	198.5	193.5	60.1	5	0.7	
RIABVC	-20	200	30	1550	150	198.5	193.5	60.1	5	0.7	
RJABVC	-20	200	40	1550	150	198.5	193.5	60.1	5	0.7	
RAACVC	-20	220	-50	1550	145	198.5	193.5	60.1	5	0.7	
RBACVC	-20	220	-40	1550	145	198.5	193.5	60.1	5	0.7	
RCACVC	-20	220	-30	1550	145	198.5	193.5	60.1	5	0.7	
RDACVC	-20	220	-20	1550	145	198.5	193.5	60.1	5	0.7	
REACVC	-20	220	-10	1550	145	198.5	193.5	60.1	5	0.7	
RFACVC	-20	220	0	1550	145	198.5	193.5	60.1	5	0.7	
RGACVC	-20	220	10	1550	140	198.5	193.5	60.1	5	0.7	
RHACVC	-20	220	20	1550	140	198.5	193.5	60.1	5	0.7	
RIACVC	-20	220	30	1550	140	198.5	193.5	60.1	5	0.7	
RJACVC	-20	220	40	1550	140	198.5	193.5	60.1	5	0.7	break

Filename	Langmuir Probe Position (mm)			Power (W)		Matching Network		Magnet		Pressure	notes
	Vert	Axial	rad	Input	reflected	loading	tuning	cur(A)	Vol (V)	(mtorr)	
RAADVC	-20	240	-50	1550	150	198.5	193.5	60.1	5	0.7	
RBADVC	-20	240	-40	1550	150	198.5	193.5	60.1	5	0.7	
RCADVC	-20	240	-30	1550	150	198.5	193.5	60.1	5	0.7	
RDADVC	-20	240	-20	1550	150	198.5	193.5	60.1	5	0.7	
READVC	-20	240	-10	1550	150	198.5	193.5	60.1	5	0.7	
RFADVC	-20	240	0	1550	150	198.5	193.5	60.1	5	0.7	
RGADVC	-20	240	10	1550	150	198.5	193.5	60.1	5	0.7	
RHADVC	-20	240	20	1550	150	198.5	193.5	60.1	5	0.7	
RIADVC	-20	240	30	1550	150	198.5	193.5	60.1	5	0.7	
RJADVC	-20	240	40	1550	150	198.5	193.5	60.1	5	0.7	
RAAEVC	-20	260	-50	1550	150	198.5	193.5	60.1	5.1	0.7	
RBAEVC	-20	260	-40	1550	150	198.5	193.5	60.1	5.1	0.7	
RCAEVC	-20	260	-30	1550	150	198.5	193.5	60.1	5.1	0.7	
RDAEVC	-20	260	-20	1550	150	198.5	193.5	60.1	5.1	0.7	
REAEVC	-20	260	-10	1550	150	198.5	193.5	60.1	5	0.7	
RFAEVC	-20	260	0	1550	150	198.5	193.5	60.1	5	0.7	
RGAEVC	-20	260	10	1550	150	198.5	193.5	60.1	5	0.7	
RHAEVC	-20	260	20	1550	150	198.5	193.5	60.1	5	0.7	
RIAEVC	-20	260	30	1550	150	198.5	193.5	60.1	5	0.7	
RJAEVC	-20	260	40	1550	150	198.5	193.5	60.1	5	0.7	
RAAFVC	-20	280	-50	1550	150	198.5	193.5	60.1	5.1	0.7	
RBAFVC	-20	280	-40	1550	145	198.5	193.5	60.1	5.1	0.7	
RCAFVC	-20	280	-30	1550	145	198.5	193.5	60.1	5.1	0.7	
RDAFVC	-20	280	-20	1550	145	198.5	193.5	60.1	5.1	0.7	
REAFVC	-20	280	-10	1550	145	198.5	193.5	60.1	5.1	0.7	
RFAFVC	-20	280	0	1550	145	198.5	193.5	60.1	5.1	0.7	
RGAFVC	-20	280	10	1550	145	198.5	193.5	60.1	5.1	0.7	
RHAFVC	-20	280	20	1550	145	198.5	193.5	60.1	5.1	0.7	
RIAFVC	-20	280	30	1550	145	198.5	193.5	60.1	5.1	0.7	
RJAFVC	-20	280	40	1550	145	198.5	193.5	60.1	5.1	0.7	
RAAGVC	-20	300	-50	1550	140	198.5	193	60.1	4.7	0.7	4-18-08
RBAGVC	-20	300	-40	1550	130	198.5	193	60.1	4.8	0.7	
RCAGVC	-20	300	-30	1550	130	198.5	193	60.1	4.8	0.7	
RDAGVC	-20	300	-20	1550	130	198.5	193	60.1	4.8	0.7	
REAGVC	-20	300	-10	1550	130	198.5	193	60.1	4.8	0.7	
RFAGVC	-20	300	0	1550	130	198.5	193	60.1	4.8	0.7	
RGAGVC	-20	300	10	1550	130	198.5	193	60.1	4.8	0.7	
RHAGVC	-20	300	20	1550	130	198.5	193	60.1	4.8	0.7	
RIAGVC	-20	300	30	1550	130	198.5	193	60.1	4.8	0.7	
RJAGVC	-20	300	40	1550	130	198.5	193	60.1	4.8	0.7	
RAAHVC	-20	320	-50	1550	130	198.5	193	60.1	4.8	0.7	
RBAHVC	-20	320	-40	1550	130	198.5	193	60.1	4.8	0.7	
RCAHVC	-20	320	-30	1550	130	198.5	193	60.1	4.8	0.7	
RDAHVC	-20	320	-20	1550	130	198.5	193	60.1	4.8	0.7	
REAHVC	-20	320	-10	1550	130	198.5	193	60.1	4.8	0.7	
RFAHVC	-20	320	0	1550	130	198.5	193	60.1	4.8	0.7	
RGAHVC	-20	320	10	1550	130	198.5	193	60.1	4.8	0.7	
RHAHVC	-20	320	20	1550	130	198.5	193	60.1	4.8	0.7	
RIAHVC	-20	320	30	1550	130	198.5	193	60.1	4.8	0.7	
RJAHVC	-20	320	40	1550	130	198.5	193	60.1	4.8	0.7	
RAAIVC	-20	340	-50	1550	130	198.5	193	60.1	4.8	0.7	
RBAIVC	-20	340	-40	1550	130	198.5	193	60.1	4.8	0.7	
RCAIVC	-20	340	-30	1550	130	198.5	193	60.1	4.8	0.7	
RDAIVC	-20	340	-20	1550	130	198.5	193	60.1	4.8	0.7	
REAIVC	-20	340	-10	1550	130	198.5	193	60.1	4.8	0.7	
RFAIVC	-20	340	0	1550	130	198.5	193	60.1	4.8	0.7	
RGAIVC	-20	340	10	1500	120	198.5	193	60.1	4.8	0.7	
RHAIVC	-20	340	20	1500	120	198.5	193	60.1	4.8	0.7	
RIAIVC	-20	340	30	1500	120	198.5	193	60.1	4.8	0.7	
RJAIVC	-20	340	40	1500	120	198.5	193	60.1	4.8	0.7	break

Filename	Langmuir Probe Position (mm)			Power (W)		Matching Network		Magnet		Pressure	notes
	Vert	Axial	rad	Input	reflected	loading	tuning	cur(A)	Vol (V)	(mtorr)	
RAAAVB	-10	180	-50	1550	140	198.5	193	60.1	4.8	0.7	
RBAAVB	-10	180	-40	1550	140	198.5	193	60.1	4.8	0.7	
RCAAVB	-10	180	-30	1550	140	198.5	193	60.1	4.8	0.7	
RDAAVB	-10	180	-20	1550	145	198.5	193	60.1	4.8	0.7	
REAAVB	-10	180	-10	1550	145	198.5	193	60.1	4.8	0.7	
RFAAVB	-10	180	0	1550	145	198.5	193	60.1	4.8	0.7	
RGAAVB	-10	180	10	1550	145	198.5	193	60.1	4.8	0.7	
RHAAVB	-10	180	20	1550	140	198.5	193	60.1	4.9	0.7	
RIAAVB	-10	180	30	1550	140	198.5	193	60.1	4.9	0.7	
RJAAVB	-10	180	40	1550	140	198.5	193	60.1	4.9	0.7	
RAABVB	-10	200	-50	1550	135	198.5	193	60.1	4.9	0.7	
RBABVB	-10	200	-40	1550	135	198.5	193	60.1	4.9	0.7	
RCABVB	-10	200	-30	1550	135	198.5	193	60.1	4.9	0.7	
RDABVB	-10	200	-20	1550	135	198.5	193	60.1	4.9	0.7	
REABVB	-10	200	-10	1550	135	198.5	193	60.1	4.9	0.7	
RFABVB	-10	200	0	1550	135	198.5	193	60.1	4.9	0.7	
RGABVB	-10	200	10	1550	135	198.5	193	60.1	4.9	0.7	
RHABVB	-10	200	20	1550	140	198.5	193	60.1	4.9	0.7	
RIABVB	-10	200	30	1550	140	198.5	193	60.1	4.9	0.7	
RJABVB	-10	200	40	1550	140	198.5	193	60.1	4.9	0.7	
RAACVB	-10	220	-50	1550	135	198.5	193	60.1	4.9	0.7	
RBACVB	-10	220	-40	1550	135	198.5	193	60.1	4.9	0.7	
RCACVB	-10	220	-30	1550	135	198.5	193	60.1	4.9	0.7	
RDACVB	-10	220	-20	1550	130	198.5	193	60.1	4.9	0.7	
REACVB	-10	220	-10	1550	130	198.5	193	60.1	4.9	0.7	
RFACVB	-10	220	0	1550	130	198.5	193	60.1	4.9	0.7	
RGACVB	-10	220	10	1550	130	198.5	193	60.1	4.9	0.7	
RHACVB	-10	220	20	1550	130	198.5	193	60.1	5	0.7	
RIACVB	-10	220	30	1550	130	198.5	193	60.1	5	0.7	
RJACVB	-10	220	40	1550	130	198.5	193	60.1	5	0.7	break
RAADVB	-10	240	-50	1550	145	198.5	193	60.1	4.9	0.7	
RBADVB	-10	240	-40	1550	145	198.5	193	60.1	4.9	0.7	
RCADVB	-10	240	-30	1550	140	198.5	193	60.1	4.9	0.7	
RDADVB	-10	240	-20	1550	140	198.5	193	60.1	4.9	0.7	
READVB	-10	240	-10	1550	140	198.5	193	60.1	5	0.7	
RFADVB	-10	240	0	1550	140	198.5	193	60.1	5	0.7	
RGADVB	-10	240	10	1550	140	198.5	193	60.1	5	0.7	
RHADVB	-10	240	20	1550	140	198.5	193	60.1	5	0.7	
R1ADVB	-10	240	30	1550	140	198.5	193	60.1	5	0.7	
RJADVB	-10	240	40	1550	140	198.5	193	60.1	5	0.7	
RAAEVB	-10	260	-50	1550	135	198.5	193	60.1	5	0.7	
RBAEVB	-10	260	-40	1550	140	198.5	193	60.1	5	0.7	
RCAEVB	-10	260	-30	1550	140	198.5	193	60.1	5	0.7	
RDAEVB	-10	260	-20	1550	140	198.5	193	60.1	5	0.7	
REAEVB	-10	260	-10	1550	140	198.5	193	60.1	5	0.7	
RFAEVB	-10	260	0	1550	140	198.5	193	60.1	5	0.7	
RGAEVB	-10	260	10	1550	140	198.5	193	60.1	5	0.7	
RHAEVB	-10	260	20	1550	140	198.5	193	60.1	5	0.7	
RIAEVB	-10	260	30	1550	140	198.5	193	60.1	5	0.7	
RJAEVB	-10	260	40	1550	140	198.5	193	60.1	5	0.7	
RAAFVB	-10	280	-50	1550	135	198.5	193	60.1	5	0.7	
RBAFVB	-10	280	-40	1550	135	198.5	193	60.1	5	0.7	
RCAFVB	-10	280	-30	1550	135	198.5	193	60.1	5	0.7	
RDAFVB	-10	280	-20	1550	135	198.5	193	60.1	5	0.7	
REAFVB	-10	280	-10	1550	135	198.5	193	60.1	5	0.7	
RFAFVB	-10	280	0	1550	135	198.5	193	60.1	5	0.7	
RGAFVB	-10	280	10	1550	135	198.5	193	60.1	5	0.7	
RHAFVB	-10	280	20	1550	135	198.5	193	60.1	5	0.7	
RIAFVB	-10	280	30	1550	130	198.5	193	60.1	5	0.7	
RJAFVB	-10	280	40	1550	130	198.5	193	60.1	5	0.7	break

Filename	Langmuir Probe Position (mm)			Power (W)		Matching Network		Magnet		Pressure	notes
	Vert	Axial	rad	Input	reflected	loading	tuning	cur(A)	Vol (V)	(mtorr)	
RAAGVB	-10	300	-50	1550	145	198.5	193	60.1	5.1	0.7	didn't turn off
RBAGVB	-10	300	-40	1550	145	198.5	193	60.1	5.1	0.7	magnet supply
RCAGVB	-10	300	-30	1550	145	198.5	193	60.1	5.1	0.7	for break
RDAGVB	-10	300	-20	1550	140	198.5	193	60.1	5.1	0.7	
REAGVB	-10	300	-10	1550	140	198.5	193	60.1	5.1	0.7	
RFAGVB	-10	300	0	1550	140	198.5	193	60.1	5.1	0.7	
RGAGVB	-10	300	10	1550	140	198.5	193	60.1	5.1	0.7	
RHAGVB	-10	300	20	1550	140	198.5	193	60.1	5.1	0.7	
RIAGVB	-10	300	30	1550	140	198.5	193	60.1	5.1	0.7	
RJAGVB	-10	300	40	1550	140	198.5	193	60.1	5.1	0.7	
RAAHVB	-10	320	-50	1550	140	198.5	193	60.1	5.1	0.7	
RBAHVB	-10	320	-40	1550	140	198.5	193	60.1	5.1	0.7	
RCAHVB	-10	320	-30	1550	140	198.5	193	60.1	5.1	0.7	
RDAHVB	-10	320	-20	1550	140	198.5	193	60.1	5.1	0.7	
REAHVB	-10	320	-10	1550	140	198.5	193	60.1	5.1	0.7	
RFAHVB	-10	320	0	1550	140	198.5	193	60.1	5.1	0.7	
RGAHVB	-10	320	10	1550	140	198.5	193	60.1	5.1	0.7	
RHAHVB	-10	320	20	1550	140	198.5	193	60.1	5.1	0.7	
RIAHVB	-10	320	30	1550	140	198.5	193	60.1	5.1	0.7	
RJAHVB	-10	320	40	1550	140	198.5	193	60.1	5.1	0.7	
RAAIVB	-10	340	-50	1550	140	198.5	193	60.1	5.1	0.7	
RBAIVB	-10	340	-40	1550	140	198.5	193	60.1	5.1	0.7	
RCAIVB	-10	340	-30	1550	140	198.5	193	60.1	5.1	0.7	
RDAIVB	-10	340	-20	1550	140	198.5	193	60.1	5.1	0.7	
REAIVB	-10	340	-10	1550	140	198.5	193	60.1	5.2	0.7	
RFAIVB	-10	340	0	1550	140	198.5	193	60.1	5.2	0.7	
RGAIVB	-10	340	10	1550	140	198.5	193	60.1	5.2	0.7	
RHAIVB	-10	340	20	1550	140	198.5	193	60.1	5.2	0.7	
RIAIVB	-10	340	30	1550	140	198.5	193	60.1	5.2	0.7	
RJAIVB	-10	340	40	POINT MISSING							break
RAAAVA	0	180	-50	1500	110	198.5	193	60.1	5.1	0.7	
RBAAVA	0	180	-40	1500	110	198.5	193	60.1	5.1	0.7	
RCAAVA	0	180	-30	1500	110	198.5	193	60.1	5.1	0.7	
RDAAVA	0	180	-20	1500	110	198.5	193	60.1	5.1	0.7	
REAAVA	0	180	-10	1500	110	198.5	193	60.1	5.1	0.7	
RFAAVA	0	180	0	1500	110	198.5	193	60.1	5.1	0.7	
RGAAVA	0	180	10	1500	110	198.5	193	60.1	5.1	0.7	
RHAAVA	0	180	20	1500	110	198.5	193	60.1	5.1	0.7	
RIAAVA	0	180	30	1500	110	198.5	193	60.1	5.2	0.7	
RJAAVA	0	180	40	1500	110	198.5	193	60.1	5.2	0.7	
RAABVA	0	200	-50	1500	100	198.5	193	60.1	5.2	0.7	
RBABVA	0	200	-40	1500	100	198.5	193	60.1	5.2	0.7	
RCABVA	0	200	-30	1500	100	198.5	193	60.1	5.2	0.7	
RDABVA	0	200	-20	1500	100	198.5	193	60.1	5.2	0.7	
REABVA	0	200	-10	1500	100	198.5	193	60.1	5.2	0.7	
RFABVA	0	200	0	1500	100	198.5	193	60.1	5.2	0.7	
RGABVA	0	200	10	1500	100	198.5	193	60.1	5.2	0.7	
RHABVA	0	200	20	1500	100	198.5	193	60.1	5.2	0.7	
RIABVA	0	200	30	1500	100	198.5	193	60.1	5.1	0.7	
RJABVA	0	200	40	1500	100	198.5	193	60.1	5.1	0.7	
RAACVA	0	220	-50	1500	100	198.5	193	60.1	5.2	0.7	
RBACVA	0	220	-40	1500	100	198.5	193	60.1	5.2	0.7	
RCACVA	0	220	-30	1500	95	198.5	193	60.1	5.2	0.7	
RDACVA	0	220	-20	1500	95	198.5	193	60.1	5.2	0.7	
REACVA	0	220	-10	1500	95	198.5	193	60.1	5.2	0.7	
RFACVA	0	220	0	1500	95	198.5	193	60.1	5.2	0.7	
RGACVA	0	220	10	1500	95	198.5	193	60.1	5.2	0.7	
RHACVA	0	220	20	1500	95	198.5	193	60.1	5.2	0.7	
RIACVA	0	220	30	1500	95	198.5	193	60.1	5.2	0.7	
RJACVA	0	220	40	1500	95	198.5	193	60.1	5.2	0.7	break

Filename	Langmuir Probe Position (mm)			Power (W)		Matching Network		Magnet		Pressure	notes
	Vert	Axial	rad	Input	reflected	loading	tuning	cur(A)	Vol (V)	(mtorr)	
RAADVA	0	240	-50	1500	110	198.5	193	60.1	5.1	0.7	
RBADVA	0	240	-40	1500	110	198.5	193	60.1	5.1	0.7	
RCADVA	0	240	-30	1500	110	198.5	193	60.1	5.1	0.7	
RDADVA	0	240	-20	1500	110	198.5	193	60.1	5.1	0.7	
READVA	0	240	-10	1500	110	198.5	193	60.1	5.1	0.7	
RFADVA	0	240	0	1500	110	198.5	193	60.1	5.1	0.7	
RGADVA	0	240	10	1500	110	198.5	193	60.1	5.1	0.7	
RHADVA	0	240	20	1500	110	198.5	193	60.1	5.1	0.7	
RIADVA	0	240	30	1500	110	198.5	193	60.1	5.1	0.7	
RJADVA	0	240	40	1500	110	198.5	193	60.1	5.1	0.7	
RAAEVA	0	260	-50	1500	100	198.5	193	60.1	5.2	0.7	
RBAEVA	0	260	-40	1500	100	198.5	193	60.1	5.2	0.7	
RCAEVA	0	260	-30	1500	100	198.5	193	60.1	5.2	0.7	
RDAEVA	0	260	-20	1500	100	198.5	193	60.1	5.2	0.7	
REAEVA	0	260	-10	1500	100	198.5	193	60.1	5.2	0.7	
RFAEVA	0	260	0	1500	100	198.5	193	60.1	5.2	0.7	
RGAEVA	0	260	10	1500	100	198.5	193	60.1	5.2	0.7	
RHAEVA	0	260	20	1500	100	198.5	193	60.1	5.2	0.7	
RIAEVA	0	260	30	1500	100	198.5	193	60.1	5.2	0.7	
RJAEVA	0	260	40	1500	100	198.5	193	60.1	5.2	0.7	
RAAFVA	0	280	-50	1500	100	198.5	193	60.1	5.2	0.7	
RBAFVA	0	280	-40	1500	100	198.5	193	60.1	5.2	0.7	
RCAFVA	0	280	-30	1500	100	198.5	193	60.1	5.2	0.7	
RDAFVA	0	280	-20	1500	100	198.5	193	60.1	5.2	0.7	
REAFVA	0	280	-10	1500	100	198.5	193	60.1	5.2	0.7	
RFAFVA	0	280	0	1500	100	198.5	193	60.1	5.2	0.7	
RGAFVA	0	280	10	1500	100	198.5	193	60.1	5.2	0.7	
RHAFVA	0	280	20	1500	100	198.5	193	60.1	5.2	0.7	
RIAFVA	0	280	30	1500	100	198.5	193	60.1	5.2	0.7	
RJAFVA	0	280	40	1500	100	198.5	193	60.1	5.2	0.7	break
RAAGVA	0	300	-50	1500	120	198.5	193	60.1	5.1	0.7	
RBAGVA	0	300	-40	1500	120	198.5	193	60.1	5.1	0.7	
RCAGVA	0	300	-30	1500	110	198.5	193	60.1	5.1	0.7	
RDAGVA	0	300	-20	1500	110	198.5	193	60.1	5.1	0.7	
REAGVA	0	300	-10	1500	110	198.5	193	60.1	5.1	0.7	
RFAGVA	0	300	0	1500	110	198.5	193	60.1	5.1	0.7	
RGAGVA	0	300	10	1500	110	198.5	193	60.1	5.1	0.7	
RHAGVA	0	300	20	1500	110	198.5	193	60.1	5.1	0.7	
RIAGVA	0	300	30	1500	110	198.5	193	60.1	5.2	0.7	
RJAGVA	0	300	40	1500	110	198.5	193	60.1	5.1	0.7	
RAAHVA	0	320	-50	1500	110	198.5	193	60.1	5.1	0.7	
RBAHVA	0	320	-40	1500	110	198.5	193	60.1	5.1	0.7	
RCAHVA	0	320	-30	1500	110	198.5	193	60.1	5.1	0.7	
RDAHVA	0	320	-20	1500	110	198.5	193	60.1	5.1	0.7	
REAHVA	0	320	-10	1500	110	198.5	193	60.1	5.1	0.7	
RFAHVA	0	320	0	1500	110	198.5	193	60.1	5.1	0.7	
RGAHVA	0	320	10	1500	110	198.5	193	60.1	5.1	0.7	
RHAHVA	0	320	20	1500	110	198.5	193	60.1	5.1	0.7	
RIAHVA	0	320	30	1500	110	198.5	193	60.1	5.1	0.7	
RJAHVA	0	320	40	1500	110	198.5	193	60.1	5.1	0.7	
RAAIVA	0	340	-50	1500	110	198.5	193	60.1	5.2	0.7	
RBAIVA	0	340	-40	1500	110	198.5	193	60.1	5.2	0.7	
RCAIVA	0	340	-30	1500	100	198.5	193	60.1	5.2	0.7	
RDAIVA	0	340	-20	1500	100	198.5	193	60.1	5.2	0.7	
REAIVA	0	340	-10	1500	100	198.5	193	60.1	5.2	0.7	
RFAIVA	0	340	0	1500	100	198.5	193	60.1	5.2	0.7	
RGAIVA	0	340	10	1500	100	198.5	193	60.1	5.2	0.7	
RHAIVA	0	340	20	1500	100	198.5	193	60.1	5.2	0.7	
RIAIVA	0	340	30	1500	100	198.5	193	60.1	5.2	0.7	
RJAIVA	0	340	40	1500	100	198.5	193	60.1	5.2	0.7	

Table C.4: Testing Matrix for Plasma Characterization: Ion Energy Distribution Functions

Filename	Repel Voltage	Supress voltage	Axial	Power (watts) input	Power (watts) reflected	Matching Network Loading	Matching Network Tuning	Magnets Cur (A)	Magnets Vol (V)	Pressure (mtorr)	LP filenam	notes
9/18/08												
	-60	-10	240	800								
A240	-57.2	-11.2	240	850	40	-	-	58.2	4	0.7	A240LP	10 mA q break
A230	-57.2	-11.2	230	850	45	-	-	58.4	4	0.7	A230LP	
A220	-57.2	-11.2	220	850	50	-	-	58.4	4	0.8	A220LP	
A210	-57.2	-11.2	210	850	45			60.1	4.2	0.9	A210LP	
A200	-57.2	-11.2	200	850	40	-	-	59.1	4.1	0.7	A200LP	lost the plasma scans 1 and 2 of LP good no sup sweep
A190	-57.2	-11.2	190	850	45	-	-	60	4.2	0.7	A190LP	
A180	-57.2	-11.2	180	850	45	-	-	60	4.2	0.75	A180LP	
A170	-57.2	-11.2	170	850	45	-	-	60	4.2	0.75	A170LP	break
A160	-57.2	-11.2	160	825	25	-	-	59.4	4.2	0.7	A160LP	
A150	-57.2	-11.2	148	850	45	-	-	60	4.3	0.7	A150LP	position off
A140	-57.2	-11.2	138	850	45	-	-	60	4.3	0.7	A140LP	position off
A130	-57.2	-11.2	130	850	45	-	-	60	4.3	0.8	A130LP	
A120	-57.2	-11.2	120	850	45	-	-	60	4.3	0.8	A120LP	no sup sweep
A110	-57	-11.1	110	825	25	`	`	59.3	4.2	0.7	A110LP	
A100	-57	-11.1	100	825	25	-	-	59.3	4.2	0.7	A100LP	
A90	-57	-11.1	90	850	40	-	-	60.1	4.3	0.8	A90LP	
A80	-57	-11.1	80	850	40	-	-	60.1	4.3	0.8	A80LP	no sup sweep
A70	-57	-11.1	70	825	25	-	-	59.5	4.2	0.7	A70LP	
A60	-57	-11.1	60	850	50	-	-	60.1	4.3	0.7	A60LP	
A50	-57	-11.1	50	850	50	-	-	60.1	4.3	0.7	A50LP	
A40	-57	-11.1	40	850	50	-	-	60.1	4.3	0.8	A40LP	no sup swee

Table C.5: Testing Matrix for Plasma Density Reduction Measurements with the Langmuir Probe

Filename	LP position (mm) Vert	Axial	Rad	Recomm Amps	Volts	Power (watts) input	reflected	Matching Network Loading	Tuning	Magnets Cur (A)	Vol (V)	Pressure (mtorr)	notes
RBAJVI0A	-70	350	-40	0	0	1500	70	197	198	60.1	5	0.7	1 mA
RCAJVI0A	-70	350	-30	0	0	1500	70	197	198	60.1	5	0.7	
RDAJVI0A	-70	350	-20	0	0	1500	70	197	198	60.1	5	0.7	
REAJVI0A	-70	350	-10	0	0	1500	70	197	198	60.1	5	0.7	
RFAJVI0A	-70	350	0	0	0	1500	70	197	198	60.1	5	0.7	
RBAKVI0A	-70	360	-40	0	0	1500	70	197	198	60.1	5	0.7	
RCAKVI0A	-70	360	-30	0	0	1500	70	197	198	60.1	5	0.7	
RDAKVI0A	-70	360	-20	0	0	1500	70	197	198	60.1	5	0.7	
REAKVI0A	-70	360	-10	0	0	1500	70	197	198	60.1	5	0.7	
RFAKVI0A	-70	360	0	0	0	1500	70	197	198	60.1	5	0.7	
RBALVI0A	-70	370	-40	0	0	1500	65	197	198	60.1	5	0.7	
RCALVI0A	-70	370	-30	0	0	1500	65	197	198	60.1	5	0.7	
RDALVI0A	-70	370	-20	0	0	1500	65	197	198	60.1	5	0.7	
REALVI0A	-70	370	-10	0	0	1500	65	197	198	60.1	5	0.7	
RFALVI0A	-70	370	0	0	0	1500	65	197	198	60.1	5	0.7	
RBAMVI0A	-70	380	-40	0	0	1500	70	197	198	60.1	5	0.7	
RCAMVI0A	-70	380	-30	0	0	1500	70	197	198	60.1	5	0.7	
RDAMVI0A	-70	380	-20	0	0	1500	70	197	198	60.1	5	0.7	
REAMVI0A	-70	380	-10	0	0	1500	70	197	198	60.1	5	0.7	
RFAMVI0A	-70	380	0	0	0	1500	70	197	198	60.1	5	0.7	
RBANVI0A	-70	390	-40	0	0	1500	70	197	198	60.1	5.1	0.7	
RCANVI0A	-70	390	-30	0	0	1500	70	197	198	60.1	5.1	0.7	
RDANVI0A	-70	390	-20	0	0	1500	70	197	198	60.1	5.1	0.7	
REANVI0A	-70	390	-10	0	0	1500	70	197	198	60.1	5.1	0.7	
RFANVI0A	-70	390	0	0	0	1500	70	197	198	60.1	5.1	0.7	break
RBAJVJ0A	-75	350	-40	0	0	1500	95	197	198	60	5.1	0.7	
RCAJVJ0A	-75	350	-30	0	0	1500	90	197	198	60	5.1	0.7	
RDAJVJ0A	-75	350	-20	0	0	1500	90	197	198	60	5.1	0.7	
REAJVJ0A	-75	350	-10	0	0	1500	90	197	198	60	5.1	0.7	
RFAJVJ0A	-75	350	0	0	0	1500	90	197	198	60	5.1	0.7	
RBAKVJ0A	-75	360	-40	0	0	1500	90	197	198	60	5.1	0.7	
RCAKVJ0A	-75	360	-30	0	0	1500	90	197	198	60	5.1	0.7	
RDAKVJ0A	-75	360	-20	0	0	1500	90	197	198	60	5.1	0.7	
REAKVJ0A	-75	360	-10	0	0	1500	90	197	198	60	5.1	0.7	
RFAKVJ0A	-75	360	0	0	0	1500	90	197	198	60	5.1	0.7	
RBALVJ0A	-75	370	-40	0	0	1500	85	197	198	60	5.1	0.7	
RCALVJ0A	-75	370	-30	0	0	1500	85	197	198	60	5.1	0.7	
RDALVJ0A	-75	370	-20	0	0	1500	85	197	198	60	5.1	0.7	
REALVJ0A	-75	370	-10	0	0	1500	85	197	198	60	5.1	0.7	
RFALVJ0A	-75	370	0	0	0	1500	85	197	198	60	5.1	0.7	
RBAMVJ0A	-75	380	-40	0	0	1500	85	197	198	60	5.1	0.7	
RCAMVJ0A	-75	380	-30	0	0	1500	85	197	198	60	5.1	0.7	
RDAMVJ0A	-75	380	-20	0	0	1500	85	197	198	60	5.1	0.7	
REAMVJ0A	-75	380	-10	0	0	1500	85	197	198	60	5.1	0.7	
RFAMVJ0A	-75	380	0	0	0	1500	85	197	198	60	5.1	0.7	
RBANVJ0A	-75	390	-40	0	0	1500	85	197	198	60	5.1	0.7	
RCANVJ0A	-75	390	-30	0	0	1500	85	197	198	60	5.2	0.7	
RDANVJ0A	-75	390	-20	0	0	1500	85	197	198	60	5.2	0.7	
REANVJ0A	-75	390	-10	0	0	1500	85	197	198	60	5.2	0.7	
RFANVJ0A	-75	390	0	0	0	1500	85	197	198	60	5.2	0.7	break
RBAJVI1A	-70	350	-40	150	0	1500	75	197	198	60	5.2	0.7	reads 150
RCAJVI1A	-70	350	-30	150	0	1500	75	197	198	60	5.2	0.7	on fluke
RDAJVI1A	-70	350	-20	150	0	1500	75	197	198	60	5.2	0.7	
REAJVI1A	-70	350	-10	150	0	1500	70	197	198	60	5.3	0.7	
RFAJVI1A	-70	350	0	150	0	1500	70	197	198	60	5.3	0.7	
RBAKVI1A	-70	360	-40	150	0	1500	65	197	198	60	5.3	0.7	
RCAKVI1A	-70	360	-30	150	0	1500	65	197	198	60	5.3	0.7	
RDAKVI1A	-70	360	-20	150	0	1500	65	197	198	60	5.3	0.7	
REAKVI1A	-70	360	-10	150	0	1500	65	197	198	60	5.3	0.7	

Filename	LP position (mm) Vert	Axial	Rad	Recomm Amps	Volts	Power (watts) input	reflected	Matching Network Loading	Tuning	Magnets Cur (A)	Vol (V)	Pressure (mtorr)	notes
RFAKVI1A	-70	360	0	150	0	1500	65	197	198	60	5.3	0.7	
RBALVI1A	-70	370	-40	150	0	1500	65	197	198	60	5.3	0.7	
RCALVI1A	-70	370	-30	150	0	1500	65	197	198	60	5.3	0.7	
RDALVI1A	-70	370	-20	150	0	1500	65	197	198	60	5.3	0.7	
REALVI1A	-70	370	-10	150	0	1500	65	197	198	60	5.4	0.7	
RFALVI1A	-70	370	0	150	0	1500	65	197	198	60	5.4	0.7	
RBAMVI1A	-70	380	-40	150	0	1500	65	197	198	60	5.4	0.7	
RCAMVI1A	-70	380	-30	150	0	1500	65	197	198	60	5.4	0.7	
RDAMVI1A	-70	380	-20	150	0	1500	65	197	198	60	5.4	0.7	
REAMVI1A	-70	380	-10	150	0	1500	65	197	198	60	5.4	0.7	
RFAMVI1A	-70	380	0	150	0	1500	65	197	198	60	5.4	0.7	
RBANVI1A	-70	390	-40	150	0	1500	65	197	198	60	5.3	0.7	
RCANVI1A	-70	390	-30	150	0	1500	65	197	198	60	5.3	0.7	
RDANVI1A	-70	390	-20	150	0	1500	65	197	198	60	5.3	0.7	
REANVI1A	-70	390	-10	150	0	1500	65	197	198	60	5.3	0.7	
RFANVI1A	-70	390	0	150	0	1500	65	197	198	60	5.3	0.7	break
RBAJVJ1A	-75	350	-40	150	0	1500	90	197	198	60	5.2	0.7	
RCAJVJ1A	-75	350	-30	150	0	1500	90	197	198	60	5.2	0.7	
RDAJVJ1A	-75	350	-20	150	0	1500	85	197	198	60	5.2	0.7	
REAJVJ1A	-75	350	-10	150	0	1500	85	197	198	60	5.2	0.7	
RFAJVJ1A	-75	350	0	150	0	1500	80	197	198	60	5.3	0.7	
RBAKVJ1A	-75	360	-40	150	0	1500	80	197	198	60	5.3	0.7	
RCAKVJ1A	-75	360	-30	150	0	1500	80	197	198	60	5.3	0.7	
RDAKVJ1A	-75	360	-20	150	0	1500	80	197	198	60	5.3	0.7	
REAKVJ1A	-75	360	-10	150	0	1500	80	197	198	60	5.3	0.7	
RFAKVJ1A	-75	360	0	150	0	1500	80	197	198	60	5.3	0.7	
RBALVJ1A	-75	370	-40	150	0	1500	80	197	198	60	5.3	0.7	
RCALVJ1A	-75	370	-30	150	0	1500	80	197	198	60	5.3	0.7	
RDALVJ1A	-75	370	-20	150	0	1500	75	197	198	60	5.3	0.7	
REALVJ1A	-75	370	-10	150	0	1500	75	197	198	60	5.3	0.7	
RFALVJ1A	-75	370	0	150	0	1500	75	197	198	60	5.3	0.7	
RBAMVJ1A	-75	380	-40	150	0	1500	75	197	198	60	5.3	0.7	
RCAMVJ1A	-75	380	-30	150	0	1500	75	197	198	60	5.3	0.7	
RDAMVJ1A	-75	380	-20	150	0	1500	75	197	198	60	5.3	0.7	
REAMVJ1A	-75	380	-10	150	0	1500	75	197	198	60	5.3	0.7	
RFAMVJ1A	-75	380	0	150	0	1500	75	197	198	60	5.3	0.7	
RBANVJ1A	-75	390	-40	150	0	1500	75	197	198	60	5.3	0.7	
RCANVJ1A	-75	390	-30	150	0	1500	75	197	198	60	5.3	0.7	
RDANVJ1A	-75	390	-20	150	0	1500	75	197	198	60	5.3	0.7	
REANVJ1A	-75	390	-10	150	0	1500	75	197	198	60	5.3	0.7	
RFANVJ1A	-75	390	0	150	0	1500	75	197	198	60	5.3	0.7	break
RBAJVI2A	-70	350	-40	225	0	1500	80	197	194.5	60	5.4	0.7	
RCAJVI2A	-70	350	-30	225	0	1500	75	197	194.5	60	5.5	0.7	
RDAJVI2A	-70	350	-20	225	0	1500	75	197	194.5	60	5.5	0.7	
REAJVI2A	-70	350	-10	225	0	1500	75	197	194.5	60	5.6	0.7	
RFAJVI2A	-70	350	0	225	0	1500	75	197	194.5	60	5.6	0.7	
RBAKVI2A	-70	360	-40	225	0	1500	75	197	194.5	60	5.6	0.7	
RCAKVI2A	-70	360	-30	225	0	1500	75	197	194.5	60	5.6	0.7	
RDAKVI2A	-70	360	-20	225	0	1500	75	197	194.5	60	5.6	0.7	
REAKVI2A	-70	360	-10	225	0	1500	75	197	194.5	60	5.6	0.7	
RFAKVI2A	-70	360	0	225	0	1500	75	197	194.5	60	5.6	0.7	
RBALVI2A	-70	370	-40	225	0	1500	75	197	194.5	60	5.6	0.7	
RCALVI2A	-70	370	-30	225	0	1500	75	197	194.5	60	5.6	0.7	
RDALVI2A	-70	370	-20	225	0	1500	75	197	194.5	60	5.6	0.7	
REALVI2A	-70	370	-10	225	0	1500	75	197	194.5	60	5.6	0.7	
RFALVI2A	-70	370	0	225	0	1500	75	197	194.5	60	5.6	0.7	
RBAMVI2A	-70	380	-40	225	0	1500	75	197	194.5	60	5.6	0.7	
RCAMVI2A	-70	380	-30	225	0	1500	75	197	194.5	60	5.6	0.7	

Filename	LP position (mm) Vert	Axial	Rad	Recomm Amps	Volts	Power (watts) input	reflected	Matching Network Loading	Tuning	Magnets Cur (A)	Vol (V)	Pressure (mtorr)	notes
RDAMVI2A	-70	380	-20	225	0	1500	75	197	194.5	60	5.6	0.7	
REAMVI2A	-70	380	-10	225	0	1500	75	197	194.5	60	5.6	0.7	
RFAMVI2A	-70	380	0	225	0	1500	75	197	194.5	60	5.6	0.7	
RBANVI2A	-70	390	-40	225	0	1500	75	197	194.5	60	5.6	0.7	
RCANVI2A	-70	390	-30	225	0	1500	75	197	194.5	60	5.6	0.7	
RDANVI2A	-70	390	-20	225	0	1500	75	197	194.5	60	5.6	0.7	
REANVI2A	-70	390	-10	225	0	1500	75	197	194.5	60	5.6	0.7	
RFANVI2A	-70	390	0	225	0	1500	75	197	194.5	60	5.6	0.7	break
RBAJVI2A	-75	350	-40	225	0	1500	90	197	194.5	60	5.3	0.7	
RCAJVI2A	-75	350	-30	225	0	1500	85	197	194.5	60	5.4	0.7	
RDAJVI2A	-75	350	-20	225	0	1500	85	197	194.5	60	5.4	0.7	
REAJVI2A	-75	350	-10	225	0	1500	75	197	194.5	60	5.4	0.7	
RFAJVI2A	-75	350	0	225	0	1500	75	197	194.5	60	5.4	0.7	-1 rad
RBAKVI2A	-75	360	-40	225	0	1500	75	197	194.5	60	5.4	0.7	
RCAKVI2A	-75	360	-30	225	0	1500	75	197	194.5	60	5.5	0.7	
RDAKVI2A	-75	360	-20	225	0	1500	75	197	194.5	60	5.5	0.7	
REAKVI2A	-75	360	-10	225	0	1500	75	197	194.5	60	5.5	0.7	
RFAKVI2A	-75	360	0	225	0	1500	75	197	194.5	60	5.5	0.7	-1 rad
RBALVI2A	-75	370	-40	225	0	1500	75	197	194.5	60	5.5	0.7	
RCALVI2A	-75	370	-30	225	0	1500	75	197	194.5	60	5.5	0.7	
RDALVI2A	-75	370	-20	225	0	1500	75	197	194.5	60	5.5	0.7	
REALVI2A	-75	370	-10	225	0	1500	75	197	194.5	60	5.5	0.7	
RFALVI2A	-75	370	0	225	0	1500	75	197	194.5	60	5.5	0.7	
RBAMVI2A	-75	380	-40	225	0	1500	75	197	194.5	60	5.5	0.7	
RCAMVI2A	-75	380	-30	225	0	1500	75	197	194.5	60	5.5	0.7	
RDAMVI2A	-75	380	-20	225	0	1500	75	197	194.5	60	5.5	0.7	
REAMVI2A	-75	380	-10	225	0	1500	75	197	194.5	60	5.5	0.7	
RFAMVI2A	-75	380	0	225	0	1500	75	197	194.5	60	5.5	0.7	
RBANVI2A	-75	390	-40	225	0	1500	75	197	194.5	60	5.5	0.7	
RCANVI2A	-75	390	-30	225	0	1500	75	197	194.5	60	5.5	0.7	
RDANVI2A	-75	390	-20	225	0	1500	75	197	194.5	60	5.5	0.7	
REANVI2A	-75	390	-10	225	0	1500	75	197	194.5	60	5.5	0.7	
RFANVI2A	-75	390	0	225	0	1500	75	197	194.5	60	5.5	0.7	
RBAJVI3A	-70	350	-40	300	0	1500	60	197	198	60.1	5.2	0.7	
RCAJVI3A	-70	350	-30	300	0	1500	60	197	198	60.1	5.3	0.7	
RDAJVI3A	-70	350	-20	300	0	1500	60	197	198	60.1	5.3	0.7	
REAJVI3A	-70	350	-10	300	0	1500	60	197	198	60.1	5.3	0.7	
RFAJVI3A	-70	350	0	300	0	1500	60	197	198	60.1	5.3	0.7	
RBAKVI3A	-70	360	-40	300	0	1500	60	197	198	60.1	5.3	0.7	
RCAKVI3A	-70	360	-30	300	0	1500	60	197	198	60.1	5.3	0.7	
RDAKVI3A	-70	360	-20	300	0	1500	60	197	198	60.1	5.3	0.7	
REAKVI3A	-70	360	-10	300	0	1500	60	197	198	60.1	5.3	0.7	
RFAKVI3A	-70	360	0	300	0	1500	60	197	198	60.1	5.3	0.7	
RBALVI3A	-70	370	-40	300	0	1500	60	197	198	60.1	5.3	0.7	
RCALVI3A	-70	370	-30	300	0	1500	60	197	198	60.1	5.3	0.7	
RDALVI3A	-70	370	-20	300	0	1500	60	197	198	60.1	5.3	0.7	
REALVI3A	-70	370	-10	300	0	1500	60	197	198	60.1	5.3	0.7	
RFALVI3A	-70	370	0	300	0	1500	55	197	198	60.1	5.3	0.7	
RBAMVI3A	-70	380	-40	300	0	1500	55	197	198	60.1	5.3	0.7	
RCAMVI3A	-70	380	-30	300	0	1500	55	197	198	60.1	5.3	0.7	
RDAMVI3A	-70	380	-20	300	0	1500	55	197	198	60.1	5.3	0.7	
REAMVI3A	-70	380	-10	300	0	1500	55	197	198	60.1	5.3	0.7	
RFAMVI3A	-70	380	0	300	0	1500	55	197	198	60.1	5.3	0.7	.1 mA
RBANVI3A	-70	390	-40	300	0	1500	55	197	198	60.1	5.3	0.7	
RCANVI3A	-70	390	-30	300	0	1500	55	197	198	60.1	5.3	0.7	
RDANVI3A	-70	390	-20	300	0	1500	55	197	198	60.1	5.3	0.7	
REANVI3A	-70	390	-10	300	0	1500	55	197	198	60.1	5.3	0.7	
RFANVI3A	-70	390	0	300	0	1500	55	197	198	60.1	5.3	0.7	break

Filename	LP position (mm) Vert	Axial	Rad	Recomm Amps	Volts	Power (watts) input	reflected	Matching Network Loading	Tuning	Magnets Cur (A)	Vol (V)	Pressure (mtorr)	notes
RBAJVI3A	-75	350	-40	300	0	1500	65	197	198	60	5.2	0.7	
RCAJVI3A	-75	350	-30	300	0	1500	65	197	198	60	5.3	0.7	
RDAJVI3A	-75	350	-20	300	0	1500	65	197	198	60	5.3	0.7	
REAJVI3A	-75	350	-10	300	0	1500	65	197	198	60	5.3	0.7	
RFAJVI3A	-75	350	0	300	0	1500	60	197	198	60	5.6	0.7	-1 rad
RBAKVI3A	-75	360	-40	300	0	1500	60	197	198	60	5.6	0.7	
RCAKVI3A	-75	360	-30	300	0	1500	60	197	198	60	5.6	0.7	
RDAKVI3A	-75	360	-20	300	0	1500	60	197	198	60	5.6	0.7	
REAKVI3A	-75	360	-10	300	0	1500	60	197	198	60	5.6	0.7	
RFAKVI3A	-75	360	0	300	0	1500	60	197	198	60	5.6	0.7	-1 rad
RBALVI3A	-75	370	-40	300	0	1500	60	197	198	60	5.6	0.7	
RCALVI3A	-75	370	-30	300	0	1500	60	197	198	60	5.6	0.7	
RDALVI3A	-75	370	-20	300	0	1500	60	197	198	60	5.6	0.7	
REALVI3A	-75	370	-10	300	0	1500	60	197	198	60	5.5	0.7	
RFALVI3A	-75	370	0	300	0	1500	60	197	198	60	5.5	0.7	
RBAMVI3A	-75	380	-40	300	0	1500	55	197	198	60	5.4	0.7	
RCAMVI3A	-75	380	-30	300	0	1500	55	197	198	60	5.4	0.7	
RDAMVI3A	-75	380	-20	300	0	1500	55	197	198	60	5.4	0.7	
REAMVI3A	-75	380	-10	300	0	1500	55	197	198	60	5.5	0.7	
RFAMVI3A	-75	380	0	300	0	1500	55	197	198	60	5.5	0.7	
RBANVI3A	-75	390	-40	300	0	1500	55	197	198	60	5.4	0.7	
RCANVI3A	-75	390	-30	300	0	1500	55	197	198	60	5.4	0.7	
RDANVI3A	-75	390	-20	300	0	1500	55	197	198	60	5.4	0.7	
REANVI3A	-75	390	-10	300	0	1500	55	197	198	60	5.4	0.7	
RFANVI3A	-75	390	0	300	0	1500	55	197	198	60	5.3	0.7	break
RBAJVI1B	-70	350	-40	150	100	1500	95	197	194.5	59.9	5.5	0.7	
RCAJVI1B	-70	350	-30	150	100	1500	95	197	194.5	59.9	5.6	0.7	
RDAJVI1B	-70	350	-20	150	100	1500	95	197	194.5	59.9	5.6	0.7	
REAJVI1B	-70	350	-10	150	100	1500	95	197	194.5	59.9	5.6	0.7	
RFAJVI1B	-70	350	0	150	100	1500	90	197	194.5	59.9	5.5	0.7	
RBAKVI1B	-70	360	-40	150	100	1500	90	197	194.5	60	5.5	0.7	
RCAKVI1B	-70	360	-30	150	100	1500	90	197	194.5	60	5.5	0.7	
RDAKVI1B	-70	360	-20	150	100	1500	90	197	194.5	60	5.5	0.7	
REAKVI1B	-70	360	-10	150	100	1500	90	197	194.5	59.9	5.5	0.7	
RFAKVI1B	-70	360	0	150	100	1500	90	197	194.5	59.9	5.5	0.7	
RBALVI1B	-70	370	-40	150	100	1500	85	197	194.5	59.9	5.5	0.7	
RCALVI1B	-70	370	-30	150	100	1500	85	197	194.5	59.9	5.5	0.7	
RDALVI1B	-70	370	-20	150	100	1500	85	197	194.5	59.9	5.5	0.7	
REALVI1B	-70	370	-10	150	100	1500	85	197	194.5	59.9	5.5	0.7	
RFALVI1B	-70	370	0	150	100	1500	85	197	194.5	59.9	5.5	0.7	
RBAMVI1B	-70	380	-40	150	100	1500	85	197	194.5	59.9	5.5	0.7	
RCAMVI1B	-70	380	-30	150	100	1500	85	197	194.5	59.9	5.5	0.7	
RDAMVI1B	-70	380	-20	150	100	1500	85	197	194.5	59.9	5.5	0.7	
REAMVI1B	-70	380	-10	150	100	1500	85	197	194.5	59.9	5.5	0.7	
RFAMVI1B	-70	380	0	150	100	1500	85	197	194.5	59.9	5.5	0.7	
RBANVI1B	-70	390	-40	150	100	1500	85	197	194.5	59.9	5.5	0.7	
RCANVI1B	-70	390	-30	150	100	1500	85	197	194.5	59.9	5.5	0.7	
RDANVI1B	-70	390	-20	150	100	1500	85	197	194.5	59.9	5.5	0.7	
REANVI1B	-70	390	-10	150	100	1500	85	197	194.5	59.9	5.5	0.7	
RFANVI1B	-70	390	0	150	100	1500	85	197	194.5	59.9	5.5	0.7	break
RBAJVI1B	-75	350	-40	150	100	1500	100	197	194.5	60	5.3	0.7	
RCAJVI1B	-75	350	-30	150	100	1500	100	197	194.5	60	5.3	0.7	
RDAJVI1B	-75	350	-20	150	100	1500	95	197	194.5	60	5.4	0.7	
REAJVI1B	-75	350	-10	150	100	1500	95	197	194.5	60	5.4	0.7	
RFAJVI1B	-75	350	0	150	100	1500	95	197	194.5	60	5.4	0.7	
RBAKVI1B	-75	360	-40	150	100	1500	95	197	194.5	60	5.6	0.7	
RCAKVI1B	-75	360	-30	150	100	1500	95	197	194.5	60	5.6	0.7	
RDAKVI1B	-75	360	-20	150	100	1500	95	197	194.5	60	5.6	0.7	

Filename	LP position (mm)			Recomm		Power (watts)		Matching Network		Magnets		Pressure	notes
	Vert	Axial	Rad	Amps	Volts	input	reflected	Loading	Tuning	Cur (A)	Vol (V)	(mtorr)	
REAKVI1B	-75	360	-10	150	100	1500	95	197	194.5	60	5.6	0.7	
RFAKVI1B	-75	360	0	150	100	1500	95	197	194.5	60	5.6	0.7	
RBALVI1B	-75	370	-40	150	100	1500	95	197	194.5	60	5.6	0.7	
RCALVI1B	-75	370	-30	150	100	1500	95	197	194.5	60	5.6	0.7	
RDALVI1B	-75	370	-20	150	100	1500	95	197	194.5	60	5.6	0.7	
REALVI1B	-75	370	-10	150	100	1500	95	197	194.5	60	5.6	0.7	
RFALVI1B	-75	370	0	150	100	1500	95	197	194.5	60	5.6	0.7	
RBAMVI1B	-75	380	-40	150	100	1500	95	197	194.5	60	5.6	0.7	
RCAMVI1B	-75	380	-30	150	100	1500	95	197	194.5	60	5.6	0.7	
RDAMVI1B	-75	380	-20	150	100	1500	95	197	194.5	60	5.6	0.7	
REAMVI1B	-75	380	-10	150	100	1500	95	197	194.5	60	5.6	0.7	
RFAMVI1B	-75	380	0	150	100	1500	95	197	194.5	60	5.6	0.7	
RBANVI1B	-75	390	-40	150	100	1500	95	197	194.5	60	5.6	0.7	
RCANVI1B	-75	390	-30	150	100	1500	95	197	194.5	60	5.6	0.7	
RDANVI1B	-75	390	-20	150	100	1500	95	197	194.5	60	5.6	0.7	
REANVI1B	-75	390	-10	150	100	1500	95	197	194.5	60	5.6	0.7	
RFANVI1B	-75	390	0	150	100	1500	95	197	194.5	60	5.6	0.7	break
RBAJVI2B	-70	350	-40	225	100	1500	85	197	194.5	60	5.5	0.7	
RCAJVI2B	-70	350	-30	225	100	1500	80	197	194.5	60	5.6	0.7	
RDAJVI2B	-70	350	-20	225	100	1500	80	197	194.5	60	5.6	0.7	
REAJVI2B	-70	350	-10	225	100	1500	80	197	194.5	60	5.6	0.7	
RFAJVI2B	-70	350	0	225	100	1500	75	197	194.5	60	5.7	0.7	
RBAKVI2B	-70	360	-40	225	100	1500	75	197	194.5	60	5.6	0.7	
RCAKVI2B	-70	360	-30	225	100	1500	75	197	194.5	60	5.7	0.7	
RDAKVI2B	-70	360	-20	225	100	1500	75	197	194.5	60	5.7	0.7	
REAKVI2B	-70	360	-10	225	100	1500	75	197	194.5	60	5.7	0.7	
RFAKVI2B	-70	360	0	225	100	1500	75	197	194.5	60	5.7	0.7	
RBALVI2B	-70	370	-40	225	100	1500	75	197	194.5	60	5.6	0.7	
RCALVI2B	-70	370	-30	225	100	1500	75	197	194.5	60	5.6	0.7	
RDALVI2B	-70	370	-20	225	100	1500	75	197	194.5	60	5.6	0.7	
REALVI2B	-70	370	-10	225	100	1500	75	197	194.5	60	5.7	0.7	
RFALVI2B	-70	370	0	225	100	1500	75	197	194.5	60	5.7	0.7	
RBAMVI2B	-70	380	-40	225	100	1500	70	197	194.5	60	5.7	0.7	
RCAMVI2B	-70	380	-30	225	100	1500	70	197	194.5	60	5.7	0.7	
RDAMVI2B	-70	380	-20	225	100	1500	75	197	194.5	60	5.7	0.7	
REAMVI2B	-70	380	-10	225	100	1500	75	197	194.5	60	5.7	0.7	
RFAMVI2B	-70	380	0	225	100	1500	75	197	194.5	60	5.7	0.7	
RBANVI2B	-70	390	-40	225	100	1500	75	197	194.5	60	5.7	0.7	
RCANVI2B	-70	390	-30	225	100	1500	75	197	194.5	60	5.7	0.7	
RDANVI2B	-70	390	-20	225	100	1500	75	197	194.5	60	5.7	0.7	
REANVI2B	-70	390	-10	225	100	1500	75	197	194.5	60	5.7	0.7	
RFANVI2B	-70	390	0	225	100	1500	75	197	194.5	60	5.7	0.7	break
RBAJVI2B	-75	350	-40	225	100	1500	85	197	194.5	60	5.4	0.7	
RCAJVI2B	-75	350	-30	225	100	1500	85	197	194.5	60	5.4	0.7	
RDAJVI2B	-75	350	-20	225	100	1500	80	197	194.5	60	5.4	0.7	
REAJVI2B	-75	350	-10	225	100	1500	80	197	194.5	60	5.4	0.7	
RFAJVI2B	-75	350	0	225	100	1500	80	197	194.5	60	5.4	0.7	-1 rad
RBAKVI2B	-75	360	-40	225	100	1500	75	197	194.5	60	5.5	0.7	
RCAKVI2B	-75	360	-30	225	100	1500	75	197	194.5	60	5.5	0.7	
RDAKVI2B	-75	360	-20	225	100	1500	75	197	194.5	60	5.5	0.7	
REAKVI2B	-75	360	-10	225	100	1500	75	197	194.5	60	5.5	0.7	
RFAKVI2B	-75	360	0	225	100	1500	75	197	194.5	60	5.5	0.7	
RBALVI2B	-75	370	-40	225	100	1500	75	197	194.5	60	5.5	0.7	
RCALVI2B	-75	370	-30	225	100	1500	75	197	194.5	60	5.5	0.7	
RDALVI2B	-75	370	-20	225	100	1500	75	197	194.5	60	5.5	0.7	
REALVI2B	-75	370	-10	225	100	1500	75	197	194.5	60	5.5	0.7	
RFALVI2B	-75	370	0	225	100	1500	75	197	194.5	60	5.5	0.7	
RBAMVI2B	-75	380	-40	225	100	1500	75	197	194.5	60	5.5	0.7	

Filename	LP position (mm)			Recomm		Power (watts)		Matching Network		Magnets		Pressure	notes
	Vert	Axial	Rad	Amps	Volts	input	reflected	Loading	Tuning	Cur (A)	Vol (V)	(mtorr)	
RCAMVI2B	-75	380	-30	225	100	1500	75	197	194.5	60	5.5	0.7	
RDAMVI2B	-75	380	-20	225	100	1500	75	197	194.5	60	5.5	0.7	
REAMVI2B	-75	380	-10	225	100	1500	75	197	194.5	60	5.5	0.7	
RFAMVI2B	-75	380	0	225	100	1500	75	197	194.5	60	5.5	0.7	
RBANVI2B	-75	390	-40	225	100	1500	75	197	194.5	60	5.5	0.7	
RCANVI2B	-75	390	-30	225	100	1500	75	197	194.5	60	5.5	0.7	
RDANVI2B	-75	390	-20	225	100	1500	75	197	194.5	60	5.5	0.7	
REANVI2B	-75	390	-10	225	100	1500	75	197	194.5	60	5.5	0.7	
RFANVI2B	-75	390	0	225	100	1500	75	197	194.5	60	5.5	0.7	break
RBAJVI3B	-70	350	-40	300	100	1500	65	197	194.5	60	5.4	0.7	
RCAJVI3B	-70	350	-30	300	100	1500	65	197	194.5	60	5.4	0.7	
RDAJVI3B	-70	350	-20	300	100	1500	65	197	194.5	60	5.4	0.7	
REAJVI3B	-70	350	-10	300	100	1500	60	197	194.5	60	5.4	0.7	
RFAJVI3B	-70	350	0	300	100	1500	60	197	194.5	60	5.4	0.7	
RBAKVI3B	-70	360	-40	300	100	1500	60	197	194.5	60	5.5	0.7	
RCAKVI3B	-70	360	-30	300	100	1500	60	197	194.5	60	5.5	0.7	
RDAKVI3B	-70	360	-20	300	100	1500	60	197	194.5	60	5.5	0.7	
REAKVI3B	-70	360	-10	300	100	1500	60	197	194.5	60	5.5	0.7	
RFAKVI3B	-70	360	0	300	100	1500	60	197	194.5	60	5.5	0.7	
RBALVI3B	-70	370	-40	300	100	1500	60	197	194.5	60	5.5	0.7	
RCALVI3B	-70	370	-30	300	100	1500	60	197	194.5	60	5.5	0.7	
RDALVI3B	-70	370	-20	300	100	1500	60	197	194.5	60	5.5	0.7	
REALVI3B	-70	370	-10	300	100	1500	60	197	194.5	60	5.5	0.7	
RFALVI3B	-70	370	0	300	100	1500	60	197	194.5	60	5.5	0.7	
RBAMVI3B	-70	380	-40	300	100	1500	60	197	194.5	60	5.5	0.7	
RCAMVI3B	-70	380	-30	300	100	1500	60	197	194.5	60	5.5	0.7	
RDAMVI3B	-70	380	-20	300	100	1500	60	197	194.5	60	5.5	0.7	
REAMVI3B	-70	380	-10	300	100	1500	60	197	194.5	60	5.5	0.7	
RFAMVI3B	-70	380	0	300	100	1500	60	197	194.5	60	5.5	0.7	
RBANVI3B	-70	390	-40	300	100	1500	60	197	194.5	60	5.5	0.7	
RCANVI3B	-70	390	-30	300	100	1500	60	197	194.5	60	5.5	0.7	
RDANVI3B	-70	390	-20	300	100	1500	60	197	194.5	60	5.5	0.7	
REANVI3B	-70	390	-10	300	100	1500	60	197	194.5	60	5.5	0.7	
RFANVI3B	-70	390	0	300	100	1500	60	197	194.5	60	5.5	0.7	break
RBAJVI3B	-75	350	-40	300	100	1500	70	197	194.5	60	5.4	0.7	
RCAJVI3B	-75	350	-30	300	100	1500	65	197	194.5	60	5.4	0.7	
RDAJVI3B	-75	350	-20	300	100	1500	65	197	194.5	60	5.4	0.7	
REAJVI3B	-75	350	-10	300	100	1500	65	197	194.5	60	5.5	0.7	
RFAJVI3B	-75	350	0	300	100	1500	65	197	194.5	60	5.5	0.7	-1 rad
RBAKVI3B	-75	360	-40	300	100	1500	60	197	194.5	60	5.6	0.7	
RCAKVI3B	-75	360	-30	300	100	1500	60	197	194.5	60	5.6	0.7	
RDAKVI3B	-75	360	-20	300	100	1500	60	197	194.5	60	5.6	0.7	
REAKVI3B	-75	360	-10	300	100	1500	60	197	194.5	60	5.6	0.7	
RFAKVI3B	-75	360	0	300	100	1500	60	197	194.5	60	5.6	0.7	
RBALVI3B	-75	370	-40	300	100	1500	60	197	194.5	60	5.8	0.7	
RCALVI3B	-75	370	-30	300	100	1500	60	197	194.5	60	5.8	0.7	
RDALVI3B	-75	370	-20	300	100	1500	60	197	194.5	60	5.7	0.7	
REALVI3B	-75	370	-10	300	100	1500	60	197	194.5	60	5.7	0.7	
RFALVI3B	-75	370	0	300	100	1500	60	197	194.5	60	5.7	0.7	
RBAMVI3B	-75	380	-40	300	100	1500	60	197	194.5	60	5.6	0.7	
RCAMVI3B	-75	380	-30	300	100	1500	60	197	194.5	60	5.6	0.7	
RDAMVI3B	-75	380	-20	300	100	1500	60	197	194.5	60	5.6	0.7	
REAMVI3B	-75	380	-10	300	100	1500	60	197	194.5	60	5.6	0.7	
RFAMVI3B	-75	380	0	300	100	1500	60	197	194.5	60	5.6	0.7	
RBANVI3B	-75	390	-40	300	100	1500	60	197	194.5	60	5.6	0.7	
RCANVI3B	-75	390	-30	300	100	1500	60	197	194.5	60	5.6	0.7	
RDANVI3B	-75	390	-20	300	100	1500	60	197	194.5	60	5.6	0.7	
REANVI3B	-75	390	-10	300	100	1500	60	197	194.5	60	5.6	0.7	

	LP position (mm)			Recomm		Power (watts)		Matching Network		Magnets		Pressure	
Filename	Vert	Axial	Rad	Amps	Volts	input	reflected	Loading	Tuning	Cur (A)	Vol (V)	(mtorr)	notes
RFANVI3B	-75	390	0	300	100	1500	60	197	194.5	60	5.6	0.7	break
RBAJVI2C	-70	350	-40	225	250	1500	85	197	194.5	60	5.3	0.7	
RCAJVI2C	-70	350	-30	225	250	1500	80	197	194.5	60	5.3	0.7	
RDAIVI2C	-70	350	-20	225	250	1500	80	197	194.5	60	5.3	0.7	
REAIVI2C	-70	350	-10	225	250	1500	80	197	194.5	60	5.4	0.7	
RFAJVI2C	-70	350	0	225	250	1500	80	197	194.5	60	5.4	0.7	
RBAKVI2C	-70	360	-40	225	250	1500	75	197	194.5	60	5.4	0.7	
RCAKVI2C	-70	360	-30	225	250	1500	75	197	194.5	60	5.4	0.7	
RDAKVI2C	-70	360	-20	225	250	1500	75	197	194.5	60	5.4	0.7	
REAKVI2C	-70	360	-10	225	250	1500	80	197	194.5	60	5.4	0.7	
RFAKVI2C	-70	360	0	225	250	1500	80	197	194.5	60	5.4	0.7	
RBALVI2C	-70	370	-40	225	250	1500	75	197	194.5	60	5.5	0.7	
RCALVI2C	-70	370	-30	225	250	1500	75	197	194.5	60	5.5	0.7	
RDALVI2C	-70	370	-20	225	250	1500	75	197	194.5	60	5.5	0.7	
REALVI2C	-70	370	-10	225	250	1500	75	197	194.5	60	5.5	0.7	
RFALVI2C	-70	370	0	225	250	1500	75	197	194.5	60	5.5	0.7	
RBAMVI2C	-70	380	-40	225	250	1500	75	197	194.5	60	5.5	0.7	
RCAMVI2C	-70	380	-30	225	250	1500	75	197	194.5	60	5.5	0.7	
RDAMVI2C	-70	380	-20	225	250	1500	75	197	194.5	60	5.5	0.7	
REAMVI2C	-70	380	-10	225	250	1500	75	197	194.5	60	5.5	0.7	
RFAMVI2C	-70	380	0	225	250	1500	75	197	194.5	60	5.5	0.7	
RBANVI2C	-70	390	-40	225	250	1500	75	197	194.5	60	5.5	0.7	
RCANVI2C	-70	390	-30	225	250	1500	75	197	194.5	60	5.5	0.7	
RDANVI2C	-70	390	-20	225	250	1500	75	197	194.5	60	5.5	0.7	
REANVI2C	-70	390	-10	225	250	1500	75	197	194.5	60	5.5	0.7	
RFANVI2C	-70	390	0	225	250	1500	75	197	194.5	60	5.5	0.7	break
RBAJVI2C	-75	350	-40	225	250	1500	90	197	194.5	60	5.3	0.7	
RCAJVI2C	-75	350	-30	225	250	1500	85	197	194.5	60	5.4	0.7	
RDAIVI2C	-75	350	-20	225	250	1500	85	197	194.5	60	5.4	0.7	
REAIVI2C	-75	350	-10	225	250	1500	85	197	194.5	60	5.4	0.7	
RFAJVI2C	-75	350	0	225	250	1500	85	197	194.5	60	5.4	0.7	-1 rad
RBAKVI2C	-75	360	-40	225	250	1500	80	197	194.5	60	5.5	0.7	
RCAKVI2C	-75	360	-30	225	250	1500	80	197	194.5	60	5.5	0.7	
RDAKVI2C	-75	360	-20	225	250	1500	80	197	194.5	60	5.5	0.7	
REAKVI2C	-75	360	-10	225	250	1500	80	197	194.5	60	5.5	0.7	
RFAKVI2C	-75	360	0	225	250	1500	80	197	194.5	60	5.5	0.7	
RBALVI2C	-75	370	-40	225	250	1500	80	197	194.5	60	5.5	0.7	
RCALVI2C	-75	370	-30	225	250	1500	80	197	194.5	60	5.5	0.7	
RDALVI2C	-75	370	-20	225	250	1500	80	197	194.5	60	5.5	0.7	
REALVI2C	-75	370	-10	225	250	1500	80	197	194.5	60	5.5	0.7	
RFALVI2C	-75	370	0	225	250	1500	80	197	194.5	60	5.5	0.7	
RBAMVI2C	-75	380	-40	225	250	1500	75	197	194.5	60	5.5	0.7	
RCAMVI2C	-75	380	-30	225	250	1500	75	197	194.5	60	5.5	0.7	
RDAMVI2C	-75	380	-20	225	250	1500	75	197	194.5	60	5.5	0.7	
REAMVI2C	-75	380	-10	225	250	1500	80	197	194.5	60	5.5	0.7	
RFAMVI2C	-75	380	0	225	250	1500	80	197	194.5	60	5.5	0.7	
RBANVI2C	-75	390	-40	225	250	1500	75	197	194.5	60	5.5	0.7	
RCANVI2C	-75	390	-30	225	250	1500	75	197	194.5	60	5.5	0.7	
RDANVI2C	-75	390	-20	225	250	1500	75	197	194.5	60	5.5	0.7	
REANVI2C	-75	390	-10	225	250	1500	75	197	194.5	60	5.5	0.7	
RFANVI2C	-75	390	0	225	250	1500	75	197	194.5	60	5.5	0.7	break
RBAJVI3C	-70	350	-40	300	250	1500	55	197	194.5	60	5	0.7	4-22-08
RCAJVI3C	-70	350	-30	300	250	1500	55	197	194.5	60	5	0.7	
RDAIVI3C	-70	350	-20	300	250	1500	55	197	194.5	60	5.1	0.7	
REAIVI3C	-70	350	-10	300	250	1500	55	197	194.5	60	5.1	0.7	
RFAJVI3C	-70	350	0	300	250	1500	55	197	194.5	60	5.1	0.7	
RBAKVI3C	-70	360	-40	300	250	1500	50	197	194.5	60	5.2	0.7	
RCAKVI3C	-70	360	-30	300	250	1500	50	197	194.5	60	5.2	0.7	

	LP position (mm)			Recomm		Power (watts)		Matching Network		Magnets		Pressure	
Filename	Vert	Axial	Rad	Amps	Volts	input	reflected	Loading	Tuning	Cur (A)	Vol (V)	(mtorr)	notes
RDAKVI3C	-70	360	-20	300	250	1500	50	197	194.5	60	5.1	0.7	
REAKVI3C	-70	360	-10	300	250	1500	50	197	194.5	60	5.1	0.7	
RFAKVI3C	-70	360	0	300	250	1500	50	197	194.5	60	5.1	0.7	
RBALVI3C	-70	370	-40	300	250	1500	50	197	194.5	60	5.2	0.7	
RCALVI3C	-70	370	-30	300	250	1500	50	197	194.5	60	5.2	0.7	
RDALVI3C	-70	370	-20	300	250	1500	50	197	194.5	60	5.2	0.7	
REALVI3C	-70	370	-10	300	250	1500	50	197	194.5	60	5.2	0.7	
RFALVI3C	-70	370	0	300	250	1500	50	197	194.5	60	5.2	0.7	
RBAMVI3C	-70	380	-40	300	250	1500	50	197	194.5	60	5.2	0.7	
RCAMVI3C	-70	380	-30	300	250	1500	50	197	194.5	60	5.2	0.7	
RDAMVI3C	-70	380	-20	300	250	1500	50	197	194.5	60	5.2	0.7	
REAMVI3C	-70	380	-10	300	250	1500	50	197	194.5	60	5.2	0.7	
RFAMVI3C	-70	380	0	300	250	1500	50	197	194.5	60	5.2	0.7	
RBANVI3C	-70	390	-40	300	250	1500	50	197	194.5	60	5.2	0.7	
RCANVI3C	-70	390	-30	300	250	1500	50	197	194.5	60	5.2	0.7	
RDANVI3C	-70	390	-20	300	250	1500	50	197	194.5	60	5.2	0.7	
REANVI3C	-70	390	-10	300	250	1500	50	197	194.5	60	5.3	0.7	
RFANVI3C	-70	390	0	300	250	1500	50	197	194.5	60	5.3	0.7	break
RBAJVI3C	-75	350	-40	300	250	1500	50	197	194.5	60	5.1	0.7	
RCAJVI3C	-75	350	-30	300	250	1500	50	197	194.5	60	5.1	0.7	
RDAIVI3C	-75	350	-20	300	250	1500	50	197	194.5	60	5.1	0.7	
REAIVI3C	-75	350	-10	300	250	1500	45	197	194.5	60	5.2	0.7	
RFAJVI3C	-75	350	0	300	250	1500	45	197	194.5	60	5.2	0.7	-1 rad
RBAKVI3C	-75	360	-40	300	250	1500	45	197	194.5	60	5.3	0.7	
RCAKVI3C	-75	360	-30	300	250	1500	45	197	194.5	60	5.3	0.7	
RDAKVI3C	-75	360	-20	300	250	1500	45	197	194.5	60	5.3	0.7	
REAKVI3C	-75	360	-10	300	250	1500	45	197	194.5	60	5.2	0.7	
RFAKVI3C	-75	360	0	300	250	1500	45	197	194.5	60	5.2	0.7	
RBALVI3C	-75	370	-40	300	250	1500	45	197	194.5	60	5.3	0.7	
RCALVI3C	-75	370	-30	300	250	1500	45	197	194.5	60	5.3	0.7	
RDALVI3C	-75	370	-20	300	250	1500	45	197	194.5	60	5.3	0.7	
REALVI3C	-75	370	-10	300	250	1500	45	197	194.5	60	5.3	0.7	
RFALVI3C	-75	370	0	300	250	1500	45	197	194.5	60	5.3	0.7	
RBAMVI3C	-75	380	-40	300	250	1500	45	197	194.5	60	5.3	0.7	
RCAMVI3C	-75	380	-30	300	250	1500	45	197	194.5	60	5.3	0.7	
RDAMVI3C	-75	380	-20	300	250	1500	45	197	194.5	60	5.3	0.7	
REAMVI3C	-75	380	-10	300	250	1500	45	197	194.5	60	5.3	0.7	
RFAMVI3C	-75	380	0	300	250	1500	45	197	194.5	60	5.3	0.7	
RBANVI3C	-75	390	-40	300	250	1500	45	197	194.5	60	5.3	0.7	
RCANVI3C	-75	390	-30	300	250	1500	45	197	194.5	60	5.3	0.7	
RDANVI3C	-75	390	-20	300	250	1500	45	197	194.5	60	5.3	0.7	
REANVI3C	-75	390	-10	300	250	1500	45	197	194.5	60	5.3	0.7	
RFANVI3C	-75	390	0	300	250	1500	45	197	194.5	60	5.3	0.7	break
RBAJVI4D	-70	350	-40	325	500	1500	50	197	194.5	60	5.3	0.7	
RCAJVI4D	-70	350	-30	325	500	1500	50	197	194.5	60	5.3	0.7	
RDAIVI4D	-70	350	-20	325	500	1500	50	197	194.5	60	5.3	0.7	
REAIVI4D	-70	350	-10	325	500	1500	50	197	194.5	60	5.3	0.7	
RFAJVI4D	-70	350	0	325	500	1500	50	197	194.5	60	5.3	0.7	
RBAKVI4D	-70	360	-40	325	500	1500	45	197	194.5	60	5.3	0.7	
RCAKVI4D	-70	360	-30	325	500	1500	45	197	194.5	60	5.3	0.7	
RDAKVI4D	-70	360	-20	325	500	1500	50	197	194.5	60	5.3	0.7	
REAKVI4D	-70	360	-10	325	500	1500	50	197	194.5	60	5.3	0.7	
RFAKVI4D	-70	360	0	325	500	1500	50	197	194.5	60	5.3	0.7	
RBALVI4D	-70	370	-40	325	500	1500	45	197	194.5	60	5.4	0.7	
RCALVI4D	-70	370	-30	325	500	1500	45	197	194.5	60	5.4	0.7	
RDALVI4D	-70	370	-20	325	500	1500	45	197	194.5	60	5.4	0.7	
REALVI4D	-70	370	-10	325	500	1500	45	197	194.5	60	5.4	0.7	
RFALVI4D	-70	370	0	325	500	1500	45	197	194.5	60	5.4	0.7	

Filename	LP position (mm) Vert	Axial	Rad	Recomm Amps	Volts	Power (watts) input	reflected	Matching Network Loading	Tuning	Magnets Cur (A)	Vol (V)	Pressure (mtorr)	notes
RBAMVI4D	-70	380	-40	325	500	1500	45	197	194.5	60	5.4	0.7	
RCAMVI4D	-70	380	-30	325	500	1500	45	197	194.5	60	5.4	0.7	
RDAMVI4D	-70	380	-20	325	500	1500	45	197	194.5	60	5.4	0.7	
REAMVI4D	-70	380	-10	325	500	1500	45	197	194.5	60	5.4	0.7	
RFAMVI4D	-70	380	0	325	500	1500	45	197	194.5	60	5.4	0.7	
RBANVI4D	-70	390	-40	325	500	1500	45	197	194.5	60	5.5	0.7	
RCANVI4D	-70	390	-30	325	500	1500	45	197	194.5	60	5.5	0.7	
RDANVI4D	-70	390	-20	325	500	1500	45	197	194.5	60	5.5	0.7	
REANVI4D	-70	390	-10	325	500	1500	45	197	194.5	60	5.5	0.7	
RFANVI4D	-70	390	0	325	500	1500	45	197	194.5	60	5.5	0.7	break
RBAJVI4D	-75	350	-40	325	500	1500	50	197	194.5	60	5.2	0.7	
RCAJVI4D	-75	350	-30	325	500	1500	50	197	194.5	60	5.2	0.7	
RDAJVI4D	-75	350	-20	325	500	1500	50	197	194.5	60	5.3	0.7	
REAJVI4D	-75	350	-10	325	500	1500	50	197	194.5	60	5.3	0.7	
RFAJVI4D	-75	350	0	325	500	1500	50	197	194.5	60	5.3	0.7	-1 rad
RBAKVI4D	-75	360	-40	325	500	1500	45	197	194.5	60	5.4	0.7	
RCAKVI4D	-75	360	-30	325	500	1500	45	197	194.5	60	5.4	0.7	
RDAKVI4D	-75	360	-20	325	500	1500	45	197	194.5	60	5.4	0.7	
REAKVI4D	-75	360	-10	325	500	1500	45	197	194.5	60	5.4	0.7	
RFAKVI4D	-75	360	0	325	500	1500	45	197	194.5	60	5.4	0.7	
RBALVI4D	-75	370	-40	325	500	1500	45	197	194.5	60	5.4	0.7	
RCALVI4D	-75	370	-30	325	500	1500	45	197	194.5	60	5.5	0.7	
RDALVI4D	-75	370	-20	325	500	1500	45	197	194.5	60	5.5	0.7	
REALVI4D	-75	370	-10	325	500	1500	45	197	194.5	60	5.5	0.7	
RFALVI4D	-75	370	0	325	500	1500	45	197	194.5	60	5.6	0.7	
RBAMVI4D	-75	380	-40	325	500	1500	40	197	194.5	60	5.6	0.7	
RCAMVI4D	-75	380	-30	325	500	1500	40	197	194.5	60	5.6	0.7	
RDAMVI4D	-75	380	-20	325	500	1500	45	197	194.5	60	5.6	0.7	
REAMVI4D	-75	380	-10	325	500	1500	45	197	194.5	60	5.6	0.7	
RFAMVI4D	-75	380	0	325	500	1500	45	197	194.5	60	5.6	0.7	
RBANVI4D	-75	390	-40	325	500	1500	40	197	194.5	60	5.6	0.7	
RCANVI4D	-75	390	-30	325	500	1500	40	197	194.5	60	5.6	0.7	
RDANVI4D	-75	390	-20	325	500	1500	40	197	194.5	60	5.6	0.7	
REANVI4D	-75	390	-10	325	500	1500	40	197	194.5	60	5.6	0.7	
RFANVI4D	-75	390	0	325	500	1500	40	197	194.5	60	5.6	0.7	break
RBAJVI4E	-70	350	-40	325	650	1500	40	197	194.5	60	5.2	0.7	1 mA
RCAJVI4E	-70	350	-30	325	650	1500	40	197	194.5	60	5.3	0.7	
RDAJVI4E	-70	350	-20	325	650	1500	40	197	194.5	60	5.3	0.7	
REAJVI4E	-70	350	-10	325	650	1500	35	197	194.5	60	5.3	0.7	
RFAJVI4E	-70	350	0	325	650	1500	35	197	194.5	60	5.3	0.7	
RBAKVI4E	-70	360	-40	325	650	1500	35	197	194.5	60	5.4	0.7	
RCAKVI4E	-70	360	-30	325	650	1500	35	197	194.5	60	5.4	0.7	
RDAKVI4E	-70	360	-20	325	650	1500	35	197	194.5	60	5.4	0.7	
REAKVI4E	-70	360	-10	325	650	1500	35	197	194.5	60	5.4	0.7	
RFAKVI4E	-70	360	0	325	650	1500	35	197	194.5	60	5.4	0.7	
RBALVI4E	-70	370	-40	325	650	1500	35	197	194.5	60	5.4	0.7	
RCALVI4E	-70	370	-30	325	650	1500	35	197	194.5	60	5.4	0.7	
RDALVI4E	-70	370	-20	325	650	1500	35	197	194.5	60	5.4	0.7	
REALVI4E	-70	370	-10	325	650	1500	30	197	194.5	60	5.4	0.7	
RFALVI4E	-70	370	0	325	650	1500	30	197	194.5	60	5.4	0.7	
RBAMVI4E	-70	380	-40	325	650	1500	30	197	194.5	60	5.5	0.7	1 mA
RCAMVI4E	-70	380	-30	325	650	1500	30	197	194.5	60	5.5	0.7	1 mA
RDAMVI4E	-70	380	-20	325	650	1500	30	197	194.5	60	5.4	0.7	1 mA
REAMVI4E	-70	380	-10	325	650	1500	30	197	194.5	60	5.4	0.7	.1 mA
RFAMVI4E	-70	380	0	325	650	1500	30	197	194.5	60	5.4	0.7	.1 mA
RBANVI4E	-70	390	-40	325	650	1500	30	197	194.5	60	5.5	0.7	1 mA
RCANVI4E	-70	390	-30	325	650	1500	30	197	194.5	60	5.5	0.7	
RDANVI4E	-70	390	-20	325	650	1500	30	197	194.5	60	5.5	0.7	

Filename	LP position (mm) Vert	Axial	Rad	Recomm Amps	Volts	Power (watts) input	reflected	Matching Network Loading	Tuning	Magnets Cur (A)	Vol (V)	Pressure (mtorr)	notes
REANVI4E	-70	390	-10	325	650	1500	30	197	194.5	60	5.5	0.7	
RFANVI4E	-70	390	0	325	650	1500	30	197	194.5	60	5.5	0.7	break
RBAJVI4E	-75	350	-40	325	650	1500	50	197	194.5	60	5.3	0.7	1 mA
RCAJVI4E	-75	350	-30	325	650	1500	50	197	194.5	60	5.3	0.7	
RDAJVI4E	-75	350	-20	325	650	1500	50	197	194.5	60	5.3	0.7	
REAJVI4E	-75	350	-10	325	650	1500	50	197	194.5	60	5.3	0.7	
RFAJVI4E	-75	350	0	325	650	1500	45	197	194.5	60	5.3	0.7	-1 rad
RBAKVI4E	-75	360	-40	325	650	1500	45	197	194.5	60	5.4	0.7	
RCAKVI4E	-75	360	-30	325	650	1500	45	197	194.5	60	5.4	0.7	
RDAKVI4E	-75	360	-20	325	650	1500	45	197	194.5	60	5.4	0.7	
REAKVI4E	-75	360	-10	325	650	1500	45	197	194.5	60	5.4	0.7	
RFAKVI4E	-75	360	0	325	650	1500	45	197	194.5	60	5.4	0.7	
RBALVI4E	-75	370	-40	325	650	1500	40	197	194.5	60	5.4	0.7	
RCALVI4E	-75	370	-30	325	650	1500	40	197	194.5	60	5.4	0.7	
RDALVI4E	-75	370	-20	325	650	1500	40	197	194.5	60	5.4	0.7	
REALVI4E	-75	370	-10	325	650	1500	40	197	194.5	60	5.5	0.7	
RFALVI4E	-75	370	0	325	650	1500	40	197	194.5	60	5.5	0.7	
RBAMVI4E	-75	380	-40	325	650	1500	40	197	194.5	60	5.5	0.7	
RCAMVI4E	-75	380	-30	325	650	1500	40	197	194.5	60	5.5	0.7	
RDAMVI4E	-75	380	-20	325	650	1500	40	197	194.5	60	5.5	0.7	
REAMVI4E	-75	380	-10	325	650	1500	40	197	194.5	60	5.5	0.7	
RFAMVI4E	-75	380	0	325	650	1500	40	197	194.5	60	5.5	0.7	-1 rad
RBANVI4E	-75	390	-40	325	650	1500	40	197	194.5	60	5.5	0.7	
RCANVI4E	-75	390	-30	325	650	1500	40	197	194.5	60	5.5	0.7	
RDANVI4E	-75	390	-20	325	650	1500	35	197	194.5	60	5.5	0.7	
REANVI4E	-75	390	-10	325	650	1500	35	197	194.5	60	5.5	0.7	
RFANVI4E	-75	390	0	325	650	1500	35	197	194.5	60	5.5	0.7	break
RBAJVI4C	-70	350	-40	325	250	1500	35	197	194.5	60	5.4	0.7	1 mA
RCAJVI4C	-70	350	-30	325	250	1500	35	197	194.5	60	5.4	0.7	
RDAJVI4C	-70	350	-20	325	250	1500	35	197	194.5	60	5.4	0.7	
REAJVI4C	-70	350	-10	325	250	1500	35	197	194.5	60	5.4	0.7	
RFAJVI4C	-70	350	0	325	250	1500	35	197	194.5	60	5.5	0.7	
RBAKVI4C	-70	360	-40	325	250	1500	35	197	194.5	60	5.5	0.7	
RCAKVI4C	-70	360	-30	325	250	1500	35	197	194.5	60	5.5	0.7	
RDAKVI4C	-70	360	-20	325	250	1500	35	197	194.5	60	5.5	0.7	
REAKVI4C	-70	360	-10	325	250	1500	35	197	194.5	60	5.5	0.7	
RFAKVI4C	-70	360	0	325	250	1500	35	197	194.5	60	5.5	0.7	
RBALVI4C	-70	370	-40	325	250	1500	35	197	194.5	60	5.5	0.7	
RCALVI4C	-70	370	-30	325	250	1500	35	197	194.5	60	5.5	0.7	
RDALVI4C	-70	370	-20	325	250	1500	35	197	194.5	60	5.5	0.7	
REALVI4C	-70	370	-10	325	250	1500	35	197	194.5	60	5.5	0.7	
RFALVI4C	-70	370	0	325	250	1500	35	197	194.5	60	5.5	0.7	
RBAMVI4C	-70	380	-40	325	250	1500	35	197	194.5	60	5.5	0.7	
RCAMVI4C	-70	380	-30	325	250	1500	35	197	194.5	60	5.5	0.7	
RDAMVI4C	-70	380	-20	325	250	1500	35	197	194.5	60	5.5	0.7	
REAMVI4C	-70	380	-10	325	250	1500	35	197	194.5	60	5.5	0.7	
RFAMVI4C	-70	380	0	325	250	1500	35	197	194.5	60	5.5	0.7	
RBANVI4C	-70	390	-40	325	250	1500	35	197	194.5	60	5.5	0.7	
RCANVI4C	-70	390	-30	325	250	1500	35	197	194.5	60	5.5	0.7	
RDANVI4C	-70	390	-20	325	250	1500	35	197	194.5	60	5.5	0.7	
REANVI4C	-70	390	-10	325	250	1500	35	197	194.5	60	5.5	0.7	
RFANVI4C	-70	390	0	325	250	1500	35	197	194.5	60	5.5	0.7	break
RBAJVI4C	-75	350	-40	325	250	1500	45	197	194.5	60	5.3	0.7	1 mA
RCAJVI4C	-75	350	-30	325	250	1500	45	197	194.5	60	5.4	0.7	
RDAJVI4C	-75	350	-20	325	250	1500	45	197	194.5	60	5.4	0.7	
REAJVI4C	-75	350	-10	325	250	1500	45	197	194.5	60	5.4	0.7	
RFAJVI4C	-75	350	0	325	250	1500	45	197	194.5	60	5.4	0.7	-1 rad
RBAKVI4C	-75	360	-40	325	250	1500	45	197	194.5	60	5.5	0.7	

	LP position (mm)			Recomm		Power (watts)		Matching Network		Magnets		Pressure	
Filename	Vert	Axial	Rad	Amps	Volts	input	reflected	Loading	Tuning	Cur (A)	Vol (V)	(mtorr)	notes
RCAKVJ4C	-75	360	-30	325	250	1500	45	197	194.5	60	5.5	0.7	
RDAKVJ4C	-75	360	-20	325	250	1500	45	197	194.5	60	5.5	0.7	
REAKVJ4C	-75	360	-10	325	250	1500	45	197	194.5	60	5.5	0.7	
RFAKVJ4C	-75	360	0	325	250	1500	45	197	194.5	60	5.5	0.7	
RBALVJ4C	-75	370	-40	325	250	1500	45	197	194.5	60	5.5	0.7	
RCALVJ4C	-75	370	-30	325	250	1500	45	197	194.5	60	5.5	0.7	
RDALVJ4C	-75	370	-20	325	250	1500	45	197	194.5	60	5.5	0.7	
REALVJ4C	-75	370	-10	325	250	1500	45	197	194.5	60	5.5	0.7	
RFALVJ4C	-75	370	0	325	250	1500	45	197	194.5	60	5.5	0.7	
RBAMVJ4C	-75	380	-40	325	250	1500	40	197	194.5	60	5.6	0.7	
RCAMVJ4C	-75	380	-30	325	250	1500	40	197	194.5	60	5.6	0.7	
RDAMVJ4C	-75	380	-20	325	250	1500	40	197	194.5	60	5.5	0.7	
REAMVJ4C	-75	380	-10	325	250	1500	40	197	194.5	60	5.5	0.7	
RFAMVJ4C	-75	380	0	325	250	1500	40	197	194.5	60	5.5	0.7	
RBANVJ4C	-75	390	-40	325	250	1500	40	197	194.5	60	5.6	0.7	
RCANVJ4C	-75	390	-30	325	250	1500	40	197	194.5	60	5.6	0.7	
RDANVJ4C	-75	390	-20	325	250	1500	40	197	194.5	60	5.6	0.7	
REANVJ4C	-75	390	-10	325	250	1500	40	197	194.5	60	5.6	0.7	
RFANVJ4C	-75	390	0	325	250	1500	40	197	194.5	60	5.6	0.7	break
RBAJVI4B	-70	350	-40	325	100	1500	45	197	194.5	60	5.3	0.7	
RCAJVI4B	-70	350	-30	325	100	1500	45	197	194.5	60	5.3	0.7	
RDAJVI4B	-70	350	-20	325	100	1500	40	197	194.5	60	5.4	0.7	
REAJVI4B	-70	350	-10	325	100	1500	40	197	194.5	60	5.4	0.7	
RFAJVI4B	-70	350	0	325	100	1500	40	197	194.5	60	5.4	0.7	
RBAKVI4B	-70	360	-40	325	100	1500	40	197	194.5	60	5.5	0.7	
RCAKVI4B	-70	360	-30	325	100	1500	40	197	194.5	60	5.5	0.7	
RDAKVI4B	-70	360	-20	325	100	1500	40	197	194.5	60	5.5	0.7	
REAKVI4B	-70	360	-10	325	100	1500	40	197	194.5	60	5.4	0.7	
RFAKVI4B	-70	360	0	325	100	1500	40	197	194.5	60	5.4	0.7	
RBALVI4B	-70	370	-40	325	100	1500	40	197	194.5	60	5.5	0.7	
RCALVI4B	-70	370	-30	325	100	1500	40	197	194.5	60	5.5	0.7	
RDALVI4B	-70	370	-20	325	100	1500	40	197	194.5	60	5.5	0.7	
REALVI4B	-70	370	-10	325	100	1500	40	197	194.5	60	5.5	0.7	
RFALVI4B	-70	370	0	325	100	1500	40	197	194.5	60	5.5	0.7	
RBAMVI4B	-70	380	-40	325	100	1500	40	197	194.5	60	5.5	0.7	
RCAMVI4B	-70	380	-30	325	100	1500	40	197	194.5	60	5.5	0.7	
RDAMVI4B	-70	380	-20	325	100	1500	40	197	194.5	60	5.5	0.7	
REAMVI4B	-70	380	-10	325	100	1500	40	197	194.5	60	5.5	0.7	
RFAMVI4B	-70	380	0	325	100	1500	40	197	194.5	60	5.5	0.7	
RBANVI4B	-70	390	-40	325	100	1500	35	197	194.5	60	5.6	0.7	
RCANVI4B	-70	390	-30	325	100	1500	35	197	194.5	60	5.6	0.7	
RDANVI4B	-70	390	-20	325	100	1500	35	197	194.5	60	5.6	0.7	
REANVI4B	-70	390	-10	325	100	1500	40	197	194.5	60	5.6	0.7	
RFANVI4B	-70	390	0	325	100	1500	40	197	194.5	60	5.6	0.7	break
RBAJVJ4B	-75	350	-40	325	100	1500	50	197	194.5	60	5.3	0.7	1 mA
RCAJVJ4B	-75	350	-30	325	100	1500	50	197	194.5	60	5.3	0.7	
RDAJVJ4B	-75	350	-20	325	100	1500	50	197	194.5	60	5.3	0.7	
REAJVJ4B	-75	350	-10	325	100	1500	50	197	194.5	60	5.3	0.7	
RFAJVJ4B	-75	350	0	325	100	1500	50	197	194.5	60	5.4	0.7	-1 rad
RBAKVJ4B	-75	360	-40	325	100	1500	45	197	194.5	60	5.5	0.7	
RCAKVJ4B	-75	360	-30	325	100	1500	45	197	194.5	60	5.5	0.7	
RDAKVJ4B	-75	360	-20	325	100	1500	50	197	194.5	60	5.4	0.7	
REAKVJ4B	-75	360	-10	325	100	1500	50	197	194.5	60	5.4	0.7	
RFAKVJ4B	-75	360	0	325	100	1500	50	197	194.5	60	5.4	0.7	
RBALVJ4B	-75	370	-40	325	100	1500	45	197	194.5	60	5.5	0.7	
RCALVJ4B	-75	370	-30	325	100	1500	45	197	194.5	60	5.5	0.7	
RDALVJ4B	-75	370	-20	325	100	1500	45	197	194.5	60	5.5	0.7	
REALVJ4B	-75	370	-10	325	100	1500	45	197	194.5	60	5.5	0.7	

	LP position (mm)			Recomm		Power (watts)		Matching Network		Magnets		Pressure	
Filename	Vert	Axial	Rad	Amps	Volts	input	reflected	Loading	Tuning	Cur (A)	Vol (V)	(mtorr)	notes
RFALVJ4B	-75	370	0	325	100	1500	45	197	194.5	60	5.5	0.7	
RBAMVJ4B	-75	380	-40	325	100	1500	45	197	194.5	60	5.5	0.7	
RCAMVJ4B	-75	380	-30	325	100	1500	45	197	194.5	60	5.5	0.7	
RDAMVJ4B	-75	380	-20	325	100	1500	45	197	194.5	60	5.5	0.7	
REAMVJ4B	-75	380	-10	325	100	1500	45	197	194.5	60	5.5	0.7	
RFAMVJ4B	-75	380	0	325	100	1500	45	197	194.5	60	5.5	0.7	
RBANVJ4B	-75	390	-40	325	100	1500	45	197	194.5	60	5.5	0.7	
RCANVJ4B	-75	390	-30	325	100	1500	45	197	194.5	60	5.5	0.7	
RDANVJ4B	-75	390	-20	325	100	1500	45	197	194.5	60	5.5	0.7	
REANVJ4B	-75	390	-10	325	100	1500	45	197	194.5	60	5.6	0.7	
RFANVJ4B	-75	390	0	325	100	1500	45	197	194.5	60	5.6	0.7	break
RBAJVI4A	-70	350	-40	325	0	1500	60	197	194.5	60	5.2	0.7	1 mA
RCAJVI4A	-70	350	-30	325	0	1500	50	197	194.5	60	5.3	0.7	
RDAJVI4A	-70	350	-20	325	0	1500	50	197	194.5	60	5.3	0.7	
REAJVI4A	-70	350	-10	325	0	1500	50	197	194.5	60	5.3	0.7	
RFAJVI4A	-70	350	0	325	0	1500	50	197	194.5	60	5.3	0.7	
RBAKVI4A	-70	360	-40	325	0	1500	50	197	194.5	60	5.5	0.7	
RCAKVI4A	-70	360	-30	325	0	1500	50	197	194.5	60	5.4	0.7	
RDAKVI4A	-70	360	-20	325	0	1500	50	197	194.5	60	5.4	0.7	
REAKVI4A	-70	360	-10	325	0	1500	50	197	194.5	60	5.4	0.7	
RFAKVI4A	-70	360	0	325	0	1500	50	197	194.5	60	5.4	0.7	
RBALVI4A	-70	370	-40	325	0	1500	50	197	194.5	60	5.5	0.7	
RCALVI4A	-70	370	-30	325	0	1500	50	197	194.5	60	5.5	0.7	
RDALVI4A	-70	370	-20	325	0	1500	50	197	194.5	60	5.5	0.7	
REALVI4A	-70	370	-10	325	0	1500	50	197	194.5	60	5.5	0.7	
RFALVI4A	-70	370	0	325	0	1500	50	197	194.5	60	5.5	0.7	
RBAMVI4A	-70	380	-40	325	0	1500	50	197	194.5	60	5.6	0.7	
RCAMVI4A	-70	380	-30	325	0	1500	50	197	194.5	60	5.6	0.7	
RDAMVI4A	-70	380	-20	325	0	1500	50	197	194.5	60	5.5	0.7	
REAMVI4A	-70	380	-10	325	0	1500	50	197	194.5	60	5.5	0.7	
RFAMVI4A	-70	380	0	325	0	1500	50	197	194.5	60	5.5	0.7	
RBANVI4A	-70	390	-40	325	0	1500	50	197	194.5	60	5.6	0.7	
RCANVI4A	-70	390	-30	325	0	1500	50	197	194.5	60	5.6	0.7	
RDANVI4A	-70	390	-20	325	0	1500	50	197	194.5	60	5.6	0.7	
REANVI4A	-70	390	-10	325	0	1500	50	197	194.5	60	5.6	0.7	
RFANVI4A	-70	390	0	325	0	1500	50	197	194.5	60	5.6	0.7	
RBAJVJ4A	-75	350	-40	325	0	1500	45	197	194.5	60	5.7	0.7	
RCAJVJ4A	-75	350	-30	325	0	1500	45	197	194.5	60	5.7	0.7	
RDAJVJ4A	-75	350	-20	325	0	1500	45	197	194.5	60	5.7	0.7	
REAJVJ4A	-75	350	-10	325	0	1500	45	197	194.5	60	5.7	0.7	
RFAJVJ4A	-75	350	0	325	0	1500	45	197	194.5	60	5.7	0.7	
RBAKVJ4A	-75	360	-40	325	0	1500	45	197	194.5	60	5.7	0.7	
RCAKVJ4A	-75	360	-30	325	0	1500	45	197	194.5	60	5.7	0.7	
RDAKVJ4A	-75	360	-20	325	0	1500	45	197	194.5	60	5.7	0.7	
REAKVJ4A	-75	360	-10	325	0	1500	45	197	194.5	60	5.7	0.7	
RFAKVJ4A	-75	360	0	325	0	1500	45	197	194.5	60	5.7	0.7	
RBALVJ4A	-75	370	-40	325	0	1500	45	197	194.5	60	5.7	0.7	
RCALVJ4A	-75	370	-30	325	0	1500	45	197	194.5	60	5.7	0.7	
RDALVJ4A	-75	370	-20	325	0	1500	45	197	194.5	60	5.7	0.7	
REALVJ4A	-75	370	-10	325	0	1500	45	197	194.5	60	5.6	0.7	
RFALVJ4A	-75	370	0	325	0	1500	45	197	194.5	60	5.6	0.7	
RBAMVJ4A	-75	380	-40	325	0	1500	45	197	194.5	60	5.6	0.7	
RCAMVJ4A	-75	380	-30	325	0	1500	45	197	194.5	60	5.6	0.7	
RDAMVJ4A	-75	380	-20	325	0	1500	45	197	194.5	60	5.6	0.7	
REAMVJ4A	-75	380	-10	325	0	1500	45	197	194.5	60	5.6	0.7	
RFAMVJ4A	-75	380	0	325	0	1500	45	197	194.5	60	5.6	0.7	
RBANVJ4A	-75	390	-40	325	0	1500	45	197	194.5	60	5.6	0.7	
RCANVJ4A	-75	390	-30	325	0	1500	45	197	194.5	60	5.6	0.7	

Filename	LP position (mm)			Recomm		Power (watts)		Matching Network		Magnets		Pressure	notes
	Vert	Axial	Rad	Amps	Volts	input	reflected	Loading	Tuning	Cur (A)	Vol (V)	(mtorr)	
RDANVJ4A	-75	390	-20	325	0	1500	45	197	194.5	60	5.6	0.7	
REANVJ4A	-75	390	-10	325	0	1500	45	197	194.5	60	5.6	0.7	
RFANVJ4A	-75	390	0	325	0	1500	45	197	194.5	60	5.6	0.7	

Table C.6: Testing Matrix for Plasma Frequency and Signal Attenuation Measurements: Trial 1

	LP position (mm)			Recomm		Power (watts)		Matching Network		Magnets		Pressure	
Filename	Vert	Axial	Rad	Amps	Volts	input	reflected	Loading	Tuning	Cur (A)	Vol (V)	(mtorr)	notes
RWAV0A		0	-40	0	0	1600	210	198.5	193.5	60	5.3	0.7	
RXAV0A		0	-20	0	0	1600	210	198.5	193.5	60	5.3	0.7	
RYAV0A		0	0	0	0	1600	210	198.5	193.5	60	5.3	0.7	
RZAV0A		0	20	0	0	1600	210	198.5	193.5	60	5.3	0.7	
RWAW0A		-10	-40	0	0	1600	210	198.5	193.5	60	5.3	0.7	
RXAW0A		-10	-20	0	0	1600	210	198.5	193.5	60	5.3	0.7	
RYAW0A		-10	0	0	0	1600	210	198.5	193.5	60	5.3	0.7	
RZAW0A		-10	20	0	0	1600	210	198.5	193.5	60	5.3	0.7	
RWAX0A		-20	-40	0	0	1600	210	198.5	193.5	60	5.3	0.7	
RXAX0A		-20	-20	0	0	1600	210	198.5	193.5	60	5.3	0.7	
RYAX0A		-20	0	0	0	1600	210	198.5	193.5	60	5.3	0.7	
RZAX0A		-20	20	0	0	1600	210	198.5	193.5	60	5.3	0.7	
RWAY0A		-30	-40	0	0	1600	200	198.5	193.5	60	5.4	0.7	
RXAY0A		-30	-20	0	0	1600	200	198.5	193.5	60	5.4	0.7	
RYAY0A		-30	0	0	0	1600	200	198.5	193.5	60	5.4	0.7	
RZAY0A		-30	20	0	0	1600	200	198.5	193.5	60	5.4	0.7	break
RWAV1A		0	-40	150	0	1550	150	197	194	60	4.7	0.7	
RXAV1A		0	-20	150	0	1550	150	197	194	60	4.7	0.7	
RYAV1A		0	0	150	0	1550	150	197	194	60	4.7	0.7	
RZAV1A		0	20	150	0	1550	150	197	194	60	4.7	0.7	
RZAW1A		-10	20	150	0	1550	150	197	194	60	4.7	0.7	
RYAW1A		-10	0	150	0	1550	150	197	194	60	4.7	0.7	
RXAW1A		-10	-20	150	0	1550	140	197	194	60	4.7	0.7	
RWAW1A		-10	-40	150	0	1550	140	197	194	60	4.7	0.7	
RWAX1A		-20	-40	150	0	1550	140	197	194	60	4.7	0.7	
RXAX1A		-20	-20	150	0	1550	140	197	194	60	4.7	0.7	
RYAX1A		-20	0	150	0	1550	140	197	194	60	4.7	0.7	
RZAX1A		-20	20	150	0	1550	140	197	194	60	4.7	0.7	
RZAY1A		-30	20	150	0	1550	140	197	194	60	4.7	0.7	
RYAY1A		-30	0	150	0	1550	140	197	194	60	4.7	0.7	
RXAY1A		-30	-10	150	0	1550	140	197	194	60	4.7	0.7	
RWAY1A		-30	-40	150	0	1550	140	197	194	60	4.7	0.7	
RWAV2A		0	-40	225	0	1500	115	197	194	60	4.7	0.7	
RXAV2A		0	-20	225	0	1500	115	197	194	60	4.7	0.7	
RYAV2A		0	0	225	0	1500	115	197	194	60	4.7	0.7	
RZAV2A		0	20	225	0	1500	115	197	194	60	4.7	0.7	
RZAW2A		-10	20	225	0	1500	115	197	194	60	4.7	0.7	
RYAW2A		-10	0	225	0	1500	110	197	194	60	4.7	0.7	
RXAW2A		-10	-20	225	0	1500	110	197	194	60	4.7	0.7	
RWAW2A		-10	-40	225	0	1500	110	197	194	60	4.8	0.7	
RWAX2A		-20	-40	225	0	1500	110	197	194	60	4.8	0.7	
RXAX2A		-20	-20	225	0	1500	110	197	194	60	4.8	0.7	
RYAX2A		-20	0	225	0	1500	110	197	194	60	4.8	0.7	
RZAX2A		-20	20	225	0	1500	110	197	194	60	4.8	0.7	
RZAY2A		-30	20	225	0	1500	110	197	194	60	4.8	0.7	
RYAY2A		-30	0	225	0	1500	110	197	194	60	4.8	0.7	
RXAY2A		-30	-20	225	0	1500	110	197	194	60	4.8	0.7	
RWAY2A		-30	-40	225	0	1500	110	197	194	60	4.8	0.7	break
RWAV3A		0	-40	300	0	1500	70	197	194	60	4.7	0.7	
RXAV3A		0	-20	300	0	1500	70	197	194	60	4.7	0.7	
RYAV3A		0	0	300	0	1500	70	197	194	60	4.7	0.7	
RZAV3A		0	20	300	0	1500	70	197	194	60	4.7	0.7	
RZAW3A		-10	20	300	0	1500	70	197	194	60	4.7	0.7	
RYAW3A		-10	0	300	0	1500	70	197	194	60	4.7	0.7	
RXAW3A		-10	-20	300	0	1500	70	197	194	60	4.7	0.7	
RWAW3A		-10	40	300	0	1500	70	197	194	60	4.7	0.7	
RWAX3A		-20	-40	300	0	1500	70	197	194	60	4.7	0.7	
RXAX3A		-20	-20	300	0	1500	70	197	194	60	4.7	0.7	
RYAX3A		-20	0	300	0	1500	70	197	194	60	4.7	0.7	
RZAX3A		-20	20	300	0	1500	70	197	194	60	4.7	0.7	
RZAY3A		-30	20	300	0	1500	70	197	194	60	4.7	0.7	
RYAY3A		-30	0	300	0	1500	70	197	194	60	4.7	0.7	
RXAY3A		-30	-20	300	0	1500	70	197	194	60	4.7	0.7	
RWAY3A		-30	-40	300	0	1500	70	197	194	60	4.7	0.7	
RWAV4A		0	-40	325	0	1500	70	197	194	60	4.8	0.7	
RXAV4A		0	-20	325	0	1500	70	197	194	60	4.8	0.7	
RYAV4A		0	0	325	0	1500	70	197	194	60	4.8	0.7	
RZAV4A		0	20	325	0	1500	70	197	194	60	4.8	0.7	
RZAW4A		-10	20	325	0	1500	70	197	194	60	4.8	0.7	
RYAW4A		-10	0	325	0	1500	70	197	194	60	4.8	0.7	
RXAW4A		-10	-20	325	0	1500	70	197	194	60	4.8	0.7	
RWAW4A		-10	-40	325	0	1500	70	197	194	60	4.8	0.7	
RWAX4A		-20	-40	325	0	1500	70	197	194	60	4.8	0.7	
RXAX4A		-20	-20	325	0	1500	70	197	194	60	4.8	0.7	
RYAX4A		-20	0	325	0	1500	70	197	194	60	4.8	0.7	
RZAX4A		-20	20	325	0	1500	70	197	194	60	4.8	0.7	
RZAY4A		-30	20	325	0	1500	70	197	194	60	4.8	0.7	
RYAY4A		-30	0	325	0	1500	70	197	194	60	4.8	0.7	
RXAY4A		-30	-20	325	0	1500	70	197	194	60	4.8	0.7	
RWAY4A		-30	-40	325	0	1500	70	197	194	60	4.8	0.7	break
RWAV2B		0	-40	225	100	1500	115	197	194	60	4.7	0.7	
RXAV2B		0	-20	225	100	1500	115	197	194	60	4.7	0.7	
RYAV2B		0	0	225	100	1500	110	197	194	60	4.7	0.7	
RZAV2B		0	20	225	100	1500	110	197	194	60	4.7	0.7	
RZAW2B		-10	20	225	100	1500	110	197	194	60	4.7	0.7	
RYAW2B		-10	0	225	100	1500	110	197	194	60	4.7	0.7	
RXAW2B		-10	-20	225	100	1500	110	197	194	60	4.7	0.7	
RWAW2B		-10	-40	225	100	1500	100	197	194	60	4.7	0.7	
RWAX2B		-20	-40	225	100	1500	100	197	194	60	4.7	0.7	
RXAX2B		-20	-20	225	100	1500	100	197	194	60	4.7	0.7	
RYAX2B		-20	0	225	100	1500	100	197	194	60	4.7	0.7	
RZAX2B		-20	20	225	100	1500	100	197	194	60	4.8	0.7	
RZAY2B		-30	20	225	100	1500	100	197	194	60	4.8	0.7	
RYAY2B		-30	0	225	100	1500	100	197	194	60	4.8	0.7	
RXAY2B		-30	-20	225	100	1500	100	197	194	60	4.8	0.7	
RWAY2B		-30	-40	225	100	1500	100	197	194	60	4.8	0.7	
RWAV3B		0	-40	300	100	1500	85	197	194	60	4.8	0.7	
RXAV3B		0	-20	300	100	1500	85	197	194	60	4.8	0.7	
RYAV3B		0	0	300	100	1500	85	197	194	60	4.8	0.7	
RZAV3B		0	20	300	100	1500	85	197	194	60	4.8	0.7	
RZAW3B		-10	20	300	100	1500	85	197	194	60	4.8	0.7	
RYAW3B		-10	0	300	100	1500	85	197	194	60	4.8	0.7	
RXAW3B		-10	-20	300	100	1500	85	197	194	60	4.8	0.7	
RWAW3B		-10	-40	300	100	1500	90	197	194	60	4.8	0.7	
RWAX3B		-20	-40	300	100	1500	90	197	194	60	4.8	0.7	
RXAX3B		-20	-20	300	100	1500	90	197	194	60	4.8	0.7	
RYAX3B		-20	0	300	100	1500	90	197	194	60	4.8	0.7	
RZAX3B		-20	20	300	100	1500	85	197	194	60	4.8	0.7	
RZAY3B		-30	20	300	100	1500	85	197	194	60	4.8	0.7	
RYAY3B		-30	0	300	100	1500	85	197	194	60	4.8	0.7	
RXAY3B		-30	-20	300	100	1500	85	197	194	60	4.8	0.7	
RWAY3B		-30	-40	300	100	1500	85	197	194	60	4.8	0.7	break
RWAV4B		0	-40	325	100	1500	100	197	194	60	4.7	0.7	
RXAV4B		0	-20	325	100	1500	100	197	194	60	4.7	0.7	
RYAV4B		0	0	325	100	1500	100	197	194	60	4.7	0.7	
RZAV4B		0	20	325	100	1500	100	197	194	60	4.8	0.7	
RZAW4B		-10	20	325	100	1500	100	197	194	60	4.8	0.7	
RYAW4B		-10	0	325	100	1500	100	197	194	60	4.8	0.7	
RXAW4B		-10	-20	325	100	1500	100	197	194	60	4.8	0.7	
RWAW4B		-10	-40	325	100	1500	95	197	194	60	4.8	0.7	
RWAX4B		-20	-40	325	100	1500	95	197	194	60	4.8	0.7	
RXAX4B		-20	-20	325	100	1500	95	197	194	60	4.8	0.7	
RYAX4B		-20	0	325	100	1500	95	197	194	60	4.8	0.7	
RZAX4B		-20	20	325	100	1500	95	197	194	60	4.8	0.7	
RZAY4B		-30	20	325	100	1500	95	197	194	60	4.8	0.7	
RYAY4B		-30	0	325	100	1500	95	197	194	60	4.8	0.7	

Filename	LP position (mm)			Recomm		Power (watts)		Matching Network		Magnets		Pressure	notes
	Vert	Axial	Rad	Amps	Volts	input	reflected	Loading	Tuning	Cur (A)	Vol (V)	(mtorr)	
RXAY4B		-30	-20	325	100	1500	95	197	194	60	4.8	0.7	
RWAY4B		-30	-40	325	100	1500	85	197	194	60	4.8	0.7	
RWAV4C		0	-40	325	250	1500	85	197	194	60	4.8	0.7	lost rac
RWAW4C		-10	-40	325	250	1500	85	197	194	60	4.8	0.7	table
RWAX4C		-20	-40	325	250	1500	85	197	194	60	4.8	0.7	
RWAY4C		-30	-40	325	250	1500	85	197	194	60	4.8	0.7	
RWAV4D		0	-40	325	400	1500	85	197	194	60	4.9	0.7	very ve
RWAW4D		-10	-40	325	400	1500	85	197	194	60	4.9	0.7	arcy an
RWAX4D		-20	-40	325	400	1500	85	197	194	60	4.9	0.7	sparke
RWAY4D		-30	-40	325	400	1500	85	197	194	60	4.9	0.7	

Table C.7: Testing Matrix for Plasma Frequency and Signal Attenuation Measurements: Trial 2

time	LP position (mm)			Recomm		Power (watts)		Matching Network		Magnets		Pressure	notes
	Vert	Axial	Rad	Amps	Volts	input	reflected	Loading	Tuning	Cur (A)	Vol (V)	(mtorr)	
10:16	~.5 cm over electrode nearest to helicon source			0	0	1600	210			60.1	4.6	0.7	
10:18				50	0	1600	200			60.1	4.7	0.7	
10:20				50	100	1600	190			60.1	4.7	0.7	
10:22				100	0	1600	170			60.1	4.7	0.7	
10:24				200	?	1550	140			60.1	4.7	0.7	
10:27				325		1500	110			60.1	4.7	0.7	
10:45	~.5 cm up, midway between two electrodes			0		1600	210			60.1	4.7	0.7	
10:46				50		1600	190			60.1	4.7	0.7	
10:48				150		1600	180			60.1	4.8	0.7	
10:50				325		1500	120			60.1	4.8	0.7	
10:51				325		1500	110			60.1	4.8	0.7	
10:53	~.5 cm above electrode furthest from helicon source			325		1500	100			60.1	4.8	0.7	
10:54				0		1600	180			60.1	4.8	0.7	
11:22	Electrodes flipped, above furthest electrode			0		1600	215			60.1	4.8	0.7	
11:24				50		1600	200			60.1	4.8	0.7	
11:26				50		1600	190			60.1	4.9	0.7	
11:29	between			50		1600	185			60.1	4.9	0.7	
11:30				150		1550	150			60.1	4.9	0.7	
11:33				325		1500	110			60.1	4.9	0.7	
11:36				325		1500	100			2:24	4.9	0.7	

APPENDIX D

Additional Downstream Results from Langmuir Probe Testing

D.1 Empty Chamber Downstream

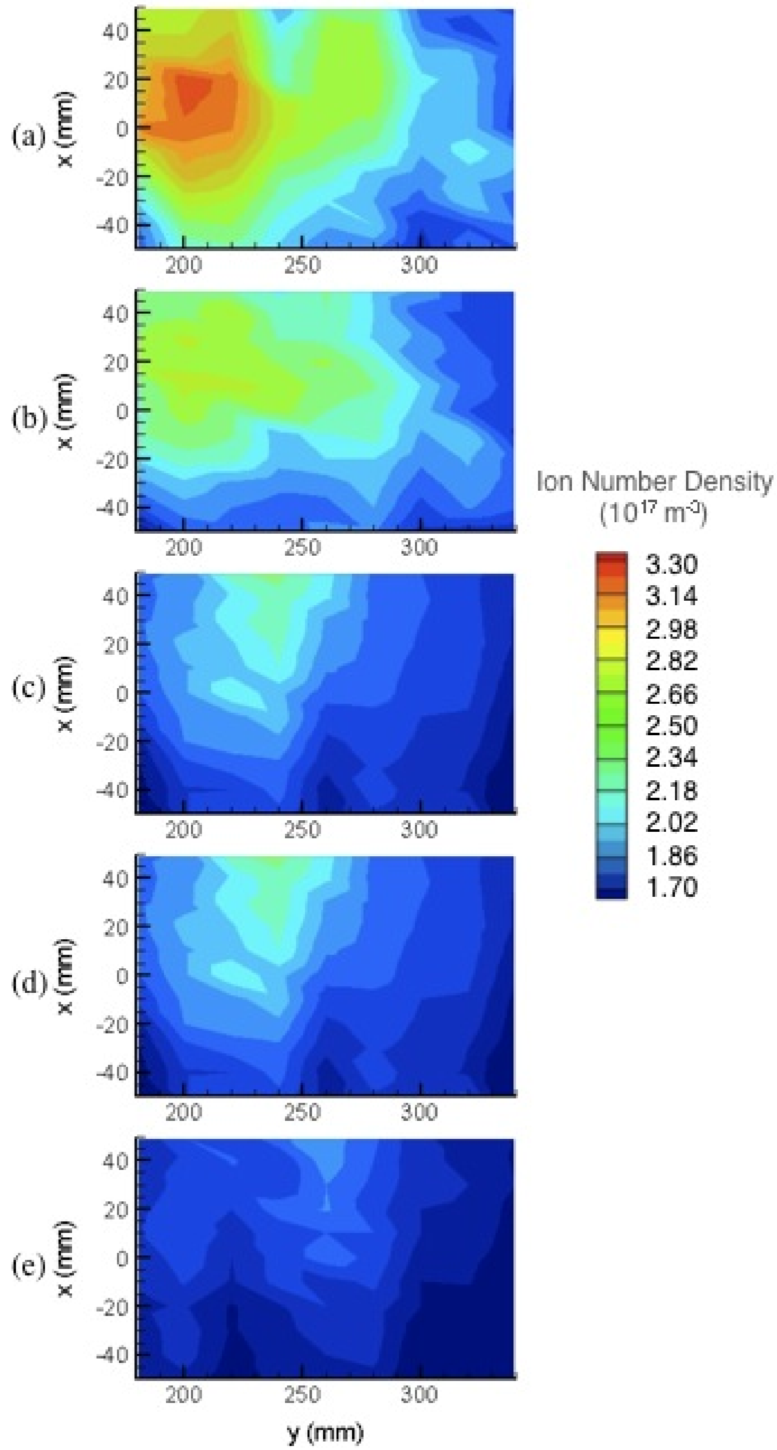

Figure D.1: Ion number density downstream - empty chamber for (a) z = -10 mm, (b) z = -20 mm, (c) z = -40 mm, (d) z = -50 mm and (e) z = -70 mm.

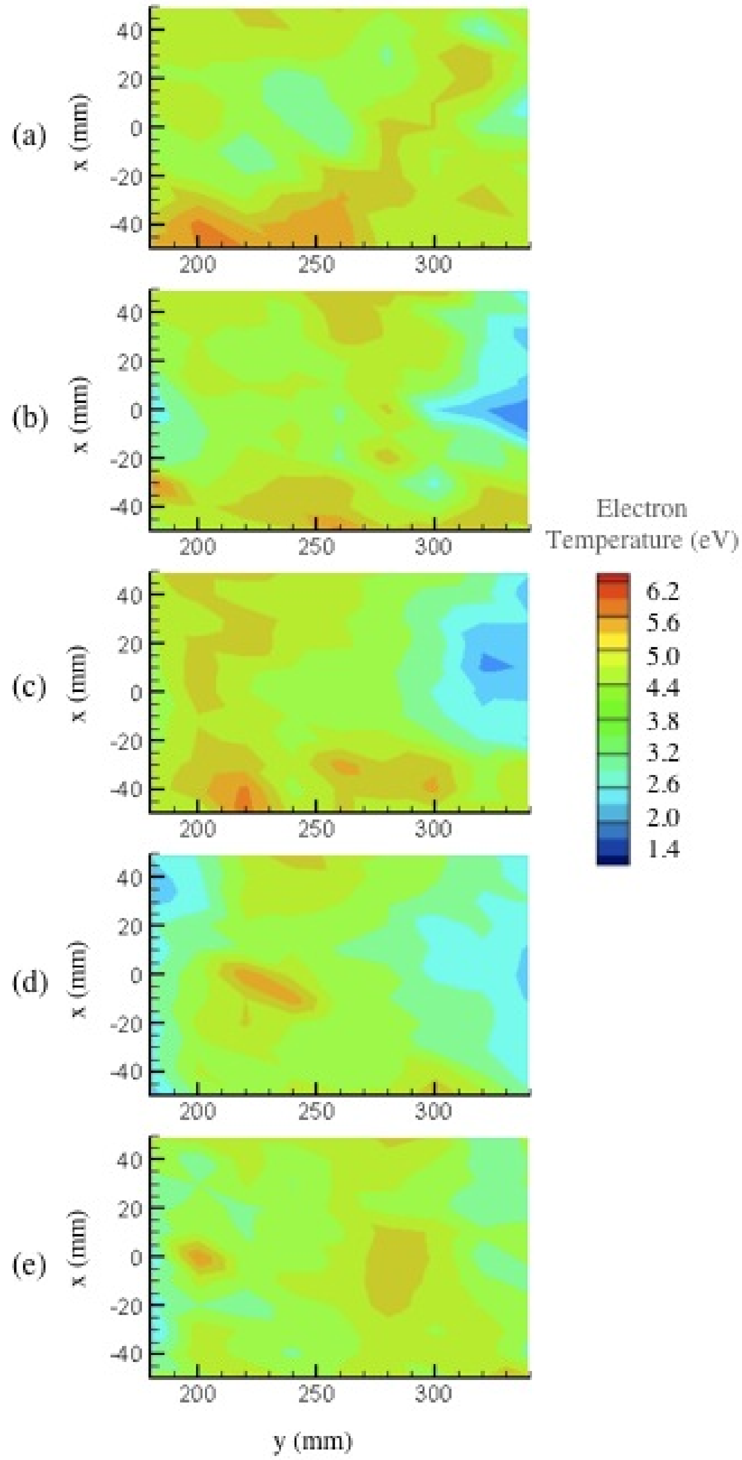

Figure D.2: Electron temperature downstream - empty chamber for (a) z = -10 mm, (b) z = -20 mm, (c) z = -40 mm, (d) z = -50 mm and (e) z = -70 mm.

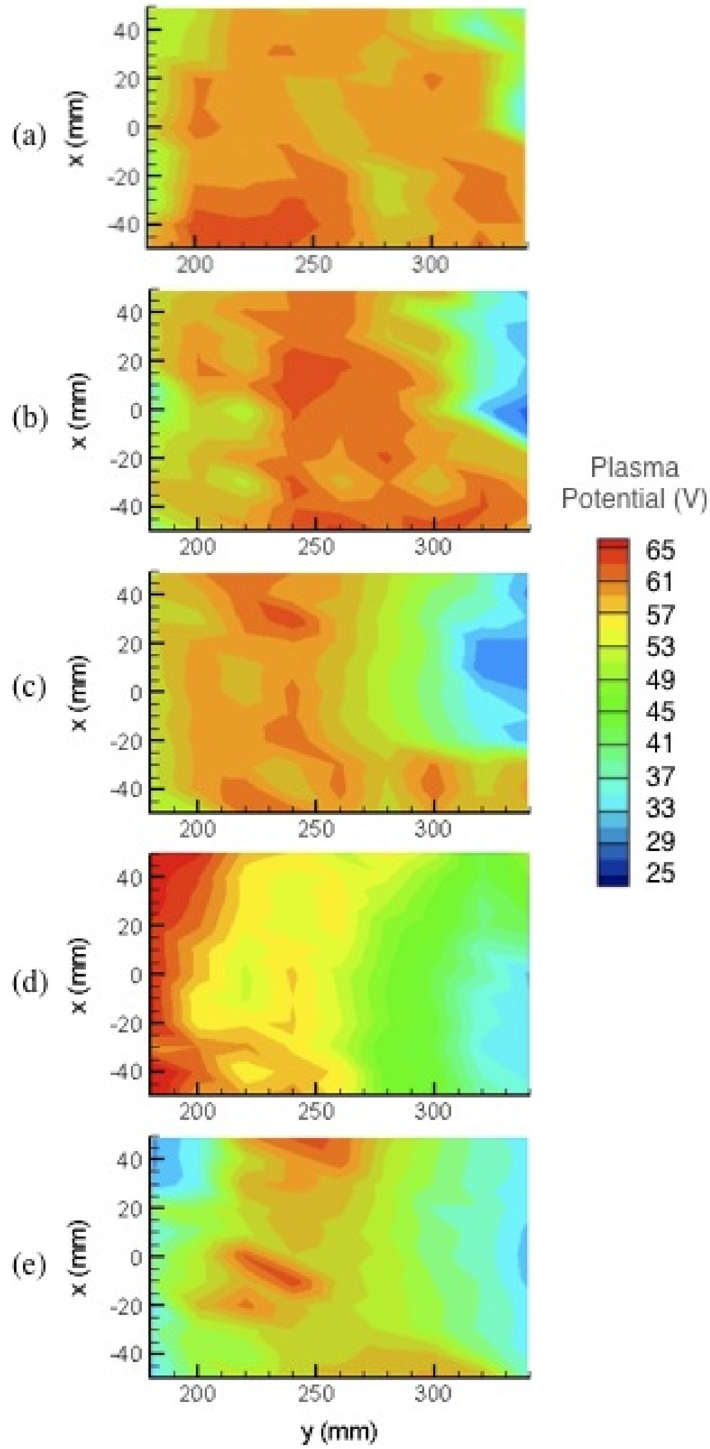

Figure D.3: Plasma potential downstream - empty chamber for (a) z = -10 mm, (b) z = -20 mm, (c) z = -40 mm, (d) z = -50 mm and (e) z = -70 mm.

D.2 ReComm System Present Downstream

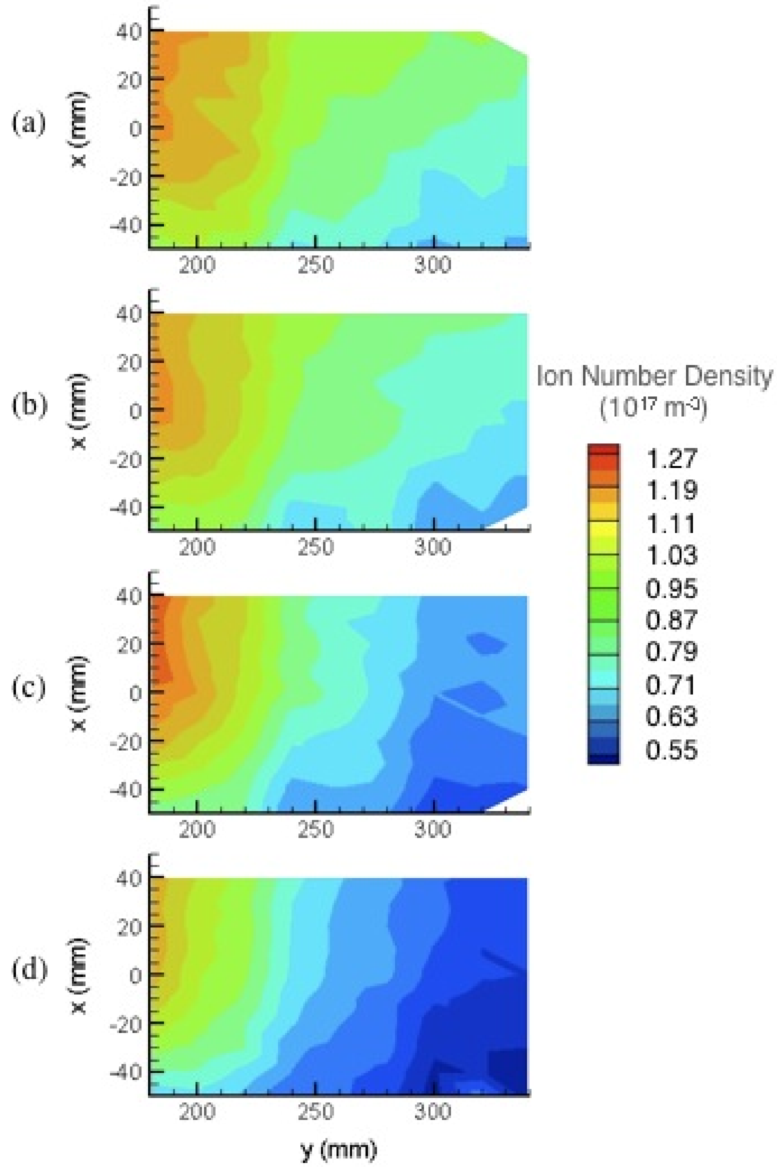

Figure D.4: Ion number density downstream - ReComm system present for (a) z = -10 mm, (b) z = -20 mm, (c) z = -40 mm and (d) z = -50 mm.

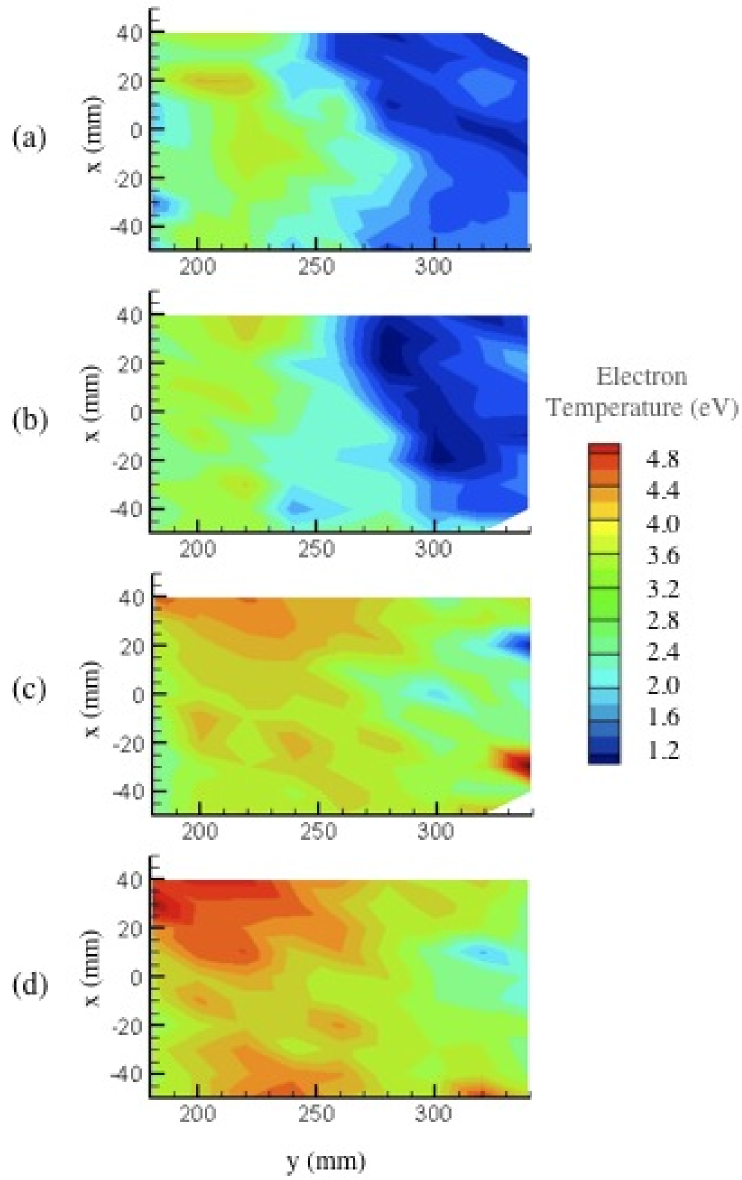

Figure D.5: Electron temperature downstream - ReComm system present for (a) z = -10 mm, (b) z = -20 mm, (c) z = -40 mm and (d) z = -50 mm.

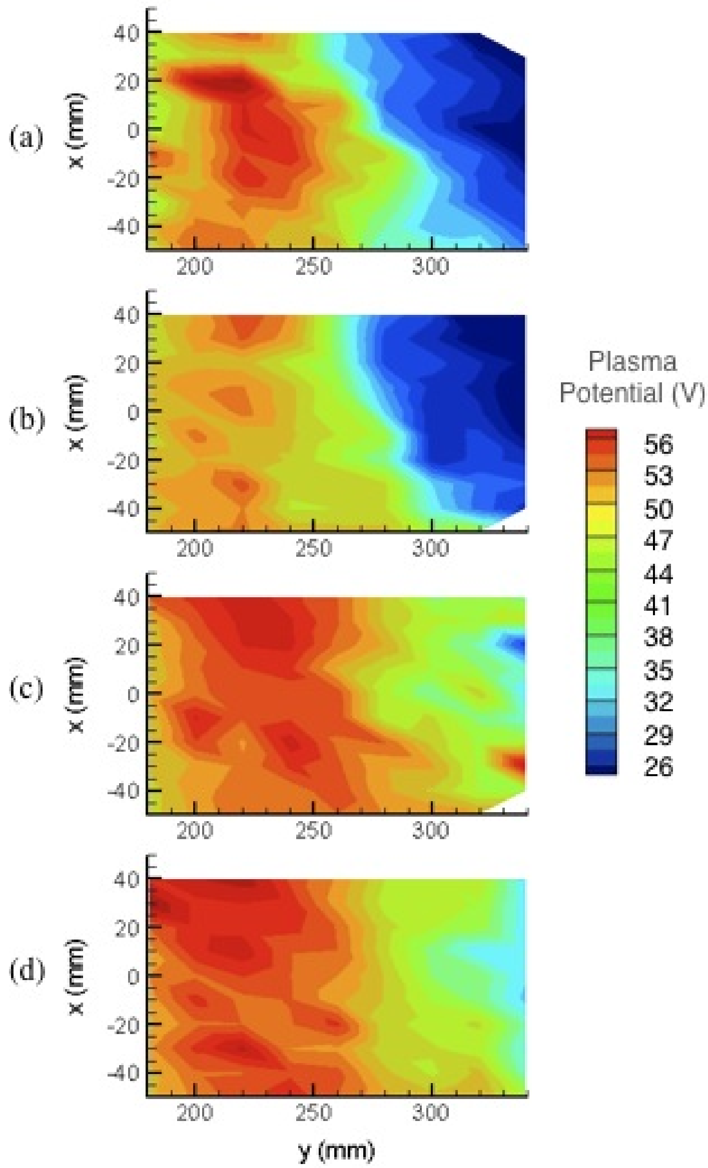

Figure D.6: Plasma potential downstream - ReComm system present for (a) z = -10 mm, (b) z = -20 mm, (c) z = -40 mm and (d) z = -50 mm.

APPENDIX E

Axial Plots of Density Reduction Along Two Axes

Plots were produced for the density reduction as a function of position along two axes for the two vertical planes (z = -70 mm and z = -75 mm). The first set were found along the x = -20 mm axis for varying y-position. The second set were found along a line varying in x and y. The axis along which the data were taken is shown in the corresponding figures. Each set of figures shows results from the ReComm system operating alone, and from the ReComm system operating with the electric field. The data are independent of these two axes, as both cases show similar behavior: the density reduction increases closer to the iron core and the cathode.

E.1 Peak B_z = 925 G

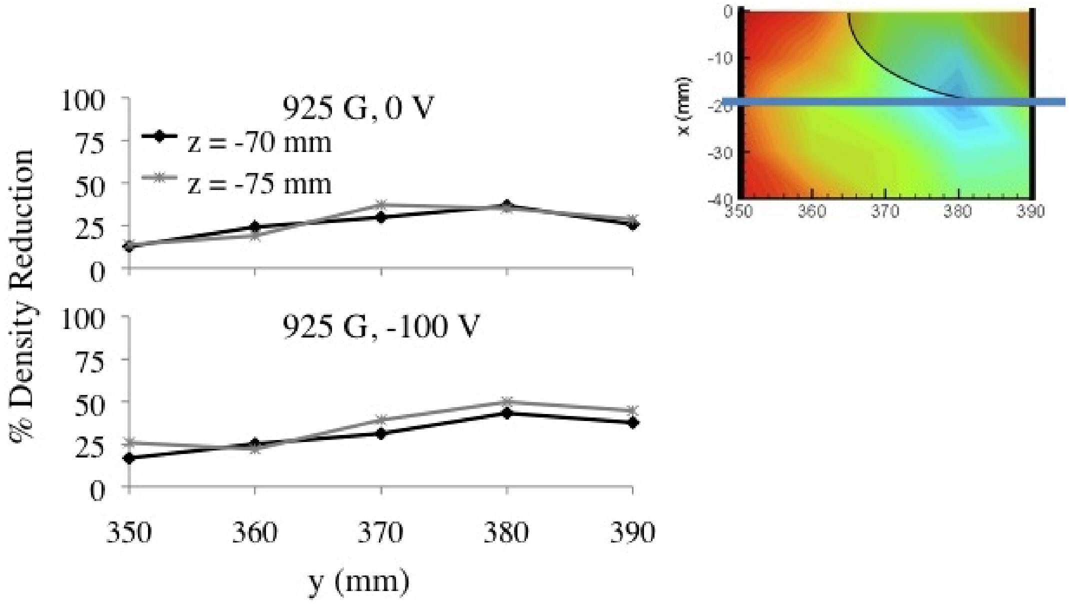

Figure E.1: Density Reduction as a function of y-position and cathode voltage along x = -20 mm for B_z = 925 G.

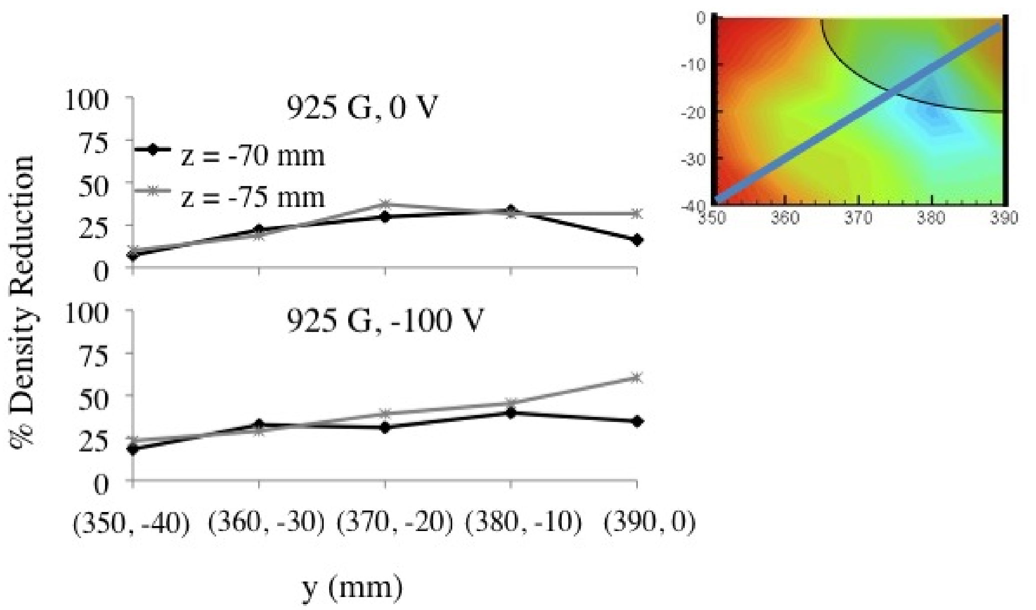

Figure E.2: Density Reduction as a function of y-position and cathode voltage along the line $x = y - 390$ for B_z = 925 G.

E.2 Peak B_z = 1385 G

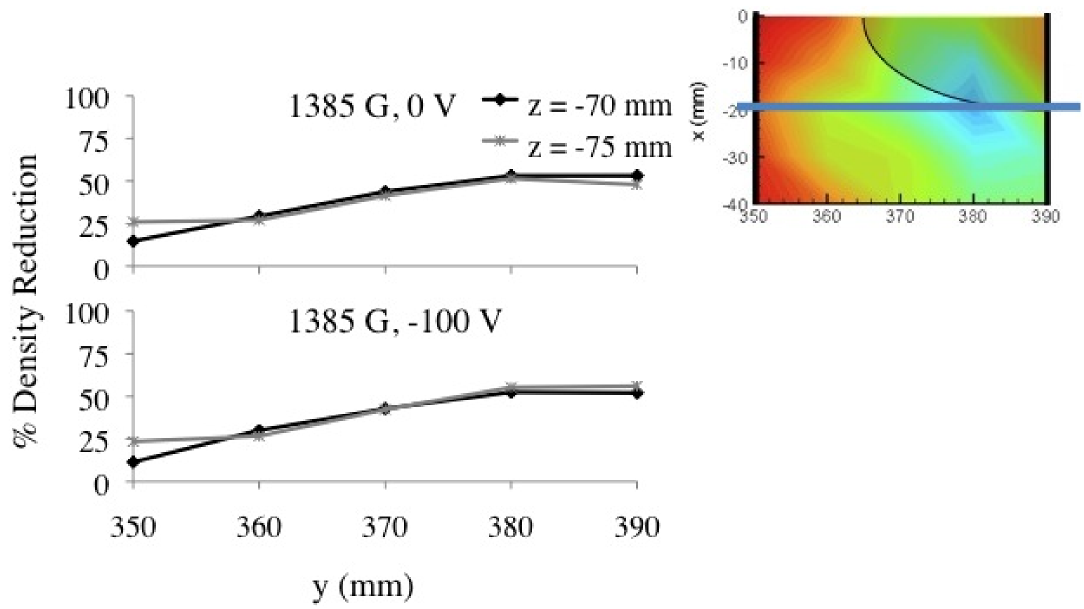

Figure E.3: Density Reduction as a function of y-position and cathode voltage along x = -20 mm for B_z = 1385 G.

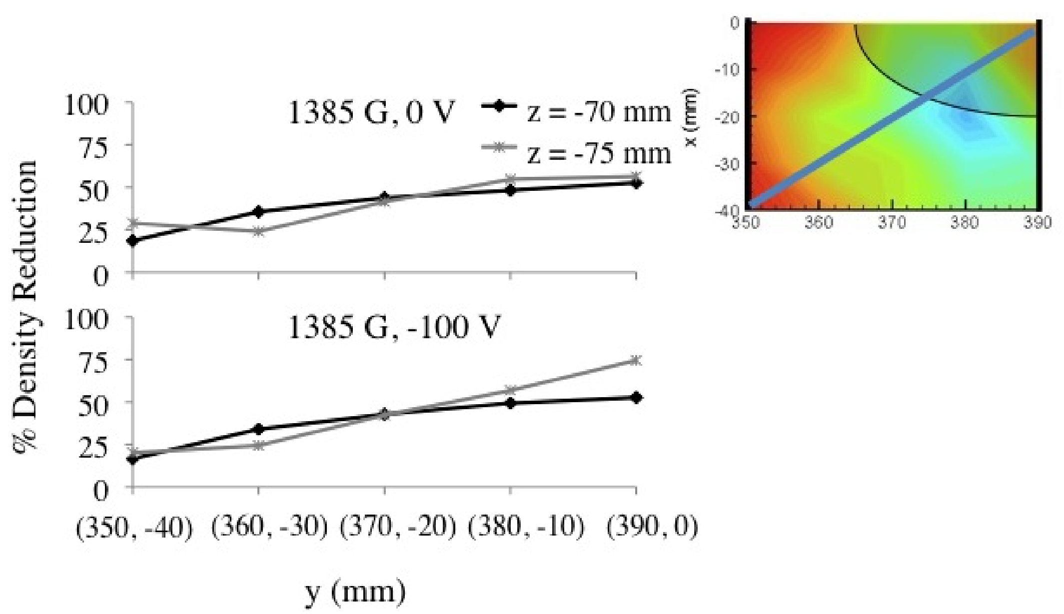

Figure E.4: Density Reduction as a function of y-position and cathode voltage along the line $x = y - 390$ for B_z = 1385 G.

E.3 Peak B_z = 1800 G

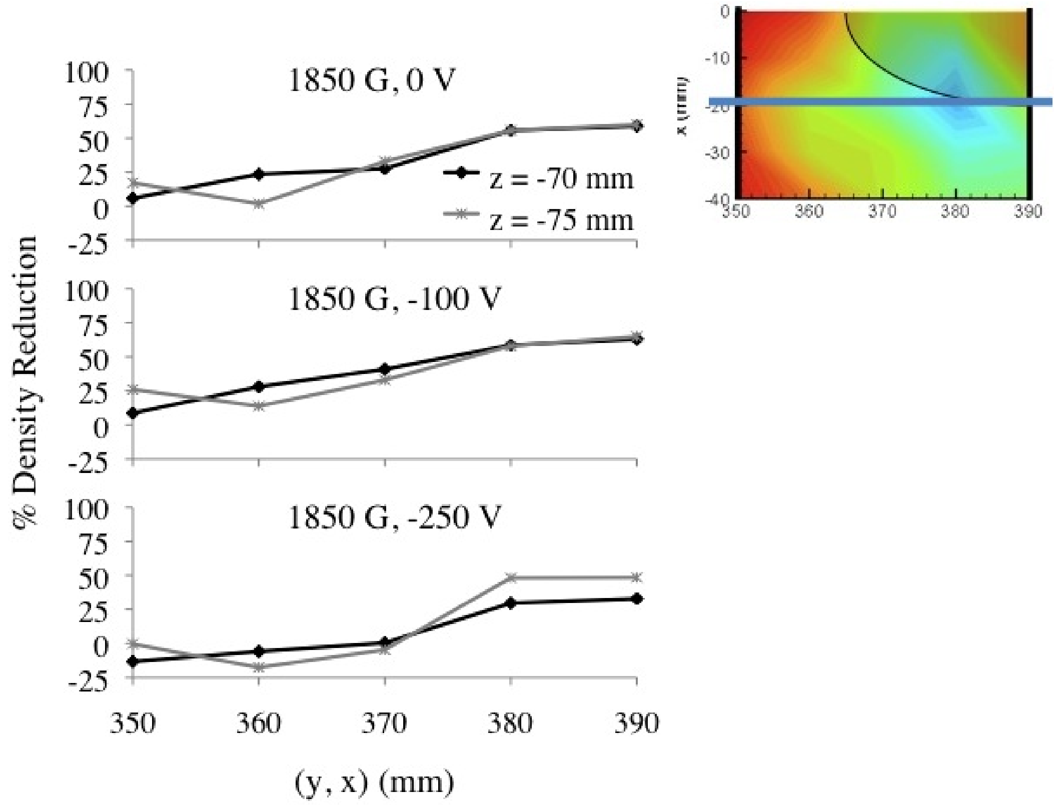

Figure E.5: Density Reduction as a function of y-position and cathode voltage along x = -20 mm for B_z = 1800 G.

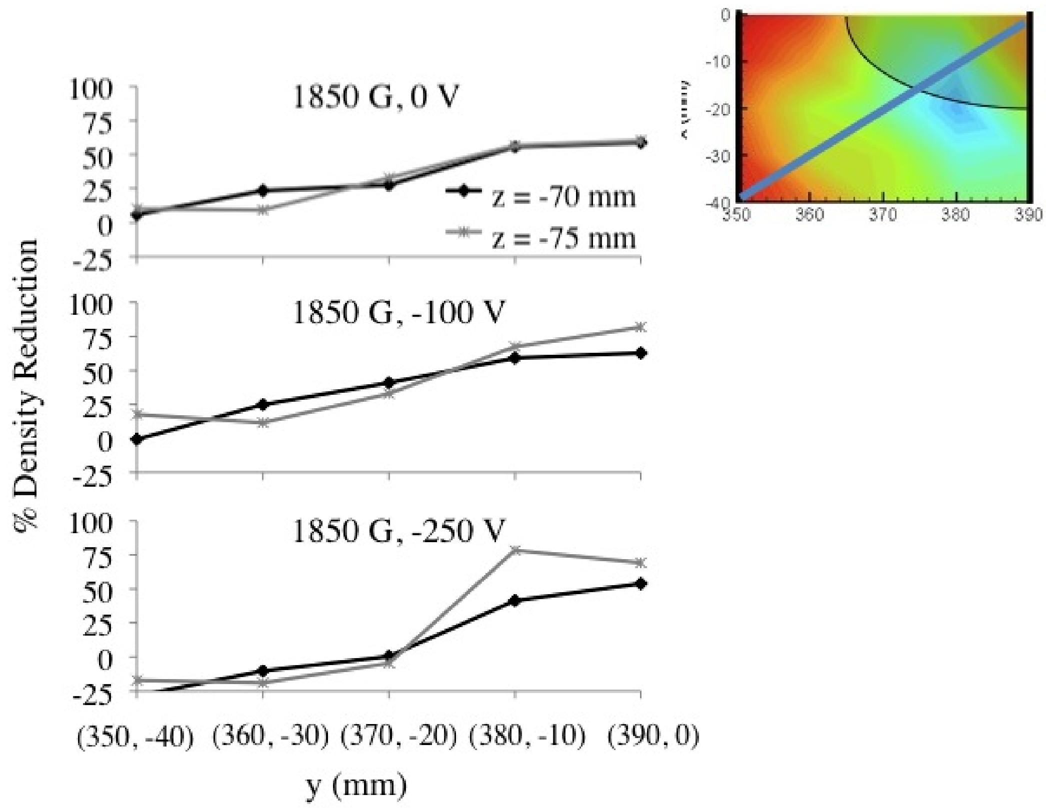

Figure E.6: Density Reduction as a function of y-position and cathode voltage along the line $x = y - 390$ for $B_z = 1800$ G.

BIBLIOGRAPHY

BIBLIOGRAPHY

[1] Montgomery, D. C. and Tidman, D. A. (1964) *Plamsa Kinetic Theory*. McGraw-Hill.

[2] Morabito, D. D. (2002) The spacecraft communications blackout problem encountered during passage or entry of planetary atmospheres. Progress Report 42-150, IPN.

[3] Air, N. and Page, S. A. W. (2009). `http://www.nasa.gov/mission_pages/genesis/main/`.

[4] Rybak, J. P. (1970) Causes, effects and diagnostic measurements of the reentry plasma sheath. Contractor Report AFCRL-70-0707, Air Force Cambridge Research Laboratory.

[5] Rybak, J. P. and Churchill, R. J. (1971) Progress in reentry communications. *IEEE Transactions on Aerospace and Electronic Systems*, **AES-7**, 879–894.

[6] Chen, F. F. (1984) *Introduction to Plasma Physics and Controlled Fusion Volume 1: Plasma Physics*. Plenum Press, 2nd edn.

[7] Lukasiewicz, J., Whitfield, J. D., and Jackson, R. (1962) Hypersonic flow research. *Progress in Astronautics and Rocketry*, **8**, 473–511.

[8] Winovich, W. and Carlson, W. C. A. (1979) The 60 MW shuttle interaction heating facility. *Proceedings of the 25th International Instrumentation Symposium*, Anaheim, CA.

[9] Auweter-Kurtz, M., Kurtz, H. L., and Laure, S. (1996) Plasma generators for re-entry simulation. *Journal of Propulsion and Power*, **12**.

[10] Seemann, G. R., Thornton, J. A., and Penfold, A. (1968) Subsonic plasma tunnel for evaluating re-entry flight instrumentation. *AIAA Journal*, **6**, 1592–1594.

[11] Chadwick, K. M., Boyer, D. W., and Andre, S. S. (1996) Plasma and flowfield induced effects on hypervelocity re-entry vehicles for l-band irradiation at near broadside aspect angles. *27th AIAA Plasmadynamics and Lasers Conference*, New Orleans, LA, June.

[12] Lewis, J. H. J. and Scallion, W. I. (1966) Flight parameters and vehicle performance for Project Fire flight II, launched May 22, 1965. Technical Note TN D-3569, NASA.

[13] Scallion, W. I. and Lewis, J. H. J. (1965) Flight parameters and vehicle performance for Project Fire flight I, launched April 14, 1964. Technical Note TN D-2996, NASA.

[14] Grantham, W. L. (1970) Flight results of a 25 000-foot-per-second reentry experiment using microwave reflectometers to measure plasma electron density and standoff distance. NASA Technical Note D-6062, Langley Research Center, Hampton, VA.

[15] Jones Jr., W. L. and Cross, A. E. (1972) Electrostatic probe measurements of plasma parameters for two reentry flight experiments at 25 000-feet-per-second. NASA Technical Note D-6617, Langley Research Center, Hampton, VA.

[16] Schwartzentruber, T. E. and Boyd, I. D. (2006) A hybrid particle-continuum method applied to shock waves. *Journal of Computational Physics*, **215**, 402–416.

[17] Scalabrin, L. C. (2007) *Numerical Simulation of Weakly Ionized Hypersonic Flow Over Reentry Capsules*. Ph.D. thesis, University of Michigan, Ann Arbor, MI.

[18] Keidar, M., Monteiro, O. R., Anders, A., and Boyd, I. D. (2002) Magnetic field effect on the sheath thickness in plasma immersion ion implantation. *Applied Physics Letters*, **81**, 1183–1185.

[19] Epstein, M. (1967) Antenna breakdown in a hypersonic re-entry environment. Report AFCRL-67-0280, Cambridge Research Labs.

[20] Huber, P. W. and Sims, T. E. (1964) The re-entry communications problem. *Astronautics and Aeronautics*, **2**, 30.

[21] Jacavanco, D. J. (1969) Electron reduction in the reentry plasma sheath. Tech. Rep. AFCRL-69-0154, USAF Cambridge Research Labs.

[22] Hodara, H. (1961) The use of magnetic fields in the elimination of the re-entry radio blackout. *Proceedings of the Institute of Radio Engineers*, **49**, 1825.

[23] Hartunian, R. A., Stewart, G. E., Fergason, S. D., Curtiss, T. J., and Seibold, R. W. (2007) Causes and mitigation of radio frequency (RF) blackout during reentry of reusable launch vehicles. Contractor Report ATR-2007(5309)-1, The Aerospace Corporation, El Segundo, CA.

[24] Dunn, M. G. and Kang, S.-W. (1973) Theoretical and experimental studies of reentry plasmas. NASA Contractor Report CR-2232, Langley Research Center, Washington D.C.

[25] Friel, P. J. and Rosenbaum, B. (1963) Propagation of electromagnetic waves through re-entry induced plasmas. *Advances in the Astronautical Sciences*, **11**, 399–430.

[26] Linnell, J. A. (2007) *An Evaluation of Krypton Propellant in Hall Thrusters*. Ph.D. thesis, University of Michigan, Ann Arbor, MI.

[27] Haas, J. M., Gulczinski, F. S., Gallimore, A. D., Spanjers, G. G., and Spores, R. A. (1998) Performance characteristics of a 5 kW laboratory Hall thruster. *34th Joint Propulsion Conference*, Cleveland, OH, July, no. AIAA-98-3503, AIAA.

[28] Davis, C. N., Gilchrist, B. E., , and Gallimore, A. D. (1999) Density and spectral measurements using a 34 GHz interferometry system. *35th Joint Populsion Conference*, Los Angeles, CA, June, no. AIAA-99-2718, AIAA.

[29] Wang, J., Brophy, J., and Brinza, D. (1996) 3-D simulations of NSTAR ion thruster plamsa envrionment. *32nd Joint Propulsion Conference*, Lake Buena Vista, FL, July, no. AIAA-96-3202, AIAA.

[30] Foster, J. E., Soulas, G. C., and Patterson, M. J. (2000) Plume and discharge plamsa measeurments of an NSTAR-type ion thruster. *36th Joint Propulsion Conference*, Huntsville, AL, July, no. A00-36940, AIAA.

[31] Kamhawi, H., Soulas, G., Patterson, M., and Frandina, M. M. (2004) NEXT ion engine 2000 hour wear test plume and erosion results. *40th Joint Propulsion Conference*, Ft. Lauderdale, FL, July, no. AIAA-2004-3792, AIAA.

[32] Domonkos, M. T., Gallimore, A. D., Williams, G. J., and Patterson, M. J. (1999) Low-current hollow cathode evaluation. *35th Joint Propulsion Conference*, Los Angeles, CA, June, no. AIAA-99-2575, AIAA.

[33] Lieberman, M. A. and Lichtenberg, A. J. (1994) *Principles of Plasma Discharges and Materials Processing*. John Wiley & Sons, Inc.

[34] Aanesland, A. and Charles, C. (2006) Plasma expansion from a dielectric electron cyclotron resonance source. *Physica Scripta*, **T122**, 19 – 24.

[35] Ohkuni, K., Ogawa, Y., Morikawa, J., Hori, D., and Yamakoshi, S. (2004) Characteristics of electron cyclotron resonance heating plasmas and experimental plans for formation of radial electric field in an internal coil device mini-rt. *Journal of Fusion Research*, **6**, 183 – 186.

[36] Boswell, R. W. and Chen, F. F. (1997) Helicons - the early years. *IEEE Transactions on Plasma Science*, **25**, 1229–1244.

[37] Chen, F. F. and Boswell, R. W. (1997) Helicons - the past decade. *IEEE Transactions on Plasma Science*, **25**.

[38] Carter, C. and Khachan, J. (1999) Downstream plasma characteristics from a single loop antenna in a helicon processing reactor. *Plasma Sources Science and Technology*, **8**, 432–439.

[39] Brown, R., Deuchars, W. M., Illingworth, R., and J., I. (1977) 10-6 micrometer interferometry and faraday rotation measurements on a theta-pinch plasma. *Journal of Physics D: Applied Physics*, **10**, 1575 – 1581.

[40] Kronast, B., Rohr, H., Glock, E., Zwicker, H., and Funfer, E. (1966) Measurements of the ion and electron temperature in a theta-pinch plasma by forward scattering. *Physical Review Letters*, **16**, 1082–1085.

[41] Chen, F. F. (1985) *High Density Plasma Sources: Design, Physics and Performance*, chap. 1: Helicon Plasma Sources, pp. 1 – 76. William Andrew Inc.

[42] Chen, F. F. (1991) Plasma ionization by helicon waves. *Plasma Physics and Controlled Fusion*, **33**, 339–364.

[43] Lehane, J. A. and Thoenmann, P. C. (1965) An experimental study of helicon wave propagation in a gaseous plasma. *Proceedings of the Physical Society*, **85**, 301.

[44] Boswell, R. W. (1970) Plasma production using a standing helicon wave. *Physics Letters*, **33A**, 457–458.

[45] Boswell, R. W. (1974) *A Study of Waves in Gaseous Plasmas*. Ph.D. thesis, Flinders University of South Australia.

[46] Blackwell, D. D., Madziwa, T. G., Arnush, D., and Chen, F. F. (2002) Evidence for Trivelpiece-Gould modes in a helicon discharge. *Physical Review Letters*, **88**, 145002–1 – 4.

[47] Keiter, P. A. (1999) *Experimental Investigation of Ion Temperature Anisotropy Driven Instabilities in High Beta Plasma*. Ph.D. thesis, West Virginia University, Morgantown, WV.

[48] Chen, F. F. (1992) Experiments on helicon plasma sources. *Journal of Vacuum Science and Technology A*, **10**, 1389–1401.

[49] Balkey, M. M. (2000) *Optimization of a Helicon Plasma Source for Maximum Density with Minimal Ion Heating*. Ph.D. thesis, West Virginia University.

[50] Chi, K.-K., Sheridan, T. E., and Boswell, R. W. (1999) Resonant cavity modes of a bounded helicon discharge. *Plasma Sources Science and Technology*, **8**, 421–431.

[51] Chen, F. F. (2007) Permanent magnet helicon source for ion propulsion. *IEEE Transactions on Plasma Science*, **36**, 2095.

[52] Beal, B. E., Gallimore, A. D., Morris, D. P., Davis, C., and Lemmer, K. M. (2006) Development of an annular helicon source for electric propulsion applications. *42nd AIAA/ASME/SAE/ASEE Joint Propulsion Conference and Exhibit*, Sacramento, California, July, no. AIAA-2006-4841, AIAA, AIAA.

[53] Degeling, A. W., Jung, C. O., Boswell, R. W., and Ellingboe, A. R. (1996) Plasma production from helicon waves. *Physics of Plasmas*, **3**, 2788–2796.

[54] Shinohara, S., Takechi, S., Kaneda, N., and Kawa, Y. (1997) Helicon m = 0 mode characteristics in large-diameter plasma produced by a planar spiral antenna. *Plasma Physics and Controlled Fustion*, **39**, 1479–1486.

[55] Boswell, R. W. and Vender, D. (1995) An experimental study of breakdown in a pulsed helicon plasma. *Plasma Sources Science and Technology*, **4**, 534–540.

[56] Sutherland, O., Charles, C., Plihon, N., and Boswell, R. W. (2005) Experimental evidence of a double layer in a large volume helicon reactor. *Physical Review Letters*, **95**.

[57] Porte, L., Yun, S. M., Arnush, D., and Chen, F. F. (2003) Superiority of half-wavelength helicon antennae. *Plasma Sources Science and Technology*, **12**, 287–293.

[58] Macheret, S. O., Shneider, M. N., and Miles, R. B. (2002) Magnetohydrodynamic control of hypersonic flows and scramjet inlets using electron beam ionization. *AIAA Journal*, **40**, 74–81.

[59] Usui, H., Matsumoto, H., Yamashita, F., Yamane, M., and Takenaka, S. (1999) Computer experiments on the measurements of reentry plasma with radio waves. *Active Experiments in Space Plasmas*, **24**, 1069–1072.

[60] Keidar, M., Kim, M., and Boyd, I. D. (2008) Electromagnetic reduction of plasma density during atmospheric reentry and hypersonic flights. *Journal of Spacecraft and Rockets*, **45**, 445–453.

[61] Kim, M., Keidar, M., and Boyd, I. D. (2008) Analysis of an electromagnetic mitigation scheme for reentry telemetry through plasma. *Journal of Spacecraft and Rockets*, **45**, 1223–1229.

[62] Huba, J. D. NRL plasma formulary. Office of Naval Research, Washington D.C.

[63] Rochelle, W. C., Tillian, D. J., Heaton, T. M., Battley, H. H., Murry, L. P., and Grimaud, J. E. (1983) Orbiter TPS development and certification testing at the NASA/JSC 10 MW atmospheric reentry materials and structures evaluation facility. *Aerospace Sciences Meeting*, Reno, Nevada, no. AIAA-1983-147, AIAA, AIAA.

[64] Burm, K. T. A. L. (2007) Calculation of the Townsend discharge coefficients and the Paschen curve coefficients. *Contributions to Plasma Physics*, **47**, 177–182.

[65] Mott-Smith, H. M. and Langmuir, I. (1926) The theory of collectors in gaseous discharges. *Physical Review*, **28**, 727–763.

[66] Langmuir, I. (1929) The interaction of electron and positive ion space charges in cathode sheaths. *Physical Review*, **33**, 954–989.

[67] Hutchinson, I. H. (2002) *Principles of Plasma Diagnostics*. Cambridge University Press, second edn.

[68] Sudit, I. D. and Chen, F. F. (1994) RF compensated probes for high-density discharges. *Plasma Sources Science and Technology*, **3**, 162–168.

[69] Chen, F. F. (1965) *Plasma Diagnostic Techniques, Electric Probes*. Academic Press.

[70] Laframboise, J. G. and Parker, L. W. (1973) Probe design for the orbit-limited current collection. *Journal of Fluids*, **6**, 629–636.

[71] Laframboise, J. G. and Rubinstein, J. (1976) Theory of a cylindrical probe in a collisionless magnetoplasma. *Journal of Fluids*, **19**, 1900–1908.

[72] Hershkowitz, N. (1989) *Plasma Diagnostics*, chap. 3: How Langmuir Probes Work, pp. 113–183. Academic Press.

[73] Chung, P. M., Talbot, L., and Touryan, K. J. (1974) Electric probes in stationary and flowing plasma: Part 1. collisionless and transitional probes. *AIAA Journal*, **12**, 133.

[74] Bohm, D., Burhop, E. H. S., and Massey, H. S. W. (1949) *The Characteristics of Electrical Discharges in Magnetic Fields*, chap. The Use of Probes for Plasma Exploration in Strong Magnetic Fields. McGraw-Hill Book Company, Inc.

[75] Bohm, D. (1949) *The Characteristic of Electrical Discharges in Magnetic Fields*. McGraw-Hill Book Company.

[76] Ruzic, D. N. (1994) *Electric Probes for Low Temperature Plasmas*. The Education Committee American Vacuum Society.

[77] Schott, L. (1968) *Plasma Diagnostics*, chap. 11: Electrical Probes, pp. 688–731. North-Holland Publishing Company.

[78] Herman, D. A. (2005) *The Use of Electrostatic Probes to Characterize the Discharge Plasma Structure and Identify Discharge Cathode Erosion Mechanisms in Ring-Cusp Ion Thrusters*. Ph.D. thesis, University of Michigan, Ann Arbor, MI.

[79] Peterson, E. W. and Talbot, L. (1970) Collisionless electrostatic single-probe and double-probe measurements. *AIAA Journal*, **8**, 2215–2219.

[80] Narasimhan, G. and Seteinbruchel, C. (2001) Analysis of Langmuir probe data: Analytical parametrization and the importance of the end effect. *Journal of Vacuum Science and Technology A*, **19**, 376–378.

[81] Rovey, J. L. (2006) *A Multiple-Cathode, High-Power, Rectangular Ion Thruster Discharge Chamber for Increasing Thruster Lifetime*. Phd thesis, University of Michigan, Ann Arbor, MI.

[82] Chen, F. F. (2001) Langmuir probe analysis for high density plasma. *Physics of Plasmas*, **8**, 3029–3041.

[83] Passoth, E., Kaurdna, P., Csambal, C., Behnke, J. F., Tichy, M., and Helbig, V. (1997) An experimental study of plasma density determination by a cylindrical Langmuir probe at different pressures and magnetic fields in a cylindrical magnetron discharge in heavy rare gases. *Journal of Physics D: Applied PHysics*, **30**, 1763.

[84] Pytlinski, J. T., Donnert, H. J., and Alexeff, I. (1978) Behavior of a single Langmuir probe in a magnetic field. *American Journal of Physics*, **46**, 1276–1278.

[85] Sugawara, M. (1966) Electron probe current in a magnetized plasma. *Physics of Fluids*, **9**, 797–800.

[86] Brown, I. G., Compher, A. B., and Kunkel, W. B. (1971) Response of a Langmuir probe in a strong magnetic field. *Physics of Fluids*, **14**, 1377–1383.

[87] Aikawa, H. (1976) The measurement of the anisotropy of electron distribution function of a magnetized plasma. *Journal of the Physical Society of Japan*, **40**, 1741.

[88] Foster, J. E. and Gallimore, A. D. (1997) The effect of an auxiliary discharge on anode sheath potentials in a transverse discharge. *Journal of Applied Physics*, **81**, 3422–3432.

[89] Foster, J. E. (2002) Intercusp electron transport in an NSTAR-derivative ion thruster. *Journal of Propulsion and Power*, **18**, 213–217.

[90] Piejak, R. B., Godyak, V. A., and Alexandrovich, B. M. (2004) The hairpin resonator: A plasma density measuring technique revisited. *Journal of Applied Physics*, **95**, 3785–3791.

[91] Karkari, S. K., Gaman, C., Ellingboe, A. R., Swindells, I., and Bradley, J. W. (2007) A floating hairpin resonance probe technique for measuring time-resolved electron density in pulse discharge. *Measurement Science and Technology*, **18**, 2649–2656.

[92] Stenzel, R. L. (1975) Microwave resonator probe for localized density measurements in weakly magnetized plasma. *Review of Scientific Instruments*, **47**, 603–607.

[93] Curley, G. A., Maric, D., Booth, J.-P., Corr, C. S., Chabert, P., and Guillon, J. (2007) Negative ions in single and dual frequency capacitively coupled fluorocarbon plasmas. *Plasma Sources Science and Technology*, **16**, S87–S93.

[94] Milosavljevic, V., Karkari, S. K., and Ellingboe, A. R. (2007) Characterization of the pulse plasma source. *Plasma Sources Science and Technology*, **16**, 304–309.

[95] Sands, B. L., Siefert, N. S., and Ganguly, B. N. (2007) Design and measurement considerations of hairpin resonator probes for determining electron number density in collisional plasmas. *Plasma Sources Science and Technology*, **16**, 716–725.

[96] Warne, L. K., Johnson, W. A., Coats, R. S., Jorgenson, R. E., and Hebner, G. A. (2007) Model for resonant plasma probe. Technical Report SAND 2007-2513, Sandia National Laboratories.

[97] Chatterjee, R. (1996) *Antenna Theory and Practice*. New Age International, 2nd edn.

[98] Sun, X., Keesee, A. M., Biloiu, C., and Scime, E. E. (2005) Observations of ion-beam formation in a current-free double layer. *Physical Review Letters*, **95**.

[99] Charles, C., Degeling, A. W., Sheridan, T. E., Harris, J. H., Lieberman, M. A., and Boswell, R. W. (2000) Absolute measurements and modeling of radio frequency electric fields using a retarding field energy analyzer. *Physics of Plasmas*, **2**, 5232–5241.

[100] Beal, B. E. and Gallimore, A. D. (2003) Energy analysis of a hall thruster cluster. *28th International Electric Propulsion Conference*, Tolouse, France, March.

[101] Smith, T. B., Ngom, B. B., Linnell, J. A., and Gallimore, A. D. (2005) Diode laser-induced fluorescence of xenon ion velocity distributions. *41st AIAA/ASME/SAE/ASEE Joint Propulsion Conference*, Tucson, AZ, July, no. AIAA-2005-4406.

[102] Reinsche, C. H. (1967) Smoothing by spline functions. *Numerische Mathematik*, **10**, 177–183.

[103] Bohm, C. and Perrin, J. (1993) Retarding-field analyzer for measurements of ion energy distributions and secondary electron emission coefficients in low-pressure radio frequency discharges. *Review of Scientific Instruments*, **64**, 31–44.

[104] Perry, A., Conway, G., Boswell, R., and Persing, H. (2002) Modulated plasma potentials and cross field diffusion in a helicon plasma. *Physics of Plasmas*, **9**, 3171–3177.

[105] Conway, G., Perry, A., and Boswell, R. W. (1998) Evolution of ion and electron energy distributions in pulsed helicon plasma discharges. *Plasma Sources Science and Technology*, **7**, 337–347.

[106] Reilly, M. P., Miley, G. H., Kritley, D. E., Koo, J., and Hargus, W. (2007) Effects of helicon wave propagation based on a conical antenna design: Part i. Technical Paper ADA473488, Air Force Research Laboratory Edwards AFB CA Propulsion.

[107] Kitajima, T., Izawa, M., Nakano, N., and Makabe, T. (1997) The time-resolved two-dimensional profile of a radio frequency capacitively coupled plasma. *Journal of Physics D: Applied Physics*, **30**, 1783–1989.

[108] Ventzek, P. L. G., Sommerer, T. J., Hoekstra, R. J., and Kushner, M. J. (1993) Two-dimensional hybrid model of inductively coupled plasma sources for etching. *Applied Physics Letters*, **63**, 605–607.

[109] Charles, C. and Boswell, R. (2003) Current-free double-layer formation in a high-density helicon discharge. *Applied Physics Letters*, **82**, 1356–1358.

[110] Kim, M., Keidar, M., and Boyd, I. D. (2009) Two-dimensional model of an electromagnetic layer for the mitigation of communications blackout. *47th AIAA Aerospace Sciences Meeting*, Orlando, FL, January, no. AIAA 2009-1232.

[111] Kline, J. L., Scime, E. E., Boivin, R. F., Keesee, A. M., and Sun, X. (2002) Rf absorption and ion heating in helicon sources. *Physical Review Letters*, **88**.

ABSTRACT

Use of a Helicon Source for Development of a Re-Entry Blackout Amelioration System

by

Kristina Marian Lemmer

Chair: Alec D. Gallimore

During atmospheric re-entry and hypersonic flight, a bow shock forms around the vehicle leading edge. The air becomes super-heated as it passes through the shock, ionizes and forms a plasma sheath. This sheath prevents transmission of electromagnetic waves with frequencies similar to those used for radio communications. This phenomenon is referred to as the "communications blackout." In this dissertation, hypersonic communications blackout is studied, and a method for ameliorating the blackout is presented.

A plasma source was designed and built for the purpose of simulating a re-entry plasma sheath. The plasma number density in a re-entry plasma sheath ranges from 10^{14} m^{-3} to 10^{18} m^{-3}. A helicon source was chosen to simulate the conditions during atmospheric re-entry because it produces high-density plasma while maintaining that density downstream of the source. For this reason, and because the electron temperature downstream of the source (1 eV to 6.5 eV) is of a similar order of magnitude as

that found during re-entry (0.4 eV to 1 eV), the helicon source was deemed appropriate. The Plasmadynamics and Electric Propulsion Laboratory helicon source was found to produce an upstream ion number density of 2.5×10^{19} m^{-3}. Downstream, where experiments with the plasma amelioration system were performed, the number density ranged from 0.55×10^{17} m^{-3} to 3.3×10^{17} m^{-3}, which represent altitudes between 65 km and 75 km.

After characterizing the helicon plasma source, the amelioration system was placed downstream. The **re**-entry and hypersonic vehicle plasma **comm**unications (ReComm) system consists of a single solenoid electromagnet with two electrodes perpendicular to the magnetic field. The crossed fields direct plasma away from a region surrounding an antenna, creating a "window" in the sheath through which radio signals can pass. Langmuir probe, hairpin resonance probe and signal attenuation measurements show that the system is effective at reducing the number density to 80% of that measured when no fields are present. However, the system did not perform as expected. The majority of the reduction occurred with only the presence of the magnetic field. Possible explanations were studied using both analytical methods and COMSOL to model the fields. The shape of the magnetic field itself contributed greatly to the plasma number density reduction.